Université du Québec

Institut National de la Recherche Scientifique

Centre Énergie, Matériaux Télécommunications

THE PRODUCTION OF NOVEL NICKEL AND TITANIUM 3D SKELETON ELECTRODES AND THE SYNTHESIS OF CATALYSTS ON THE NI 3D SKELETON ELECTRODES (NI-WHISKERS) FOR WATER ELECTROLYSIS

Par
Mohsen Fakourihassanabadi

Thèse présentée pour l'obtention du grade de Philosophiae Doctor (Ph.D.)
en sciences de Énergie et Matériaux

Jury d'évaluation

Président du jury et examinateur interne	Shuhui Sun Institut national de la recherche scientifique
Examinateur externe	Houshang Darvishi-Alamdari Laval University
Examinateur externe	Samaneh Shahgaldi University of Quebec at Trois-Rivières
Directeur de recherche	Daniel Guay Institut national de la recherche scientifique

ACKNOWLEDGEMENTS

I would like to express my gratitude to Professor Daniel Guay for granting me the permission to work on two projects simultaneously and providing the necessary conditions to carry out both projects concurrently. He generously provided me with the required resources and facilities to execute these projects. Furthermore, he allowed me to acquire essential training for various equipment, including TEM, XRD, SEM, electrochemistry, and more, which were crucial for the successful completion of the projects. His guidance and collaboration played a significant role in ensuring that both projects progressed swiftly and achieved successful outcomes within a short period of time. I extend my heartfelt appreciation to him.

In addition, I extend my deepest gratitude to Professor Kenneth Beyerlein for his tremendous help and unwavering support during my work on Transmission Electron Microscopy (TEM). His patience and guidance greatly helped me with my TEM project, making the learning process faster and the experiments more efficient, even in a short time. I also extend my thanks to Aida, Rasoul, and Rezvan for their valuable assistance during the TEM analyses. Their contributions have been instrumental in achieving meaningful TEM results in this thesis.

I am also very grateful to Dr. Kashyap for his invaluable assistance in learning electrochemistry. His presence, along with my other colleagues, Somayyeh, Arash, and Navid, has been a constant source of encouragement, and they generously supported me whenever I faced unanswered questions during the project. Their camaraderie made the time in the lab truly enjoyable and delightful. Also, I would also like to express my gratitude to Julie Gaudet for all the efforts she put in. She was always present in the laboratory, working tirelessly to advance the porous titanium project.

I am deeply grateful to my family for their unwavering support throughout my journey. Their encouragement and love have been my pillars of strength. I am truly blessed to have them in my life.

RÉSUMÉ

Il est essentiel de développer des électrocatalyseurs présentant une excellente activité, de faibles surtensions et une rentabilité économique pour les applications de conversion et de stockage d'énergie. Dans cette étude, des méthodes innovantes ont été utilisées pour fabriquer deux structures tridimensionnelles (3D) distinctes destinées à l'électrolyse alcaline de l'eau (AWE) et à l'électrolyse de l'eau avec membrane d'échange de protons (PEMWE), dans le but de surmonter la surtension de la réaction d'évolution de l'oxygène (OER), notamment à haute densité de courant.

Une nouvelle structure tridimensionnelle (whisker de Ni) a été développée en formant un alliage fondu hypereutectique de Ni-Al, suivi d'une solidification directionnelle sur une plaque de Ni. En conséquence d'une lixiviation ultérieure, des whiskers de Ni se forment. En ajustant la masse d'aluminium et le processus de traitement thermique, les whiskers de Ni peuvent être contrôlés en termes de volume, de taille et de distribution. Nous avons optimisé les paramètres pour minimiser la surtension à faible et haute densités de courant. Les résultats ont révélé que l'échantillon optimal nécessite une surtension de seulement 240 mV à 10 mA.cm^{-2} et de 350 mV à 500 mA.cm^{-2}.

Dans cette étude, nous avons synthétisé deux catalyseurs, l'oxyde d'iridium et le LDH Fe-Ni, avec une activité très élevée sur les whiskers de Ni, puis nous avons comparé les résultats obtenus. En résumé, les résultats ont montré que les deux catalyseurs présentaient d'excellentes performances à faible densité de courant. Cependant, à haute densité de courant, les whiskers de Ni-Fe ont surpassé les whiskers de Ni-Ir. Ceci est attribué au détachement du Ni et à l'obstruction ultérieure de la structure lors du dépôt de l'Ir dans des milieux acides, ce qui entrave le transfert de masse.

Une autre approche consiste à produire une couche de transport poreuse (PTL) pour PEMWE via la méthode de dépôt par choc induit par ondes de choc (SWIS), éliminant ainsi le traitement thermique pour la stabilité structurale et mécanique. Deux types de porogènes (Cuivre et Aluminium) ont également été utilisés pour étudier l'effet de la densité du porogène sur l'efficacité du dépôt et la porosité des revêtements obtenus. Le porogène à base d'Aluminium a permis la production de revêtements de PTL à base de titane avec une porosité d'environ 60%, ce qui est une caractéristique très recherchée pour produire des PTL avec une perméabilité gazeuse plus élevée.

Mots-clés: L'électrolyse de l'eau alcaline, l'électrolyse de l'eau à membrane d'échange de protons, la réaction d'évolution de l'oxygène, les électrodes tridimensionnelles, l'eutectique Ni-Al, le Ni de Raney, la couche de transport poreuse, la pulvérisation induite par les ondes de choc.

ABSTRACT

In the realm of energy conversion and storage, developing electrocatalysts that are highly active, cost-effective, and have a low overpotential for oxygen evolution reactions (OER) is imperative. Here, innovative methods were employed to fabricate two distinct three-dimensional (3D) structures for alkaline water electrolysis (AWE) and proton exchange membrane water electrolysis (PEMWE) in order to overcome OER overpotential, especially at high current density.

A novel 3D Ni structure (Ni whisker) is developed by the formation of a hypereutectic molten alloy of Ni-Al, followed by directional solidification on a Ni plate. As a result of subsequent leaching, Ni whiskers are formed. By adjusting Al mass and heat treatment process, Ni whiskers can be controlled in volume, size, and distribution. We optimized the parameters to minimize the overpotential at low and high current densities. The results revealed that the optimal sample requires an overpotential of just 240 mV at 10 mA.cm^{-2} and 350 mV at 500 mA.cm^{-2}.

In this study, we synthesized two catalysts with very high activity (Iridium oxide and Fe-Ni LDH) on Ni-whiskers and compared the results with each other. In summary, the results indicated that both catalysts exhibited excellent performance at low current density. However, at high current density, Ni-Fe-whiskers outperformed Ni-Ir-whiskers. This is attributed to the detachment of Ni whiskers and subsequent blockage of the structure during Ir deposition in acidic media, which hinders mass transport.

Another approach involves producing a porous transport layer (PTL) for PEMWE. The majority of PTLs are made from titanium powder or fibers that are compressed and sintered for structural and chemical integrity. In this study, a Ti-based PTL was produced via Shock-Wave Induced Spraying (SWIS) deposition, eliminating heat treatment for structural and mechanical stability. In conjunction with SWIS process conditions, porogens were examined for their effect on controlling and increasing Ti-based PTL porosity. Two types of porogen (Cu and Al) were used to investigate the effect of porogen density on the deposition efficiency and porosity of the resulting coatings. The Al porogen allowed for the production of Ti-based PTLs coatings with ca. 60% porosity, which is a very desirable feature for producing PTLs with higher gas permeability.

Keywords: Alkaline water electrolysis; Proton exchange membrane water electrolysis; Oxygen evolution reaction; three dimensional electrodes; Ni-Al eutectic; Raney Ni; Porous transport layer; Shock-Wave Induced Spraying

SOMMAIRE RÉCAPITULATIF

PRODUCTION DE NOUVELLES ÉLECTRODES À SQUELETTE 3D EN NICKEL ET EN TITANE ET SYNTHÈSE DE CATALYSEURS SUR LES ÉLECTRODES À SQUELETTE 3D EN NICKEL (Ni-WHISKERS) POUR L'ÉLECTROLYSE DE L'EAU

1. Introduction

La demande croissante en énergie et la préoccupation croissante concernant la pollution environnementale causée par les combustibles fossiles suscitent un grand intérêt de recherche dans le domaine de la conversion et du stockage de l'énergie à partir de sources d'énergie durables alternatives, telles que l'énergie éolienne, solaire et hydraulique. La transition complète vers les énergies renouvelables est impossible sans une solution permettant de combler le fossé entre la génération intermittente d'électricité des énergies renouvelables et la demande. La réaction de dissociation de l'eau offre une méthode pratique et respectueuse de l'environnement pour stocker les énergies renouvelables intermittentes sous forme d'hydrogène et d'oxygène [1, 2, 3, 4].

La technologie d'électrolyse de l'eau peut être classée en quatre catégories : l'électrolyse alcaline de l'eau (AWE), l'électrolyse de l'eau à membrane d'échange de protons (PEMWE), l'électrolyse de l'eau à membrane d'échange d'anions (AEMWE) et l'électrolyse de l'eau à l'état solide (SOWE) [5, 6, 7]. Parmi toutes ces technologies, la PEMWE et l'AWE sont largement considérées comme des technologies prometteuses pour le stockage de l'énergie renouvelable.

L'électrolyse alcaline de l'eau est une technique bien établie pour une utilisation commerciale dans la plage du mégawatt à travers le monde, ce qui permet l'utilisation de matériaux abondants et peu coûteux, car ces matériaux ont une faible solubilité dans ce milieu par rapport aux milieux acides (PEMWE) [8]. En raison de l'environnement acide dans la PEMWE, actuellement, des catalyseurs nobles et des matériaux résistants à la corrosion sont utilisés comme composants de la partie anodique. Bien que l'utilisation de ces matériaux augmente le coût en capital, la PEMWE présente plusieurs avantages par rapport aux méthodes d'électrolyse alcaline de l'eau (AWE). Le processus a une efficacité plus élevée et des taux de transfert d'hydrogène plus bas que les autres processus. De plus, le processus présente une réponse dynamique rapide avec une haute efficacité pour les énergies renouvelables intermittentes en mode de charge partielle ou de surcharge [6, 9, 10, 11]. Certains chercheurs estiment que la PEMWE sera la technologie dominante après 2030. Cependant, toutes les prédictions relatives au développement de toute technologie d'électrolyse sont associées à de l'incertitude, et la plupart des experts conviennent qu'il est essentiel de poursuivre l'avancement simultané de toutes les technologies d'électrolyse [12].

Cette thèse se concentre sur la PEMWE, tandis que l'AWE est considérée comme une technologie prometteuse pour le stockage de l'énergie renouvelable. Pour rendre les deux électrolyseurs économiquement viables pour une utilisation industrielle, il est nécessaire de réduire leurs coûts en capital et d'augmenter leur efficacité [13].

Un des plus grands défis de la division de l'eau est le processus lent de l'évolution de l'oxygène (OER). L'OER se produit en raison de processus de transfert d'électrons couplés à des protons complexes et en plusieurs étapes, et la cinétique de l'OER est beaucoup plus lente que celle de l'évolution de l'hydrogène (HER). Les surpotentiels élevés (>0,35 V) entraînent des pertes significatives de performance dans les cellules de réaction de division de l'eau [14, 15, 16, 17, 18, 19, 20]. Par conséquent, de nouveaux catalyseurs doivent être explorés pour accélérer le processus et augmenter l'efficacité de la réaction [21, 22].

Une réaction d'électrocatalyse consiste généralement en trois étapes : le transfert de charge et la conversion en surface (les réactifs se chimisorbent sur les surfaces de l'électrode et les produits se désorbent), le transport de charge, et le transport de masse [23]. À chaque étape, un surpotentiel se manifeste et le surpotentiel global est déterminé par la somme des surpotentiels [24]. Le surpotentiel global peut être classé en trois catégories : 1- Surpotentiel d'activation dû à l'énergie d'activation du transfert de charge et de la conversion de surface, 2- Surpotentiel ohmique causé par la résistance au transport de charge, et 3- Surpotentiel de transfert de masse [24, 25, 26]. Des efforts sont faits pour réduire le potentiel d'activation en ajustant les compositions des catalyseurs et en introduisant des défauts qui régulent les énergies de liaison [23, 27]. Il est possible de réduire le surpotentiel ohmique d'un système en diminuant la résistance des composants, en contrôlant les concentrations d'électrolyte dans l'électrolyse alcaline de l'eau (AWE) et en concevant une membrane plus fine avec une conductivité plus élevée dans l'électrolyse à membrane cathodique (PEMWE) [24, 28]. Le surpotentiel de transfert de masse diminue également si les réactifs peuvent atteindre rapidement l'électrode [29]. La méthode la plus prometteuse pour y parvenir consiste à recouvrir une nanostructure bien définie d'un catalyseur hautement actif [30] sur une électrode squelettique 3D appropriée présentant une grande surface effective [31].

L'électrode squelettique 3D doit être hautement conductrice et stable dans les milieux acides ou alcalins. En outre, la conception des pores doit permettre de réduire la longueur de diffusion des ions et de faciliter la libération des bulles. Une surface effective élevée et la facilitation de la diffusion des ions et de la libération des bulles contribuent à réduire le surpotentiel de transfert de masse. En outre, la structure 3D doit être produite selon une technique écologiquement durable et peu coûteuse [31, 32, 33].

2. Objectif de la thèse

Dans cette thèse, nous nous concentrons sur la production d'hydrogène par électrolyse de l'eau. Nous mettons l'accent sur la réduction du coût de la production d'hydrogène par le développement de catalyseurs bon marché à haute efficacité et à longue durée de vie pour la réaction d'évolution de l'oxygène (OER). L'augmentation de l'efficacité joue un rôle important dans la réduction du coût de la production d'hydrogène. La production d'électrocatalyseurs avec un potentiel cellulaire plus faible peut avoir un impact significatif sur l'augmentation de l'efficacité. Notre objectif dans cette thèse est de réduire le potentiel de cellule à toutes les densités de courant en augmentant la surface spécifique des catalyseurs. Nous développons deux nouveaux types d'électrodes tridimensionnelles pour les électrolyseurs acides et alcalins, puis nous synthétisons des catalyseurs sur ces électrodes. Cependant, en raison des contraintes de temps, seules les expériences électrochimiques et la synthèse de catalyseurs sur les électrodes tridimensionnelles fabriquées pour l'électrolyte alcalin (Ni-whiskers) seront réalisées.

3. Électrodes squelettes 3D pour PEMWE et électrolyseur alcalin

La section suivante passe en revue les électrodes tridimensionnelles fabriquées pour les environnements AWE et PEMWE. Malgré les fonctions communes des électrodes tridimensionnelles dans le PEMWE et l'AWE, elles ont été développées séparément à l'aide de méthodes différentes en raison de la différence des matériaux utilisés et de la méthode d'assemblage dans l'électrolyseur. C'est pourquoi la structure et les méthodes de construction de ces électrodes sont examinées dans deux sections distinctes.

3.1. Couche de transport poreuse pour PEMWE

La couche de transport poreuses (PTL) est un composant essentiel pris en sandwich entre la membrane recouverte de catalyseur et le canal d'écoulement. Elle est responsable du transport de l'eau et des produits de réaction vers et depuis la surface du catalyseur, ainsi que du transfert des électrons vers la surface du catalyseur. Lorsque la densité de courant augmente, les bulles d'oxygène s'accumulent dans les pores et empêchent l'eau d'atteindre les sites actifs du catalyseur, ce qui augmente le surpotentiel de transport de masse et, en fin de compte, le potentiel global de 25 %. Il est donc très important de faciliter l'élimination des bulles et l'acheminement de l'eau depuis et vers la surface du catalyseur [10]. En outre, les PTLs doivent avoir une conductivité électrique et thermique élevée pour réduire la résistance ohmique et prévenir les dommages thermiques de la membrane. Compte tenu de tout ce qui précède, les paramètres de fabrication des PTLs comprennent le type de matériau, la taille des pores et la porosité [34, 35, 36, 37, 38, 39]. Actuellement, les matériaux de pointe pour la partie anodique sont le titane en raison de son potentiel anodique élevé [40, 41, 42]. Les chercheurs ont constaté que la porosité optimale pour la PTL est de 50 à 75 % [43]. En outre, pour le PTL produit par le processus de métallurgie des poudres, une taille de pore optimale de 10 microns a été rapportée, qui est produite par des particules de 50 à 75 µm [36].

Les PTLs sont fabriquées selon différentes méthodes, notamment à partir de poudres métalliques frittées au four, de lithographie, de coulage sur bande et de pulvérisation au plasma sous vide [44, 45, 46]. Malgré les avantages des poudres métalliques frittées au four et des technologies de coulage sur bande, le processus de frittage dans ces approches augmente le temps et les coûts de fabrication [47]. La pulvérisation de plasma sous vide (VPS) a été étudiée pour supprimer l'étape du traitement thermique. Dans ce processus, les poudres sont fondues et accélérées par un jet de plasma et impactent la surface du substrat, produisant une structure poreuse avec une liaison métallurgique. L'environnement protecteur du VPS minimise l'oxydation des poudres fondues [48]. Cependant, en raison de la fusion des poudres, la valeur de la porosité est limitée à moins de 30 % [49, 50].

Pour bénéficier des avantages du procédé VPS sans fusion de poudre, nous étudions dans cette étude la production de PTL par revêtement par pulvérisation à froid (CGDS) [51] et par le procédé de pulvérisation induite par ondes de choc (SWIS) [49]. Les études indiquent que la porosité du revêtement CGDS est limitée à 30 % [51, 52, 53]. Cependant, les chercheurs affirment que le procédé SWIS est capable de produire un revêtement poreux avec une porosité plus élevée [49].

L'utilisation d'un porogène suivi de son élimination peut augmenter la porosité du revêtement dans tous les processus mentionnés. Les traitements thermiques ou les processus de lixiviation sont des approches qui ont été utilisées pour éliminer le porogène. J.Sun et al. ont créé un revêtement pulvérisé à froid poreux avec une porosité de 49 % en pulvérisant à froid un mélange de Ti+Mg, puis en le traitant thermiquement dans une chambre à vide à 1250°C pour évaporer le Mg [54]. D. Qiu et al. ont également produit un revêtement pulvérisé à froid poreux avec une porosité de 48 % en pulvérisant à froid un mélange de Ti+Al, puis en éliminant l'Al dans une solution de NaOH [55]. Un avantage du processus de lixiviation par rapport au frittage est qu'il peut être réalisé à température ambiante, réduisant ainsi les risques d'oxydation et de changements de microstructure.

3.2. Électrodes 3D pour l'AWE

La méthode la plus prometteuse pour réduire le transport de masse pour l'AWE est de recouvrir le catalyseur sur un substrat de structures 3D avec une surface spécifique élevée. Les scientifiques ont développé de nombreuses structures 3D non nobles telles que le Ni DHBT [56], le fil de Ni [57], la mousse de Ni, l'acier inoxydable ou la maille de Ni [58], le papier carbone [59, 60] et le FTO [61] pour l'OER en milieu alcalin. Bien qu'elles aient toutes une surface élevée par épaisseur, la majorité des structures ne peuvent pas être suffisamment développées dans les trois directions de l'espace (X, Y et Z) pour fournir une surface totale plus élevée. Par exemple, l'épaisseur du DHBT de Ni est limitée à un maximum de 200 μm [56]. En termes de stabilité et de surface, le papier carbone et la mousse de Ni sont des structures 3D appropriées largement utilisées comme squelettes d'électrodes 3D pour le OER. Ces deux éléments peuvent être fabriqués commercialement dans les dimensions souhaitées. Toutefois, il est encore difficile de contrôler avec précision l'espace accessible entre les matériaux actifs déposés sur la structure 3D du papier carbone. La longueur de diffusion des ions augmente considérablement lorsque l'espace est réduit, ce qui entrave la conductivité ionique [62]. C'est la raison pour laquelle la mousse de Ni a attiré beaucoup d'attention pour le OER en milieu alcalin. La mousse de Ni a une conductivité électrique et une stabilité mécanique élevées et contient des éléments de nickel qui permettent de construire facilement un catalyseur composé de Ni sur la surface [58]. Les mousses de nickel ont un pourcentage de porosité très élevé (85-98%) [63] pour faciliter la diffusion des ions dans la structure [64] et la sortie des bulles de la structure [65]. Cependant, ce pourcentage de porosité réduit la surface spécifique [66]. Par conséquent, la conception de la porosité de la structure 3D du Ni doit être reconsidérée. La taille, la distribution, la forme et la connectivité des pores peuvent être des paramètres de conception [67]. Un autre point à prendre en compte est le coût de production de la mousse de Ni. La mousse de Ni est principalement fabriquée à l'aide d'un processus d'électrodéposition dans lequel la mousse de polyuréthane est utilisée comme squelette et subit ensuite un traitement thermique [68]. Les procédures de fabrication sophistiquées et gourmandes en énergie rendent le processus de production coûteux.

Le nickel de Raney (une autre structure 3D du Ni) est largement utilisé dans la synthèse organique et une variété de processus industriels [69] et a été récemment remarqué pour l'OER dans les milieux alcalins [70, 71].

Le Ni de Raney est une structure poreuse de Ni avec une taille de pore inférieure à 5 nm, qui est créée par la lixiviation de l'Al de l'intermétallique Ni-Al (Al_3Ni ou Ni_2Al_3) [72, 73, 74]. Sa surface est plus grande (100 $m^2.g^{-1}$) que celle d'une électrode de Ni classique, ce qui permet d'obtenir plus de sites actifs. Le Ni Raney est fabriqué à l'aide de diverses technologies, notamment l'électrodéposition, la pulvérisation plasma et le laminage à chaud [75, 76, 77].

Malgré les avantages du nickel de Raney, le transport des ions est limité dans la profondeur de la structure en raison de ses structures nanoporeuses. Les nanopores suppriment le flux ionique dans le matériau et font que la plupart des réactions ont lieu à la surface du nickel de Raney (sur une surface 2D) [64].

On trouve dans la littérature des tentatives de réalisation de Raney-Ni en 3D [72, 73, 78]. Étant donné qu'une structure 3D a une surface sensiblement plus grande qu'une structure 2D [79], la mousse de Ni peut être convertie en une structure 3D de Ni de Raney (mousse de Ni de Raney) à l'aide d'un traitement thermique, puis d'un processus de lixiviation. Cependant, le processus de formation de la mousse de Ni de Raney comporte de nombreuses étapes, la première étant la production de la mousse de Ni [80, 81]. Pour supprimer cette étape, nous présentons une nouvelle méthode simple et rentable pour produire un nouveau type de structure 3D de Ni (trichites longues et fines de Ni Raney) qui peut fournir une surface beaucoup plus grande que la mousse de Ni (ou la mousse de Ni Raney) tout en conservant des performances élevées en matière de dégagement d'oxygène. La structure peut être facilement fabriquée pour l'électrodéposition de n'importe quel catalyseur. L'espace entre les fibres étant facilement contrôlable au cours du processus de production, la structure peut être facilement fabriquée pour l'électrodéposition de n'importe quel catalyseur.

Nous avons été inspirés par la structure eutectique Ni-Al pour construire cette structure. Pendant la solidification d'un eutectique fondu de Ni-Al, les fibres d'Al_3Ni poussent de manière préférentielle dans une direction pour former des fibres longues et fines de la phase Al_3Ni, et une phase riche en aluminium (α-Al) se forme ensuite en tant qu'enveloppe autour de la fibre d'Al_3Ni. En conséquence, les fibres d'Al_3Ni sont séparées et bien alignées dans une matrice d'aluminium [82]. Si α-Al est dissous et que l'aluminium est éliminé des fibres d'Al_3Ni à l'aide d'hydroxyde de potassium (KOH), seuls les whiskers de Raney Ni (de type ruban) resteront.

Il n'y a aucun rapport sur la production de fibres de Raney Ni, et tous les rapports sont liés à la poudre ou au revêtement en vrac de Raney Ni [72, 73, 74]. Dans cet article, la relation entre la longueur, la largeur, l'épaisseur et la densité des whiskers (nombre/cm2) avec la surtension de la réaction d'oxydation de l'eau (OER) est discutée, et une nouvelle perspective pour le développement de catalyseurs OER est proposée.

Il n'existe aucun rapport sur la production de fibres de Raney Ni, et tous les rapports concernent la poudre ou le revêtement en vrac de Raney Ni [72, 73, 74]. Dans cet article, la relation entre la longueur, la largeur, l'épaisseur et la densité des whiskers (nombre/cm^2) avec le surpotentiel de la réaction d'évolution de l'oxygène (OER) est discutée, et une nouvelle perspective pour le développement de catalyseurs OER est proposée.

4. Méthodologie

Comme la thèse est divisée en trois chapitres principaux, les expériences sont également structurées en trois sections correspondantes.

4.1. Méthodologie expérimentale pour la production des whiskers de Ni

Des feuilles de nickel ont été utilisées comme substrats. Des feuilles de Ni (99,5%, Alfa Aesar) d'une épaisseur de 1,0 mm et d'une surface de 1 cm^2 ont été découpées et polies avec du papier de verre de grain 600. Elles ont ensuite été lavées avec de l'eau dé ionisée et rincées avec de l'isopropanol. Une masse prédéterminée de poudre d'aluminium a ensuite été déposée sur la surface de chaque substrat. Les échantillons ont été traités thermiquement dans une atmosphère d'argon de très haute pureté (99,999 %) selon le protocole décrit à la Fig.4-2. Le four a d'abord été purgé avec de l'argon afin d'éliminer toute trace d'oxygène. Cette opération a duré 10 minutes à un débit de 80 $ml.min^{-1}$. Ensuite, le protocole suivant a été appliqué. Tout d'abord, la température a été augmentée rapidement (50 $°C.min^{-1}$) pour atteindre la température ciblée. Ensuite, les échantillons ont été maintenus à cette température pendant une durée variable. Pendant les étapes 1 et 2, le four a été purgé avec de l'Ar à un débit de 80 $mL.min^{-1}$. Enfin, le four a été éteint et le débit d'Ar a été augmenté à une valeur indiquée dans le tableau 4-1 pour refroidir les échantillons.

Les échantillons traités thermiquement ont été lixiviés dans une solution de KOH 3 M pendant 24 heures à température ambiante, puis pendant 10 minutes dans du KOH 3 M porté à ébullition. Ensuite, ils ont été lavés dans de l'eau distillée portée à ébullition pendant 20 minutes.

La caractérisation électrochimique dans du KOH 1 M saturé en Ar (Air Liquid, 99,999%) (Fisher Chemical, ACS Reagent grade) a été réalisée dans un système conventionnel à trois électrodes, en utilisant une gaze de Pt et une électrode Hg/HgO remplie d'une solution de KOH 1 M comme électrodes auxiliaire et de référence, respectivement. La distance entre l'électrode de travail et la contre-électrode était de 5 mm et la surface exposée était de 1 cm^2.

L'analyse XRD a été réalisée à l'aide de l'instrument X'pert Pro, avec une cible en Cu (rayonnement Kα pondéré λ = 1,54178 Å) fonctionnant à 45 kV et 40 mA. Les oxydes de surface des échantillons ont été polis à l'aide d'un papier de verre de grain 600 avant de procéder à l'analyse par diffraction des rayons X (DRX). La taille du domaine de diffusion cohérente (τ) a été calculée par l'équation de Debye-Scherrer (équation 39) [72].

La morphologie de la surface des échantillons a été caractérisée par microscopie électronique à balayage (JEOL, JSM-6300F), et leur composition chimique a été évaluée par spectroscopie de rayons X à dispersion d'énergie (EDX) (VEGA3 TESCAN).

Le whisker de Ni a également été examiné par analyse TEM. Dans un premier temps, des fibres de Ni détachées et séparées ont été obtenues en soniquant le S670-1-350 pendant 10 minutes dans de l'eau distillée. Ces fibres ont ensuite été transférées à la surface d'une grille de cuivre Tedpella à l'aide d'une pipette, et la grille a été laissée au repos pendant 12 heures pour permettre à l'eau de sécher. Les fibres ont ensuite été analysées à l'aide d'un microscope électronique à transmission JEOL Ltd. (modèle : JEM 2100, 200kv), qui produit des électrons d'une longueur d'onde de 0,0025 nm.

4.2. Méthodologie expérimentale pour la synthèse de catalyseurs sur les whiskers de nickel (Ni)

Conformément à la section précédente, nous avons généré des échantillons S670-1-350. Toutefois, pour simplifier la nomenclature des échantillons, nous l'avons renommé S1, comme le montre le tableau 5-1.

Les échantillons ont été immergés dans une solution de précurseur K_2IrCl_6 0,001M + HCl 0,01M pendant la durée spécifiée dans le tableau 5-2 pour déposer de l'iridium sur la surface des fibres de Ni. Les échantillons sont nommés en fonction du nom de l'échantillon utilisé dans le tableau 5-1 et de la durée d'immersion.

Pour étudier la synthèse des trichites d'hydroxyde de Ni-Fe, nous avons suivi un processus en deux étapes impliquant des voltammogrammes cycliques (CV) et une immersion. Les voltammogrammes cycliques (CV) dans 1M KOH, entre 0.4 et 1.8 V vs. RHE à 50 mV s^{-1} et 5 mV s-1 ont été effectués trois fois pour convertir les whiskers de Ni des échantillons S1 en $Ni(OH)_2$. Les échantillons ont ensuite été immergés dans 80 mL de 0,1 M KOH ou 0,1 M KOH+10 ppm $FeCl_2.4H_2O$ pendant 20 minutes alors que la solution était agitée à 70℃. Ensuite, les échantillons ont été lavés et conservés dans 100 mL d'eau distillée pendant une heure pour éliminer toute contamination de la profondeur de la structure 3D. Les échantillons ont été renommés après le traitement comme indiqué dans le tableau 5-3.

L'analyse électrochimique, le MEB et l'analyse EDX ont été réalisés de manière similaire à l'explication donnée dans la section précédente.

4.3. Méthodologie expérimentale pour la production de la couche de transport poreuse (PTL)

Cette expérience a utilisé trois poudres de Ti de tailles de particules différentes et deux types de porogènes, notamment des poudres sphériques de Cu et d'Al. Les valeurs D50 des particules de poudre de Ti sont de 30 µm, 73 µm et 90 µm, tandis que la valeur D50 des particules de poudre d'Al est de 83 µm. Les particules de poudre de Cu ont des valeurs D50 de 50 µm et 70 µm, respectivement.

Tout d'abord, trois tailles différentes de particules de poudre de Ti ont été déposées sur la surface de l'acier doux à l'aide du SWIS afin de trouver la taille optimale des particules de poudre de Ti pour obtenir la porosité la plus élevée. Le tableau 6-1 indique le nom des échantillons et la taille des particules de poudre. Le tableau 6-2 présente les paramètres SWIS pour cette étape.

Ensuite, la poudre de Ti (D50=73 µm) a été mélangée à différents pourcentages de poids de poudre de Cu (tableau 6-1). Ils ont ensuite été déposés sur la surface de l'acier doux une fois à l'aide du procédé SWIS et une fois à l'aide du procédé CGDS (les paramètres des deux procédés étaient conformes au tableau 6-2). Les échantillons ont ensuite été lixiviés dans de l'HNO_3 5M pendant une heure sous agitation et lavés dans de l'eau distillée pendant une heure en ébullition et sous agitation.

La poudre de Ti a également été mélangée à différents pourcentages de poids de poudre d'Al (tableau 6-1) et pulvérisée sur la surface de l'acier doux en utilisant le processus SWIS avec les paramètres indiqués dans le tableau 6-2. Les échantillons ont ensuite été soumis à un processus de lixiviation en trois étapes. Ils ont d'abord été lixiviés trois fois, chaque lixiviation étant effectuée dans de la soude caustique (NaOH) fraîche à 6M à 70-90℃ pendant une heure sous agitation. Ensuite, ils ont été lavés dans de l'eau distillée pendant une heure sous agitation et ébullition. Dans l'étape suivante, les échantillons ont été immergés pendant une heure dans de l'acide sulfurique (H_2SO_4) à 0,5 M sous agitation pour détacher le revêtement du substrat. Ensuite, de l'eau distillée a été utilisée pour laver le revêtement détaché pendant une heure sous agitation et ébullition. Trois fois de lixiviation et de lavage ont été effectués dans la dernière étape, similaire à la première étape

La porosité a été obtenue par l'analyse de la section transversale de l'échantillon au moyen d'un microscope optique, Olympus stream motion 2.3.2 (build 17014). La microscopie électronique à balayage (JEOL, JSM-6300F) et les rayons X à dispersion d'énergie (EDX, VEGA3 TESCAN) ont été effectués sur tous les échantillons avant et après la lixiviation.

5. Résultats pour la production de whiskers de Ni

La Fig.4-6 montre une coupe transversale au microscope électronique à balayage (MEB) de l'échantillon S670-1-150 avant la lixiviation. Plusieurs structures ont été identifiées. A la surface du substrat de Ni, on observe une couche continue (D1) dont la composition Ni:Al est de 43:57 at.%. La composition de D1 ne varie pas avec la masse d'Al (Fig.4-7b), ni avec le temps de traitement thermique à 670 °C (Fig.4-7d), bien qu'elle ne forme pas une couche continue pour les plus petites masses d'Al. Pour m = 350 mg, l'épaisseur de D1 augmente de façon logarithmique avec le temps de traitement thermique à 670 °C (Fig.4-7c). Une couche discontinue D2 se forme à la surface de D1, dont la composition Ni:Al est de 25:75 at.%. L'épaisseur de D2 n'est pas uniforme et varie considérablement entre quelques μm et jusqu'à 15-20 μm d'un endroit à l'autre. Au-dessus de D2, on observe une épaisse couche solidifiée composée de structures allongées (whiskers) dispersées dans une matrice solide. La composition Ni:Al des structures allongées était de 25:75 at.%, similaire à celle de D2, alors que celle de la matrice est principalement composée d'Al. Sur la base de la composition Ni:Al de D1 et D2, elles sont attribuées à Ni_2Al_3 et Al_3Ni, respectivement. Sur la base de leur composition, les structures allongées noyées dans la matrice d'Al ont également été attribuées à Al_3Ni. Cette attribution sera confirmée ultérieurement par l'analyse de la diffraction des rayons X. Comme prévu, l'épaisseur de la couche solidifiée augmente linéairement avec la masse d'Al (Fig.S5).

Le diagramme XRD de l'échantillon S670-1-150 avant lixiviation est illustré à la Fig.4-8. Le diagramme XRD a été tracé sur une échelle logarithmique pour faire ressortir les pics de moindre intensité. Deux séries de pics sont observées. La première série est la plus intense et est attribuée à l'Al. La seconde série est à peine discernable sur une échelle linéaire. Ils sont attribués à Al_3Ni (triangles remplis). Cette attribution est cohérente avec la micrographie MEB de la figure 4-6. Compte tenu de la profondeur de pénétration des rayons X et de l'épaisseur de la couche solidifiée de l'échantillon S670-1-150, qui est de 400 μm, on ne devrait pas s'attendre à observer de pics de diffraction provenant de D1, dont la composition Ni:Al est de 25:75 at.%, ni du substrat Ni. L'intensité des pics de diffraction de Al_3Ni ne correspond pas à celle attendue pour une phase polycristalline. Selon la norme PDF 03-065-2418 [83], les pics les plus intenses de l'Al_3Ni polycristallin devraient être (111), (131) et (311), les trois pics ayant la même intensité. Ce n'est pas ce qui est observé dans la figure 4-8, où le pic (230) est le plus intense, ce qui suggère que les trichites d'Al_3Ni se développent le long d'un axe préférentiel perpendiculaire à la famille de plans (230). Ce phénomène a été observé indépendamment de la température maximale du traitement thermique, du temps écoulé à la température maximale du traitement thermique et de la masse d'Al (Fig.4-9).

Les micrographies en microscopie électronique à balayage (MEB) en coupe transversale et en vue de dessus de l'échantillon S670-1-150 après la lixiviation dans la solution de KOH sont présentées dans la Fig.4-11. Après la lixiviation, les whiskers de nickel (Ni), ainsi que les couches D1 et D2, sont observés. La composition Ni:Al des couches D1 et D2 a changé de manière significative, passant de 25:75 et 43:57 at.% avant lixiviation à 93:7 et 88:12 at.% après lixiviation, respectivement. Dans la Fig.4-11, la matrice d'Al qui constituait la majeure partie de la structure solidifiée de l'échantillon tel que préparé est absente. Au lieu de cela, les trichites précédemment intégrées dans la matrice d'Al sont exposées. La teneur en aluminium de la partie supérieure de l'échantillon n'est que de 7 %, ce qui suggère une dissolution presque complète de la teneur en aluminium de la structure solidifiée. Dans la Fig.4-11, chaque whiskers peut atteindre 150 μm de long et avoir une largeur allant de 0,1 μm à 0,5 μm. Ces whiskers sont regroupés pour former des faisceaux.

Le spectre de diffraction des rayons X (XRD) de l'échantillon S670-1-150 après la lixiviation est présenté sur une échelle logarithmique dans la Fig.4-8. Tous les pics peuvent être indexés comme étant du nickel (Ni) métallique, et aucun autre pic n'est observé. En particulier, tous les pics de diffraction attribués à Al_3Ni dans l'échantillon tel que préparé sont absents. Cela suggère non seulement que la matrice d'aluminium a été éliminée lors du processus de lixiviation, mais que l'aluminium a également été dissous à partir des whiskers d'Al_3Ni initialement observés dans la Fig.4-6 pour former des whiskers de Ni. La taille du domaine de diffusion cohérente calculée à partir de la moitié de la largeur à mi-hauteur du pic de diffraction est d'environ 5 nm, ce qui est cohérent avec la formation de whiskers de Ni sous forme de Raney-Ni. Ces résultats sont en accord avec ceux de Tanaka et al., indiquant que le Raney-Ni est obtenu uniquement à partir d'alliages riches en aluminium tels que l'Al_3Ni et le Ni_2Al_3. Selon eux, la forme la plus active de Raney-Ni est obtenue à partir d'Al_3Ni en raison de la lixiviation rapide de l'aluminium [84].

L'analyse de Brunauer-Emmett-Teller (BET) a été utilisée pour examiner les whiskers de Ni. Les distributions de taille de pores des whiskers de Ni sont montrées dans la Fig.4-27b, indiquant qu'ils possèdent une structure mésoporeuse avec une distribution étroite centrée autour d'une taille de pore de 3 nm. De plus, la taille moyenne des pores est de 6 nm, ce qui est similaire à d'autres structures de Raney-Ni rapportées [85, 86].

Les Fig.4-33, 4-34 et 4-35 montrent des images TEM et des motifs de diffraction TEM de trois barbes de Ni. Les bandes noires dans l'image sont les barbes de Ni, et la flèche jaune au milieu des barbes indique leur direction de croissance. Le logiciel ReciprOgraph a été utilisé pour indexer le motif de diffraction. Le logiciel a fourni les espacements interplanaires pour le Ni (Tableau 4-7). Deux plans ont d'abord été indexés en fonction des espacements interplanaires, et le produit vectoriel de ces deux vecteurs a été utilisé pour trouver le plan de projection (plan perpendiculaire à la direction du faisceau). Le plan de projection pour F2, F3 et F4 est respectivement {111}, {100} et {110}. Par conséquent, les mesures de diffraction le long de l'axe X sur les différentes fibres montrent une orientation aléatoire le long de l'axe Z car trois plans de projection différents sont observés. Cependant, les trois fibres ont une orientation similaire pour les flèches jaunes (axe Y) dans la direction <110>. Ainsi, l'axe Y démontre une orientation préférentielle dans la direction <110> le long de l'axe de croissance de la fibre. La Fig.4-36 présente une vue schématique de l'orientation cristallographique des barbes de Ni.

Les chercheurs affirment que le Ni de Raney a une taille de cristallite inférieure à 10 nm [72, 74, 85]. Le diamètre de la zone analysée pour le motif de diffraction TEM (taille du spot) était également de 600 nm. Les motifs de diffraction de monocristaux obtenus à partir de cette zone montrent que la taille des cristallites est de l'ordre de 600 nm ou plus grande.

M. Graf et al. ont étudié l'or nanoporeux pour découvrir pourquoi la cohérence de la diffusion des rayons X dans les structures nanoporeuses produites par dealloying est rompue. Leurs conclusions ont révélé qu'en plus des contraintes internes, des défauts d'empilement et de la petitesse des cristallites [87], la taille des ligaments nuit également à la cohérence de la diffusion des rayons X [88]. Leurs résultats théoriques ont montré que, bien que quasi-monocristallin, la taille des ligaments du réseau poreux influence la diffusion, et les résultats expérimentaux ont également montré que la taille du domaine de diffusion cohérent est égale à la taille des ligaments [88]. Nous n'avons pas pu quantifier la taille des ligaments à l'aide d'analyses SEM ou TEM; cependant, la taille des ligaments du Ni de Raney est rapportée dans la littérature comme étant de 5 à 10 nm [89]. La taille du domaine de diffusion cohérent calculée à partir du schéma de diffraction des rayons X des whiskers de Ni est de 5 nm. À la lumière des résultats de M. Graf et al. [88], les whiskers de Ni ont une taille moyenne de ligament d'environ 5 nm, ce qui se situe dans la plage rapportée pour le Ni de Raney [89]. En conclusion, le whisker de Ni a une taille moyenne de pore et de ligament d'environ 5 nm.

En outre, l'étude a évalué les effets des paramètres de traitement tels que la masse d'Al, la température maximale de traitement thermique et le temps écoulé à la température maximale de traitement thermique sur la structure de l'électrode et les propriétés électrochimiques. Nos résultats suggèrent une corrélation entre la structure solidifiée et les caractéristiques électrochimiques. Le nombre et la distribution des moustaches de Ni, qui déterminent la surface totale des moustaches de Ni-, sont directement proportionnels à la surface totale des fibres d'Al_3Ni. La surface totale d'Al_3Ni dans l'α-Al peut être influencée en modifiant trois variables : le volume de la structure solidifiée, la distribution des fibres d'Al_3Ni et la fraction de volume d'Al_3Ni. Ces variables peuvent être ajustées en modifiant la masse d'Al, la durée du traitement thermique et la température.

L'effet de la masse d'Al sur la surface totale des fibres Al_3Ni en α-Al peut être étudié en comparant les échantillons S670-1-150, S670-1-250 et S670-1-350. L'augmentation de la masse d'Al se traduit par une couche solidifiée plus épaisse ou plus volumineuse, mais n'affecte pas de manière significative la teneur en nickel. Comme la teneur en nickel et le processus de traitement thermique sont identiques, la densité et la distribution des fibres Al_3Ni dans tous les échantillons devraient également être les mêmes. La seule variation entre les échantillons réside dans le volume de la structure solidifiée, ce qui implique que la surface totale des fibres d'Al_3Ni est directement proportionnelle à l'épaisseur de la structure solidifiée (Fig.S5).

La durée et la température du traitement thermique sont des facteurs cruciaux qui influencent la teneur en Ni et la distribution de l'Al_3Ni dans la structure. L'augmentation de l'un ou l'autre de ces paramètres entraîne une augmentation de la teneur en Ni en raison du processus de dissolution du Ni dans l'Al fondu, contrôlé par la diffusion (Fig.4-13). Zhao et al. ont montré que le pourcentage atomique de Ni augmente avec la durée ou la température du traitement thermique [90, 91], ce qui entraîne une augmentation de la fraction volumique des fibres d'Al_3Ni [92]. Une augmentation de la fraction volumique des fibres d'Al_3Ni peut se traduire par une surface spécifique plus élevée des trichites de Ni. Cependant, la distribution de ces fibres peut être affectée par des variations dans le processus de traitement thermique [93].

La Fig.4-14 montre l'impact de la durée du traitement thermique sur la structure. Il est clair que la structure de S670-10-350 est plus grossière que celle de S670-0-350. Par conséquent, la structure plus grossière produit des whiskers de Ni- plus grossiers après la lixiviation, comme le montre la Fig.4-16.

Le processus de formation de fibres d'Al_3Ni dans l'interaction Ni-Al est entravé par l'augmentation de la température des fours [94]. Cependant, il est probable que la nucléation de l'Al_3Ni se produise à une température constante, suivie d'une croissance et d'un grossissement dans les alliages fondus [93]. Lorsque la phase du diagramme Ni-Al et la teneur en Ni des échantillons sont prises en compte, les fibres d'Al_3Ni peuvent devenir stables à 670℃. Par conséquent, une structure plus grossière est formée.

La charge cathodique et la capacité de la double couche sont des indicateurs de la surface spécifique. Comme elles présentent une relation linéaire dans tous les cas (Fig.S14), nous utilisons la charge cathodique pour évaluer la surface spécifique. La Fig.4-40 montre qu'une augmentation de la masse d'Al entraîne une augmentation correspondante de la charge cathodique et de la capacité à double couche. Lorsque la charge cathodique est plus élevée, le taux de réaction est plus important. Par conséquent, comme le montre la Fig.4-41, une augmentation de la masse d'Al entraîne une réduction des surtensions à toutes les densités de courant.

La Fig.4-44 montre comment le processus de traitement thermique affecte la production de whiskers de Ni, indiquant que des temps de traitement thermique plus longs conduisent à la formation de whiskers de Ni plus grossiers, qui ont une surface plus petite, ce qui entraîne une charge cathodique plus faible. Une charge cathodique plus élevée conduit également à un surpotentiel OER plus faible à toutes les densités de courant (Fig.4-45). Cependant, à des densités de courant plus élevées, le surpotentiel du S670-0-35 est plus important que celui du S670-1-350. Ceci peut être attribué à la densité des trichites de Ni montrée dans la Fig.4-16. Une densité de fibres très élevée (ce qui implique une distance plus courte entre les fibres) peut piéger des bulles entre elles, entravant leur échappement. En conséquence, les bulles piégées poussent l'électrolyte loin de la surface de la bande, ce qui provoque une augmentation du surpotentiel. Ainsi, deux facteurs contribuent à la surtension: (1) la surface active des Le whiskers de Ni et (2) la facilitation de l'échappement des bulles.

L'impact des bulles piégées dans la structure sur le surpotentiel OER est également évident dans les échantillons produits à une température de 700℃, comme indiqué dans la Fig.4-45. Les échantillons S700-0-350 et S700-1-350, qui ont une densité de fibres plus élevée que S670-1-350, présentent un surpotentiel OER plus élevé à haute densité de courant. Cependant, le surpotentiel OER pour S700-10-350 et S670-1-350 peut être considéré comme étant le même. Ainsi, une charge cathodique d'environ 7000 mC.cm^{-2} est optimale pour obtenir un faible surpotentiel OER dans les Le whiskers de Ni.

En conclusion, bien qu'une structure en 3D avec des Le whiskers de Ni plus fins et en plus grand nombre résulte en une surface électrochimique active plus élevée, cela peut entraver l'échappement des bulles. Lorsque les bulles sont piégées dans la structure, le transport de masse est entravé et le surpotentiel OER augmente. Par exemple, dans le cas d'une structure en 3D avec des nanopores, toutes les réactions électrochimiques se produisent à la surface de la structure [64, 95]. Par conséquent, il est nécessaire d'affiner la structure pour obtenir une surface spécifique optimale des fibres et la distance entre elles.

Dans cette étude, les échantillons S670-1-350 et S700-10-350 ont montré une performance supérieure par rapport aux autres échantillons. Cependant, étant donné que la production de S670-1-350 nécessite moins de temps et d'énergie, elle a été sélectionnée comme la structure optimale. La comparaison entre S670-1-350 (épaisseur de 0,9 mm) et une mousse de Ni (surface spécifique de 500 m^2.g^{-1}, épaisseur de 1,7 mm, porosité de 94%) dans la Fig.4-46a montre que S670-1-350 a une surface électrochimique active normalisée (C/mm) 312 fois plus grande que la mousse de Ni. Malgré sa grande surface, S670-1-350 montre également une performance supérieure par rapport à la mousse de Ni, indiquant que la structure n'entrave pas le transport de masse.

La structure en whiskers de Ni a des fibres espacées dans la plage du micromètre, ce qui permet un mouvement facile de l'électrolyte et la sortie des bulles de la structure en raison de sa forme. La facilitation de la sortie des bulles réduit les contraintes de compression causées par le piégeage des bulles et réduit le risque de dommages structurels [64, 65]. Pour évaluer la stabilité mécanique de l'échantillon S670-1-35, un test de stabilité de 6 jours (144 heures) a été réalisé à 3 densités de courant différentes (10, 50 et 500 mA.cm^{-2}) (Fig.4-46b). Comme on peut le voir sur la figure, S670-1-35 présente une grande stabilité mécanique à faible et haute densité de courant

Dans cette section, nous avons constaté que S670-1-350 surpassait tous les autres échantillons. Par conséquent, pour synthétiser un catalyseur sur les whiskers de Ni, nous utilisons cet échantillon.

6. Résultats de la synthèse du catalyseur sur les whiskers de Ni

Deux catalyseurs ont été synthétisés sur la surface des whiskers de Ni, et leurs résultats sont expliqués dans deux sections différentes.

6.1. Effet de la synthèse de l'oxyde d'ir

Les échantillons après immersion dans la solution ont été analysés par MEB et EDX. L'analyse MEB de S1-20Ir dans la Fig.5-2 montre que la majorité de l'Ir préfère précipiter en grappes au sommet des fibres et former un revêtement d'Ir non continu sur la surface.

Le mécanisme de formation de l'Ir sur les whiskers de Ni implique la dissolution du Ni dans un milieu acide, suivi de la déposition de l'Ir, comme indiqué dans l'équation suivante [96, 97]:

$$[IrCl_6]^{2-} + 2Ni \rightleftarrows Ir + 2Ni^{2+} + 6Cl^-$$

Le Ni est dissous dans la solution sous forme de Ni^{2+} et l'Ir^{2+} est réduit à la surface des fibres [97]. Comme le montre la Fig.5-3, le pourcentage atomique d'Ir déposé est de 3,5 at. % après 2 heures d'immersion. Le pourcentage atomique d'Ir augmente à plus de 10 at. % après 20 heures d'immersion.

Comme indiqué précédemment dans la section expérimentale, un CV à un taux de 50 mV.s^{-1} a été effectué trois fois. Au cours du processus d'acquisition du CV, certaines fibres se sont détachées des whiskers de Ni- et se sont déposées au fond du récipient. Le nombre de fibres était négligeable pour S1-2Ir et S1-5Ir, mais significatif pour S1-20Ir. Comme le montre la Fig.S18, après avoir effectué un CV à 50 mV.s^{-1}, plus de la moitié des fibres de S1-20Ir sont détachées. La dissolution du Ni en milieu acide provoque le détachement des fibres.

Après avoir effectué le CV à 50 mV.s-1, les expériences se sont poursuivies dans une solution fraîche de KOH 1M. La Fig.5-4 illustre les voltammogrammes cycliques à 5 mV.s-1 et la Fig.5-5 montre l'effet du temps d'immersion sur la charge cathodique pour l'échantillon S1-A à différents temps d'immersion. La charge cathodique augmente avec le temps d'immersion. Cependant, en raison d'une dissolution importante du Ni après 12 heures, certaines fibres sont détachées (lors de l'exécution du CV à 50 mV.s-1) et entraînent une diminution de la charge cathodique. La charge cathodique augmente par deux mécanismes en fonction du pourcentage atomique d'Ir :

1) L'incorporation d'Ir dans le film d'oxyhydroxyde de Ni modifie le comportement redox du couple Ni(OH)2/NiOOH et 2) La rugosité de la surface causée par la dissolution du Ni [96].

La Fig.5-7 montre l'effet du dépôt d'Ir et du détachement des fibres de Ni sur le surpotentiel de l'OER à 10, 50, 250 et 500 mA.cm^{-2} pour l'échantillon S1-A à différents temps d'immersion. Il convient de mentionner que le temps d'immersion zéro dans la figure correspond au surpotentiel de l'OER pour S1-A. Les résultats montrent qu'une augmentation du temps d'immersion réduit le surpotentiel à 10 mA.cm^{-2}. Le surpotentiel de l'OER pour S1-12Ir diminue significativement, atteignant 197 mV, ce qui est comparable aux résultats de M. Hao et al. [98].

Le dépôt d'Ir a également un impact positif sur le surpotentiel de l'OER à 50 mA.cm^{-2}. Le surpotentiel à 50 mA.cm^{-2} pour S1-5Ir et S1-12Ir est de 255 mV, soit 15 mV de moins que S1-A. Cependant, bien que le dépôt d'Ir ait un effet positif sur le surpotentiel de l'OER à faible densité de courant, le surpotentiel enregistré à haute densité de courant (250 et 500 mA.cm^{-2}) est supérieur à celui de S1-A. L'augmentation du surpotentiel est attribuée à deux facteurs : le détachement des fibres et la formation de grappes d'iridium qui bloquent la structure. Ces problèmes limitent davantage le transport de masse à haute densité de courant, ce qui entraîne une augmentation du surpotentiel à ces niveaux [33, 99, 100].

Il reste une question de savoir si la structure en 3D présente une limitation pour une haute densité de courant. Dans la prochaine étape, la synthèse du catalyseur sur la structure en 3D a été réalisée dans un milieu basique pour éviter les détachements de fibres et répondre à cette question.

6.2. Synthèse de l'hydroxyde de Ni-Fe

Les échantillons après dopage au Fe ont été analysés à l'aide d'analyses SEM et EDX. La Fig.5-8 montre que 3 at.% de Fe sont uniformément dopés dans les fibres de Ni sans bloquer la structure.

L'incorporation de Fe dans l'hydroxyde de Ni est un phénomène bien connu qui produit le catalyseur le plus actif pour l'OER dans une solution basique. Pendant l'immersion de $Ni(OH)_2$, Fe_{+2} est d'abord adsorbé à la surface des whiskers de Ni, puis incorporé avec l'hydroxyde de Ni pour former de l'hydroxyde de Ni-Fe [101, 102, 103, 104, 105].

Sur la base des courbes d'oxydation et de réduction pour les échantillons S1-A et S1-Fe, il est évident que la densité de courant d'oxydation ou de réduction diminue lorsque le Fe est incorporé. Cela peut être observé sur la Fig.5-9, où le pic d'oxydation devient significativement plus large et plus difficile à identifier après l'incorporation de Fe. De plus, la densité de courant de réduction (charge cathodique) est réduite de 30% après l'incorporation de Fe. M.B. Stevens et al. [101] ont exploré l'impact de la teneur en Fe sur la charge cathodique dans $Ni(OH)_2$ dopé au Fe. Les résultats de l'étude ont montré qu'en augmentant la teneur en Fe dans la structure, la charge cathodique diminue tandis que l'activité d'OER s'améliore, et que la charge cathodique diminue de 30% pour les échantillons avec 25% en poids de Fe dopé [103]. Il convient de noter que les changements dans la structure électronique de la co-électrodéposition de l'hydroxyde de Ni-Fe sont différents de ceux du $Ni(OH)_2$ dopé au Fe. Le Fe est dispersé de manière homogène dans la structure de la co-électrodéposition de l'hydroxyde de Ni-Fe, ce qui entraîne des changements dans la structure électronique de sorte que la charge cathodique pour cette structure augmente avec l'ajout de Fe [101].

La dopage en Fe de l'échantillon S1-A diminue le surpotentiel OER à 10 $mA.cm^{-2}$ à 208 mV, ce qui est comparable aux échantillons de dépôt d'Ir. X. Li et al. ont affirmé que l'activité OER du NiFe est même supérieure à celle des catalyseurs Ir de référence dans les milieux alcalins [106]. De plus, la formation du catalyseur Ni-Fe ne bloque ni n'endommage la structure de S1-Fe et permet à S1-Fe de nécessiter significativement moins de surpotentiel OER aux densités de courant élevées que S1-Ir déposé.

Les fibres LDH Ni-Fe dans cette étude présentent de meilleures performances que les autres catalyseurs LDH Ni-Fe rapportés ou les structures 3D de LDH Ni-Fe, tant à basse qu'à haute densité de courant dans 1 M KOH [101, 102, 103, 106, 107, 108, 109]. Il est à noter que les whiskers de Ni contiennent 7 at.% d'aluminium [110] Il a été suggéré que l'aluminium a un effet additif sur l'activité OER des LDH Ni-Fe [109].

7. Les résultats pour la production de la couche de transport poreuse (PTL)

Les résultats sont décrits dans quatre sections.

7.1 Optimisation de la porosité du revêtement

Dans une première série d'expériences, les trois différents types de poudre de Ti ont été pulvérisés sur des substrats en acier doux afin de déterminer l'effet de la taille des particules sur la porosité du revêtement obtenu. La Fig.6-3 montre des images SEM en coupe transversale d'échantillons de Ti-30, Ti-73 et Ti-90 produits par le procédé SWIS. Les zones blanches représentent le Ti et les zones noires les pores remplis par l'époxy. Afin de déterminer la porosité, une image au microscope optique de l'ensemble du revêtement a été acquise (Fig.S19). Ensuite, à l'aide du logiciel Olympus, le rapport (surface des pores) / (surface des pores + surface du Ti) a été calculé. La porosité des différents revêtements est indiquée dans le tableau 6-3.

La porosité des revêtements augmente à mesure que la taille des particules de Ti est augmentée de 30 à 73 µm. Dans le processus SWIS, la vitesse d'impact des particules diminue avec l'augmentation de la taille des particules, ce qui entraîne une réduction de la déformation des particules au point d'impact et provoque une augmentation de la porosité du revêtement [111, 112] Cependant, dans nos conditions expérimentales, cet effet se stabilise pour les particules de Ti plus grandes. Dans nos conditions de fonctionnement, la porosité maximale du revêtement pouvant être atteinte en modifiant la taille des particules de Ti est de 40%.

Dans le but d'augmenter davantage la porosité de la couche de transport poreuse à base de Ti, différents pourcentages en poids de poudre de Cu-70 µm ont été mélangés avec de la poudre de Ti-73 µm, et le mélange a été déposé sur des substrats en acier doux, d'abord en utilisant le processus SWIS, puis le processus CGDS.

7.2. Effet du porogène Cu sur la porosité des revêtements de Ti préparés par la technique SWIS

La Fig.6-4 illustre les micrographies SEM en coupe transversale des revêtements Ti+Cu produits par la technique SWIS. Les particules grises sont du Ti et les particules blanches du Cu. Les particules de Cu sont dispersées de manière homogène dans le revêtement. Après lixiviation dans HNO_3, la plupart des particules de Cu initialement présentes ont été dissoutes et ne sont plus observées dans les micrographies SEM.

L'effet de la teneur en Cu dans l'alimentateur de poudre sur la teneur en Cu des revêtements déposés a été évalué. Comme on peut le voir dans la Fig.6-5a, une augmentation de la teneur en Cu dans l'alimentateur de poudre entraîne une augmentation de la teneur en Cu du revêtement. Cependant, il existe une différence significative entre la teneur en Cu dans l'alimentateur et celle dans le revêtement.

Les rapports précédents ont montré que la composition d'un revêtement composé de deux matériaux différents A et B dépend de la teneur en A et B dans l'alimentateur de poudre ainsi que du rapport d'efficacité de dépôt (DE) de A et B, $\frac{DE_A}{DE_B}$. L'efficacité de dépôt d'un matériau dépend des paramètres de pulvérisation, de la taille des particules et du type de matériau. De plus, lorsque les propriétés mécaniques et physiques de deux poudres sont significativement différentes, l'interaction entre les poudres peut affecter la composition chimique du revêtement [113].

Pour déterminer le DE des particules de Cu, de la poudre de Cu-70 µm a été déposée sur de l'acier doux en utilisant les mêmes paramètres SWIS que ceux détaillés dans le tableau 6-2. Les résultats ont révélé qu'aucune particule de Cu-70 µm n'a été déposée, même avec une augmentation de la température du gaz à 800℃ ou une diminution à 350℃. Cependant, le Cu-50 µm avec une taille de particules plus petite a été déposé avec succès. Une comparaison des résultats indique que Cu-70 µm n'a pas atteint une vitesse de particules suffisamment élevée en utilisant les paramètres de dépôt en raison de la densité des particules de Cu qui est deux fois supérieure à celle du Ti. Néanmoins, en raison de l'interaction des poudres ou des particules de Cu piégées sur la matrice de poudre de Ti, certaines particules de Cu ont été incorporées dans le revêtement.

Comme le montre la Fig.6-5b, une augmentation de la teneur en Cu dans le chargeur de poudre diminue la porosité du revêtement obtenu, bien que cet effet se stabilise pour la teneur en Cu la plus élevée. Cela est très probablement lié à la plus grande déformation des particules de Cu lors de l'impact sur le substrat par rapport aux particules de Ti [51, 53]. Après lixiviation, tous les revêtements se séparent du substrat car le taux de corrosion de l'acier doux dans l'HNO3 est élevé [114]. Comme mentionné ci-dessus, il ne reste presque aucune particule de Cu dans le revêtement après lixiviation, ce qui indique que la solution acide doit avoir un accès facile à la surface et à la masse du revêtement. Cela est vrai même pour le revêtement le plus épais. La diffusion de la solution acide vers la masse du revêtement doit être favorisée par la porosité initiale du revêtement, qui résulte de l'utilisation de particules de Ti avec une valeur D50 de 73 µm. Même le revêtement le plus épais étudié dans la présente étude n'est pas endommagé ou fissuré en raison du processus de lixiviation. Comme prévu, la lixiviation des particules de Cu d'un revêtement augmente sa porosité (Fig.6-5b). Cette augmentation est telle que la porosité du film après lixiviation ne dépasse pas environ 45%, ce qui est la porosité des films préparés en utilisant uniquement des particules de Ti de la même taille. Cette observation renforce le fait que les particules de Cu sont plus déformables que les particules de Ti et bloquent les pores que l'assemblage de particules de Ti crée. Ainsi, dans le but de maximiser la porosité du revêtement de Ti, nous avons basculé du processus SWIS au processus CGDS, en utilisant toujours du Cu comme porogène.

7.3. Effet du porogène Cu sur la porosité des revêtements de Ti préparés par la technique CGDS

La Fig.6-6a montre une micrographie typique en coupe transversale obtenue par MEB d'un revêtement Ti+Cu déposé par la technique de projection à froid. Les particules de couleur gris foncé correspondent au Ti, tandis que les particules de couleur gris clair représentent le Cu. La micrographie en MEB du revêtement Ti + Cu déposé par la technique CGDS montre qu'il est dense, avec quasiment aucune porosité. Les revêtements CGDS préparés en utilisant différentes combinaisons de Ti et Cu dans l'alimentation présentent la même morphologie, avec peu de pores, comme illustré dans la Fig.6-6d, la porosité de tous les revêtements CGDS étant inférieure à 8%. On observe une réduction significative de la porosité des revêtements CGDS par rapport à ceux préparés par la technique SWIS. Ceci est attribué à la vitesse plus élevée des particules dans le processus CGDS, qui les déforme considérablement lors de l'impact sur le substrat, conduisant ainsi à des dépôts plus denses [51, 52, 53].

Il y a plus de particules de Cu dans les revêtements CGDS que dans les revêtements SWIS correspondants obtenus avec le même mélange d'alimentation. Ceci est confirmé par les données de la Fig.6-6c, qui montre la variation de la teneur en Cu dans le revêtement CGDS par rapport à la teneur en Cu dans le mélange d'alimentation. Pour la teneur en Cu la plus élevée dans le mélange d'alimentation (60 % en poids), la teneur en Cu dans le revêtement déposé par CGDS est de 35 % en poids, contre 25 % en poids pour la technique SWIS. On pense que la vitesse plus élevée des particules de Cu dans le revêtement Ti-Cu CGDS explique l'augmentation du pourcentage pondéral de Cu par rapport au revêtement SWIS. Cependant, contrairement à la technique SWIS, la forte déformation des particules de Ti a produit un revêtement dense dans le CGDS, ce qui indique une plus grande vitesse des particules dans le CGDS.

Les échantillons ont été soumis à une lixiviation dans un milieu acide pour dissoudre le Cu et augmenter la porosité. Comme le montre la Fig.6-6b, l'image en microscopie électronique à balayage du revêtement lixivié indique que les particules de Cu ont été dissoutes à partir de la surface du revêtement. Cependant, elles sont toujours présentes dans le cœur du revêtement. Par conséquent, une surface rugueuse avec une porosité élevée s'est formée à la surface du revêtement, mais la porosité de la partie centrale du revêtement n'a pas augmenté. Manifestement, la solution acide n'atteint pas les particules de Cu incorporées dans le cœur du revêtement car le revêtement déposé a une porosité très faible, et les particules de Cu ne sont pas connectées entre elles.

Bien que les films préparés par la technique CGDS contiennent plus de Cu que les films correspondants préparés par SWIS, l'absence de porosité et de % en poids de Cu dans les films CGDS tels que déposés signifie que la solution acide a un accès limité aux particules de Cu. En effet, la solution acide n'a accès qu'aux particules proches de la surface et ne peut donc pas dissoudre les particules de Cu qui se trouvent au cœur du revêtement. Il est évident que le choix d'un porogène dans la technique CGDS doit tenir compte des particularités de cette technique de dépôt. En raison des vitesses de particules impliquées dans le processus CGDS ou SWIS, il est essentiel de diminuer la densité des particules du porogène afin d'augmenter la vitesse des particules et le DE du porogène. En conséquence, des particules d'Al ont été choisies comme porogène.

7.4. Effet du porogène Al sur la porosité des revêtements de Ti préparés par la technique SWIS

Les figures 6-7 montre les images de microscopie optique en coupe des échantillons de Ti20Al, Ti30Al et Ti40Al tels que déposés avant la lixiviation. Les zones grises représentent l'aluminium et les zones blanches les particules de Ti. Comme on peut le voir, les particules d'Al sont réparties de manière homogène dans les revêtements. D'après l'analyse EDX, une augmentation de la teneur en Al du mélange d'alimentation entraîne une augmentation de la teneur en Al dans le revêtement (Fig.6-8a). La teneur en Al dans le revêtement SWIS est plus importante que la teneur en Al dans le mélange d'alimentation, ce qui contraste avec les résultats du Ti+Ni déposé par Nikbakht et al. [115] et nos propres résultats pour le Ti+Cu déposé par la technique CGDS ou SWIS. Comme indiqué précédemment, cela est dû à la densité plus faible de l'Al par rapport au Ni et au Cu, ce qui entraîne une plus grande vitesse des particules et une plus grande efficacité de dépôt des particules d'Al [111, 115].

La porosité des revêtements Ti + Al tels que déposés était d'environ 15 %, ce qui est inférieur à la porosité des revêtements SWIS préparés uniquement à partir de la poudre Ti-73 (Tableau 6-3) et inférieur à la porosité des revêtements SWIS préparés à partir d'un mélange de poudres Ti et Cu (Fig.6-5b). Encore une fois, cela doit être lié à la capacité des particules d'Al à se déformer lors de l'impact sur le substrat et à remplir les pores qui se seraient formés si seule la poudre Ti-73 avait été utilisée.

La lixiviation des revêtements SWIS Ti + Al a été effectuée selon la procédure décrite dans la section expérimentale, et une analyse par microscopie optique en coupe transversale a été réalisée après chaque étape. La première étape du processus de lixiviation, qui consiste à immerger successivement le revêtement SWIS Ti20Al dans une solution alcaline avant de l'immerger dans de l'eau déminéralisée, est capable de dissoudre la plupart des particules d'Al sur le dessus et les côtés du revêtement (Fig.6-9b). Cependant, plusieurs particules d'Al étaient encore présentes dans le revêtement près de l'interface entre le substrat et le revêtement. Pour créer un squelette de Ti 3D autoporté et éliminer ce qui reste de particules d'Al dans le revêtement, l'échantillon a été immergé dans du H_2SO_4 0,5 M pour détacher le revêtement du substrat (voir la section expérimentale pour plus de détails). Une fois détaché du substrat, le revêtement autoportant a été lixivié trois fois dans NaOH pour dissoudre les particules d'Al restantes. À la fin du processus, toutes les particules d'Al ont été dissoutes sans endommager le revêtement autoportant qui a conservé son intégrité mécanique (Fig.6-9c). Après la lixiviation, la teneur en Al du revêtement autoportant était proche de zéro (Fig.6-8a) et la porosité avait augmenté pour atteindre une valeur supérieure à 60 %, comme on peut le voir sur la Fig.6-8b. Deux répétitions ont été effectuées, conduisant à des résultats similaires (Fig.6-8a et 6-8b).

La lixiviation de l'aluminium des revêtements SWIS Ti40Al a entraîné la désintégration complète de ces échantillons. On soupçonne que la teneur en aluminium de ces échantillons est si élevée que le nombre de contacts entre les particules de Ti n'est pas suffisant pour assurer l'intégrité mécanique de l'électrode une fois les particules d'aluminium dissoutes. Certaines parties des revêtements SWIS Ti30Al lessivés étaient mécaniquement stables, bien qu'il n'ait pas été possible d'obtenir des électrodes complètes de la taille de celles observées à la Fig.6-9.

Des électrodes poreuses autoportantes en Ti d'une épaisseur supérieure à 2 mm et d'une surface géométrique supérieure à 1 cm2 ont pu être préparées avec une porosité supérieure à 60 %. Cette porosité est supérieure à celle obtenue avec des PTL à base de Ti préparées par le processus de frittage de poudre [116], la pulvérisation à froid [54, 55] et le processus de pulvérisation plasma sous vide [117]. Avec ces techniques de préparation, la porosité est inférieure à 50 % [49], ce qui est inférieur à la porosité optimale pour les PTL, qui doit être comprise entre 50 et 75 % [43].

8. Conclusion

Des méthodes innovantes ont été utilisées pour produire deux squelettes d'électrodes 3D différents pour l'électrolyse de l'eau alcaline (AWE) et l'électrolyse de l'eau par membrane échangeuse de protons (PEMWE).

Pour les AWE, une nouvelle structure de squelette 3D en nickel (whiskers de Ni) a été développée, qui se compose d'un grand nombre de whiskers de Ni avec une surface électrochimique exceptionnellement élevée. Pour produire les whiskers de Ni, de l'aluminium a été fondu à la surface du Ni pour créer un alliage hypereutectique de Ni-Al, qui a ensuite été solidifié de manière directionnelle, suivi de la lixiviation. Les whiskers de Ni possèdent une structure nanoporeuse, avec une épaisseur mesurant dans la plage de quelques centaines de nanomètres. Les résultats de la microscopie électronique à transmission (TEM) révèlent une orientation cristallographique préférentielle dans les whiskers de Ni, les distinguant des structures polycristallines. Ces whiskers sont également très stables mécaniquement, comme le montrent les expériences galvanostatiques menées pendant six jours à une densité de courant de 500 $mA.cm^{-2}$.

La masse d'Al et le processus de traitement thermique contrôlent le volume, la taille et la distribution des trichites de Ni.

En augmentant la masse d'aluminium, la capacité de double couche et la charge cathodique augmentent, réduisant ainsi la surtension à toutes les densités de courant mesurées.

Au fur et à mesure que le temps écoulé à une température maximale (durée du traitement thermique) augmente, des whiskers de Ni plus grossiers se forment. Il en résulte une réduction de la densité des whiskers de Ni, une augmentation de l'espacement des whiskers de Ni et une diminution de la charge cathodique.

D'autre part, l'augmentation de la température maximale augmente la teneur en Ni dans l'alliage fondu, ce qui se traduit par une plus grande densité de trichites de Ni, qui se traduit par une distance plus faible entre les trichites de Ni et une augmentation de la charge cathodique.

Initialement, une augmentation de la charge cathodique réduit le surpotentiel requis pour les réactions d'évolution de l'oxygène (OER) à des densités de courant élevées. Cependant, pour les whiskers de nickel avec une densité trop élevée, cette augmentation de la charge cathodique peut entraîner une augmentation subséquente du surpotentiel requis pour les OER. La raison de ce phénomène réside dans l'existence de bulles piégées à l'intérieur de la structure des whiskers de nickel, ce qui entrave le transport de masse. Il est donc impératif d'ajuster la distance entre les whiskers de nickel pour faciliter un transport efficace de la masse et éviter d'entraver les OER.

L'échantillon optimal a été produit à 670°C avec un temps de traitement thermique de 1 minute, nécessitant des surpotentiels de 245 mV et 345 mV pour atteindre des densités de courant de 10 $mA.cm^{-2}$ et 500 $mA.cm^{-2}$ respectivement. Le faible surpotentiel est attribué à la très grande surface électrochimique, et non à l'incorporation de Fe, car l'ajout de 10 ppm de $FeCl_2$ à l'électrolyte a entraîné des réductions significatives du surpotentiel.

Pour réduire le surpotentiel d'activation, deux catalyseurs différents ont été synthétisés sur les whiskers de Ni.

Le premier catalyseur était l'Ir, connu pour sa grande activité dans la réaction d'évolution de l'oxygène (OER). Un processus d'échange de cations a été utilisé pour déposer de l'Ir sur les whiskers de Ni. Une couche non continue d'Ir a été observée sur les whiskers de Ni grâce à des analyses en microscopie électronique à balayage (SEM) et à la spectrométrie de dispersion d'énergie (EDX). En conséquence du dépôt d'Ir, le surpotentiel d'OER a été significativement réduit à faibles densités de courant.

Bien que l'Ir déposé réduise les surpotentiels d'OER à faibles densités de courant, il les augmente à fortes densités de courant. Les augmentations du surpotentiel sont attribuées à des structures de blocage causées par une distribution inégale de l'Ir et à la détachement des fibres en raison de la dissolution du Ni dans des environnements acides.

Le dopage du Fe dans les whiskers de Ni en tant qu'autre catalyseur a été réalisé grâce à l'utilisation d'un processus d'immersion simple. Les analyses EDX et SEM ont confirmé que le Fe était uniformément réparti dans toute la structure sans bloquer ni détacher les fibres. En conséquence du dopage du Fe, la densité de courant de fond de l'oxydation et de la réduction redox a été réduite. De plus, le Fe a significativement augmenté l'activité de l'OER. L'hydroxyde de Ni dopé au Fe est presque aussi performant que les échantillons déposés à l'Ir à des densités de courant faibles, tout en conservant des performances élevées de l'OER à des densités de courant élevées.

Selon l'étude, la technique de dépôt SWIS peut créer des revêtements de Ti poreux avec une porosité allant jusqu'à 40%. À mesure que la taille des particules augmentait de 30 µm à 73 µm, la porosité du revêtement augmentait de 25% à 40%. Cependant, il n'y avait pas d'augmentation supplémentaire de la porosité pour les tailles de particules supérieures à 73 µm.

Les techniques CGDS et SWIS ont toutes deux été utilisées avec succès pour créer des revêtements de Ti+Cu, avec des mélanges d'alimentation contenant jusqu'à 60% de Cu. Les résultats ont indiqué que le pourcentage en poids de Cu dans le revêtement était beaucoup plus bas que dans l'alimentation. En raison de leur haute densité, les particules de Cu n'ont pas pu atteindre une vitesse de particules suffisante pendant le processus de revêtement, ce qui a entraîné une teneur en Cu inférieure dans les revêtements.

En utilisant la technique CGDS, une vitesse de particules plus élevée a été obtenue, ce qui a entraîné une teneur en poids en Cu plus élevée dans les revêtements CGDS par rapport aux revêtements SWIS. Cependant, les revêtements CGDS manquent d'interconnectivité, ce qui signifie que le Cu ne peut pas être lessivé de leur cœur. En revanche, le Cu dans les revêtements SWIS peut être complètement lessivé. Cependant, cela a entraîné une porosité maximale similaire à celle des revêtements en titane pur.

La technique SWIS a également permis de produire des revêtements Ti+Al avec une teneur élevée en Al à partir de mélanges d'alimentation contenant jusqu'à 40% d'Al. Le revêtement dans ce cas contenait une teneur en Al beaucoup plus élevée que le mélange d'alimentation. L'efficacité de dépôt plus élevée des particules d'Al peut être attribuée à leur vitesse plus élevée due à leur densité plus basse par rapport au Ti. Après la lixiviation de l'Al du revêtement Ti20Al, une porosité supérieure à 60 % a été obtenue.

Table of Contents

List of Tables

List of Figures

LIST OF EQUATIONS

(1) $M = \frac{Q}{F\mathrm{Z}}$

(2) $A_1(s) \rightarrow A_1^{\mathrm{Z}+}(aq) + \mathrm{Z}e^-$

(3) $H^+ + e^- = H_{ad},$

(4) $H^+ + e^- + H_{ad} = H_2,$

(5) $2H_{ad} = H_2$

(6) $H_2O + e^- \rightarrow H_{ads} + OH^-,$

(7) $H_{ads} + H_2O + e^- \rightarrow H_2 + OH^-$

(8) $2H_{ads} \rightarrow H_2$

(9) $OH^- + M \rightarrow M - OH + e^-$

(10) $M - OH + OH^- \rightarrow M - O + H_2O + e^-$

(11) $2M - O \rightarrow 2M + O_2 + 2e^- \ / M - O + OH^- \rightarrow M - OOH + e^-$

(12) $M - OOH + OH^- \rightarrow O_2 + H_2O + e^- + M$

(13) $\Delta\mathrm{G} = -\mathrm{nF}E$

(14) $\Delta G^0 = -\mathrm{nF}E^0$

(15) $\Delta G = \Delta G^0 + RTlnQ$

(16) E (T, P) = $E^0(25℃, 1\ \mathrm{atm}) - \frac{RT}{nF}lnQ$

(17) $E_T = -\frac{\Delta H}{nF}$

(18) $j = j_{cathode} - j_{anode} = FAk^0\left(C_0(0,t)e^{-\alpha f(E-E^0)}\right) - C_R(0,t)e^{f(1-\alpha)\left(E-E^0\right)})$

(19) $j = j_0\left[e^{(\frac{(1-\alpha)nF\eta}{RT})} - e^{-(\frac{\alpha nF\eta}{RT})}\right]]$

(20) j=$\frac{j_0 nF\eta}{RT}$

(21) $R_{ct} = \frac{RT}{nFj_0}$

(22) $\epsilon_{cell} = \frac{energy\ requirement\ under\ reversible\ conditions}{energy\ requirement\ under\ irreversible\ conditions} = \frac{W_{rev}\ (Jmol^{-1})}{W_{irrev}\ (Jmol^{-1})}$

(23) $\varepsilon_{cell,ther} = \frac{\Delta H_{rev}}{\Delta H_{rev} + nF\eta_{loss}}$

(24) $\varepsilon_{cell} = \frac{\Delta H_{rev}}{\Delta H_{rev} + nF\eta_{loss}} = \frac{\Delta G_{rev} + \Delta Q_{rev}}{\Delta G_{rev} + \Delta Q_{rev} + nF\eta_{loss}} = \frac{\Delta G_{rev} + \Delta Q_{rev}}{nFE_{cell} + \Delta Q_{rev}} = \frac{\Delta G_{rev}\ (1+ \ ^{\Delta Q_{rev}}/_{\Delta G_{rev}})}{\Delta G_{irrev}\ (1+ \ ^{\Delta Q_{rev}}/_{\Delta G_{irrev}})}$

(25) $\varepsilon_{cell} = \frac{E_{reve}\ (T,P)}{E_{irrev}\ (T,P)} = \varepsilon_u$

(26) $\epsilon_{thermal} = \frac{E_T}{E_{cell}} = \frac{1.48\ V}{E_{cell}}$

(27) $\eta_{H2\ yield} = \frac{HHV(25℃, 1\ at)}{\Delta G_{irrev}} = \frac{283.8\ (kj)}{E_{cell}It\ (kj)}$

(28) $\eta_{H2\ production\ rate} = \frac{\overset{\circ}{V}_{H2}}{\Delta G_{irrev}} = \frac{V\ (m^3 m^{-3} h^{-1})}{E_{cell}It\ (kj)}$

(29) $\varepsilon_{indus} = \frac{energy\ content\ of\ products\ (J.mol^{-1})}{total\ energy\ requirement\ (J.mol^{-1})}$

(30) $\varepsilon_{indus} = \frac{HHV(T,P)\overset{\circ}{n}_{H2}}{P_{electrical} + P_{thermal} + P_{auxi}}$

(31) $r_d^* = (\frac{3r_0\sigma sin\theta}{2\Delta\rho g})^{1/3} \quad 90° < \theta < 180°$

(32) $\theta_g = 180 - \theta_w$

(33) $F = 2\ \sigma\ \mathrm{d}\ \sin\theta$

(34) $Weight\ percent\ of\ \alpha\ at\ eutectic = \frac{C\beta - Ce}{C\beta - C\alpha}$

(35) $volume\ fraction\ of\ \alpha\ (Vf\ \%)\ at\ eutctic = \frac{\frac{M\alpha}{\rho\alpha}}{\frac{M\alpha}{\rho\alpha} + \frac{M\beta}{\rho\beta}} * 100$

(36) $\lambda_s^2\ V = constant$

(37) $\lambda_{col}^3\ V = constant$

(38) $n\lambda = 2d \sin \theta;\ n = 1,\ 2;\ \ldots$

(39) $\tau = \mathrm{K}\lambda/$

(40) $\frac{1}{V(1-x)} = \frac{1}{V_m C} + \frac{x(1-c)}{V_m C}$

(41) $Slope = \frac{C-1}{V_m.C}$

(42) $Intercept = \frac{C-1}{V_m.C}$

(43) $V_m = \frac{1}{slpoe+Intercept}$

(44) $SSA = \frac{V_m N_A a_m}{v_m m_s}$

(45) $\mathrm{ECSA} = \frac{C_{DL}}{C_S}$

(46) $[IrCl_6]^{2-} + 2Ni \rightleftarrows Ir + 2Ni^{2+} + 6Cl^{-}$

LIST OF ABBREVIATIONS

AEMWE	Anion exchange membrane water electrolysis
Al	Aluminium
AWE	Alkaline Water Electrolysis
BET	Brunauer–Emmett–Teller (BET) analysis
CDL	Double layer capacitance
CGDS	Cold gas dynamic spray
CNT	Classical nucleation theory
Cu	Copper
CV	Cyclic voltammetry
ECSA	Electrochemical active surface area
EDX	Energy-dispersive X-ray spectroscopy
EIS	Electrochemical Impedance Spectroscopy
Fe	Iron
HER	Hydrogen evolution reaction
iR	Ohmic drop
Ni	Nickel
OER	Oxygen evolution reaction
PTL	Porous transport layer
PEMWE	Proton exchange membrane water electrolysis
R	Ohmic resistance
SEM	Scanning electron microscopy
SWIS	Shock-wave induced spraying
TEM	Transmission electron microscopy
VPS	Vacuum plasma spray
XRD	X-ray diffraction

1 BACKGROUND, MOTIVATION AND THESIS STRCUTURE

1.1. The need for clean energy utilization

Energy demand and economic growth are closely related. Growth in economies increases energy demand. If energy is restricted, gross domestic product (GDP) growth will inevitably slow down [118]. Following the industrial revolution and technological advances, energy consumption and the world's population are ever-increasing. In 2018 the world's population peaked at 7.63 billion, demonstrating a 77% increase compared to 1978. The world's energy consumption in 2018 was 270.5 exa-joules, almost twice that of 1978. Energy consumption and CO_2 emissions are expected to double by 2025 compared to 2000. The majority of this energy, 84.7% in 2008, comes from fossil fuels [119]. In addition, oil and gas reserves appear to be depleting and may run out within 50 years [120].

Therefore, the next generations will not be able to generate energy from conventional resources, and this will become an inevitable challenge. A further concern is the alarming environmental pollution caused by fossil fuels, which threatens communities' future sustenance [121].

Canada joined the Paris Accord in 2015 and has taken notable measures to push back against climate change. As a vanguard in the field of climate and weather, Canada has taken initiatives to reduce pollution in observing its commitments to the Paris Accord and accomplishing the Net-Zero Economy by 2050. Notably, Canada has made substantial investments in renewable energy generation, demonstrating their commitment to reducing pollution and transitioning to sustainable energy sources [122].

Renewable energy sources can meet humankind's energy needs with minimal CO_2 emissions. Natural phenomena, such as wind, sunlight, geothermal energy, tidal, and gravitational potential energy of the water, are some instances of renewable energy resources [123]. Currently, hydropower, solar power, and wind power generate most of the renewable energy we use.

One of the challenges of renewable energies is that they cannot be used in a controlled, stable, and sustainable manner. The inescapable dependency of renewable energy production on climate and weather conditions makes the uninterrupted direct use of such energies impossible. Therefore, sole reliance on renewable energy power plants cannot feasibly fulfill the energy demands of the ever-growing human population. That being so, the extra energy can be stored via energy storage solutions to be used during peak consumption periods to regulate the supply and demand of energy when renewable energy plants cannot meet the energy requirements. This increases energy efficiency during unusual peak and off-peak hours, which can entail various economic benefits [123].

1.2. Renewable energy storage

Various storage methods have been suggested for renewable energies, which include 1. Electrical, 2. Mechanical, 3. Electrochemical, and 4. Thermal storage [124, 125].

Among mechanical storage technologies, storage through a hydraulic pump is a mature energy storage method in which energy is stored by transferring water to another reservoir on a higher platform. This technology has been in use for almost a century and currently accounts for the largest share (around 90%) of energy storage. However, the expansion of this storage method is restricted by geographical and environmental conditions. Many suitable locations for water dams are within protected and conservation areas, where building dams would significantly impact the ecosystem [125].

Supercapacitors store the energy directly via electrical charges in the capacitor. They have gained significant attention from scientists due to their high charging and discharging rates with up to 95% efficiency, low maintenance costs, and environmental friendliness. Low internal resistance and high energy release rates are some of the important advantages of supercapacitors compared to rechargeable batteries. Nevertheless, their storage capacity is significantly lower than the batteries. Supercapacitors are often used as stabilizers in the transmission lines to prevent a voltage or current drop or frequency alternations [125].

Thermal storage involves storing energy in various media, including sand, MgO plates, molten salt, paraffin wax, and organic materials. With an efficiency of 95% to 97% for thermal input and output energy, the stored energy can be used to heat houses or water in power plants to generate electricity. Thermal storage offers lower costs per energy unit and capital than large-scale battery storage, making it an attractive option for heating and cooling buildings. However, for electrical energy storage, other storage solutions may be more advantageous [126, 127].

Electrochemical methods, including various types of batteries, are an efficient way for energy storage. The efficiency of rechargeable batteries is high and can reach up to 99% for lithium-ion batteries [128]. However, this type of storage has several major downsides. The methods of producing these batteries are not environmentally friendly. The manufacturing of lithium-ion batteries, which are widely utilized in various industries, requires cobalt and lithium. The extraction process of these materials severely damages the environment and is done in low-income countries through unethical and questionable methods [129]. Furthermore, they have a limited life cycle and should be replaced by new batteries at the end of their life, and their storage density ratio makes them bulky. The problem with energy density and bulkiness becomes more challenging when the batteries are used in the automotive industry [130].

Hydrogen production can result in a longer-lasting and higher density of energy storage when compared to the other storage methods mentioned [6]. The energy density ratio of hydrogen (39.4kWh/kg) is almost 100 times more than conventional rechargeable batteries (0.3kWh/kg) [130, 131]. Hydrogen can be produced by various methods, among which only hydrogen produced by electrolysis of water powered by renewable energies is known as green hydrogen since its entire production and use process is environmentally friendly. Nonetheless, compared to hydrocarbons, the higher final costs of this method, including the cost of hydrogen production, storage, and transport, limit the production of green hydrogen. As the final costs are declining, hydrogen can be used as a sustainable and stable source of energy in industries, heating, and transportation in the future. Aside from fuel, green hydrogen can replace the hydrogen used as a feedstock in producing various materials [132].

1.3. Overall aims and structure of thesis

The purpose of this thesis is to study hydrogen production through water electrolysis. We focus on reducing hydrogen production costs by developing low-cost catalysts with higher lifetime and efficiency. The increase in efficiency plays a significant role in lowering hydrogen production costs. Electrocatalysts with a lower cell potential significantly increase efficiency. In this context, we aim to reduce the cell potential across all current densities by enhancing the specific surface area of catalysts. This thesis pursues this goal through the development of new 3D skeleton electrodes for both alkaline and PEM water electrolysis.

1- Development of a three-dimensional nickel electrode for alkaline electrolysis:

The goal is to fabricate a three-dimensional nickel electrode characterized by an exceptionally high specific surface area. This electrode can serve either as a catalyst or as a substrate with a large surface area for the synthesis of catalysts. Our approach takes into account considerations of manufacturing cost, efficiency, and environmental impact. A novel method is introduced to produce a 3D skeleton electrode of nickel (Ni-whiskers), and all parameters influencing specific surface area and OER overpotential are systematically evaluated. Furthermore, catalyst synthesis on the surfaces of Ni whiskers will be conducted to further decrease OER overpotential.

2- Three-dimensional titanium electrode for Porous Transport Layer in PEMWE:

This aspect involves the exploration of a three-dimensional titanium electrode tailored specifically for the porous transport layer of PEMWE. The principal objective is to concurrently reduce production costs and increase porosity to an optimal level within the range of 50-75%. We explore the application of novel thermal spray technology, Shock-Wave Induced Spraying (SWIS), to produce a highly porous titanium structure. The study also investigates the use of two distinct porogens to enhance porosity and evaluates the method for selecting the most suitable porogen. Due to time constraints, electrochemical tests were not conducted on this 3D skeleton.

This thesis consists of 9 chapters with the following description:

An overview of the thesis structure and motivations for producing green hydrogen is presented in the first chapter.

Chapter Two begins with an introduction to the principles of water electrolysis, including an explanation of the equilibrium potential. The hydrogen and oxygen half-reactions are described, and the need for developing catalysts for oxygen evolution is discussed. A description of the different types of overpotentials and methods for reducing them is also provided in the chapter. Then, the role of three-dimensional electrodes in reducing cell potential is explained, followed by an explanation of the three types of catalysts examined in this thesis.

Chapter Three describes the details of the experiments and the used materials.

Chapter Four begins by examining the mechanism for making a new 3D Ni electrode, and the BET and TEM analysis results are presented. After that, the chapter discusses the effect of Al mass and heat treatment on the microstructure and electrochemical characteristics of Ni whiskers. The last section of the chapter studies the development of Ni whiskers on Ni foam and compares it with long Ni whiskers on Ni plate.

Chapter Five studies the synthesis of two highly active catalysts of Iridium and Ni-Fe on the surface of Ni whiskers and their impact on the activation and mass transport overpotential.

Chapter Six provides an account of how a new 3D electrode is made from Ti using the SWIS process. The chapter then explores the impact of two different porogens, Al and Cu, on the porosity of the coating.

Chapter Seven gives an overview of the research results and sets forth the future research prospects.

2 LITERATURE REVIEW

2.1. Fundamental electrochemical principles of water electrolysis

Water electrolysis was first demonstrated in 1789 by Jan Rudolph Deiman and Adriaan Paets van Troostwijk who used an electrostatic generator as a current source [133]. Water electrolysis is an electrochemical process. Electrochemistry is a scientific field that explores chemical reactions that occur when electric currents pass through a system. In an electrochemical process, direct electric current results in a chemical reaction on the surface of the two electrodes within the electrolyte. Numerous scientists have helped lay the foundation principles of electrochemistry. In 1823, Michael Faraday made significant contributions to electrochemistry in his efforts to understand electrochemical processes. He distinguished between negative charge carriers, known as electrons, and positive charge carriers, known as ions. He demonstrated that during an electrochemical process, a certain amount of substances could be deposited or decomposed, which is proportional to the electric charge transferred. Also, the quantity of atoms deposited or liberated is determined by their equivalent weights or valences. The larger the valence, the fewer atoms formed on the electrode, and vice versa. According to Faraday's Law:

$$M = \frac{Q}{F\mathrm{Z}} \quad (1)$$

In the equation above, M is the deposited/liberated mass, Q is the electric charge (C), F is the charge of one mole of electrons, 96485 C/mol, which is called Faraday’s Constant, and Z is the valency of the element [134]. Notably, the electrochemical reactions do not reach 100 percent efficiency as a portion of the energy is lost as heat; therefore, Faraday's formula contains a correction factor [135].

Electrochemical processes take place in two distinct locations, corresponding to two half-reactions of oxidation and reduction. One typical example of these half-reactions is as follows:

$$A(s) \rightarrow A^{Z+}(aq) + \mathrm{Z}e^{-} \quad (2)$$

In the above half-reaction, through an oxidation reaction, $A(s)$ loses Z number of electrons and dissolves as A^{Z+} ion in the electrolyte. Another reduction reaction simultaneously occurs on the other side, and a reduced element is deposited on the electrode or evolved as gas [136]. During the electrolysis of water, the two reactions of hydrogen evolution and oxygen evolution on the cathode and anode surfaces simultaneously occur. However, the electrochemical reactions involved in water electrolysis are not as simple as the ones shown in Equation 2 and go through several steps depending on the catalyst and electrolyte [137, 138]. The following section further explains the steps in the water electrolysis reaction.

2.2. Redox rection in water electrolysis

2.2.1. The Hydrogen Evolution Reaction (HER) mechanism

Hydrogen is reduced in the cathode through the HER half-reaction. Numerous theories and experiments have been developed on the HER mechanism based on the Volmer-Heyrovsky and Volmer Tafel steps. The steps involved in the HER mechanism differ depending on the environment, so the steps involved in acidic and alkaline environments differ. In an acidic environment, there are three probable steps:

$H^+ + e^- = H_{ad},$ (3) Volmer step

$H^+ + e^- + H_{ad} = H_2,$ (4) Heyrovsky step

$2H_{ad} = H_2$ (5) Tafel step

In the Volmer step, hydrogen is adsorbed on the electrode due to a reaction between the electron and proton, called Electrochemical Hydrogen Adsorption, and is shown as H_{ad} in the equations. In the next stage, hydrogen evolution can occur through the Heyrovsky step, Tafel step, or both steps. In these steps, a hydrogen molecule is formed and desorbed by the combination of the two adsorbed hydrogens (Vomer-Tafel) or the reaction between the proton, electron, and the adsorbed hydrogen.

The HER half-reaction in alkaline environments starts with the dissociation of the water molecules into protons and hydroxide ions. In the next stage, hydrogen evolution can occur through the Heyrovsky step, the Tafel, or both steps [139, 140].

$H_2O + e^- \rightarrow H_{ads} + OH^-,$ (6) Volmer step

$H_{ads} + H_2O + e^- \rightarrow H_2 + OH^-,$ (7) Heyrovsky step

$2H_{ads} \rightarrow H_2$ (8) Tafel step

The HER reaction rate depends on the Gibbs free energy of hydrogen adsorption and desorption. Substances that have optimum binding energy to the adsorbed hydrogen have a higher HER rate [140].

2.2.2. The Oxygen Evolution Reaction (OER) mechanism

The reaction steps in OER in the acidic and alkaline electrolytes are more complex than the HER steps and involve four stages of electron transfer, shown in Fig.2-1 [141]. The OER reaction steps in an alkaline electrolyte can be simplified as follows:

$$OH^- + M \rightarrow M - OH + e^- \quad (9)$$

$$M - OH + OH^- \rightarrow M - O + H_2O + e^- \quad (10)$$

$$2M - O \rightarrow 2M + O_2 + 2e^- \ / \ M - O + OH^- \rightarrow M - OOH + e^- \quad (11)$$

$$M - OOH + OH^- \rightarrow O_2 + H_2O + e^- + M \quad (12)$$

In the reactions above, M is the active site. First, the hydroxide ions are adsorbed on the surface to form M-OH. Next, M-O forms through the deprotonation process. There are two ways to generate O_2. 1: M-O reacts with OH^- to form M-OOH, and then O_2 is made by M-OOH deprotonation. 2: Oxygen evolution directly from M-O through an electrochemical process which requires overcoming a high activation energy and is shown in green in Fig. 2-1.

Here, the OER reaction steps are shown in the most simplified form. Nonetheless, they demonstrate the fundamental challenges of the OER half-reaction. Only one intermediate is involved in the HER; however, at least three intermediates are involved in the OER, which indicates that the binding free energy of the three intermediates should be at a level that all the four stages of the reaction proceed at a potential close to the equilibrium potential [142]. This has caused the OER to be considered a bottleneck in the electrolysis reaction, and most of the research has been focused on developing these catalysts [140, 141, 142]. Our thesis also aimed to optimize catalysts for the half-reaction of OER.

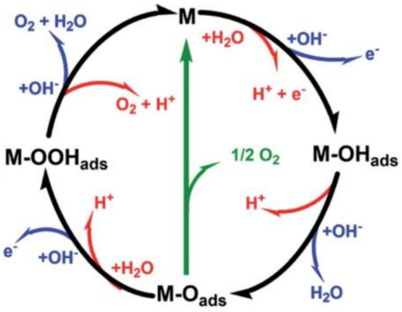

Figure 2-1: OER mechanism for acidic (red) and alkaline (blue) conditions [141].

2.3. Water electrolysis technologies

Several low-temperature technologies are being developed for industrial-scale hydrogen production, which can be divided into three categories: 1- Alkaline Water Electrolysis (AWE), 2- Anion Exchange Membrane Water Electrolysis (AEMWE) and 3- Proton Exchange Membrane Water Electrolysis (PEMWE).

2.3.1. Alkaline Water Electrolysis (AWE)

Alkaline electrolysis was the first process used for industrial water electrolysis. Therefore, it is a well-established and mature process currently commercially utilized for hydrogen production. As the name suggests, the electrolyte in this process is an alkaline solution. An acidic solution can also be used instead; however, due to the high rate of corrosion of the equipment in an acidic solution, an alkaline electrolyte is preferred. The electrolyte is 25% to 30% wt.% Potassium hydroxide or Sodium hydroxide which can be increased up to 40% wt.%. Higher concentrations increase the rate of corrosion. The operating temperature ranges from 70 to 90°C. Low-carbon steel electrodes are used as the cathode, and Nickel, Cobalt, Platinum, Iridium, and Ruthenium, as the anode. Nickel is more frequently used as an anode because of its higher electrical conductivity and lower cost. The cathode is attached to the negative terminal, the anode to the positive terminal, and a diaphragm separates the anode and cathode electrolyte (Fig. 2-2).

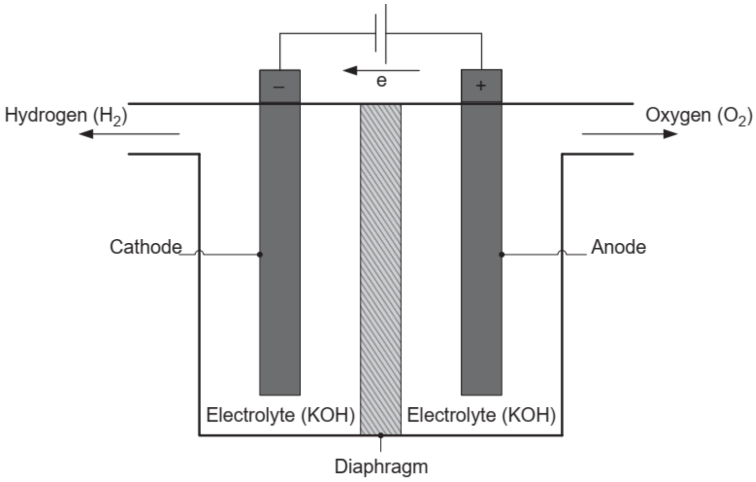

Figure 2-2: Schematic representation of an alkaline water electrolyzer utilizing KOH as an electrolyte [141].

As water enters the cell at the cathode, it dissociates into hydrogen gas and hydroxide ions. The produced hydrogen exits the cell, and the hydroxide ions pass through the diaphragm and reach the anode, where oxygen is evolved and exits the cell afterward [143].

2.3.2. Proton Exchange Membrane Water Electrolysis (PEMWE).

Another electrolysis method currently used in the market is PEMWE. The operating temperature in PEMWE ranges from 25 to 90°C. Fig.2-3 illustrates a schematic cross-sectional view of a PEMWE electrochemical cell with 5 to 7 mm thickness. A proton exchange membrane with a thickness of 90 to 200 μm is seen at the cell core. Porous anode and cathode catalysts sandwich the membrane. The next layer is a conductive porous transport layer called PTL (3 and 3'), which is responsible for the steady transfer of electrical current to the catalysts. Anode and cathode catalysts can either be directly coated on the membrane or PTL. Water flows around the anode and cathode through 4 and 4' (spacers and disruptors) to feed the reaction on the anode side and remove the extra generated heat from the system. All the components are locked in place by two end plates (5 and 5') and water-sealed. The porosity of the PTL allows the produced hydrogen and oxygen gases to exit and collect at the back. Ultimately, the produced gas and the water fed into the system exit the cell, and the fluid and gas are separated by gravimetric separation [144].

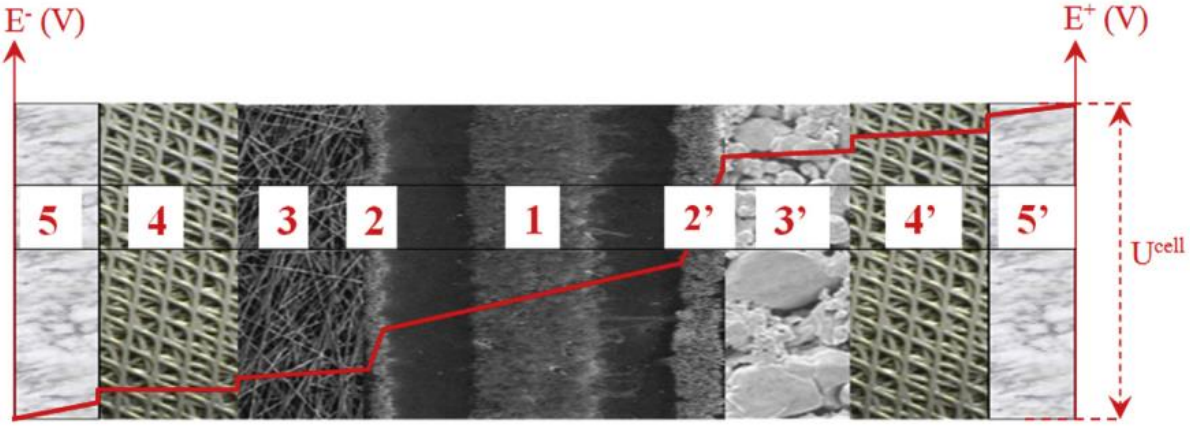

Figure 2-3: Schematic representation (cross-sectional view) of a PEM water electrolysis cell. 1- Cation exchange membrane, 2- Catalytic layers, 3- Porous transport layers, 4- Spacers and flow disrupters, 5- End-plates [144].

In this technique, water is split into oxygen gas and proton at the anode. Oxygen is removed from the system via the water flow, the proton reaches the cathode surface through the membrane, and hydrogen is evolved on the cathode. Since the membrane acts as the electrolyte in this process, PEMWE is also called Solid Polymer Electrolyte Electrolyzer [143].

In PEMWE, the fluid electrolyte and diaphragm are eliminated from the design, and a thin membrane is used to transport the ions. This is advantageous as it reduces ohmic resistance and increases efficiency [5, 145]. Further, it allows higher operating pressures [146], thereby decreasing the energy needed for gas compression and resulting in further efficiency improvements [147].

Nonetheless, the sulfuric acid group in the structure of PEM membranes and the proton generation cause the electrolyte to become strongly acidic so that only noble metals, such as platinum, can be sustained under these conditions [143]. Using noble metals in electrolyzers is the main reason for the higher capital cost of PEMWE compared to AWE.

2.3.3. Anion Exchange Membrane Water Electrolyzer (AEMWE)

AEMWE is currently being developed to benefit from both the advantages of the inexpensive catalysts in AWE and the high efficiency of PEMWE. Like PEMWE, AEMWE uses a membrane for ion transport; however, the main difference is that it uses an anion exchange membrane.

This technology is still rather new, and several challenges need to be addressed before it can reach its full potential. To achieve this, low-cost catalysts must be developed, and efficiency and durability improved to a level comparable to PEMWE [6].

2.3.4. Comparison of water electrolysis processes

Table 2-1 provides a summary of the comparison between water electrolysis technologies. Regardless of the advantages of AEMWE, this process is still being developed at a laboratory scale, and the gaps between this technology and AEM and PEMWE in terms of efficiency and durability should be filled. The vision for AEMWE technology is to reach an efficiency matching that of PEMWE with a life of 100,000 hours by 2050; however, there are a lot of uncertainties in this regard [5, 6, 8, 148].

AWE is currently a mature technology in the industry, and PEMWE has also been commercialized in small-scale industries. Many experts believe PEMWE will gradually replace AWE as the preferred technology after 2030 [12].

All the predictions regarding the development of electrolyzer technology have a certain degree of uncertainty, and most experts believe that all electrolyzers should be developed simultaneously [12].

AWE and PEMWE are currently used commercially, and we aim to improve them by developing 3D anode electrodes. In the following sections, we will explain the significance of 3D electrodes in AWE and PEMWE cells. The discussion will start with the reversible cell potential.

Table 2-1: Comparison of electrolyzers [5, 6, 148, 149, 150].

Electrolysis Process	Advantages	Disadvantages
Alkaline Water Electrolysis (AWE)	1- Well established technology 2- Non-noble catalyst 3- Energy efficiency (voltage efficiency) 70–80% is Commercialized	1- Low current density 2- Low gas purity 3- Low operating pressure (3-30 bar)
Proton Exchange Membrane Electrolysis (PEMWE)	1- Higher energy efficiency (80–90%) Commercialized 2- High current density 3- High gas purity (99.999%) 4- Low gas cross over 5- Quick response	1- Noble catalyst 2- Low durability
Anion Exchange Membrane Electrolysis (AEMWE)	1- High energy efficiency (88% has been reported) 2- High current density 3- High gas purity (99.999%) 4- Non-noble catalyst 5- Low gas cross over 6- Quick response	Laboratory-scale production

2.4. Electrochemical Thermodynamics

The relation between Gibbs free energy and reaction potential can be expressed as follows:

$$\Delta \mathrm{G} = -\mathrm{nF}E \qquad (13)$$

The minus signifies that when E is positive, the reaction occurs spontaneously.

In the equation above, n is the number of moles transferred in the reaction, and F is the Faraday Constant (96485 $C.mol^{-1}$). The standard Gibbs free energy for the standard potential is:

$$\Delta G^0 = -\mathrm{n}\mathrm{F}E^0 \quad (14)$$

According to thermodynamic relations, if temperature, pressure, or activity in a system are not at standard conditions, Gibbs free energy changes as follows:

$$\Delta G = \Delta G^0 + RTlnQ \quad (15)$$

In the equation above, R is the universal gas constant (8.314 $J.mol^{-1}.Kg^{-1}$), T is the temperature in Kelvin (K), and Q is the reaction quotient. The equilibrium potential of the cell in non-standard conditions is obtained by substituting equations (13) and (14) into the equation (15), which is called the Nernst equation [151]:

$$\mathrm{E}\ (\mathrm{T, P}) = E^0(25℃, 1\ \mathrm{atm}) - \frac{RT}{nF}lnQ \quad (16)$$

As an example, the thermodynamic OER potential in alkaline media is calculated as follows:

$$\mathrm{E}\ (\mathrm{V}, 25℃, 1\ \mathrm{atm}) = E^0(V, 25℃, 1\ \mathrm{atm}) - \frac{RT}{nF}lnQ = 1.23 - \frac{0.059}{4}log\frac{1}{(OH^-)^4} = 1.23+0.059\mathrm{PH}$$

The standard Gibbs free energy for water electrolysis is 237.2 $KJ.mol^{-1}$ [24]. Standard potential under these conditions, which is the least potential required for water electrolysis, is called reversible potential and equals 1.23 V. The reversible potential of the reaction indicates that the flux of events to the right equals the flux of events to the left in this potential. In other words, the net current is zero. The reversible potential depends on temperature. Increasing temperature decreases the Gibbs free energy of the electrolysis of water, resulting in a decrease in the reversible potential (Fig.2-4).

Based on thermodynamic relations, it is expected that the onset of water electrolysis reaction occurs at a higher potential very close to 1.23 V; however, water electrolysis reaction under real conditions requires overcoming many internal resistances, and the onset of water electrolysis occurs at potentials much higher than the equilibrium potential.

The excessive energy given to the system is wasted as heat. Nonetheless, if the water electrolysis reaction occurs in an adiabatic system under standard conditions at a potential less than 1.48 V, the temperature of the system drops. The reason is that water electrolysis is endothermic, and the heat produced due to the overpotentials is consumed for water electrolysis by the system. The heat produced in an adiabatic system under standard conditions at a potential of 1.48 V equals the heat required for water electrolysis, called Thermoneutral Potential. Thermoneutral Potential is obtained via the following relation:

$$E_T = -\frac{\Delta H}{nF} \qquad (17)$$

In (17), the ΔH is the enthalpy of the formation of water. Since the enthalpy change of the reaction remains relatively constant with temperature, the thermoneutral potential also remains stable and does not experience significant changes with temperature variations [152].

Fig.2-4 depicts the changes in thermoneutral potential at different temperatures. Compared to the thermoneutral potential, the reversible potential undergoes considerable changes with the temperature as it depends on $\Delta G = \Delta H - T\Delta S$ [152].

Water electrolysis is endothermic between the thermoneutral potential and the reversible potential. However, it becomes exothermic at potentials greater than the thermoneutral potential [153, 154].

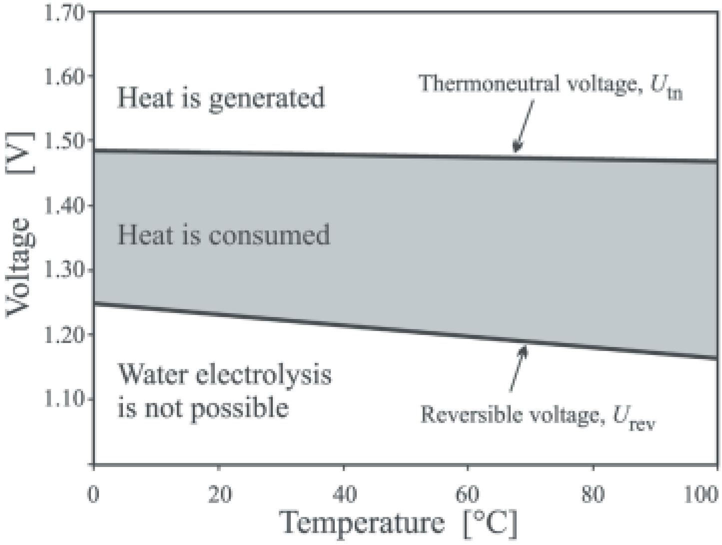

Figure 2-4: Reversible and thermoneutral voltage for water electrolysis as a function of temperature at a pressure of 1 bar [154].

2.5. The Anatomy of a Polarization Curve

The polarization curve shows the functioning of an electrochemical system by illustrating the relationship between current and potential. In electrochemical engineering, as shown in Fig.2-5, a polarization curve consists of three regions: 1- Kinetic region, 2- Ohmic region, and 3- Mass transport region. Each region increases the potential due to an energy barrier. In other words, each region generates an overpotential, which is defined as the difference between the cell potential and the reversible potential.

In low current density regions, electrochemical reactions should overcome the activation energy barrier. At higher current density, it should also overcome the ohmic resistance resulting from the transfer of ions in the electrolyte and electrons in the equipment. In the same way as Ohm's Law, this region behaves linearly. The transfer of species becomes the most important factor as the current density is further increased. During water electrolysis, bubble formation on the surface is one of the major reasons for an increase in the mass transport overpotential [26]. Each of these issues will be separately discussed in the next sections.

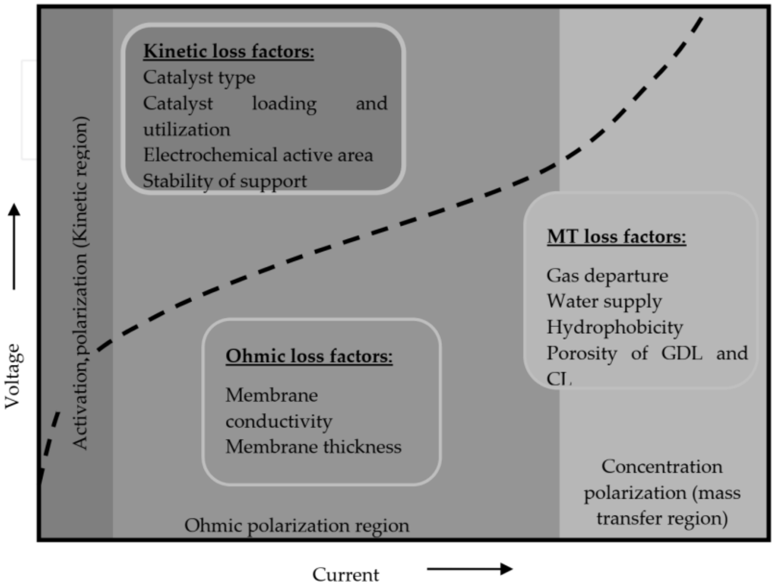

Figure 2-5: Schematic view of the polarization curve for PEMWE, demonstrating the different areas affecting the electrolysis potential [26].

2.5.1. Electrode kinetics

Overcoming the activation energy barrier is the first energy barrier for OER onset, which manifests as activation overpotential. Activation overpotential depends on electrode properties (chemical composition, crystal structure, and surface topography) and the chemical composition of the electrolyte near the electrode.

The classic description of the chemical composition of the electrolyte near the electrode (double layer) is based on Helmholtz et al. theory. Fig.2-6 demonstrates a schematic view of the Helmholtz layer near an electrode. According to this theory, when an electrode is submerged in an electrolyte, two movable layers of positive and negative ions develop surrounding the electrode. These layers are arranged to counterbalance the opposite charges present on the electrode.

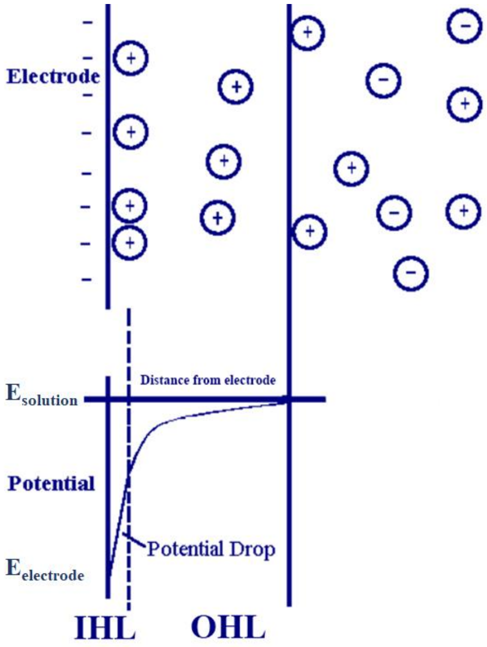

Figure 2-6: Simplistic view of the electric double layer near a metal electrode.

In the Inner Helmholtz plane, the ions are organized around the electrode, but in the Outer Helmholtz plane, the ions are arranged randomly due to thermal energy. Around the electrode, a potential distribution similar to Fig.2-6 can be observed depending on the strength of the electric field. The Helmholtz layer thickness is several nanometers [155, 156].

If the electrode is polarized to initiate an electrochemical reaction, the ions present in the Helmholtz layer are depleted. To sustain the reaction, energy is required to bring ions into the Helmholtz layer, which is necessary for the reaction to take place on the surface of the electrode [157]. Since the Helmholtz layer is only several nanometers thick, only the ions located at this distance effectively interact with the electrode [155, 156]. Therefore, the availability of ions close to the Helmholtz layer (electrolyte concentration) and the electrode potential significantly impacts the reaction rate.

To date, advanced models have been proposed for relating process parameters to reaction rates [158, 159]. However, V. Butler and M. Volmer equation represents one of the most fundamental relationships in electrochemical kinetics, which provides several connections between the electrolyte concentration, electrode potential, and reaction rate. These relations are suggested for a single-step reaction with a single electron transfer. Though they lack sufficient accuracy for multi-step reactions, they provide a logical description of the relationship between potential, electrolyte concentration, and current density [158, 159].

The Butler-Volmer equation for a single-step and single-electron transfer is written as follows.

$$j = j_{cathode} - j_{anode} = FAk^0\big(C_0(0,t)e^{-\alpha f(E-E^0)}\big) - C_R(0,t)e^{f(1-\alpha)(E-E^0)}) \quad (18)$$

In the equation above, j is the current density, F the Faraday Constant (96485 C.mol^{-1}), A the electrode surface area, C_0 is the initial concentration ($H^+ \; or \; OH^-$), C_R is the concentration of products (hydrogen or oxygen), f equals the ratio of F/RT, k^0 the standard rate constant, and α the transfer coefficient between 0 to 1 [160]. The transfer coefficient determines the geometry of the energy barrier and demonstrates whether the electrode reaction favors an anodic or cathodic direction at an applied potential.

The relation between the applied overpotential (η) and the net current in the cell (j) can be simplified as Equation (19).

$$j = j_0\left[e^{(\frac{(1-\alpha)nF\eta}{RT})} - e^{-(\frac{\alpha nF\eta}{RT})}\right] \quad (19)$$

In the equation above, j_0 is the exchange current density at a state of equilibrium. Exchange current density reflects the intrinsic electron transfer rate of the electrode. The larger the exchange current density, the quicker the electrode reaction.

For sufficiently low overpotentials, Equation (19) is written by the Taylor expansion as:

$$j=\frac{j_0 nF\eta}{RT} \quad (20)$$

Equation (20) demonstrates the existence of a linear relationship between the overpotential and the net current at a narrow and limited range of potentials close to the equilibrium potential. The slope of this line equals the charge transfer resistance:

$$R_{ct} = \frac{RT}{nFj_0} \quad (21)$$

Charge transfer resistance indicates the energy barrier for electron transfer from the electrode to the ions, which can be directly measured by electrochemical analysis methods such as Electrochemical Impedance Spectroscopy (EIS) [158]. Charge transfer resistance manifests as activation overpotential and includes two parts: 1- electrical energy for ion transfer to the inner Helmholtz plane, and 2- energy barrier for electron transfer to the ions within the inner Helmholtz plane.

Vincent et al. showed that with an increase in the overpotential (E-E^0) at low voltages, the charge transfer resistance decreases at first and then reaches a constant value. This indicates that the reaction rate at low voltages is controlled by the charge transfer resistance; therefore, catalyst activity should be measured at low potentials [146]. There is no precise definition for this potential. Nonetheless, one method is to measure the activation overpotential at 10 μA.cm^{-2} for catalysts with a small active surface (catalysts created on 2D surfaces) and at 10 mA.cm^{-2} for catalysts with a very high active surface (created on 3D structures such as Ni foam) [161, 162].

2.5.2. Ohmic resistance

Ohmic region forms due to the internal ohmic resistances of the electrochemical system, including electron resistance and solution resistance. Electron resistance results from the resistance against the charge transfer of electrons in the cables, PTL, connections, and electrodes. Solution resistance is due to the resistance of ions in the electrolyte solution or the membrane to migrate from one electrode to another. When a current is applied to the system, the ohmic overpotential increases linearly according to Ohm's Law $\eta = iR$, where η is ohmic overpotential, i is current, and R is the resistance. In most electrochemical systems solution resistance is the dominant factor. Nevertheless, electron resistance can surpass solution resistance due to the utilization of semiconductive materials in the electrochemical system or an electrode with low conductivity [163].

Ohmic drop (iR) has no direct impact on the reaction rate of a catalyst with high electrical conductivity, as it is affected by other factors such as the electrolyte, membrane, and temperature. As a result, when researchers evaluate the activity of such a catalyst, they do not consider the ohmic overpotential [164]. Ohmic resistance is calculated by measuring the impedance at high frequencies and at a frequency where the imaginary resistance is zero [160].

2.5.3. Mass transport

In high current density, the reaction rate is higher than the rate of transferring the product outside the electrode surface, which results in the accumulation of reaction products and a reduction in the content of reactants near the electrode. This phenomenon limits mass transport and reaction rate at high current density.

Mass transport in OER is limited by oxygen bubble formation on the catalyst surface. During OER, the gas bubbles heterogeneously nucleate and grow on defects on the electrode surface, such as a crevice. The bubble detaches when bubble growth reaches a threshold. When growing, the bubbles effectively cover the active surface area and cause a drop in the reaction rate due to the decrease in the active surface area. Bubble formation leads to a non-uniform distribution of current near the bubble. This non-uniform distribution causes an increase in the current density near the bubble and raises the reaction rate in that region. Therefore, bubble formation accelerates in that region, and a more active surface area is covered. The bubbles can also block the path of reactant (OH or water) transfer in the 3D structure and cause an increase in the solution resistance. The increase in potential due to the formation of bubbles, which is observed at high current density, is called mass transport overpotential [165].

2.5.4. Overall potential cell

The total cell potential is the sum of the thermodynamic potential, activation overpotential, ohmic overpotential, and mass transport overpotential [24, 25, 26]. As explained in the next section, the cell potential directly affects the efficiency and consequently, the cost of hydrogen production.

2.6. Electrolyzer Efficiency

Energy efficiency is defined as the ratio of the output energy expected from the input energy. Because of the internal resistance in water electrolysis, the expected energy is always less than the input energy. Depending on the method of evaluating an electrolysis system, various methods are available to determine the efficiency of an electrolyzer. It should be noted that since the overpotentials depend on the temperature and pressure, the calculations for obtaining the efficiency for comparison purposes should be done at a constant temperature and pressure for the electrolyzer systems.

The efficiency coefficient of water electrolysis (ϵ_{cell}) is defined as the minimum energy required to split one mole of water under equilibrium conditions (reversible where current density I=0) (W_{rev})

divided by the energy required to split one mole of water at constant pressure and temperature under operating conditions (operation condition where I≠0):

$$\epsilon_{cell} = \frac{energy\ requirement\ under\ reversible\ conditions}{energy\ requirement\ under\ irreversible\ conditions} = \frac{W_{rev}\ (Jmol^{-1})}{W_{irrev}\ (Jmol^{-1})} \qquad (22)$$

In equilibrium conditions (I=0), $W_{rev} = W_{irrev}$ and $\epsilon_{cell} = 1$. In non-equilibrium conditions (I≠0), $W_{irrev}$is larger than $W_{rev}$and $0 < \epsilon_{cell} < 1$. The reason for $W_{rev} < W_{irrev}$is that a portion of the energy is irreversibly dissipated as heat during the charge transfer (electrons and ions) [166].

Various methods are available to calculate efficiency, and different values can be placed in the numerator and denominator of the Equation (22). One of the ways to obtain efficiency is by enthalpy of the formation of water. The enthalpy can be placed as the reversible energy in the numerator of the equation (22) and added to the extra amount of electrical energy ($nF\eta_{loss}$) in the denominator.

$$\varepsilon_{cell,ther} = \frac{\Delta H_{rev}}{\Delta H_{rev} + nF\eta_{loss}} \qquad (23)$$

Since the enthalpy has minimal changes in the temperature range of 25 to 100°C, Equation (23) can be simplified as follows [166, 167]:

$$\varepsilon_{cell} = \frac{\Delta H_{rev}}{\Delta H_{rev} + nF\eta_{loss}} = \frac{\Delta G_{rev} + \Delta Q_{rev}}{\Delta G_{rev} + \Delta Q_{rev} + nF\eta_{loss}} = \frac{\Delta G_{rev} + \Delta Q_{rev}}{nFE_{cell} + \Delta Q_{rev}} = \frac{\Delta G_{rev}\ (1 + {}^{\Delta Q_{rev}}/_{\Delta G_{rev}})}{\Delta G_{irrev}\ (1 + {}^{\Delta Q_{rev}}/_{\Delta G_{irrev}})} \qquad (24)$$

If ${}^{\Delta Q_{rev}}/_{\Delta G_{rev}} \ll {}^{\Delta Q_{rev}}/_{\Delta G_{irrev}}$ the equation is simplified to

$$\varepsilon_{cell} = \frac{E_{reve}\ (T,P)}{E_{irrev}\ (T,P)} = \varepsilon_u \qquad (25)$$

Equation (25) is called voltage efficiency in the literature [168].

Only electrical work is considered for voltage efficiency. However, heat flow, specifically the reversible heat flow between the cell and the surrounding area, is not considered. Due to the approximations made and the assumption of constant enthalpy within a specific temperature range, Equation (25) only applies to temperatures between 25 and 100°C. This issue led researchers to define another type of efficiency called energy efficiency:

$$\epsilon_{thermal} = \frac{E_T}{E_{cell}} = \frac{1.48\ V}{E_{cell}} \qquad (26)$$

It is noteworthy that the blind use of equation (26) to calculate the efficiency coefficient under conditions where the cell potential is less than the thermoneutral potential that will result in values more than the unit is not logical and reasonable [166, 167].

There are other methods to determine efficiency. The thermal energy of hydrogen can be used to determine efficiency and compare it with the electrical energy required by the cell [168].

$$\eta_{H2\ yield} = \frac{HHV(25℃,1\ at)}{\Delta G_{irrev}} = \frac{285.8\ (kj)}{E_{cell}It\ (kj)} \qquad (27)$$

In the equation above, 285.8 kJ is the thermal energy capacity of one mole of hydrogen in stoichiometric pressure and temperature (enthalpy of formation of water), and t is the time required to produce one mole of hydrogen.

Another method to evaluate the efficiency is to measure the rate of hydrogen production volume and compare it with the total electrical energy of the cell [168]:

$$\eta_{H2\ production\ rate} = \frac{\overset{\circ}{V}_{H2}}{\Delta G_{irrev}} = \frac{V\ (m^3m^{-3}h^{-1})}{E_{cell}It\ (kj)} \qquad (28)$$

In the equation above, V is the hydrogen production rate at the unit of electrolysis cell volume, and t is the production time.

The efficiency calculation methods stated above are mostly used to calculate efficiency under laboratory conditions. Measuring the efficiency coefficient in the industry is to some extent different from the laboratory. In industrial scenarios, the efficiency calculation considers all components consuming energy in an electrolyzer system. Therefore, in addition to the energy required for electrolysis, the energy demands for elements such as the heat exchanger and pump are also included in the denominator of Equation (22). Additionally, the energy of produced hydrogen content is placed in the numerator of Equation (22).

$$\varepsilon_{indus} = \frac{energy\ content\ of\ products\ (J.mol^{-1})}{total\ energy\ requirement\ (J.mol^{-1})} \qquad (29)$$

The thermal energy of one mole of hydrogen is placed in the numerator of the equation above. Depending on the various applications of hydrogen, some authors use the thermal energy of one mole of hydrogen caused by its combustion in the air rather than oxygen or measure it at different temperatures and pressures.

Also, the ε_{indus} efficiency can be defined as follows:

$$\varepsilon_{indus} = \frac{HHV(T,P)\overset{\circ}{n}_{H2}}{P_{electrical} + P_{thermal} + P_{auxi}} \quad (30)$$

In the equation above, $\overset{\circ}{n}_{H2}$is the hydrogen production rate (mole per second), $HHV(T,P)$ is the thermal energy of one mole of hydrogen, $P_{electrical}$ is the electrical work, $P_{thermal}$ is the energy used to transfer heat in the system, and P_{auxi} the energy used by the auxiliary equipment for the stack plant [166].

It is crucial to reduce cell potential in all the methods mentioned above to increase efficiency. Therefore, overpotentials should be reduced to increase efficiency and reduce hydrogen production costs.

2.7. Overpotential Management

Reducing each of the reversible thermodynamic potential, activation overpotential, ohmic, or mass transport overpotential contributes to the reduction of cell potential. Increasing the temperature leads to a decrease in the reversible potential, ohmic overpotential, and activation overpotential, resulting in a decrease in the total potential. In addition, reducing the pressure decreases both the mass transport overpotential and the reversible potential. Nonetheless, increasing the cell pressure is advantageous, as it reduces the energy required for hydrogen compression, consequently increasing the overall efficiency of the electrolyzer [146, 147].

There are more important parameters than the temperature and pressure, such as the nature of the electrode, that significantly affect the reaction rate. It should be noted that there is a limit to increasing the temperature and pressure as it increases the corrosion rate of the equipment.

2.7.1. Activation Overpotential

The nature of the electrode and the surface topography have an important role in the activation overpotential. As discussed in section 2.2, during the OER process, the intermediates on the electrode surface are adsorbed, and the reactions proceed with electron transfer. It has been determined that the strength of the bond between the intermediates in heterogeneous catalysis plays a critical role in catalyst activity and selectivity [169]. The studies have demonstrated a linear relationship between the binding energy of the M-O, M-OH, and M-OOH intermediates, known as the Linear-Scaling Relationship. Accordingly, the researchers plotted the binding energy of one of the intermediates, e.g., M-O, versus the OER potential and obtained a volcano curve. The curve results indicate that the optimum level of bond strength for the highest OER performance is where the bond between the intermediates and catalyst is neither too strong nor too weak. This curve demonstrated that Ruthenium Oxide and Iridium Oxide have the highest OER performance among the metal oxides [27]. Recent studies consider the difference in the free energy of two intermediates (the difference between the energy states of two HOO and HO intermediates) instead of the bonding energy in the volcano curve. According to the results, compounds such as Ruthenium Oxide, Iridium Oxide, and Platinum Oxide have the highest OER performance [170].

The researchers are attempting to improve the catalyst performance by changing the electron configuration through changes in its chemical composition. It has been found that doping elements increase electron density near active atoms, creating a new electron configuration for intermediate adsorption, which also has positive effects on catalytic conductivity [171]. For instance, it has been theoretically and experimentally proved that doping Nickel or Cobalt into Ruthenium Oxide increases the activity of the RuO_2 catalyst [170].

Electrochemical reactions generally occur on the electrode surface and edge sites. Furthermore, only a portion of the edge site participates in the electrochemical reaction. The sites that effectively contribute to the reaction are considered active sites. The number of active sites indicates the number of simultaneous reactions that can occur at any given time (current density). Reaction rates will be limited if the number of active sites is not sufficient to support the desired current density. Incorporating defects into the structure can result in more active sites [172]. Moreover, defects have a significant impact on catalyst activity. In addition, they improve charge transfer, resulting in a decrease in charge transfer resistance [173]. Many studies on creating defects to increase the activity and the active sites are currently in progress, and this area of science is known as defect engineering. Crystal defects can be categorized into the following groups: 1-point defects, such as vacancy, interstitial, and substitutional defects, 2- line defects, such as dislocations 3- planar defects, such as grain boundaries and stacking faults and 4- bulk defects, such as pores and cracks [174]. Catalysts with one of these defects are synthesized by processes such as Electrochemical Deposition, Plasma Etching, Hydrothermal Synthesis, Chemical Vapor Deposition, etc. [172].

It is also possible to enhance catalyst activity by exposing specific crystal planes to electrolytes. Overall, crystal planes with smaller coordination (lower atomic density) have more surface energy and, electrochemical reactions on their surface occur faster. For instance, Iridium oxide demonstrates high OER activity on the {110} crystal plane [175]. Also, experiments demonstrate that exposing a large ratio of {110} planes increases NiO electrolysis efficiency [176]. Various methods are available for producing high-indexed catalyst structures, such as electrodeposition and solution methods [177]. It is noteworthy that surfaces with extremely high surface energy reduce OER activity. A volcano-shaped relationship exists between surface energy and OER activity, and optimal surface energy has the highest catalyst activity [178].

One of the most effective methods to reduce activation overpotential is to produce nanostructures (nano edges and nanopores) from high-activity catalysts. Nano edges or nanopores significantly increase the number of active sites with low charge transfer resistance. The electric field around the nano edges also amplifies and boosts the number of reactant ions (for example, hydroxide for OER) around these highly active areas. Increasing the reactant ions by changing the reaction quotient or free energy results in a manifold increase in the reaction rate [23].

2.7.2. Ohmic Overpotential

An increase in the electrolyte concentration or temperature in AWE decreases the resistance of ions. Shortening the distance between the electrodes also reduces the resistance of ions in the solution [146].

The utilization of a thin membrane with high conductivity mitigates ohmic resistance in PEMWE. This design, commonly referred to as zero-gap, involves the use of an extremely thin membrane, ranging from 90 to 200 μm. This reduces the distance required for ion transport, resulting in a pronounced decrease in cell voltage and an increase in overall process efficiency compared to AWE [5, 145]. Additionally, ohmic resistance can be further reduced in Zero-Gap technology when temperature or pressure are increased [147].

Even so, both AWE and PEMWE have limitations with increasing temperatures, concentrations, and pressures. Increasing the temperature or concentration of the electrolyte in the AWE increases the rate of equipment corrosion [143], and the excessive increase in pressure also ruins the membrane in PEMWE [5].

2.7.3. Mass transport overpotential (Bubble management)

As stated in Section 2.5.3, the formation of oxygen bubbles on the surface is one of the most critical factors contributing to mass transport overpotential in the OER. Therefore, any factor that can reduce the adhesion time of the bubble to the surface can reduce the negative impact of bubbles in mass transport. Various technologies such as ultrasonic [179], magnet [180], and ultragravity fields [181] exist that apply the necessary energy to the bubble and quickly separate it from the surface and remove it. Though these methods increase the efficiency, electrode surface engineering and increasing the effective surface area of the electrode have a greater impact on mass transport. This section reviews the effects of the parameters of the electrode surface and the specific surface area of the electrode on the mass transport overpotential.

To investigate the impact of surface properties, we should first review bubble formation and growth. During OER process, oxygen molecules dissolve in the electrolyte. The solubility of oxygen in the electrolyte depends on the electrolyte type, temperature, and partial pressure of oxygen on the electrolyte surface. Since oxygen cannot quickly exit from near the electrode, the amount of oxygen near the electrode exceeds the saturation level and becomes a driving force for bubble nucleation. Bubble nucleation can be defined through Classical Nucleation Theory (CNT). According to the CNT, a stable nuclei can form and grow by overcoming the nucleation energy barrier and having a radius larger than the critical radius, r_{crit}.

The critical radius of the bubble can be reduced by heterogeneous nucleation on the electrode surface, especially the crystal defects and grooves with lower nucleation energy barriers.

The next stage is bubble growth. During this stage, the bubble continues to expand as long as the amount of dissolved gas around it exceeds saturation. The force of buoyancy created by the density difference between the bubble and the liquid ($\Delta\rho$) increases during the growth stage, and when this force surpasses the adhesive force of the bubble and the electrode, the bubble detaches from the electrode surface. The maximum theoretical bubble departure radius (r_d^*) is calculated by Fritz's formula:

$$r_d^* = (\frac{3r_0\sigma sin\theta}{2\Delta\rho g})^{1/3} \quad 90° < \theta < 180° \quad (31)$$

Where, g=9.81 m.s^{-2}, σ is the liquid (electrolyte) surface tension, θ the bubble contact angle (in degree), and r_0 is the radius of the part where the bubble is in contact with the electrode (spherical cap bubble). According to Equation (31), an increase in the bubble contact angle leads to a decrease in the bubble departure radius which speeds up bubble detachment [165, 182].

The larger contact angle of the bubble also indicates a lower contact angle of droplets, resulting in greater wettability of the electrode and easier transport of reactants to the surface. The relation between the contact angle of droplet and the bubble is as follows:

$$\theta_g = 180 - \theta_w \quad (32)$$

Where, θ_g is the bubble contact angle, and θ_w is the droplet contact angle. Surfaces with higher surface energy exhibit greater wettability. Additionally, surfaces with higher surface energy demonstrate greater OER activity, indicating that the catalysts employed in these reactions possess this property as well [182].

Another solution to increase the bubble contact angle is to reduce the interfacial area between the bubble and the electrode. This issue can be explained through the equation describing bubble adhesion to the electrode [182]:

$$F = 2\,\sigma\,\mathrm{d}\,\sin\theta \quad (33)$$

σ is the liquid (electrolyte) surface tension, d is the width of the contact line, and θ is the bubble contact angle. One of the ways to reduce d is to produce nanoporous or 3D nanostructures. A nanoporous structure decreases the volume of electrode materials under the bubble surface, resulting in the bubble being pinned to fewer points; consequently, the bubble adhesion to the electrode decreases, and it will detach more easily and quickly [182]. Producing well-defined nanostructures can increase the bubble contact angle to more than 150 degrees. These structures are called Superaerophobic or Superhydrophic structures and have superior wettability with extremely low bubble adhesion [30].

Nanostructures have two other advantages. Nanostructures can increase both active sites and OER activity [23] and favorably affect bubble nucleation rates. Since bubbles prefer to nucleate heterogeneously on grooves and edges, nanostructures can increase nucleation areas, and reduce oxygen saturation. A decrease in saturation not only accelerates the reaction rate due to decreasing the reaction quotient but also decreases the bubble's growth speed, resulting in smaller bubbles [180].

Although developing catalysts with nanostructures can reduce the duration of the bubble’s adhesion to the structure and the gas saturation near the bubble, the problem of bubble adhesion to the structure and reduction in the active surface still exists. This issue becomes more prominent with higher current densities.

Increasing the electrode surface area can be done in two dimensions. However, expanding the surface area in two dimensions increases the ohmic resistance and the electrolyzer’s maintenance and capital costs. Another solution is to increase the thickness of the 3D nanostructures of the catalyst. Though this method enlarges the specific surface area, it has a limited impact on the overpotential. Studies indicate that the majority of electrochemical reactions occur on the surface of nanostructures because of the constraint in the diffusion of reactants into the depth of nanostructures and the difficulty in reactant departure from the structure [64].

One of the best methods to increase the specific surface area of the catalyst is to coat the nanostructured catalysts on 3D surfaces with adequate pore size for the entry and departure of reactants or products. The experimental results have demonstrated that if the 3D structure is properly made, the OER performance will significantly improve for all the low and high current densities [31].

The 3D skeletal electrode must first be made of cost-effective materials with high electrical conductivity and adequate sustainability in the environment they are being used [31, 32, 33].

After material selection, pore design is the most important factor in designing 3D structures. Pore design encompasses pore size, pore shape, and porosity.

Reducing the pore size positively affects the cell potential of 3D electrodes in an alkaline environment. The comparison between Ni foam with a pore size larger than 300 μm and 3D Ni structures with a pore size of less than 100 μm shows that the OER performance for 3D structures with a pore size less than 100 μm significantly better than that of Ni foam. The reason is linked to increasing the specific surface area. Decreasing the pore size increases the specific surface area [95]. Other researchers have suggested that the performance of bubble departure in the Boiling Heat Transfer also improves upon reducing the pore size [183]. It has also been reported that for porous transport layers used in PEMWE (PTL), the electrolyzer efficiency increases as the pore size decreases. With a decrease in the pore size, the bubble departure size decreases, and the bubble leaves the structure more quickly. Nonetheless, excessive pore size reduction can negatively impact the bubble departure time. Accordingly, there exists an optimal pore size that depends on the surface chemical composition, surface topography, pore shape and reaction rate [36].

Researchers have investigated the effect of different pore sizes on flow regimes in 3D structures to define the optimal pore size. The bubble departure mechanism from within the pores is categorized into various groups. Fig.2-7 provides a schematic view of the different two-phase flows (gas-liquid). It is generally accepted that flow regimes include Dispersed Bubbly Flow, Slug Flow, Churn Flow, and Annular Flow. Dispersed bubbly flow occurs when the bubble size is smaller than the channel (pore) size. Under these conditions, the liquid within the channel has a continuous phase while bubbles are dispersed inside. Plug flow occurs if the bubble size (according to Equation 31) is larger than the channel size. With a decrease in the channel size or increase in the transport rate of the reaction (increase in the volume fraction of the bubbles), the plug flow shifts into a slug flow, then to a churn flow, and ultimately into an annular flow. A long bubble with the length of l_b forms during the slug flow, and its length increases with a reduction in pore size or reaction rate, ultimately shifting into one continuous phase (annular flow), while the liquid flow remains as a continuous thin film alongside the walls. With an increase in the bubble length l_b, bubbles cover a larger surface of the electrode, and this issue constrains the continuous supply of reactants. According to the studies, the pore size should be decreased to a certain extent to avoid the transition from plug flow to slug flow. The shift from plug to slug flow in the PEMWE usually occurs at current density higher than 2 A.cm^{-2} [36].

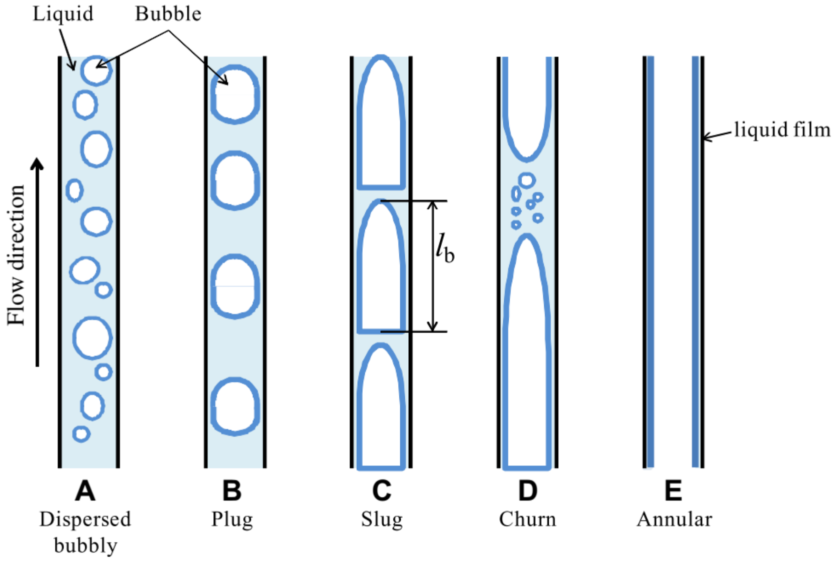

Figure 2-7: Schematic view of flow patterns of gas-liquid two-phase flow in channels [36].

The studies indicate that a reduction in pore size in the PTL made by powder metallurgy increases the electrolyzer efficiency, and as the pore size goes below 10 μm, the efficiency drops once more [36]. Other researchers have also reported similar results [35, 184].

Porosity is another critical parameter. Increasing porosity through increased permeability improves bubble escapes [10]. Nevertheless, too much increase in porosity can decrease the specific surface area [66], which leads to fewer active sites for OER and bubble nucleation [46, 185]. The impact of a lower bubble nucleation rate can be observed in 3D structures used for boiling heat transfer. Increasing porosity in these structures improves the bubble departure rate, but excessive porosity decreases it. For instance, when comparing two structures with similar pore sizes, the structure with a porosity of 61% has a better performance than the one with a 75% porosity [183]. The researchers have reported that for 3D structures made of titanium (PTL) used in he PEMWE, increasing the porosity up to 75% improves performance [43].

Along with pore size and porosity, pore shape also has a significant role in accelerating bubble escapes. The pore structure should be designed such that bubbles do not need to pass through narrow throats. Fig.2-8 shows the passage of a bubble through a throat due to changes in the pore size in the path. The results of theoretical and experimental studies indicate that bubble escape is hindered as the ratio of D_{pore}/D_{throat} increases [95]. These findings suggest that aligned plate-like fibers remove the throat effect, allowing bubble departure to be governed solely by wettability.

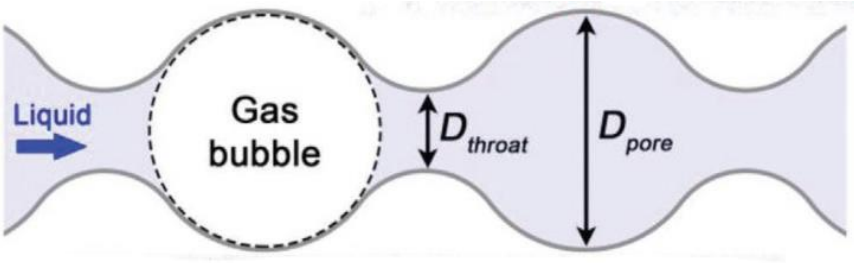

Figure 2-8: Diagram of gas bubbles traveling through the pores with pore-throat.

Based on the results presented in this section, it can be concluded that the most effective approach to reducing mass transport overpotential involves coating a well-defined nanostructure of a highly active catalyst [30] onto an appropriate 3D skeletal electrode with a large effective surface area [31].

The following sections review 3D electrodes produced for PEMWE and AWE. Despite their shared purpose, the electrodes were developed using different methods due to differences in materials and electrolyzer assembly. We, therefore, devote two separate sections to discussing their structure and manufacturing process.

2.8. Three-dimensional skeleton electrodes (PTL) for PEMWE

The porous transport layer, also known as gas diffusion layers, liquid/gas diffusion layers, or current collectors, plays a crucial role in transporting electric charges and ions to the catalysts and removing the reaction products from the catalyst surface in PEMWE. Section 2-3-2 explains PTL assembly. The catalyst is placed on the membrane and sandwiched between the PTLs (Fig.2-3). Since the components are compressed into one stack, the PTL should have a higher mechanical strength than the 3D electrodes in AWE. Catalysts are usually placed on membrane surfaces, and the PTL supplies ions and electric charges to the catalysts.

Material type is the first issue to consider in PTLs. Although currently lower-priced carbons are used in the cathode, titanium is still used for the anode due to the combination of the high anode potential and highly acidic environment. Titanium is highly corrosion-resistant in the anode and has high electrical conductivity and specific strength [40, 41, 42].

Porosity and pore size are other manufacturing parameters. Increasing the porosity result in increasing two-phase permeability (water and oxygen) and increases PEMWE efficiency [10]. However, too much porosity enhancement decreases PEMWE efficiency due to elevated oxygen saturation [46, 185]. One study indicated that porosities higher than 50% do not significantly affect efficiency [36], while another study showed that the optimal porosity for PTL is 50 to 75% [43].

Pore size and ohmic resistance are interlinked. An increase in pore size leads to a rise in ohmic resistance and a decrease in PEMWE performance. Additionally, larger ohmic resistance could result in a rise in energy loss as heat, causing local hot spots and a rise in local membrane degradation [35]. Mo et al. reported that the OER reaction only occurred at the edge of the PTL and the catalyst-coated membrane, underscoring the significance of reducing pore size or spacing between connections [184]. However, excessive reduction of the pore size reduces efficiency by hindering bubble escape. Reducing the particle size in the PTLs produced by powder metallurgy reduces the pore size. It has been reported that the optimal pore size for this technique is 10 µm, which is produced by 50 to 75 µm particles [36].

2.8.1. Literature review on PTLs manufacturing process

The manufacturing processes reported for producing porous titanium are limited to production in the solid phase due to the high melting point of titanium and the extremely high reactivity of melted titanium. PTLs are produced by powder/fiber metallurgy, lithography, tape casting, and thermal spray processes [44, 45, 46]. Lithography is an additive manufacturing process that builds complex printed items using photosensitive resins. The printed item requires heat treatment to achieve the desired strength. Though lithography provides the opportunity to produce precise 3D structures through CAD (computer-aided design), it is considerably time-consuming and costly [186]. Powder/fiber metallurgy processes or tape casting can be used to increase production speed. In powder/fiber metallurgy process, powders or fibers are consolidated through a pressing process to create a raw porous piece. To achieve the desired strength, the raw piece undergoes a sintering heat treatment. In tape casting, a slurry of removable glue and powder is fed to the tape-casting machine, and tapes made of the powder-glue blend are produced. The glue is removed during the heat treatment, and a metallurgic bonding is formed between the powders. Despite the advantages of powder metallurgy and tape-casting to produce porous pieces with the desired pore size, the sintering involved in these processes increases the manufacturing cost and time [47]. The thermal spray process has been studied to omit the heat treatment stage. In this process, powders are heated by a carrier gas, accelerated, and impacted the substrate to produce a coating with a metallurgic-mechanical bond. If the kinetic energy and temperature of powders are in the optimal range, coatings with high porosity can be created by this process. The kinetic energy and temperature of the powders should be low enough that the powders do not undergo excessive deformation upon impact the substrate and high enough to create enough strong bonds between the powders.

Since there are various methods for accelerating the carrier gas, and the temperature and speed of powders exiting the nozzle are different for each process, the thermal spray process can be classified into different categories. Fig.2-9 shows the classification of thermal spray processes [49, 187].

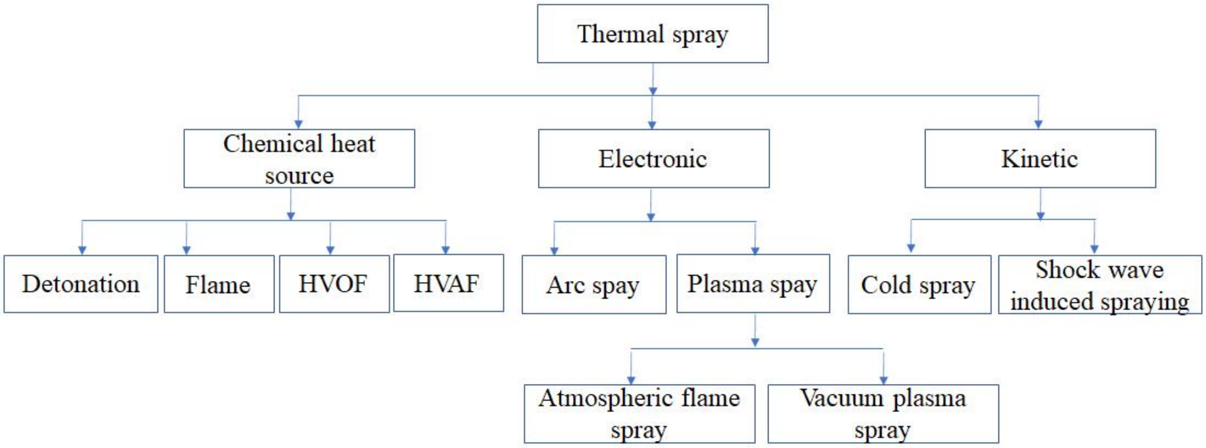

Figure 2-9: Classification of thermal spray processes [49, 187].

As seen in Fig.2-9, powders can obtain the thermal energy required from combustion, electrical, or kinetic energies. In combustion and electrical processes, powders become melted in the carrier gas and impact the surface. Since these methods fall into the category of liquid-state processing, only processes with high protection of molten titanium can be used to produce titanium coatings. Vacuum plasma spray (VPS) is the only process among the mentioned processes, used to produce porous titanium coatings due to its excellent protection of molten titanium by the shielding gas at low pressure [48]. However, the porosity is limited to less than 30 % due to powder melting and the high powder deformation during impact [49].

PTL manufacture using Cold Gas Dynamic Spraying (CGDS) was studied to benefit from the advantages of VPS without melting the powder [51].

Fig.2-10 illustrates a schematic view of a cold spray device. In this process, a carrier gas, usually an inert gas, such as Argon or Nitrogen, enters the inlet and is compressed in the converging section. As the cross-section decreases in the converging, the speed of carrier gas increases to keep a constant molar rate of the gas passing through, and it reaches the maximum speed, sound speed, at the throat. When the speed of the gas equals the speed of sound, different laws of physics apply to them than those less than the sound speed so that after passing through the throat, the speed of gas increases with the increase in the cross-section, and exceeds the speed of sound. The ultimate speed of the gas depends on temperature, pressure, initial gas speed in the inlet, and nozzle shape.

The carrier gas temperature during its passage through the nozzle is subject to change. As the gas moves toward the throat in the converging, the gas temperature increases due to the increase in pressure. After passing through the throat, as the gas speed increases, a drop in pressure and temperature occurs, and the gas temperature drops substantially.

During the gas flow passage, the powder is added to the inlet, accelerated by the gas flow, and impacted the substrate. During powder acceleration, the powder temperature is also affected depending on the carrier gas temperature. The temperature of powder exiting the nozzle depends on the initial powder temperature, gas speed, and gas temperature in the nozzle [188].

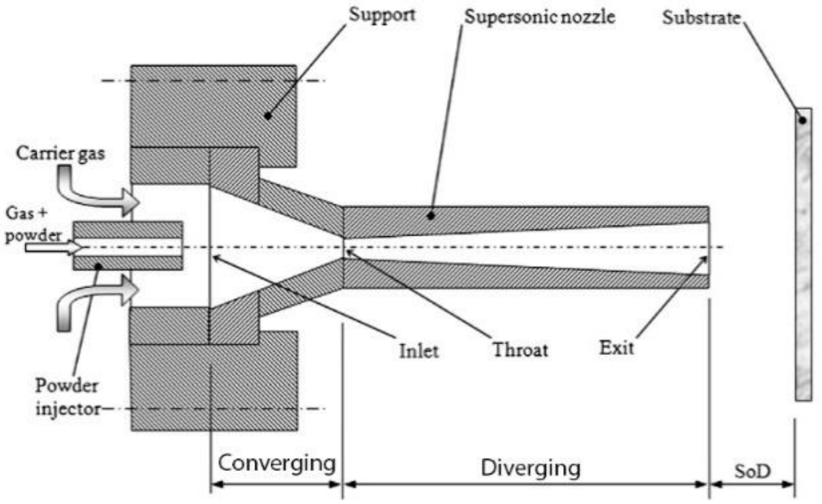

Figure 2-10: Cold Spray (CGDS) system working principles [188].

One of the advantages of this process is that the particle temperature remains below the melting point, lowering the risk of oxidation or changes in the powder microstructure. The binding mechanism is related to adiabatic shear instability that occurs on the particle surface at critical or higher velocities [51, 52, 53].

Since the particle temperature in this process significantly decreases, the particle velocity must be high enough to produce a strong bond between the particles; thus, particles undergo considerable deformation due to their high speed, and subsequently, the porosity decreases. Hence, the porosity in the CGDS coatings is limited to 30% [51, 52, 53].

Using a porogen and its subsequent removal can increase the porosity of the cold spray coating. A Ti+porogen powder mixture can be sprayed on the surface, and the porogen is later removed by leaching or heat treatment. J. Son et al. developed a porous cold spray coating with a porosity of 49% by cold spraying a Ti+Mg mixture and a subsequent heat treatment in a vacuum container at 1250°C to evaporate the Mg [54]. D. Qiu et al. also produced a porous cold spray coating with a porosity of 48% using the cold spray of a Ti+Al mixture and removing the Al in a NaOH solution [55].

2.8.2. Shock wave induce spray process: An alternative approach to producing high-porosity coatings

SWIS is another solid-phase method for producing porous coatings that combines the advantages of both VPS and CGDS. The nozzle does not have a significant role in increasing gas velocity in this process. Fig.2-11 provides a schematic view of the SWIS process. In this process, gas is compressed in a tank and the gas valve is rapidly opened and closed at a frequency of 10 to 50 Hz, generating alternating shock waves. The shock waves pass through the spray gun and heat and accelerate the powder. The particles then impact the surface, like in CGDS, but at a higher particle temperature. [50]. This results in a lower powder velocity but sufficient bonding strength and higher porosity than CGDS [49].

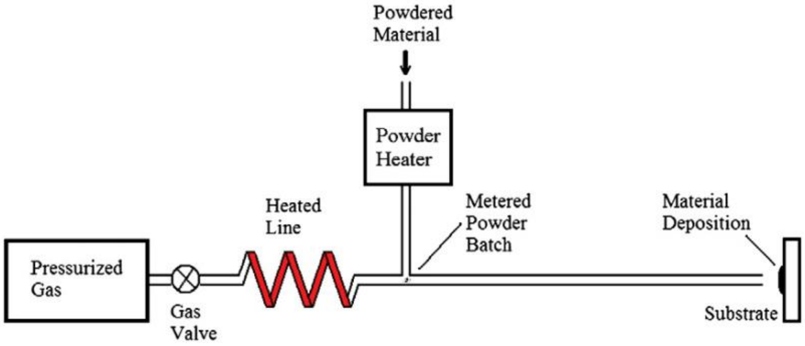

Figure 2-11: Schematic view of the shock-wave induced spraying device equipped with a powder heater.

2.9. Three-dimensional skeleton electrodes for alkaline water electrolysis

3D electrodes in alkaline solution are used as catalyst substrates. Like PTLs, these electrodes distribute electrical flow and transport reactants and products. They should have high stability, high conductivity and be cost-effective. Researchers have explored a variety of 3D non-noble structures, including Ni DHBT [56], Ni wire [57], Ni foam, stainless steel or Ni mesh [58], carbon paper [59, 60], and FTO [61], for oxygen evolution reaction (OER) in alkaline environments. While these structures generally possess a high surface area per thickness, the majority lack sufficient development in three-dimensional space (X, Y, and Z) to maximize the total surface area. For instance, the thickness of Ni DHBT is constrained to a maximum of 200 μm [56].

In terms of stability and surface area, carbon paper and Ni foam emerge as suitable 3D structures commonly employed as skeleton electrodes for OER. These materials can be commercially produced in desired dimensions. However, precise control of the accessible space between deposited active materials on the 3D structure in carbon paper remains challenging. Reducing this space increases the diffusion length of ions, impeding both ionic and electronic conductivity [62]. Consequently, Ni foam has garnered significant attention for OER in alkaline media due to its high electrical conductivity, mechanical stability, and the presence of nickel elements facilitating the formation of a Ni-compound catalyst on the surface [58]. Nickel foams exhibit a notably high porosity percentage (85-98%) [63], facilitating ion diffusion within the structure [64] and the release of bubbles from the structure [65].

An intriguing feature of nickel is its ability to undergo a heat treatment process to produce a nanoporous structure known as Raney Ni, resulting in bimodal pore sizes (micrometer and nanometer pore sizes). This newly formed structure with the dual pore size is termed Raney Ni foam [80, 81].

2.9.1. Raney Ni catalyst and Raney Ni foam

Raney Ni is a porous structure of Ni with a pore size of less than 5 nm, which is created by leaching out Al from Ni-Al intermetallic (Al_3Ni or Ni_2Al_3) [72, 73, 74], which is widely used in organic synthesis and a variety of industrial processes [69]. Raney Ni has a larger specific surface area (100 $m^2.g^{-1}$) than a typical Ni electrode, which yields more active sites.

Researchers have extensively studied the pore structure of Raney nickel [72, 85, 189, 190, 191, 192]. All the Raney nickel investigated was produced by leaching aluminum from a homogeneous

Ni-Al alloy with a chemical composition of 40-60 wt.% Ni. Researchers found that the leaching condition and chemical composition of the alloy determine the final pore structure of Raney Ni.

Raney nickel alloys with a higher Al concentration, such as Ni-58wt.% Al, have a higher volume fraction of $Al_3Ni:Ni_2Al_3$ than alloys with a lower Al concentration, such as Ni-49wt.% Al. Raney Ni generated by each alloy has a different pore structure due to variations in the volume fraction. J. Freel and G. D. Lee found that when Al content of the alloy decreases, a Raney nickel with a larger pore size is formed [189, 190]. The reactivity of Al_3Ni to an alkaline solution is significantly higher than that of Ni_2Al_3. Even at room temperature, Al_3Ni reacts strongly to alkaline solutions, whereas Ni_2Al_3 is almost unreactive [190]. Due to its high reactivity, Raney Ni derived from Al_3Ni contains less Al content, a smaller pore size, a larger specific surface area, and higher HER activity [85, 192]. Despite the advantage of Al_3Ni phases, the presence of Ni_2Al_3 is necessary for a polycrystalline Raney Ni because leached Ni_2Al_3 creates only stable skeletons [191].

The leaching conditions include leaching temperature, leaching time, and alkaline solution concentration, which are all factors that affect pore size. Lower temperature leaching of the commercial Raney nickel alloy (50:50% wt.% Ni-Al) produces Raney Ni with smaller pore size, lower pore volume, and a larger specific surface area having higher HER activity [72, 189]. The Raney nickel structure produced from Ni-50 wt.% Al alloy at 50℃ for 90 minutes results in a structure with pore size, pore volume, and specific surface area of 3 nm, 0.06 cc/g, and 100 $m^2.g^{-1}$, respectively. The values obtained when the alloy is leached at boiling temperature for 45 minutes are 6 nm, 0.125 cc/g, and 86 $m^2.g^{-1}$ [189, 190]. Elevated temperatures during leaching lead to a higher rate of hydrogen production within the structure and increased pore destruction. Although leaching at a lower temperature results in a larger specific surface area in commercial Raney nickel alloys, aluminum trihydrate is seen in the structure after leaching due to the existence of low reactive Ni_2Al_3 intermetallic in the alloy [190].

The leaching time depends on the concentration and temperature of the alkaline solution. In general, the acquired specific surface area increases as the leaching time increases. However, when samples are leached for an extended period of time, the specific surface area decreases due to the oxidation of Raney Ni [189, 190].

Raney Ni has been recently studied for OER in alkaline media [70, 71]. To manufacture a Raney Ni electrode, intermetallic Ni-Al compounds are coated on the surface of the electrode using various technologies such as electrodeposition, plasma spray, and hot rolling, and the Al is later leached out [75, 76, 77].

To manufacture a Raney Ni foam, Al powders are placed on the surface of a Ni foam. Then, Al reacts with Ni through heat treatment, forming Ni_2Al_3 or Al_3Ni intermetallic compounds on the surface. The Raney Ni foam structure is then formed on the Ni foam surface by a leaching process. Researchers have reported that the production of Raney Ni nanostructures significantly enhances the activity of Ni foam [80, 81].

Though this procedure can create 3D Ni structures with a micrometer and nanometer pore size, the manufacturing process includes several stages, and the first stage is producing Ni foam.

2.9.2. Challenges associated with Ni Foam

Ni foam is generally manufactured by electrodeposition, in which a Polyurethane foam is used as the skeleton, which is then heated to form the foam [68]. The complex and energy-consuming process of producing this foam makes manufacturing costly.

Although the high porosity of Ni foam is advantageous in mass transport, it also decreases the specific surface area [66]. In addition, Ni foam has pore sizes of more than 300 μm, while 3D microstructure with a pore size of less than 100 μm has higher OER efficiency [95]. Therefore, the porosity design in Ni foam requires a revision to increase the specific surface area without negatively affecting mass transport. The size, distribution, shape, and connectivity of the pores can act as design parameters [67].

To resolve the mentioned issues, we propose an innovative 3D structure of Ni (long and thin Raney Ni whiskers) in this thesis that can provide a significantly larger specific surface area than Ni foam or Raney foam while maintaining a high-performance OER. Through the inventive technique, we concurrently generate a Ni 3D Skeleton with micrometer-scale pores and Raney Ni with nanometer-scale pores in a single manufacturing stage, utilizing a straightforward and cost-efficient process. Since the space between the fibers during the production process can be easily controlled in this method, this structure can be easily manufactured for the electrodeposition of any catalyst.

2.9.3. Novel method for producing New 3D structures of nickel

We were inspired by the Ni-Al eutectic structure to make this structure. During the eutectic solidification of molten Ni-Al, Al_3Ni fibers preferentially grow in one direction to form long and thin fibers of the Al_3Ni phase, and a phase rich in aluminum (α-Al) is then formed as a shell around the Al_3Ni fiber. As a result, Al_3Ni fibers are separated and well-aligned in the aluminum matrix [82]. If the α-Al dissolves and the Al is leached out of the Al_3Ni fibers using potassium hydroxide

(KOH), only very thin and long Raney Ni whiskers (which are ribbon-like) remain. To enable the Raney Ni fibers to attach to the nickel plate after leaching, the Ni-Al eutectic on the nickel plate was directionally solidified. There is no report on the production of Raney Ni fibers, and all reports are related to the powder or bulk coating of Raney Ni [72, 73, 74].

Since Ni whiskers are obtained from the leaching of Al_3Ni fibers, the dimensions and density (number per cm^{-2}) of Ni whiskers directly depend on the dimensions and density of Al_3Ni fibers. As with other metal alloys, heat treatment and alloy chemical composition determine the dimensions and density of Al_3Ni phases. Understanding phase changes requires knowledge of alloy growth patterns, phase diagrams, etc. Therefore, section 1-11 is dedicated to eutectic alloys, specifically Ni-Al eutectic.

2.10. Eutectic structure

Eutectic solidification is the direct transformation of the liquid phase solution of elements A and B into two solid phases, $L\rightarrow\alpha+\beta$, where α is a solid solution rich in element A, and β is a solid solution rich in element B. To comprehend the solidification process of these alloys, the phase diagram of these alloys should be plotted via free energy-composition curves. Fig.2-12 shows a typical type of these curves.

The free energy of each phase is defined as (G=H-TS), where H is the enthalpy, T is the temperature, and S is the entropy value of the system. The value of TS increases significantly at sufficiently high temperatures (T1) so that it has less free energy than the free energy of the solid phases at all A and B concentrations. As the temperature decreases, the G-X curve of the solid phase drops lower than that of the liquid, allowing for a common tangent line to be drawn between the G-X curve of the liquid and β phase at temperature T2. Compositions on the tangent line will transform into L(β) and β(L) to reach a lower energy level. In these circumstances, a part of the melt rejects element B to form a liquid phase with the composition L(β), and the rest of the melt solidifies as a solid phase β(L). Any composition outside the chemical composition range of the tangent line is either a liquid solution or a β solid phase. At lower temperatures (T3), two tangent lines can be drawn, resulting in the production of two solid solutions of α(L) and β(L) within a certain range of chemical compositions. At temperature T4, there is a tangent line for all three phases L(β), α(L), and β(L), indicating that all three phases can be in equilibrium at this temperature. The free energy α and β at temperature T5 is lower than the free energy of the liquid phase, and only the two phases of α or β are observed in the structure.

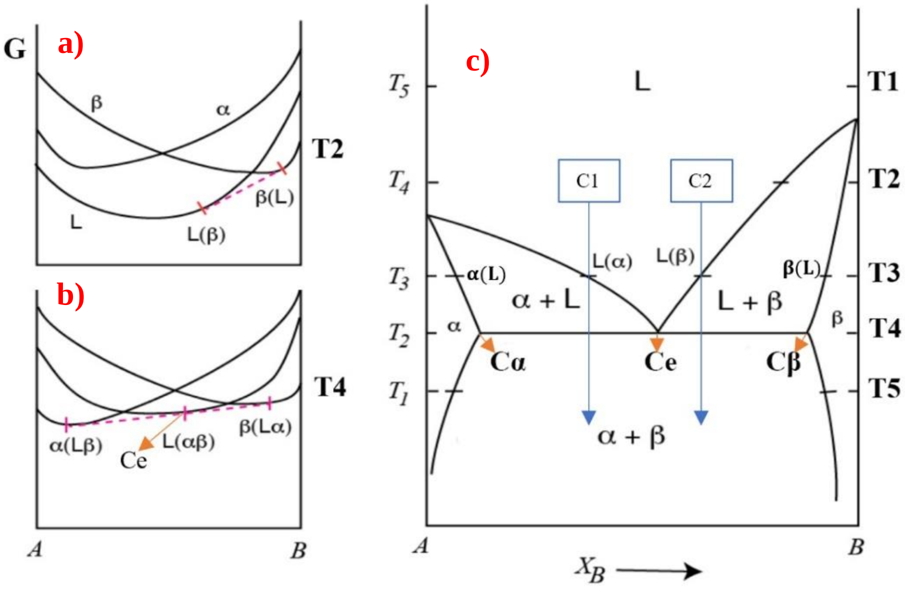

Figure 2-12: Constructing a eutectic T-X diagram from several G-X diagrams.

An alloy with the chemical composition of Ce is called an Eutectic Alloy. A eutectic alloy begins to solidify at the eutectic point (Ce in Fig.2-12c), and both α and β phases simultaneously nucleate and grow at this point, until they collide and form colonies of a eutectic structure. The volume or weight fraction of α or β phases in the eutectic structure in the eutectic line (T4) can be calculated by the Lever Rule. If the horizontal axis in the phase diagram is the weight percent of element B, the weight and volume percent of phase α and the eutectic structure are calculated as follows:

$$Weight\ percent\ of\ \alpha\ at\ eutectic = \frac{C\beta - Ce}{C\beta - C\alpha} \qquad (34)$$

$$Volume\ fraction\ of\ \alpha\ (Vf\ \%)\ at\ eutctic = \frac{\frac{M\alpha}{\rho\alpha}}{\frac{M\alpha}{\rho\alpha}+\frac{M\beta}{\rho\beta}} * 100 \qquad (35)$$

Where Mα and Mβ (Mβ=100-Mα) are the weight percent of α and β phases, respectively, and $\rho\alpha$ and $\rho\beta$ are their density.

Alloys with a chemical composition between *Cα<C<Ce*, such as C1, are called hypoeutectic alloys, and alloys with a chemical composition of *Ce<C<Cβ*, such as C2, are called hypereutectic alloys. In hypoeutectic and hypereutectic alloys, the pre-hypoeutectic and pre-hypereutectic phases nucleate and grow first.

During the solidification of an alloy such as C2, the pre-hypereutectic phase (enriched in B element) at the T3 temperature with the chemical composition $\beta(L)$ first nucleates in the melt and changes the molten chemical composition to L(β) due to the rejection of element A. As the temperature decreases, the volume fraction of the pre-hypereutectic phase increases while the chemical composition of liquid and solid changes on the solidus line of L(β) the β phase, respectively. Just before the eutectic line, the weight percent of pre-hypereutectic reaches $(\frac{Ce-C2}{Ce-C\beta})$, while the rest of the melt has a chemical composition of Ce. As the temperature decreases, the remaining melt is solidified as a eutectic alloy [92, 193]. Fig.2-13 shows a schematic view of the solidified structure of the eutectic, hypoeutectic, and hypereutectic alloys.

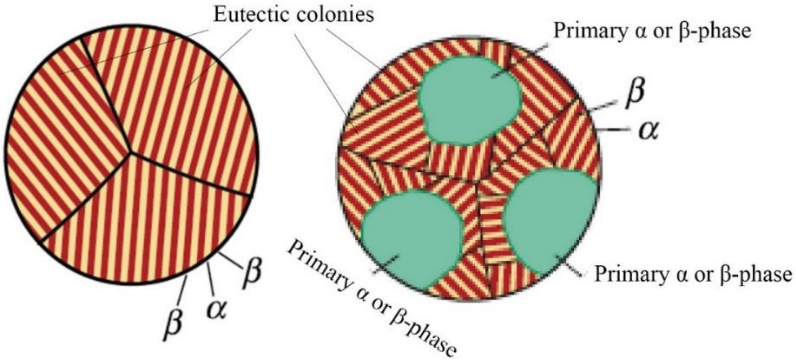

Figure 2-13: Schematic visualization of microstructures of Hypoeutectic, eutectic and Hypereutectic alloys.

The nucleation of phases in the eutectic alloy can be defined by Classical Nucleation Theory. Nucleation starts below the eutectic temperature and with the heterogeneous nucleation of one of the α or β phases. The growth of phases begins when a stable nuclei is formed [194].

Phase growth in eutectic alloys occurs in two ways: 1- Divorced Growth, in which the two eutectic phases grow separately. In this case, like spheroidal graphite cast iron, each phase grows separately without a diffusion couple. 2- Cooperative Growth, in which two phases grow together as a diffusion couple. Most commercial eutectic alloys, including Ni-Al, Pb-Sn, and Al-Si, commonly display lamellar structures and demonstrate cooperative growth [195].

A schematic representation of cooperative solidification is shown in Fig.2-14. During the solidification process of this type of alloy, both soluble elements A and B are rejected from the phases. Soluble element A accumulates in front of the β phase, while element B accumulates in front of the α phase. The solute only needs diffusion from one phase to another along the S/L interface. Sideway diffusion is responsible for the formation of alternating layered phases in the eutectic phase. The eutectic layer spacing is controlled by two opposing factors: diffusion tends to decrease eutectic layer spacing, while surface energy tends to increase it [195].

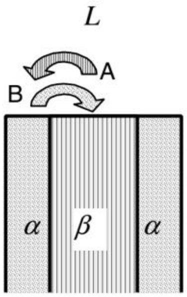

Figure 2-14: Schematic representation of eutectic cooperative growth.

Commercial alloys are not usually solidified in equilibrium and are cooled at a specific cooling rate. As the cooling rate increases, the thermal undercooling increases and causes two changes in the eutectic solidification: 1) an increase in the nucleation rate of either the α or β phases by reducing the nucleation energy barrier, 2) an increase in the progression speed of the S/L interface. The nucleation rate and progression speed of the S/L interface determine the eutectic growth rate. It is generally accepted that the relationship between eutectic layer spacing (λ) and eutectic growth rate (V) is as follows:

$$\lambda_s^2 V = constant \qquad (36)$$

Equation (36) also applies to the Ni-Al eutectic. Additionally, according to the findings, eutectic growth rate and colony size are correlated for the Ni-Al eutectic as follows:

$$\lambda_{col}^3 V = constant \qquad (37)$$

According to equations (36) and (37), increasing the cooling rate has a greater effect on eutectic layer spacing than on colony size [195, 196, 197].

The cooling rate has other impacts on the hypoeutectic and hypereutectic alloys. A high cooling rate suppresses the formation of the primary phases and shifts the eutectic point to the left (for hypoeutectic alloy) or right (for hypereutectic alloy) [150, 198].

Q. C. Jiang et al. Investigated the effects of cooling rate on eutectic point displacement for Al-Si hypereutectic alloys containing varying amounts of Si. Fig.2-15 shows the phase diagram of Al-Si alloys in both equilibrium and non-equilibrium states. When a hypereutectic alloy with C0 composition solidifies at a high cooling rate, the eutectic point shifts down and to the right. The researchers also observed that the eutectic point shifts further to the right as the amount of silicon in the alloy increases [198].

According to the lever rule, a shift of the eutectic point towards the right causes the volume fraction of the primary β phase to be reduced and added to the volume fraction of the fine phase β in eutectic colonies. In other words, the volume fraction of fine phase β in eutectic colonies increases on the one hand, and the volume fraction of eutectic colonies increases on the other.

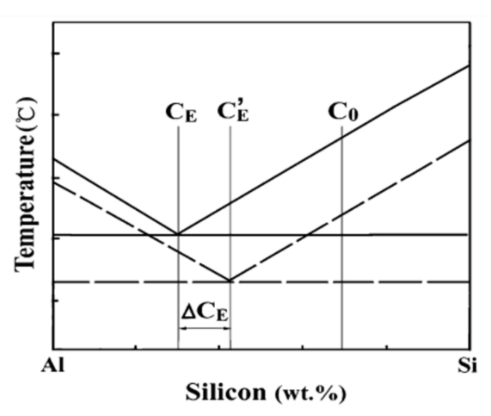

Figure 2-15: Schematic view of the equilibrium (continuous line) and non-equilibrium (dash line) phase diagram for the Al-Si system [198].

Microstructures of eutectics are influenced by the volume fractions of phases and their melting entropies. When the volume fraction of a phase is less than 0.25, fibers are formed, while when the volume fraction is greater than 0.25, lamellar structures are formed (see Fig.2-16).

The eutectics grow in faceted or non-faceted forms depending on the melting entropy of the phases. Faceted crystals are formed as a result of the growth of specific crystal plates, and the formed crystal has angle shapes, whereas non-faceted crystals form without the development of well-defined crystal faces.

Eutectics are divided into three categories based on their faceted or non-faceted growth: 1- non-faceted /non-faceted eutectics (nf/nf), 2- non-faceted / faceted (nf /f) and 3- faceted/faceted (f/f). Among these three categories, the first two are common and have commercial applications. The dimensionless melting entropy of each phase, $\Delta S_f/R$, where ΔS_f is the melting entropy, and R is the gas constant, is used to distinguish the growth of faceted or non-faceted eutectic phases. If $\frac{\Delta S_f}{R} < 2$, the phase growth is non-faceted. If $\frac{\Delta S_f}{R} > 2$, the phase growth is faceted.

Fig.2-16 illustrates the impact of melting entropy and phase volume fraction on eutectic microstructures. When the volume fraction of one phase is significantly lower than the other phase (<0.28), and both phases are non-faceted, the system minimizes surface energy by forming cylindrical fibers. Compared to lamellae, cylindrical fibers have less interface energy. When the minor phase is faceted, growth behavior is determined by specific atomic planes. In this case, atomic planes grow in a way that exposes planes with low interfacial energy to each other. Al-Si and Ni-Al alloys fall into this category [195].

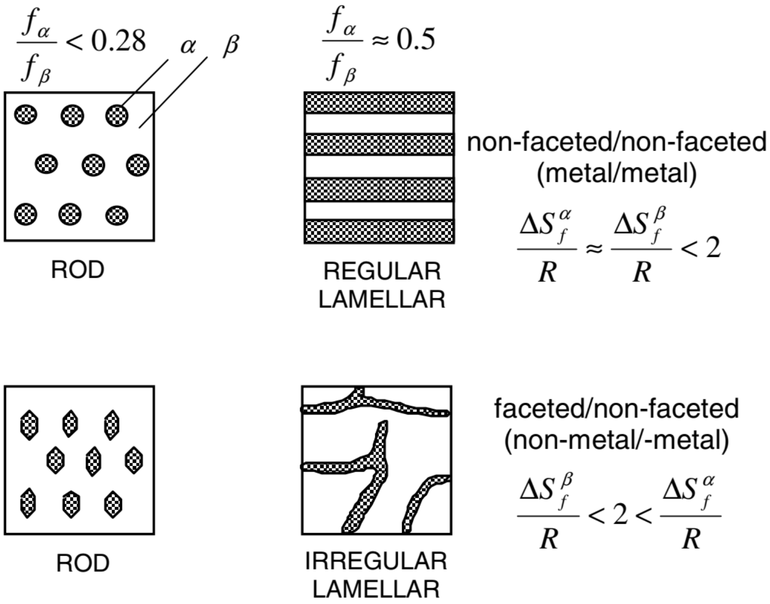

Figure 2-16: Types of cooperative eutectics [195].

2.10.1. Ni-Al eutectic, diagram phase of Ni-Al and growth of Al_3Ni

Ni-Al eutectic alloys fall into the cooperative growth category. According to the Ni-Al phase diagram in Fig.2-17, the eutectic is formed under equilibrium conditions at a concentration of 5.7 wt.% Ni and at a temperature of 640 °C. Eutectic Ni-Al alloys consist of fine Al_3Ni fibers that are well-aligned within α-Al (Fig.2-18a). Alloys that contain less than 5.7% Ni are hypoeutectic alloys containing both Ni-Al eutectic and α-Al primary phases. Those alloys containing between 5.7 and 42 wt.% Ni are hypereutectic, consisting of eutectic phases mixed with primary Al_3Ni phases [82, 92, 199]. Fig.2-18b shows a typical microstructure of a hypereutectic Ni-Al alloy.

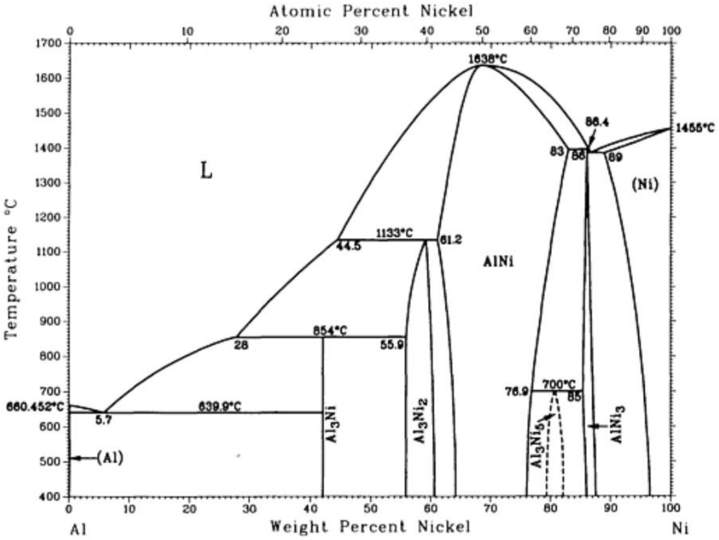

Figure 2-17: The Ni-Al diagram phase [92].

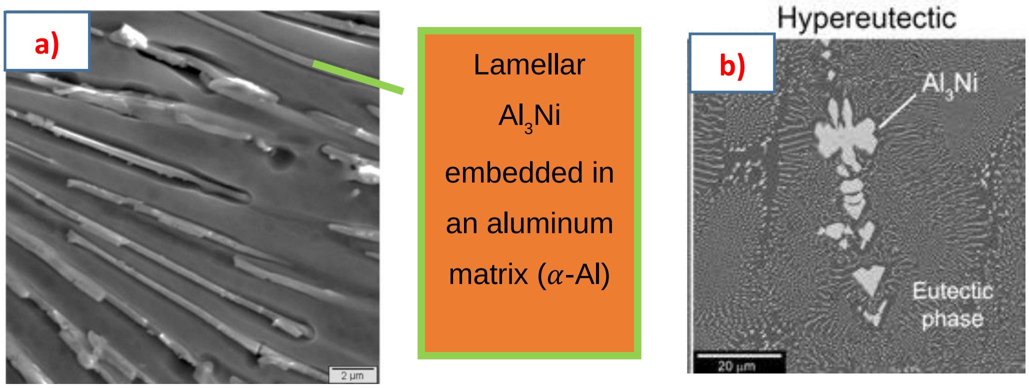

Figure 2-18: Microstructure of Ni-Al eutectic. a) Al_3Ni fibers imbedded in Aluminum matrix, b) SEM image of microstructure of typical Hypereutectic Ni-Al alloy [82, 199].

Ni-Al equilibrium phase diagram can be used to predict intermetallic formation sequences in the Ni-Al system. When a molten hypereutectic Ni-Al is cooled, Al_3Ni is the first solid phase which nucleates in the melt [92]. The lower the amount of Ni in the hypereutectic molten alloy, the more cooling is needed to form a stable Al_3Ni nuclei; consequently, solidification starts at a lower temperature than the Al_3Ni solidification point [150]. After the formation of stable nuclei, Al_3Ni grows rapidly and consumes Ni in the molten alloy. During cooling, Ni content and temperature of the molten alloy decrease, and when the temperature and chemical composition meet the criteria to stabilize the nucleus of α-Al, eutectic solidification begins.

During a Ni-Al eutectic solidification, the liquid simultaneously solidifies into two phases, α-Al and Al_3Ni. Initially, Al_3Ni nucleates heterogeneously, then grows while simultaneously rejecting Al solutes. Al rejection generates supercooled α-Al that solidifies around Al_3Ni fibers [94].

It is well known that the growth of Al3Ni fibers in the direction of the length is much higher than in the width due to the high melting entropy and strong growth anisotropy of Al3Ni fibers [94]. Al3Ni has high melting entropy, leading to a faceted interface, while α-Al has a non-faceted interface [200]. When a crystal grows faceted, it preferentially grows in the direction dictated by specific atomic planes, as some planes may have the lowest surface energy. The growth of surfaces with the lowest growth rate determines the shape of a faceted crystal [201]. The Al_3Ni crystal grows rapidly along the packed plane, forming a crystal bounded by (001) and (101) facets. Long whiskers of Al_3Ni, which have a rectangular shape in the eutectic, are formed due to this growth (Fig.2-19) [200].

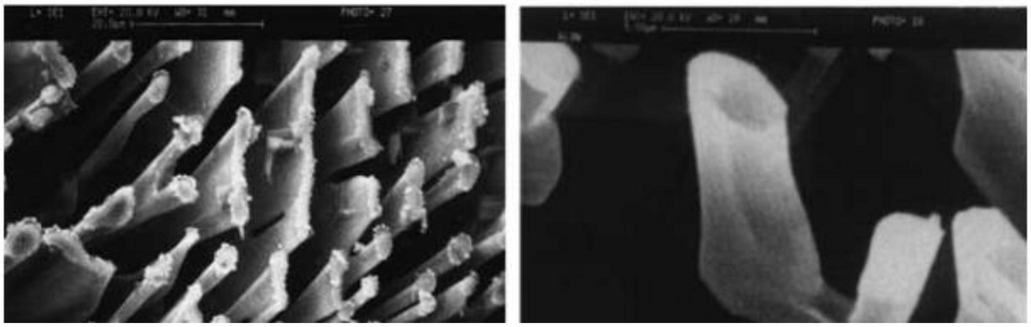

Figure 2-19: Cross section of Al3Ni fibers at two different magnifications [202].

2.10.2. Directional solidification of Ni-Al eutectic

The fibers of Al_3Ni grow in one direction and then stop after a maximum growth of about 150 μm, forming eutectic colonies. Eutectic colonies can be levelled and aligned using directional solidification. Research has demonstrated that a minimum cooling rate is required to align eutectic colonies. Increasing the cooling rate also suppresses the generation of the Al_3Ni primary phase and creates a finer eutectic phase with a higher weight percentage of Al_3Ni fibers in the eutectic. For instance, a study reported that by increasing the cooling rate to 10 °C/s, it is possible to prevent the formation of the Al_3Ni primary phase in the Al-8wt.% Ni hypereutectic alloy until the whole structure is solidified in a eutectic form [203].

2.11. OER Catalysts

OER catalysts are generally classified into two Noble Catalysts and Non-Noble Catalysts categories.

2.11.1. Noble catalysts

The most common metals used for the OER catalysts are iridium, ruthenium, platinum, and palladium. The oxides of these metals have the highest activity among metal oxides. The activity of these metals is Ru>Ir>Pt>Pd. Although ruthenium has the highest activity, its use is limited due to its low stability. Iridium is the most widely used in electrolyzers in terms of stability and performance among noble metals [5]. Iridium is located near the peak of the volcano-shaped trend and is one of the most active monometallic oxides [27].

Despite noble catalysts' high activity, they are expensive metals, and their catalysts are also costly. To reduce the cost of making a noble catalyst, many efforts have been made to increase the utilization, stability, and activity of the noble catalyst [5].

Attempts have been made to make compounds of noble oxides to increase Iridium stability and activity. Li e. al produced compounds of iridium oxide and ruthenium, which have higher stability and activity than iridium [204]. In another example, Liyanage e. al developed a high-efficiency, low-cost catalyst from ternary phosphide nanoparticles ($Ni_{2-x}Ru_xP$). Using nickel as an inexpensive metal lowered catalyst production costs while the activity and stability of Ru oxide increased [205].

To increase catalyst utilization, noble metals can be deposited on polymer templates to create a three-dimensional porous structure of noble metals after removing the polymer. To further increase the utilization, researchers have investigated the decoration of iridium on carbon, and thus increased the catalyst utilization to a great extent. Mingui et al. also performed an iridium decoration on a Ni 3D structure using the simple and inexpensive method of cation exchange. They reported that the catalyst required an overpotential of only 195 mV for a current density of 10 $mA.cm^{-2}$ [206].

Despite many attempts to reduce the cost of noble catalysts by increasing their utilization, their high price is still an obstacle to their widespread and commercial application. One alternative approach is to develop structures and compounds of non-noble metals instead of noble metals [5, 140].

2.11.2. Non-noble catalysts

Catalysts with different morphologies and compounds of non-noble metals are being developed to reduce the cost of hydrogen production. These catalysts should be developed so as to provide a high intrinsic activity for OERs, have high electrical conductivity, and be non-toxic, corrosion stable, abundant, and cost-effective to be economically justified [5, 140].

The use of transition metals such as Ni, Co, and Fe, which are very abundant, has been widely investigated in recent years to prepare OER catalysts for use in alkaline environments. The electrocatalytic activity of the mentioned elements is Ni>Co>Fe. Nickel oxide, which is converted into nickel hydroxide ($Ni(OH)_2$) in the vicinity of the atmosphere [70], is known as an important catalyst for OER due to its high stability and activity in alkaline media, and its activity can be increased through nanostructure production [5].

Nickel hydroxide (II) exists in two different polymorphs, α-$Ni(OH)_2$ and β-$Ni(OH)_2$. α-$Ni(OH)_2$ is transformed to β-$Ni(OH)_2$ under a chemical reaction. In addition, if nickel hydroxides undergo anodic polarization, they transform into oxy-nickel hydroxides with $\gamma - NiOOH$ or $\beta - NiOOH$ polymorphs. Fig.2-20 shows a summary of various polymorphs of nickel hydroxide and oxy-nickel hydroxide, as well as the chemical and electrochemical reactions for their transformation [207].

α-$Ni(OH)_2$ is not stable in the presence of water, and all α-$Ni(OH)_2$ is chemically converted to β-$Ni(OH)_2$ through an aging process. Aging can be achieved by keeping α-$Ni(OH)_2$ in water for a sufficient time or inducing cyclic voltammetry after sufficient cycles [208].

As $Ni(OH)_2$ phase is anodically polarized, it is oxidized to NiOOH by an oxidation process just before OER begins. In the structure of NiOOH, there are active sites of Ni^{3+} or a mixture of Ni^{3+} and Ni^{4+} that are known as active sites for OER. Both β-NiOOH and γ-NiOOH can contribute to OER, but several studies suggest that β-$Ni(OH)_2$ structure has lower capacity and higher OER activity than α-$Ni(OH)_2$. In contrast, another study suggests that the reason for the increased OER is the addition of Fe impurities to nickel hydroxide during aging [208, 209].

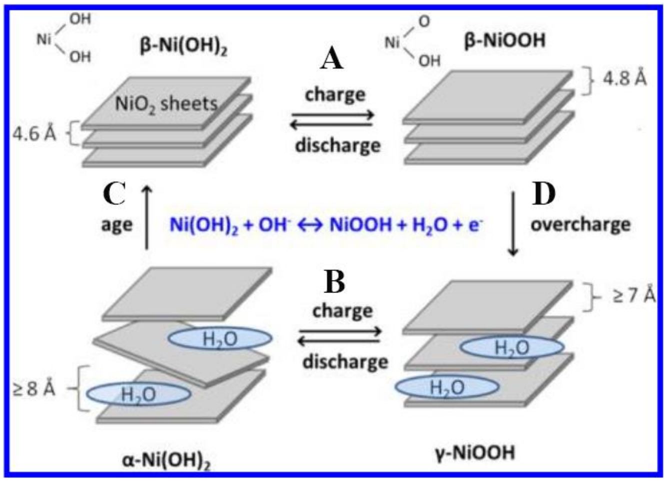

Figure 2-20: A and B represent the electrochemical reactions with one electron, and C and D represent chemical reactions for polymorphs of Ni hydroxide and oxy-Ni hydroxide [207, 209].

Various nickel compounds have been synthesized to increase Ni OER activity. Compounds containing Ni are highly active, stable, and cost-effective for oxygen evolution in alkaline environments [5]. Nickel compounds can be classified into three categories: Ni-Based layered double hydroxides (LDH) [210], Ni Phosphides [211] and Ni-Based Alloys [212]. Ni-Fe compounds or Ni-Fe LDH are well-known among these compounds. Some researchers claim that Ni-Fe LDHs are the most active OER catalysts in alkaline environments. This is probably why they are the catalysts of choice for industrial water electrolysis [106, 107].

The impact of iron on nickel catalyst activity is to a substantial extent undetermined. Recent studies indicate that the synergistic interactions between Fe and Ni (oxy) Hydroxide, and the high oxidation states of Fe and Ni centers contribute to high OER activity [213].

Ni-Fe catalysts can be coated onto nickel foam through electrochemical processes to increase the specific surface area [106, 214, 215]. The iron can also be doped to nickel foams using acidic [102, 103, 105] or basic solutions [104, 216] to produce these catalysts.

3 MATERIALS AND METHODS

3.1. Materials

The materials used in the study have been divided into two categories: those utilized in the production of Ni whiskers, catalyst synthesis and electrochemical characterization, and those employed in the creation of the porous transport layer, as detailed in Table 3-1.

Table 3-1: The materials used in the study.

	Material / Grade	Supplier
Ni whisker production, Electrochemical characterization, and catalyst synthesis	Ni foil (99.994%)	Alfa Aesar
	Al powder (99.7%), D50=20 μm	Valimet
	Argon (99.999%)	Air Liquid
	KOH (99.99%)	Fisher Chemical, ACS Reagent grade
	$FeCl_2 \cdot 6H_2O$ (98%)	Alfa Aesar
	K_2IrCl_6, Ir 39% minimum	Thermo scientific
The production of the porous transport layer	Ti powder (99.5%), spherical, D50= 30 μm	AP&C
	Ti powder, irregular, D50=73 μm	Wah Chang
	Ti powder (>99.5%), irregular, D50= 90 μm	Goodfellow
	Cu powder (>91%, 7 wt.% Si), spherical, D50= 70 μm	Metco 55
	Al powder (>99.3%), spherical, D50= 83 μm	A357

3.2. Equipment

The production of Ni whiskers involved the use of a tube furnace, while two types of thermal spray processes, namely cold spray and shock wave-induced, were employed to fabricate Ti 3D structures.

3.2.1. Tube furnace

For the experiments, a tube furnace (Model No. F21135) with a glass tube having an inner diameter of 30 mm was utilized (Fig.3-1). To carry out the experiments under an Ar atmosphere of high purity (99.999%), the tube was linked to an Ar capsule.

Figure 3-1: The tube furnace utilized for heat treatment procedures.

3.2.2. Cold spray dynamic spray (CGDS)

In this study, Cold gas dynamic spray (Kinetiks 4000 from CGT-GmbH, currently part of Impact-Innovations, Germany) with a SiC nozzle was utilized. Nitrogen gas was used as the carrier gas for the process. It should be noted that a brief explanation of CGDS process was provided in Chapter Two.

3.2.3. Shock-Wave Induced Spray (SWIS)

In Chapter Two, a brief overview of SWIS process was provided. For this study, the Shock-Wave Induced Spray (SWIS) deposition system was supplied by Centerline Ltd. It utilized a stainless-steel tube nozzle (650 mm long with 5 mm internal diameter) connected to a divergent stainless-steel tube coated with Inconel (5 mm inlet diameter, 6 mm outlet diameter, and 120 mm long).

3.3. Physical characterization methods

Scanning electron microscopy (SEM), energy-dispersive X-ray spectroscopy (EDX), transmission electron microscopy (TEM), X-ray diffraction (XRD), pole figure analysis, Brunauer–Emmett–Teller (BET) analysis, and electrochemical analysis were all employed in this study.

3.3.1. Scanning electron microscopy and energy-dispersive X-ray spectroscopy

Scanning Electron Microscopy (SEM) is a crucial analytical technique employed in many scientific disciplines for the imaging and analysis of materials at the micro and nanoscale. The technique involves scanning a focused beam of electrons across the sample surface, generating a wealth of data in the form of emitted electrons and images. These signals contain information about the sample topography, morphology, and composition, making SEM a powerful tool for characterizing a wide range of materials. The size and shape of the interaction volume produced during electron-matter interaction, as illustrated in Fig.3-2, are influenced by a variety of factors, including the atomic number of the sample, the angle of incidence, and the accelerating voltage.

Secondary electrons and backscattered electrons are two types of signals that form SEM images. Secondary electrons are generated through inelastic interactions between the primary electron beam and the sample surface, resulting in electrons with lower energy compared to the backscattered electrons. These secondary electrons are then detected by the SEM and used to create an image of the sample's surface morphology. Backscattered electrons, on the other hand, are high-energy electrons that are scattered back from the sample's inner layers when the primary electron beam interacts elastically with the sample. These electrons provide compositional and crystallographic information and are used to create contrast in the SEM image.

In addition to SEM imaging, Energy Dispersive X-ray Spectroscopy (EDX) is commonly used in conjunction with SEM analysis to identify the elemental composition of a sample. EDX works by detecting the X-rays emitted by the sample when it is bombarded with high-energy electrons from the primary beam. Each element in the sample produces a unique X-ray signature, allowing for the identification and quantification of the elements present. This information can be used to determine the sample's chemical composition and to investigate the distribution of elements within the sample [217].

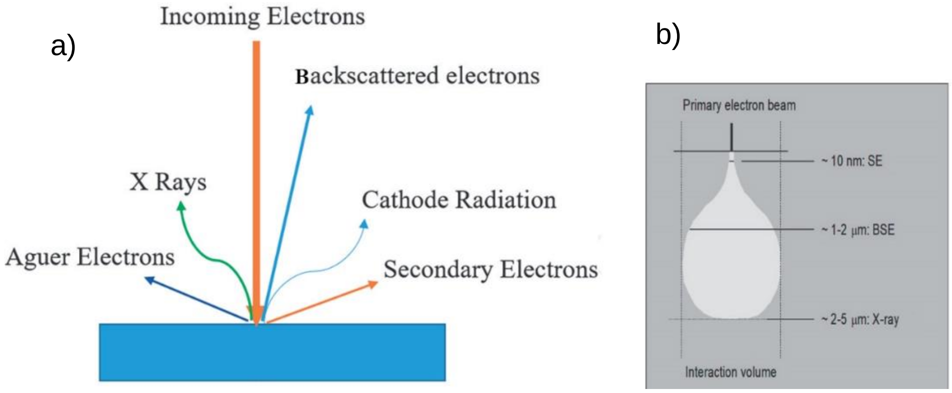

Figure 3-2: a) Formation of rays and electrons due to incoming electron beam interaction, b) The size and shape of the interaction volume produced during electron-matter interaction.

The characterization of the sample surface morphology was carried out using scanning electron microscopy (SEM) in secondary electron (SE) mode, utilizing a JEOL JSM-6300F instrument. To assess the chemical composition of the sample, Energy Dispersive X-ray Spectroscopy (EDX) was performed using a VEGA3 TESCAN instrument. EDX analysis in the experiment involved analyzing a minimum of three regions, and the median value was then recorded. Magnification was adjusted to ensure that the three regions selected represented the entire structure.

3.3.2. X-ray diffraction

X-ray diffraction (XRD) is a non-destructive analytical technique used to investigate the crystal structure of materials. XRD works by emitting a beam of X-rays onto a material, which causes the

X-rays to scatter in a specific pattern depending on the crystal structure of the material. This pattern can be detected and measured using a detector.

The scattering of X-rays by a crystal can be explained by Bragg's Law *(Equation (38) and Fig.3-3)*, which states that when X-rays of a certain wavelength (λ) interact with a crystal at a specific angle (θ), the X-rays will interfere constructively and produce a diffraction pattern. The angle at which the X-rays diffract depends on the distance between planes of atoms within the crystal lattice (d) and the wavelength of the X-rays. By measuring the angles of the diffracted X-rays, the distance between the planes of atoms within the crystal lattice can be determined.

$$n\lambda = 2d \sin \theta;\ n = 1, 2; \ldots \qquad (38)$$

The XRD pattern obtained contains information about the atomic arrangement of the material, which can be used to identify the type and quantity of crystalline phases present, their orientation, as well as the spacing between their atomic planes [218].

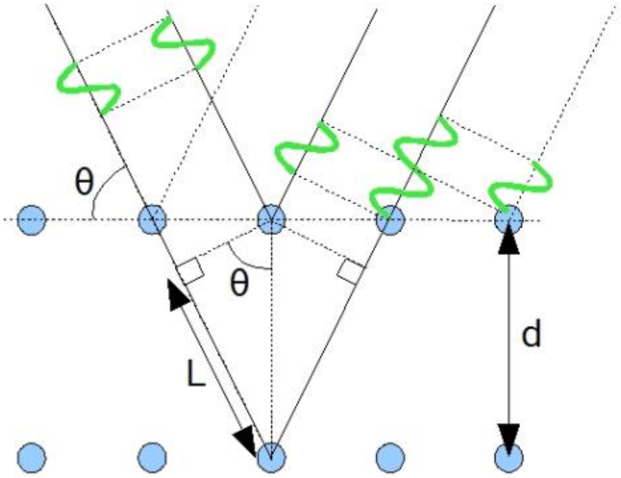

Figure 3-3: This image demonstrates how X-ray radiation interacts with a crystal lattice, resulting in constructive interference. When the Bragg conditions are met for specific angles and interplanar distances, this interference can be detected through X-ray diffraction measurements.

XRD analysis was performed using the X’pert Pro instrument, with a Cu target (weighted Cu $K\alpha1$ and Cu $K\alpha2$ radiation λ = 1.54178 Å) operated at 45 kV and 40 mA. The surface oxides of the samples were polished using 600-grit sandpaper prior to conducting X-ray diffraction (XRD) analysis. Coherent scattering domain size (τ) was calculated by the Debye-Scherrer equation [72]:

$$\tau = K\lambda/\beta cos\theta \qquad (39)$$

Where λ is the X-ray wavelength, β is full width at half maximum (FWHM), θ is the peak Bragg angle, and K = 0.9 is a constant.

3.3.3. Pole figure

Pole figure analysis is a technique that uses X-ray diffraction to study the preferred orientation (texture) of crystalline materials. In this study, a Panalytical X-Pert Pro MRD instrument (weighted Cu $K\alpha1$ and Cu $K\alpha2$ radiation λ = 1.54178 Å) is used with a 4-circle cradle that allows the sample to be rotated along different axes, including 2θ, ω, φ, and χ. A schematic of the beam path and various goniometer motions is shown in Fig.3-4. The incident angle, ω, is the angle between the X-ray source and the sample, while the diffracted angle, 2θ, is defined by the angle between the incident beam and the detector. The sample can be rotated in two additional directions: φ, which is the sample rotation angle, and χ, which is the sample tilt angle. By moving the sample in different directions and performing various scans, pole figures can be generated that provide information about the distribution and intensity of crystallographic orientations within the material.

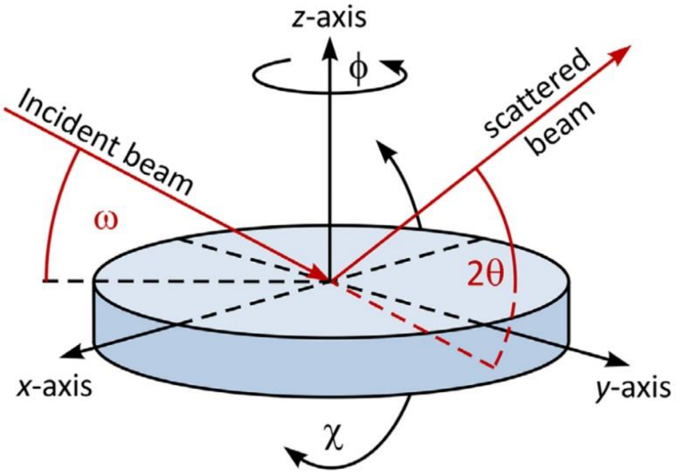

Figure 3-4: The illustration depicts the beam path and various goniometer motions [219].

The analysis of pole figures was conducted on two sets of samples. Table 3-2 provides a summary of the values for 2θ, ω, φ, and χ that were utilized to study the samples.

Table 3-2: summary of the values for 2θ, ω, φ, and χ that were utilized to study the samples.

Family plane	ω (degree)	2θ (degree)	φ	X (degree)
{111}	12.94	25.88	rotation	0-85
{230}	22.975	45.95	rotation	0-85

3.3.4. Transmission electron microscopy

In a Transmission Electron Microscope (TEM), diffraction patterns and images are formed by the interaction of a high-energy electron beam with a thin specimen.

The electron beam is generated by an electron gun and accelerated to a high voltage, typically between 100 and 300 kV, to achieve a short wavelength of about 0.005 nm. The beam then passes through a series of electromagnetic lenses that focus it onto the specimen, which is typically less than 100 nm thick.

As the electron beam passes through the specimen, it interacts with the atoms in the crystal lattice, causing elastic and inelastic scattering. Elastic scattering occurs when the electrons are scattered without losing energy, while inelastic scattering occurs when the electrons lose energy due to interactions with the specimen. In TEM, while the inelastic scattering of electrons can play a role in forming the diffraction pattern or images, it is the elastic scattering of electrons that primarily contributes to the formation of images and diffraction patterns.

The scattered electrons then pass through the objective lens, which is a magnetic lens that focuses the electrons onto a small spot on a detector or camera. The objective lens is crucial in forming both diffraction patterns and images in TEM.

The process of forming a diffraction pattern (Fig.3-5a) involves adjusting or removing the objective aperture to increase the convergence angle of the electron beam, allowing for a larger range of diffraction angles to be collected. The scattered electrons then interfere with each other constructively or destructively, resulting in a diffraction pattern. The diffraction pattern is formed at the back focal plane of the objective lens and is magnified on a screen using intermediate lenses. The pattern is typically made up of dots, circles, or arcs, with each spot corresponding to a set of planes in the crystal lattice that diffract electrons in a specific direction. Diffraction patterns can be collected from a particular area of a specimen if the Selected Area Diffraction (SAD) aperture is used in TEM.

To form an image (Fig.3-5b), an objective aperture is applied to select only the electrons that pass through a small region of the specimen. An image is formed after the aperture in the image plane of the objective lens. The image is then further magnified on a screen using an intermediate lens. The contrast in the image is determined by differences in the intensity of the scattered electrons in different regions of the specimen, which can be due to differences in thickness, composition, density, or crystallographic structure [220].

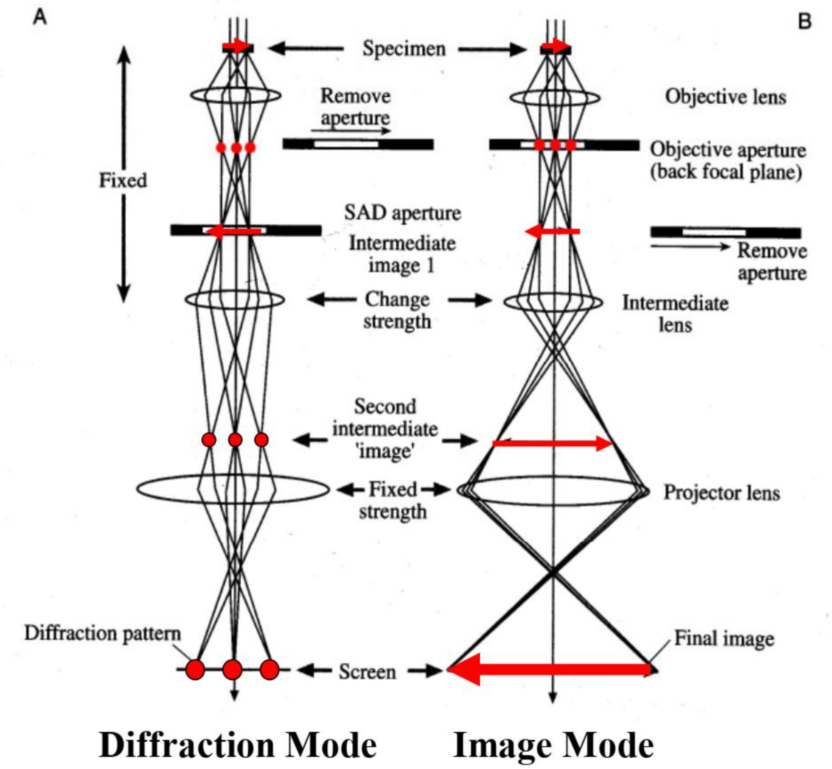

Figure 3-5: A schematic illustrating the placement of the aperture for obtaining either an image (A) or a diffraction pattern (B) in TEM.

For this investigation, fibers were deposited onto Transmission Electron Microscopy (TEM) grids (Tedpella, 200 mesh copper). The samples were then analyzed using TEM equipment (JEOL Ltd., model JEM 2100) operated at 200kV. The wavelength of the electrons thus generated was 0.0025 nm.

3.3.5. Brunauer-Emmett-Teller Method (BET) analysis

The Brunauer-Emmett-Teller analysis measures the adsorption and desorption of gas molecules on a solid surface to determine the specific surface area and pore size of a porous material.

Adsorption can occur through two mechanisms: chemisorption and physisorption, which are differentiated by the nature of the intermolecular attractions and chemical bonding that are involved.

Chemisorption involves the formation of strong chemical valence forces (ranging from 10-100 kcal.mol^{-1}) between the adsorbate and the substrate. Adsorbed molecules bond with reactive sites on the surface, resulting in significant changes in electron density. As a result of this type of adsorption, adsorbate molecules undergo chemical reactions on the surface that can be irreversible. Chemisorption is confined to monolayers and it is useful for analyzing catalyst surfaces.

By contrast, physisorption involves weak van der Waals forces between adsorbate and substrate, which require little energy to desorb (1-2 kcal.mol^{-1}). It has fast kinetics in the gas phase, and surfaces in high vacuum (10-8 - 10-10 Pa) are typically free of physisorbed species. In contrast to chemisorption, physisorption does not significantly redistribute electron density in the adsorbate molecule or on the substrate surface. Physisorption is therefore reversible, and desorption can be induced simply by reducing vapor pressure or increasing temperature. Physisorption is also a non-dissociative adsorption mode, which can accommodate multilayer molecules. Physisorption is useful for determining the surface properties of materials, such as surface area and pore size distribution [221].

Several factors influence the amount of gas adsorbent in BET surface area analysis, such as the surface area, temperature, and pressure of the gas. Nitrogen is often used in BET analysis because of its strong interaction with most solids and its high purity.

Liquid nitrogen or another cooling method is used to cool the sample surface so that adsorption can begin. By cooling the sample surface, gas molecules are less energetic and are more likely to be adsorbed on the material.

Then, a known amount of nitrogen gas is incrementally introduced into the sample cell. In order to achieve relative pressures below atmospheric levels, a partial vacuum is created. Once saturation pressure is reached, no further adsorption occurs no matter how high the pressure is raised. Pressure transducers monitor the changes in pressure during adsorption meticulously. Following the formation of adsorption layers, the sample is extracted from the nitrogen atmosphere and heated to release the adsorbed nitrogen. The resulting data is presented as a BET isotherm, which displays the amount of gas adsorbed as a function of relative pressure. An isotherm can provide insight into the relationship between porosity and absorption. Adsorption isotherms can be classified into five types (Fig.3-6) [221, 222].

Isotherms of type I indicate microporous adsorbents with pore diameters up to 2 nm. Adsorbents with larger pore diameters, typically greater than 50 nm, exhibit type II and III isotherms. A mesoporous adsorbent falls into types IV or V, with pores typically ranging between 2 and 50 nm in diameter. The factors that influence the shape of an isotherm in each category include temperature, pore size distribution, pore geometry, and pore connectivity [222, 223].

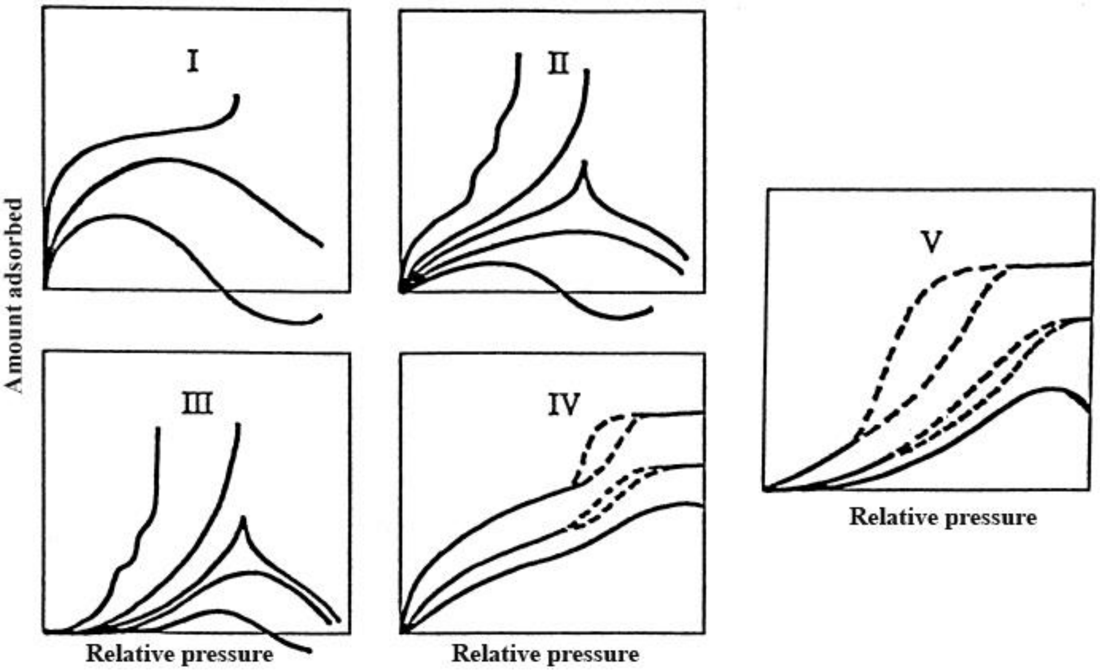

Figure 3-6: The classification of adsorption isotherms based on the IUPAC classification [222].

Generally, the BET equation is used to estimate the amount of gas needed to form a monolayer, V_m, of adsorbed gas on a solid surface. In BET equation, V is the volume of gas molecules adsorbed at a given relative pressure (P/P0), where C is the BET constant.

$$\frac{1}{V(1-x)} = \frac{1}{V_m C} + \frac{x(1-c)}{V_m C} \qquad (40)$$

In Equation (40), x is the relative pressure (P/P0), V is the volume of nitrogen adsorbed at a given relative pressure (P/Po), V_m is the monolayer volume, which is the amount of gas adsorbed at standard temperature and pressure (STP), and C is constant. STP is defined as 273 K and 1 atm.

A plot of $\frac{X}{V(1-X)}$ vs. X , usually in the P/P0 range of 0.05 to 0.35, should give a straight line. This linear plot is used to calculate V_m by determining the slope and intercept.

$$Slope = \frac{C-1}{V_m.C} \quad (41)$$

$$Intercept = \frac{C-1}{V_m.C} \quad (42)$$

$$V_m = \frac{1}{slpoe+Intercept} \quad (43)$$

Specific surface area (SSA) can then be derived:

$$SSA = \frac{V_m N_A a_m}{v_m m_s} \quad (44)$$

Where N_A represents Avogadro's number (6.022 x 10^{23} mol^{-1}), $a_m$represents the effective cross-section area of one adsorbed molecule (which is approximately 0.162 nm^2 for nitrogen), $v_m$represents the molar volume of one adsorbed molecule (which is equivalent to 22,400 mL, the volume occupied by 1 mol of adsorbate gas at standard conditions), and $m_s$represents the mass of the substrate or adsorbent [221].

3.4. Electrochemical characterization

To evaluate the electrochemical properties of the introduced electrocatalysts, we utilized electrochemical techniques and conducted all electrochemical characterization in a three-electrode system. The electrolyte used was 1 M KOH (Fisher Chemical, ACS Reagent grade) which was agitated with Ar-saturated (Air Liquid, 99.999%). In some experiments, 10 ppm $Fecl_2$ was added to the electrolyte solution. We employed a conventional three-electrode system, with a Pt gauze and a Hg/HgO electrode filled with 1 M KOH as the auxiliary and reference electrodes, respectively.

3.4.1. Electrode preparation

The production of the electrode is shown in Fig.3-7. To begin, a wire was brazed onto the back of the samples. Next, the sample was attached to a glass tube using glue. The electrode was then immersed in 3 M KOH solution for 24 hours at ambient temperature and subsequently for 10 minutes in boiling 3M KOH. Then, they were washed in boiling distilled water for 20 minutes.

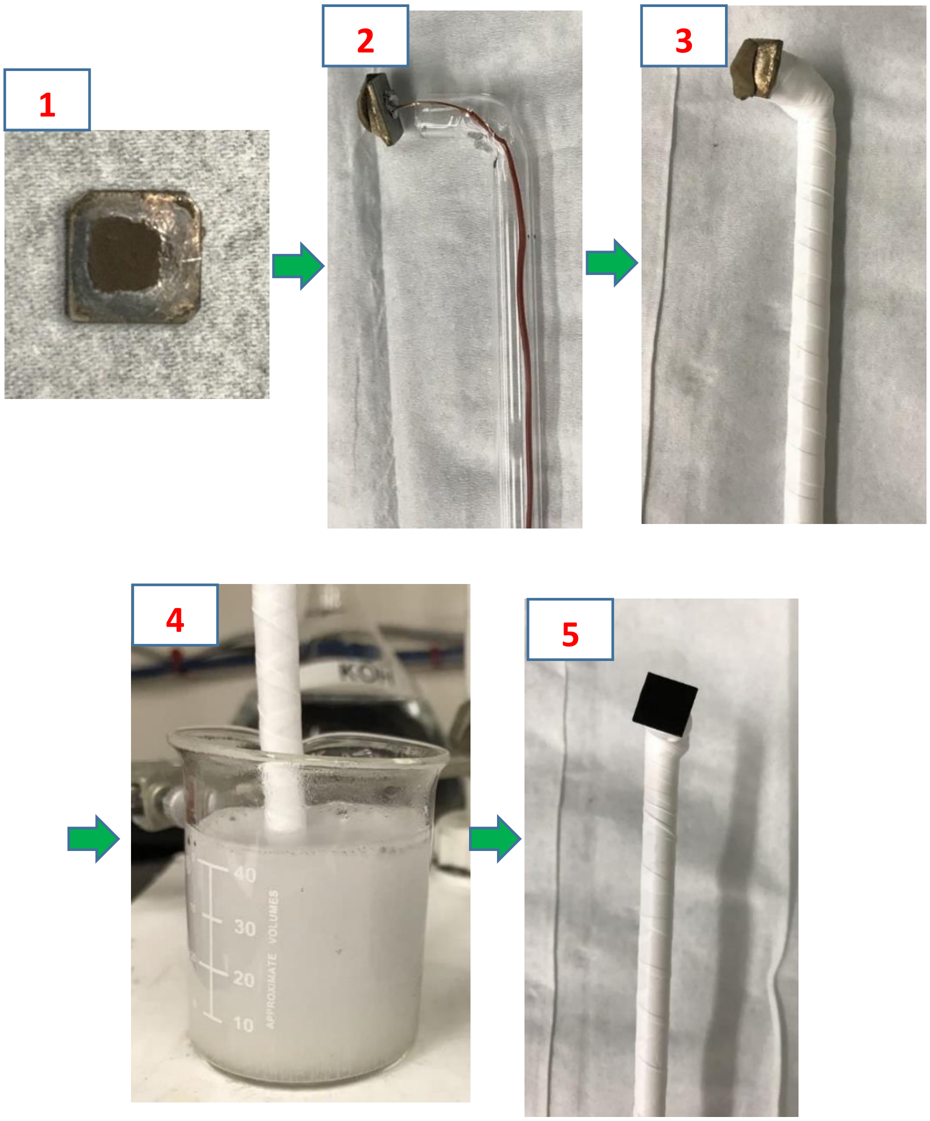

Figure 3-7: The sequence of electrode production for electrochemical tests.

3.4.2. Cyclic voltammetry

In this study, we utilized cyclic voltammetry (CV) to investigate the oxidation and reduction reactions, measure electrochemical active surface area, and determine the capacitance of the catalyst, which helped us investigate the effective surface area of the electrode. Furthermore, we employed CV to evaluate the performance of the catalyst in oxygen evolution reaction (OER) [224].

3.4.3. Electrochemical active surface area (Cathodic charges)

In this study, cathodic charge refers to the total amount of electrical charge required for the reduction of oxy-Ni hydroxide to Ni hydroxide. Since oxidation and reduction reactions typically occur at the surface of an electrode, the current density required to produce a specific cathodic charge is proportional to the specific surface area of the electrode [225].

To calculate the cathodic charge, we computed the coulombic charge from the reduction area of the cyclic voltammetry curve (as shown in the hatched area in Fig.3-8.

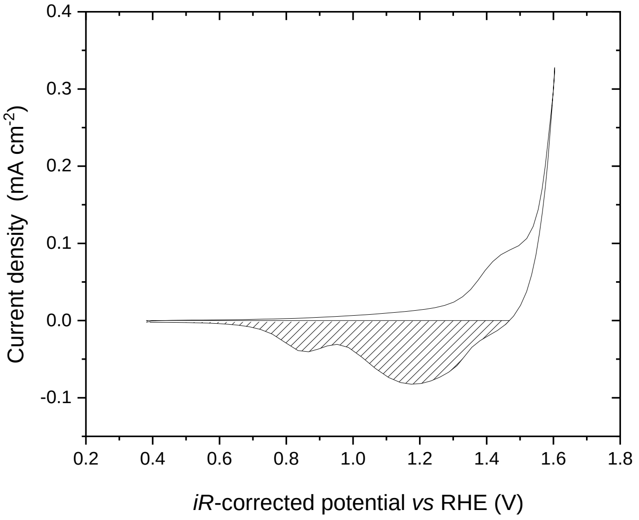

Figure 3-8: Cyclic voltammogram of sample S670-1-350 recorded in 1M KOH at 5 mV s^{-1}. The coulombic charge was computed from the hatched area.

3.4.4. Double layer capacitance

Electric double layers are formed when electrode surfaces are immersed in an electrolyte, causing a layer of charged ions to form near the electrode surface. The double layer acts like a capacitor, storing electrical charge via an electrostatic field. This capacitance is called double-layer capacitance (CDL). The double layer capacitance (CDL) is conventionally measured in Farads per cubic centimetre and can be measured with cyclic voltammetry or electrochemical impedance spectroscopy. Double layer capacitance (CDL) is a characteristic that relates to the specific surface area or electrochemical active surface area (ECSA) of an electrode. CDL and ECSA are related in the following way:

$$\mathrm{ECSA} = \frac{C_{DL}}{C_S} \quad (45)$$

Where C_S is specific capacitance [226].

To calculate the double-layer capacitance (CDL) using cyclic voltammetry (CV), a suitable potential range (E_{min} to E_{max} V vs. RHE) where no redox processes occur is first chosen from the CV curve. Then the potential sweep is applied to the electrode in the electrolyte while recording the resulting current density response. Capacitance current density (iC) can be calculated by subtracting the anodic and cathodic current densities at potential $E = (\frac{E_{max} + E_{min}}{2})$ V vs. RHE, which equals $\frac{\Delta J}{2} = (\frac{J_{anodic} - J_{cathodic}}{2})$. The current densities reflect the capacitive currents which are generated by the charging and discharging of the electrical double layer. When $\frac{\Delta J}{2}$ values are plotted against the scan rates, the slope corresponds to double-layer capacitance [226, 227]. Fig.3-9a shows a typical cyclic voltammogram (CV) plot of Ni whiskers as a function of scan rates. Fig.3-9b, on the other hand, shows the plot of $\frac{\Delta J}{2} = (\frac{J_{anodic} - J_{cathodic}}{2})$ vs scan rates, where the slope of the plot is found to be equal to 124 mF.cm^{-2}.

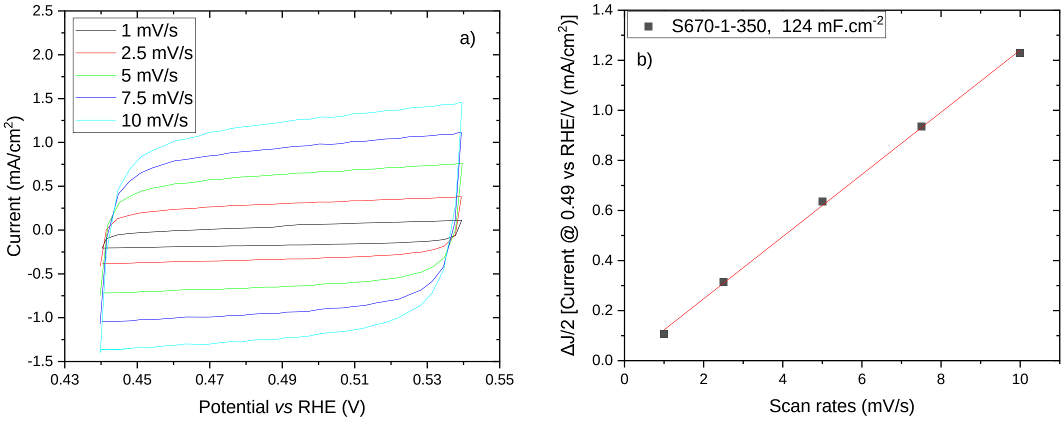

Figure 3-9: a) Cyclic voltammograms of sample S670-1-350 recorded in 1M KOH at room temperature. b) ΔJ/2= ($\frac{J_{anodic}-J_{cathodic}}{2}$) at 0.49V vs. scan rates for sample S670-1-350.

3.4.5. OER overpotential

To measure cell voltage at various current densities, galvanostatic oxidation was employed. The electrode potentials (vs. Hg/HgO) were measured in all cases and then converted to the corresponding reversible hydrogen electrode (RHE) scale using the formula $E_{RHE} = E_{Hg/HgO} + 0.098$ V + 0.059V × pH, where the pH of 1 M KOH at room temperature is 13.5. The overpotential (η) of the OER was calculated by adjusting for the ohmic drop, using the formula $\eta = E_{RHE} – iR - 1.23$ V, where i is the current density and R is the ohmic resistance. The ohmic resistance was determined by measuring the impedance at high frequencies and at a frequency where the imaginary resistance is zero.

3.5. Software

The data analysis in this study was performed using several software tools, namely Image J, DigitalMicrograph, ReciprOgraph, and HighScore Plus.

3.5.1. Image J

Image J is open-source image processing software widely used for scientific image analysis. It offers a user-friendly interface and a variety of features for processing, analyzing, and visualizing images. Image J can be customized with various plugins and scripts to perform advanced image analysis tasks. We utilized Image J to analyze and quantify the microstructural features in our images.

3.5.2. DigitalMicrograph

DigitalMicrograph, also known as Gatan Microscopy Suite, is a versatile software that enables the control of digital cameras and other components to support various microscopy applications, such as tomography, in-situ, spectrum, and diffraction imaging. We used DigitalMicrograph to capture and analyze images and diffraction patterns of TEM in this study.

3.5.3. ReciprOgraph

ReciprOgraph software was utilized to index the TEM diffraction patterns obtained in this study. In order to perform the indexing, the software requires a CIF file of the material being analyzed. The CIF file for the Ni crystal structure was obtained from the "crystallography.net" website. To ensure the validity of the CIF file, we compared the d-spacing values obtained from the CIF file with those obtained from HighScore Plus software and found that they were identical.

3.5.4. HighScore Plus

HighScore Plus is a powerful software used for X-ray diffraction analysis of materials. It is designed to analyze and interpret XRD patterns, allowing for the identification of crystal structures and phases present in the sample. In this study, we used HighScore Plus to capture and analyze XRD patterns for our samples, enabling us to identify the crystal structure and phase composition of the materials.

4 THE PRODUCTION, FORMATION MECHANISM AND PROPERTIES OF NI WHISKERS

4.1. Introduction

Raney Ni has been recently studied for OER in alkaline media [70, 71]. Despite the high activity of Raney Nickel, ion transportation is limited at the depth of the structure due to its nanoporous structure. The nanopores suppress the ionic flow in the material and cause most of the reaction to take place on the surface of Raney Ni (on a 2D surface) [64].

Since a 3D structure has a substantially larger surface area than a 2D structure [79], Ni foam can be converted to a 3D structure of Raney Ni (Raney Ni foam) using a heat treatment, and subsequently, a leaching process. However, the process of forming Raney Ni foam entails many steps, the first of which is Ni foam production [80, 81]. To remove this step, we introduce a new, simple, and cost-effective method to produce a new type of 3D structure of Ni (long and thin whiskers of Raney Ni) that can provide a surface area much higher than Ni foam (or Raney Ni foam) while keeping high oxygen evolution performance. The structure could be easily manufactured for the electrodeposition of any catalyst. Because the space between their fibers is easily controllable during the production process.

We were inspired by the Ni-Al eutectic structure to build this structure. During solidification of a molten eutectic of Ni-Al, Al_3Ni fibers grow preferentially in one direction to form long and thin fibers of the Al_3Ni phase, and a phase that is rich in aluminum (α-Al) is then formed as a shell around the Al_3Ni fiber. As a result, the Al_3Ni fibers are separated and well-aligned in the aluminum matrix [82]. If α-Al is dissolved and Al is leached out from Al_3Ni fibers using potassium hydroxide (KOH), only the whiskers of Raney Ni will remain. Ni whiskers exhibit high mechanical stability and a strong bond with the Ni foil. As evidence, galvanostatic stability tests were performed over a period of six days at 500 $mA.cm^{-2}$, demonstrating the outstanding mechanical stability of the Ni whiskers.

There is no report on the production of Raney Ni fibers, and all the reports are related to powder or bulk coating of Raney Ni [72, 73, 74]. In the production of Ni whiskers, potassium aluminate is the only waste product. Nevertheless, this byproduct can be converted into potassium alum, a material that finds numerous industrial applications [228]. Additionally, Green Al can be used to make manufacturing processes more environmentally friendly.

4.2. Experimental

Numerous experiments have been conducted in the field of materials analysis and electrochemistry with the aim of comprehending the connection between the structure and electrochemistry characteristics of Ni whiskers. These experiments have been divided into ten sections for better organization and understanding of the data.

4.2.1. Heat treatment process

Ni foils were used as substrates. Ni foil (99.5%, Alfa Aesar) 1.0 mm thick and 1 cm^2 surface area was cut and polished by 600 Grit sandpaper (Fig.4-1a). Next, they were washed with de-ionized water and rinsed with isopropanol. Then, a pre-determined mass of Al powder was deposited on the surface of each substrate (Fig.4-1b). In the next step, the Ni plate containing Al powder is meticulously placed on a ceramic combustion boat for heat treatment (Fig.4-1c).

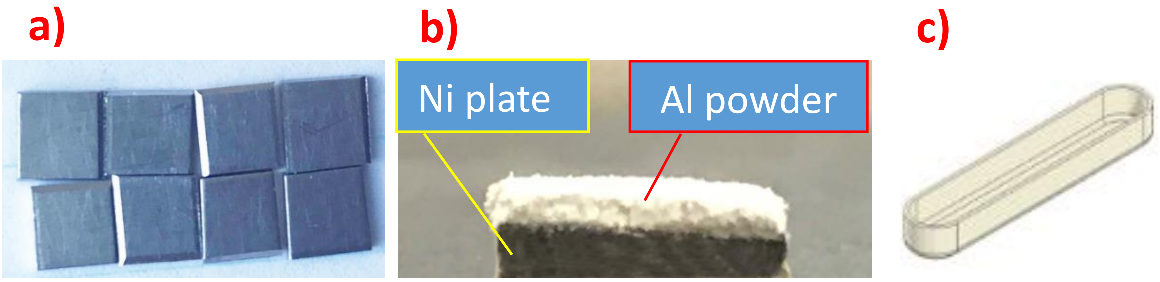

Figure 4-1: a) Ni plates, b) Al powders on the surface of Ni plates, c) Ceramic combustion boats.

The samples were heat-treated in an ultra-high purity Argon atmosphere (99.999%) following the protocol schematically depicted in Fig.4-2. First, the furnace was purged with Ar to remove any trace of oxygen. This was done for 10 minutes at a flow rate of 80 $mL.min^{-1}$. Then the following protocol was applied. First, the temperature increased rapidly (50 °C min^{-1}) to reach the targeted temperature. Then, the samples were kept at that temperature for a period of time that was varied. During steps one and two, the furnace was purged with Ar at a flow rate of 80 $mL.min^{-1}$. Finally, the furnace was turned off and the Ar flow was increased to 10 $L.min^{-1}$ to cool down the samples. The samples are denoted as follows: S-*T*-*t*-*m*, where *T* is the maximum temperature reached, *t* is the period of time the sample was kept at the maximum temperature, and *m* is the mass of aluminum deposited at the surface of the substrate (Table 4-1).

In addition, two samples with identical parameters as S670-1-350 but at a lower Ar flow were created to investigate the influence of the cooling rate on the structure. Since lower Ar flow results in a lower cooling rate, the cooling rate for samples is as follows S670-1-350 > SC40 > SCS.

Heat-treated samples were leached in 3 M KOH solution. To achieve a higher surface area, the leaching process is carried out at room temperature initially for 24 hours. Subsequently, the leaching process is conducted at higher temperatures (10 minutes in boiling 3M KOH) to remove a greater amount of Al content. Then, they were washed in boiling distilled water for 20 minutes.

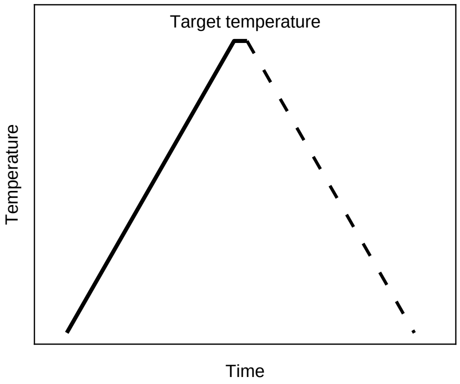

Figure 4-2: Heat treatment was performed in 3 steps shown in this figure.

Table 4-1: Parameters of the heat-treatment protocol.

Name of sample	Maximum heat treatment temperature (℃)	Time at maximum heat treatment temperature (min)	Mass of aluminum deposited at the surface of the substrate (mg)	Ar flow / mL.min^{-1}
S670-1-0.3	670	1	0.3	10000
S670-1-1.5	670	1	1.5	10000
S670-1-15	670	1	15	10000
S670-1-150	670	1	150	10000
S670-1-250	670	1	250	10000
S670-1-350	670	1	350	10000
S670-0-350	670	0	350	10000
S670-5-350	670	5	350	10000
S670-10-350	670	10	350	10000
S700-0-350	700	0	350	10000
S700-1-350	700	1	350	10000
S700-5-350	700	5	350	10000
S700-10-350	700	10	350	10000
S750-1-350	750	1	350	10000
S800-1-350	800	1	350	10000
SC40	670	1	350	4000
SCS	670	1	350	80

4.2.2. Production of self supported Ni-whiskers

In this section, some of the samples generated in Table 4-1 undergo a heat treatment process at 570°C to assess the impact of a temperature below the eutectic point on the microstructure. The results obtained in this section are used to create samples for BET analysis in Section 4-2-3.

S670-1-150 was initially created according to Table 4-1. The samples were then subjected to an additional heat treatment at 570℃ for 1, 4 and 9 hours. The samples were then renamed as illustrated in Table 4-2.

Table 4-2: Parameters of the heat-treatment protocol

Name of sample	Heat treatment time at 570℃ (hours)
S670-1-150 (SH0)	0
SH1	1
SH4	4
SH9	9

4.2.3. BET analysis

The BET analysis was conducted to investigate the pore size of the Ni whisker. The sample S670-1-350, produced in accordance with Table 4-1, was heat-treated for 4 hours at 570℃ and subsequently leached in 3M KOH. As per the results stated in the previous section, the Ni-whiskers detached after leaching. The detached Ni-whiskers were washed in distilled water, dried at 60℃ in the oven for 1 hour, and then analyzed using Quantachrome Instruments (version 2.1).

4.2.4. Investigation of different approaches to separate fibers for TEM analysis

Transmission electron microscopy (TEM) is a microscopy technique in which an image is formed by transmitting a beam of electrons through a specimen. To transmit electrons through the sample, the thickness of the sample is limited to a few hundred nanometers [229]. Therefore, the first step in TEM analysis is to make a thin sample so that electrons can pass through it.

Ni-whiskers is made up of many plate-like fibers. SEM analysis revealed that some fibers have a thickness of less than 200 nm. As a result, TEM can be used to study a single thin fiber. All we need to do is separate the fibers from Ni-whiskers and then place them on TEM grid. This section examines several methods for making separated Ni fibers (non-agglomerated) and compares them.

In order to separate fibers, three methods were used: (1) detaching fibers using sticky tapes, (2) scraping the fibers and (3) sonication.

The initial approach for detachment involved the use of sticky tapes. A normal clear plastic scotch tape was placed onto the surface of both the S670-0-350 and S670-1-350 samples. The scotch tape was then submerged in a 2M KOH solution for 5 minutes. The potassium hydroxide dissolved the glue and released the fibers into the solution. In order to decrease the solution concentration, the solution was removed from the container using a pipette, and distilled water was added to the container. This step was repeated three times to wash the fibers.

In the second approach, fibers were scraped using a scalpel in distilled water.

In the sonication method, the samples were sonicated for 2, 5, and 10 minutes in distilled water. The samples were named as shown in Table 4-3.

Using three different approaches, fibers were detached and submerged in distilled water. A pipette was used to relocate the submerged fibers to the surface of a microscope slide. The microscope slide was then left undisturbed for 12 hours overnight in order to allow the water to evaporate. In the next step, optical microscopes were used to examine the remaining fibers on the slide.

Table 4-3: Name of sonicated samples.

Name of sample	The sample used	Sonication time / min
S670-0-350 (2 min)	S670-0-350	2
S670-0-350 (5 min)	S670-0-350	5
S670-0-350 (10 min)	S670-0-350	10
S670-1-350 (2 min)	S670-1-350	2
S670-0-350 (5 min)	S670-1-350	5
S670-0-350 (10 min)	S670-1-350	10

4.2.5. Samples preparation for TEM analysis

Based on the results that will be presented in Section 4-2-4, the sonication process was selected for sample preparation, and S670-0-350 (10 minutes) was chosen to obtain separated fibers. Following sonication, a few fibers were observed floating on the water surface. Although the number of fibers was small, they appeared to gather in a single spot, possibly due to the magnetic properties of Ni whiskers. A pipette was used to transfer them to the surface of a Tedpella 200 mesh copper grid. However, it was difficult to transfer all fibers with a single pipetting. Consequently, I pipetted them three times on three grids. In total, two S670-0-350 samples were prepared, and six TEM samples were analyzed.

Ni whiskers have a plate-like shape and are very thin. Therefore, when they are placed on a TEM grid, their width is always in contact with it. Fig.4-3 depicts a fiber on the grid and an electron beam striking its surface perpendicularly. According to the figure, the beam is always perpendicular to a given fiber surface.

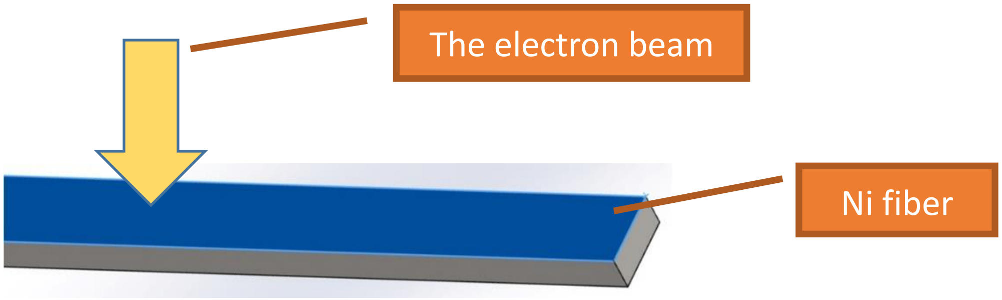

Figure 4-3: Schematically shows an electron beam that strikes the surface of a fiber.

4.2.6. Calibration and analysis of TEM

The samples were analysed using transmission electron microscopy produced by JEOL Ltd. (model: JEM 2100, 200kv) which generates electrons with a wavelength of 0.0025 nm. Both TEM images and diffraction pattern images were taken. Two camera lengths (5 and 8 cm) were applied for capturing diffraction patterns. Higher camera length results in higher magnification in the diffraction patterns.

TEM images rotate as magnification levels are changed due to the arrangement of the microscope lenses. For determining fiber crystallographic orientation, TEM images were captured in diffraction mode at the same magnification used to capture diffraction patterns. This approach avoided image rotation, allowing for an accurate determination of the crystallographic orientation of the fibers.

With the help of ReciprOgraph software, single diffraction patterns were indexed. To determine the projection plane (the plane is perpendicular to the beam direction), two vectors of each diffraction pattern were first indexed based on their interplanar spacing, and then the projection plane was determined by applying the cross-product of two vectors.

Prior to measuring the distances or adding a scale bar, the DigitalMicrograph software, which captures images and diffraction patterns in transmission electron microscopy (TEM), underwent calibration for two different camera lengths. To achieve this, gold nanoparticles was utilized as a reference material, and two diffraction patterns were captured at each camera length, as shown in Fig.4-4. The resulting d-spacing measurements were compared with the d-spacing of gold in ReciprOgraph, and the values are presented in Table 4-4. Based on the results, the decision was made to retain the calibration. However, the measurements revealed that a minimum uncertainty of ±0.01Å should be taken into account for the measured values. It is worth noting that previous studies have reported that the precision and accuracy of TEM diffraction patterns can be corrected to near 0.1% [230].

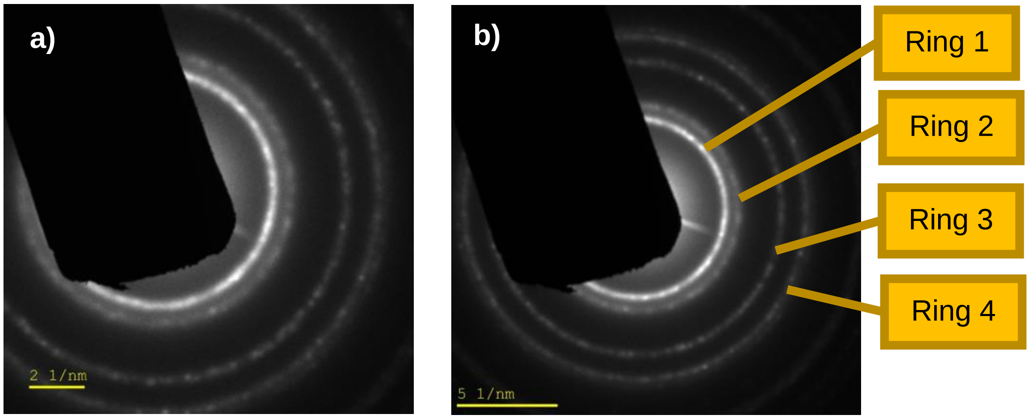

Figure 4-4. Diffraction patterns for nanoparticles of gold. a) Camera length is 8 cm, b) Camera length is 5 cm.

Table 4-4: Measured d-spacing versus Reference d-spacing. Reference d-spacing was obtained from ReciprOgraph software.

Ring	(hkl)	Measured d (Å) / 5 cm camera length	Measured d (Å) / 8 cm camera length	Reference d (Å) for gold
1	(111)	2.36	2.36	2.35
2	(220)	2.03	2.03	2.03
3	(322)	1.44	1.45	1.44
4	(431)	1.22	1.23	1.23

4.2.7. Electrochemical experiments

Electrochemical characterization in Ar-saturated (Air Liquid, 99.999%) 1 M KOH (Fisher Chemical, ACS Reagent grade) was conducted in a conventional three-electrode system, using a Pt gauze and a Hg/HgO electrode filled with 1 M KOH solution as auxiliary and reference electrodes, respectively. The distance between the working and the counter electrode was 5 mm, and the exposed surface area was 1 cm^2.

Electrochemical tests were performed by first performing a series of cyclic voltammograms (CVs) between 0.4 and 1.8 V *vs.* RHE at 50 mV s^{-1} until steady-state potentiodynamic features were obtained. Typically, steady-state CVs were obtained after five cycles. Then, the sweep rate was decreased to 5 mV s^{-1}. These last CVs are shown later and were used to calculate the cathodic charge under the $Ni(OH)_2$/NiOOH redox peaks. In addition, CVs were performed at different scan rates in a restricted potential region (0.44 - 0.54 V *vs.* RHE), where no faradic reaction is occurring, and current is mostly due to the double-layer charging. The double-layer capacitance was then calculated by computing the scan rate dependence of the current density, *j*, measured at 0.49 V vs. RHE. The double layer capacitance was given by the slope of the *j* vs scan rate curve. Then, a series of galvanostatic curves were recorded at increasingly larger current density (10 mA cm^{-2}, 50 cm^{-2}, 250 mA cm^{-2} and 500 mA cm^{-2}). These measurements were performed in two different electrolytes: 1M KOH (99.999%) and 1 M KOH (99.999%) spiked with 10 ppm $FeCl_2$. All electrolytes were prepared using de-ionized water (Milli-Q, resistivity > 18 MΩ cm).

In all cases, the experimentally measured electrode potentials (*vs.* Hg/Hg0) were converted to the corresponding reversible hydrogen electrode (RHE) scale using $E_{RHE} = E_{Hg/HgO} + 0.098$ V + 0.059V × pH, with the pH of 1 M KOH at room temperature being 13.5. The ohmic drop-corrected OER overpotential (η) was calculated using $\eta = E_{RHE} - iR$ - 1.23 V, where i is the current and R is the ohmic resistance.

4.2.8. The effect of the aging process on overpotential

In accordance with Section 4.2.1, we first generated S670-0-350, S670-1-350, S670-5-350 and S670-10-350 samples. However, to simplify the nomenclature of the samples, we renamed them S0, S1, S5 and S10, respectively.

To investigate the effect of the aging process, we followed a two-step process involving cyclic voltammograms (CVs) and immersion. The cyclic voltammograms (CVs) in 1M KOH, between 0.4 and 1.8 V vs. RHE at 50 mV s^{-1} and 5 mV s^{-1} were performed three times to convert Ni whiskers of S0-S10 samples into $Ni(OH)_2$. The samples were next immersed in 80 mL of 0.1 M KOH for 20 minutes while the solution was stirred at 70℃. Then, the samples were washed and kept in 100 mL of distilled water for one hour to remove any contamination from the depth of the 3D structure. The samples were renamed after the treatment as seen in Table 4-5. The Electrochemical experiments were carried out in the same manner as in Section 4.2.7.

Table 4-5: Name and Used Parameters

Solution Type	Sample Name			
0.1M KOH (70℃)	S0-A	S1-A	S5-A	S10-A

4.2.9. Heat treatment to form Raney Ni foam

The Raney Ni foam is made in the same manner as described in section 4-2-1 by depositing Al powder on the surface of Ni foam and then heat treating them. Table 4-6 shows the parameters used to produce samples. The produced samples are labelled as N-T-t-m, as shown in Table 4-

6. The leaching procedure and electrochemical experiments were carried out in the same manner as in sections 4-2-1 and 4-2-7, respectively.

Table 4-6: Parameters of the heat-treatment protocol

Name of sample	Maximum heat treatment temperature (℃)	Time at maximum heat treatment temperature (min)	Mass of aluminum deposited at the surface of the substrate (mg)	Ar flow / mL.min^{-1}
N670-1-150	670	1	150	10000
N670-0-150	670	0	150	10000
N660-0-350	660	0	350	10000
N660-0-250	660	0	250	10000
N660-0-150	660	0	150	10000

4.3. Results and discussions

The results are presented in ten sections. Firstly, the formation mechanism of Ni whiskers is described. Then, BET and TEM analyses are provided. Following this, all parameters affecting the structure and electrochemical properties are described. Finally, the produced Raney Ni foam is compared with Ni-whiskers.

4.3.1. Formation mechanism of Ni-whiskers

Fig.4-5 displays a top SEM view of S670-1-150 following heat treatment. The heat treatment process leads to the formation of complex oxides of Ni and Al on the surface of the molten alloy. These oxides are not soluble in KOH. However, during the leaching process, they detach from the structure and settle at the bottom of the container. Therefore, it is not necessary to analyze these oxides and the material underneath them is only studied.

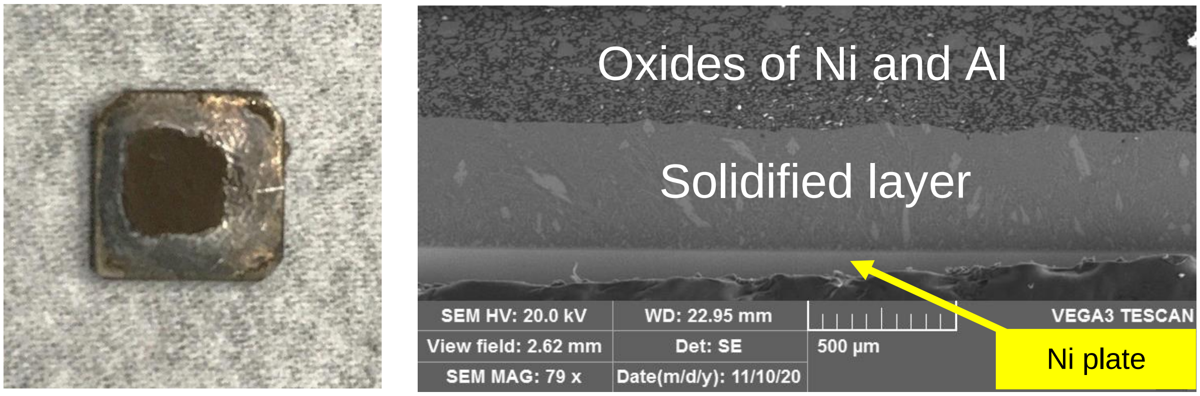

Figure 4-5: Top view and cross section of S670-1-150 before leaching.

Fig.4-6 shows a scanning electron microscopy (SEM) cross-section micrograph of sample S670-1-150 before leaching. Several structures were identified including Ni plate, D1, D2 and Solidified structure.

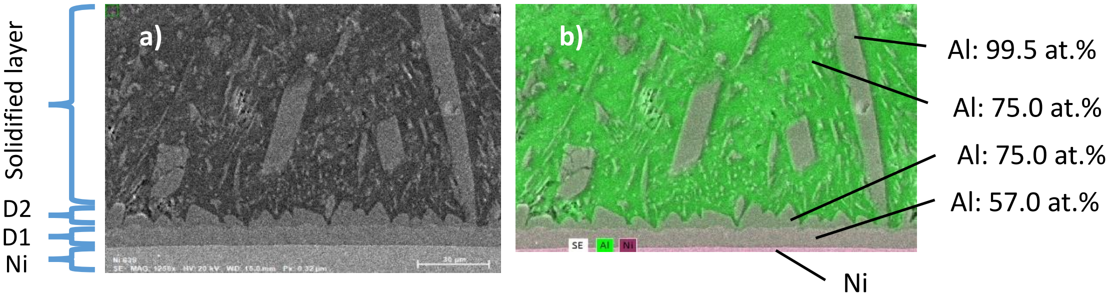

Figure 4-6: Cross sections of S670-1-150 sample before leaching. a) SEM image, b) EDX mapping

At the surface of the Ni substrate, a continuous layer (D1) is observed, whose Ni:Al composition is 43:57 at.%. A discontinuous layer D2 is formed at the surface of D1, whose Ni:Al composition is 25:75 at.%. The thickness of D2 is not uniform and varies considerably between a few μm to up to 15-20 μm from one location to the other. On top of D2, a thick solidified layer composed of elongated structures (whiskers) dispersed in a solid matrix is observed. The Ni:Al composition of the elongated structures was 25:75 at.%, similar to D2, while that of the matrix is mostly Al. Based on the Ni:Al composition of D1 and D2 they are assigned to Ni_2Al_3 and Al_3Ni, respectively. Based on their composition, the elongated structures embedded in the Al matrix were also assigned to Al_3Ni. This assignment will be confirmed later through X-ray diffraction analysis.

The study investigated the effect of Al mass and time elapsed at maximum heat treatment temperature on the structure and composition of D1 and D2. For the smallest Al mass (0.3 mg), the Al particles were placed on the surface of the Ni plate with a certain distance between them. Upon heat treatment, the Al particles melted in their respective areas, resulting in the formation of spots of Ni_2Al_3 (Fig.S1). When the Al mass increased to 1.5 mg, a continuous layer of Ni_2Al_3 was formed, but Al_3Ni and the solidified layer were not yet observed in the cross-section (Fig.S2). Both layers were only seen when the Al mass increased to 15 mg (Fig.S3). Fig.4-7a shows the effect of Al mass on the thickness of the D1 layer for samples produced under the same heat treatment. By increasing the mass of Al, the thickness of D1 first increased and then decreased. For an Al mass of more than 150 mg, the thickness remained constant. In the given figure, the changes in thickness are divided into three parts, and each part is explained based on the findings of the researchers.

Z. Ding *et al.* revealed stages of D1 and D2 formation, after Ni-Al interaction at 850℃, using synchrotron X-ray diffraction analysis. They found that the D1 (Ni_2Al_3) layer is formed via bulk diffusion mechanism in four stages: (1) Al diffuses into Ni, (2) a peritectic reaction forms Ni_2Al_3 (in D1 layer) and prevents the growth of D1 layer, (3) the peritectic reaction is completed, and growth of D1 continues via bulk diffusion, and (4) during cooling down, the growth rate of D1 diminishes due to the decrease in temperature [231]. Therefore, the increase in D1 thickness in part 1 of Fig.4-7a is due to the provision of more Al moles.

In the case where the mass of Al is more than 15 mg, a peritectic reaction occurs between the Ni_2Al_3 layer and the molten Al to form the Al_3Ni layer (D2) on the interface between the solid and the melt [231]. This reaction is responsible for the observed decrease in thickness of the D1 layer in part 2 of Fig.4-7a. However, when sufficient Al mass is present on the surface of Ni, the thickness of the D1 layer remains constant for all samples produced at the same heat treatment time in part 3. This is attributed to the bulk diffusion mechanism of D1 formation. The thickness of D1 only increases with increasing heat treatment time, as shown in Fig.4-7c. However, despite variations in heat treatment time or Al mass, D1 composition remains constant, as demonstrated in Fig.4-7b and Fig.4-7d.

This finding also aligns with earlier observations of the interaction between Ni and various Al masses within a temperature range of 720-950℃, where only these specific layers of Ni_2Al_3 and Al_3Ni were observed [90, 94, 232].

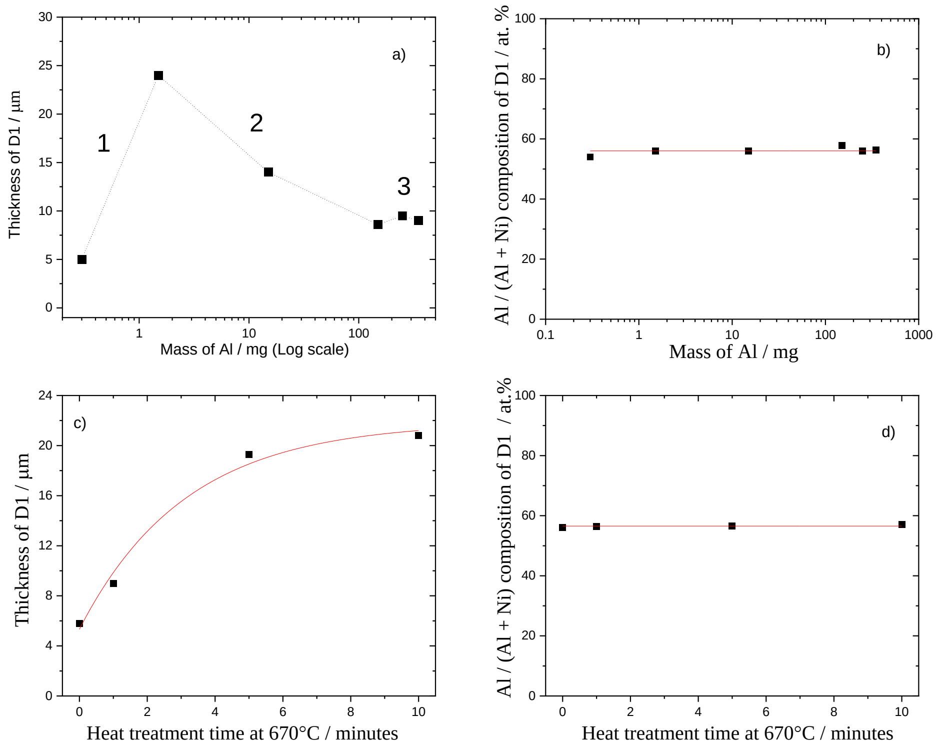

Figure 4-7: The influence of aluminum mass and elapsed time on D1 layer thickness and chemical composition. (a) demonstrates the effect of aluminum mass on D1 layer thickness and (b) on the chemical composition of D1, where the maximum operating temperature was 670°c, and the elapsed time at the maximum operating temperature was one minute. (c) depicts the effect of elapsed time at maximum operating temperature of 670°c on D1 layer thickness and (d) on the composition of D1, where the aluminum mass was 350 mg.

The XRD pattern of sample S670-1-150 before leaching is shown in Fig.4-8. The XRD pattern was plotted on a log scale to emphasize peaks with a lesser intensity. Two sets of peaks are observed. The first set is the most intense and is attributed to Al. The second set can barely be discerned on a linear scale. They are attributed to Al_3Ni (filled triangles). This assignment is consistent with the SEM micrograph of Fig.4-6. Considering that the X-ray penetration depth and the thickness of the solidified layer of sample S670-1-150, which is 400 µm, one should not expect to observe any diffraction peaks from D1, whose Ni:Al composition is 25:75 at.%., nor from the Ni substrate. The intensity of the diffraction peaks of Al_3Ni does not match up with that expected for a polycrystalline phase. According to PDF 03-065-2418 [83], the most intense peaks of polycrystalline Al_3Ni should be (111), (131) and (311), all three peaks having the same intensity.

This is not what is observed in Fig.4-8, where the (230) peak is the most intense, suggesting the Al_3Ni whiskers are growing along a preferential axis perpendicular to the family of (230) planes. This was observed independently of the maximum heat treatment temperature, time elapsed at the maximum heat treatment temperature and mass of Al (Fig.4-9).

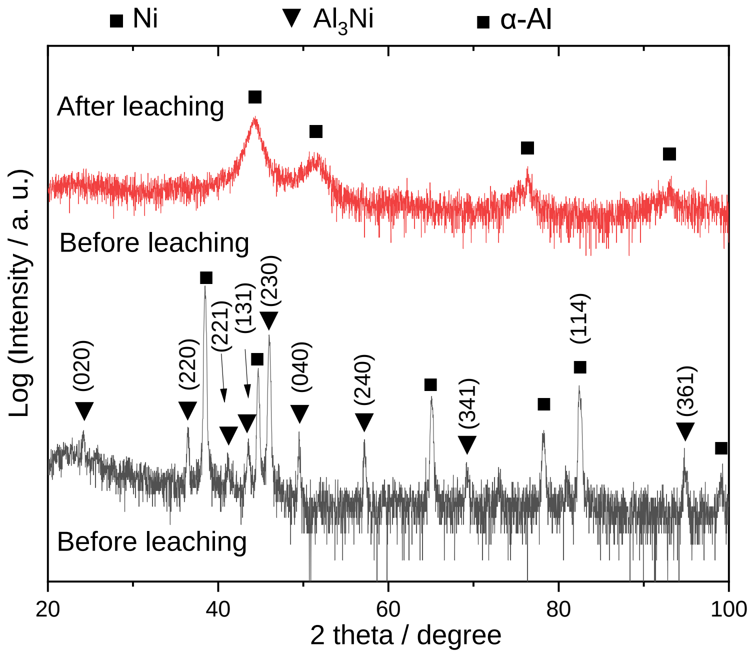

Figure 4-8: X-ray diffraction of sample S670-1-150 before and after leaching.

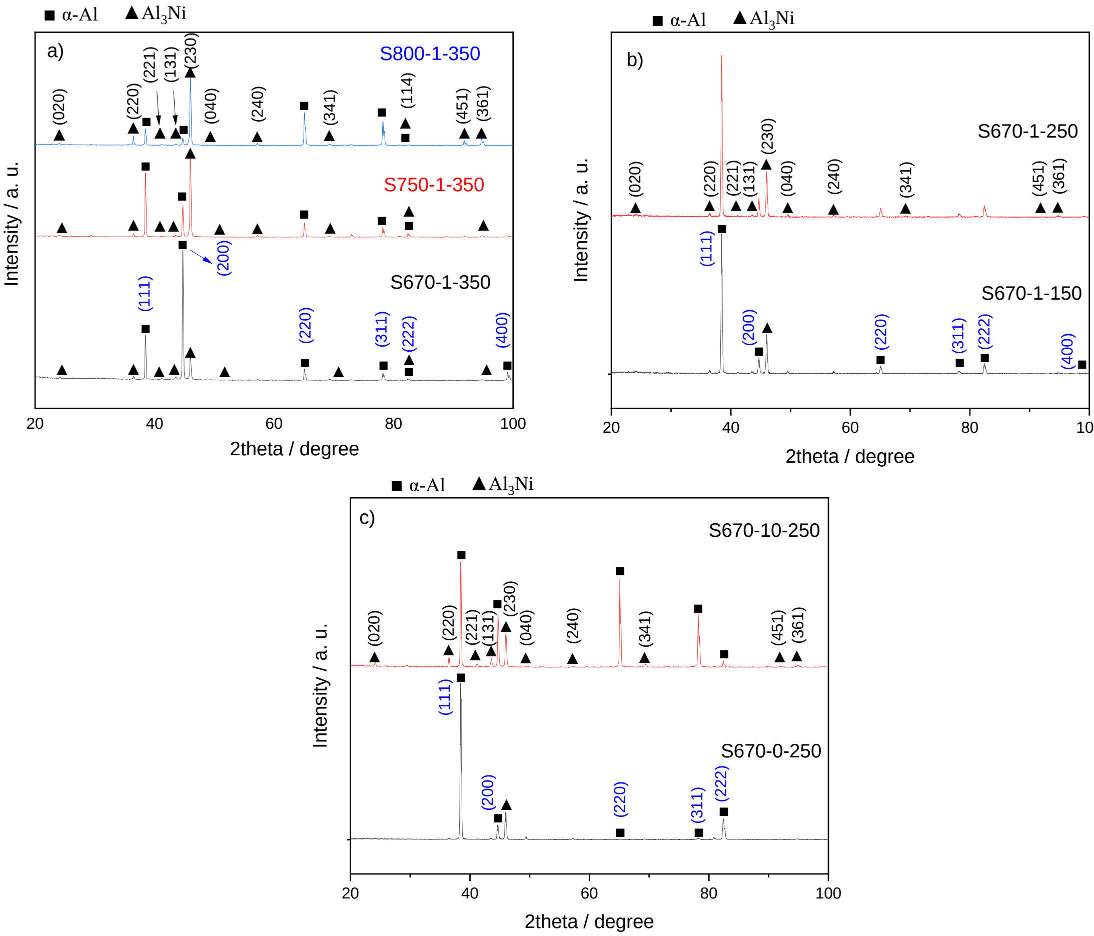

Figure 4-9: X-ray diffraction of samples a) S670-1-350, S750-1-350 and S800-1-350, b) S670-1-150 and S670-1-250, and c) S670-0-250 and S670-10-250 before leaching.

The growth characteristics of Al_3Ni were further investigated by analyzing the {230} planes through Pole figure analysis. The results, shown in Fig.4-10, indicate that the {230} plane of Al_3Ni grows in the direction of [001]. On the contrary, the finding of previous researchers has indicated that the Al_3Ni crystal exhibits preferentially growth along the densely packed plane (010), resulting in the formation of a needle-like Al_3Ni structure [82, 94, 233]. The observed difference in results is attributed to the growth direction of Al_3Ni fibers because these fibers do not grow perfectly perpendicular to the Ni plate. Further investigation into the preferential crystallographic growth will be conducted in section 4.3.5.

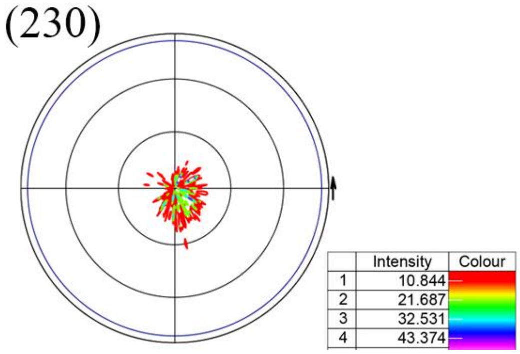

Figure 4-10: Pole figure for (230) planes of Al_3Ni for S670-1-150.

The formation mechanism of the structure of the solidified layer has been investigated by previous researchers [90, 91, 94]. In cases where there is a sufficient mass of Al on Ni plate, some molten Al remains on the surface as Ni dissolves into it [91, 90]. J.F. Zhao *et al.* have demonstrated that the dissolution of Ni into molten Al during Ni-Al interaction is a diffusion-controlled process. As diffusion is a time and temperature-dependent process, increases in temperature or time result in increased Ni content in the melt [90, 91].

Synchrotron X-ray diffraction analysis has revealed the solidification stages of the molten alloy on the surface of nickel following interaction. During the cooling process, Al_3Ni fibers nucleate heterogeneously on D2 layer [94], growing in the liquid and depleting the nickel in their immediate surroundings, resulting in significant undercooling of the α-Al phase. As a result of the significant undercooling, a thin shell of α-Al forms coherently around the Al_3Ni fibers, resulting in a eutectic structure [82]. Al_3Ni has a high fusion entropy which results in a faceted interface, whereas α-Al has a non-faceted interface [200]. When a crystal grows in the faceted mode, it tends to grow preferentially in a specific direction dictated by specific atomic planes because some planes may have the lowest interfacial energy [201]. The Al_3Ni crystal rapidly grows along a close-packed plane, forming a crystal that is bounded by low surface energy facets. This growth leads to the formation of long Al_3Ni whiskers [200].

Cross-sectional and top-view SEM micrographs of sample S670-1-150 after leaching in KOH are shown in Fig.4-11. After leaching, the Ni whiskers, and D1 and D2 layers are observed. Ni:Al composition of the D1 and D2 layers changed significantly from 25:75 and 43:57 at.% before leaching to 93:7 and 88:12 at.% after leaching, respectively. In Fig.4-11, the Al matrix that was making most of the solidified structure of the as-prepared sample is missing. Instead, the whiskers previously embedded in the Al matrix are exposed. The Al content from the upper section of the sample is only 7 at.%, suggesting almost complete dissolution of the aluminum content of the solidified structure. In Fig.4-11, each individual whisker can grow up to 150 μm long and have a width ranging from 0.1 μm to 0.5 μm. These whiskers are bunched together to form bundles.

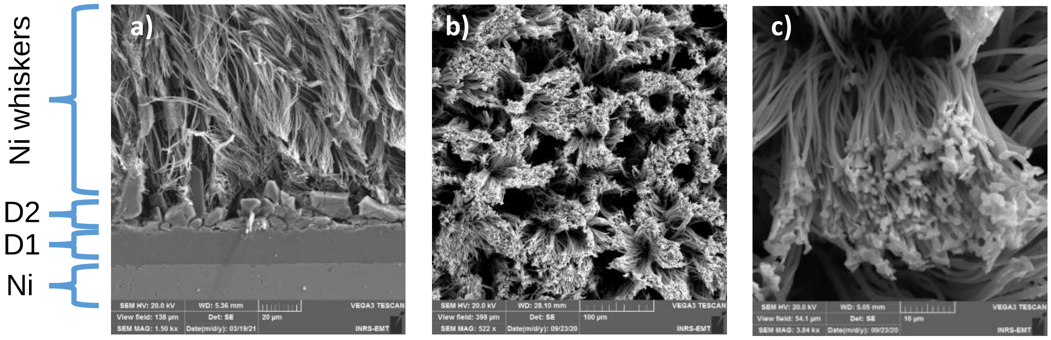

Figure 4-11: Cross section (a) and top view (b and c) SEM micrographs of S670-1-150 after leaching.

The XRD pattern of sample S670-1-150 after leaching is shown on a log scale in Fig.4-8. All peaks can be indexed to metallic Ni, and no other peaks are observed. In particular, all the diffraction peaks attributed to Al_3Ni in the as-prepared sample are absent. This suggests that not only the Al matrix has been removed during the leaching process, but that Al has also been dissolved from the Al_3Ni whiskers initially observed to form Ni whiskers. The coherent scattering domain size calculated from the half width at half maximum of the diffraction peak is *ca.* 5 nm, consistent with the reported Raney Ni powder [73, 74, 78, 85]. These results are consistent with those of Tanaka *et al.*, indicating that Raney-Ni is obtained only from Al-rich alloys such as Al_3Ni and Ni_2Al_3. According to them, the most active form of Raney-Ni is obtained from Al_3Ni due to the rapid Al leaching [84]. Conclusively, Ni-whiskers is fibers of Raney Ni structure. The XRD pattern and coherent scattering of the samples were not affected by the mass of Al and the heat treatment process, as seen in Fig.4-12. Ni whiskers have one of the lowest atomic percent aluminum contents among reported Raney Ni structures [72, 85, 189, 190, 191, 192]. Furthermore, as shown by X-ray diffraction in Fig.4-8, no trace of aluminum trihydrate is detected after leaching.

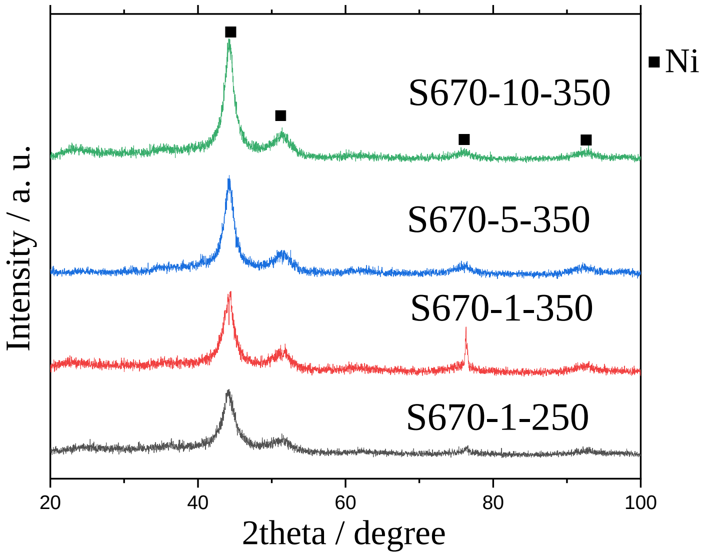

Figure 4-12: X-ray diffraction for the surface of all samples after 24 hours leaching.

The density (number per cm^{-2}) and distribution of Ni whiskers, which determine the total surface area of Ni-whiskers, are directly proportional to the density and distribution of Al_3Ni fibers. Parameters that affect the total surface area of Al_3Ni in α-Al include: (1) volume of solidified structure, (2) Al_3Ni fiber distribution, and (3) Al_3Ni volume fraction. These three variables can be altered by changing Al mass and heat treatment process (time, temperature, and cooling rate).

Heat treatment time and temperature are crucial factors affecting the Ni content and distribution of Al_3Ni in the structure. Increasing either parameter results in higher Ni content (Fig.4-13). The research conducted by Zhao et al. further demonstrated that during the interaction between Ni and molten Al, an increase in heat treatment time or temperature causes an increase in the atomic percentage of Ni in the molten Al. This is due to the diffusion-controlled process of Ni dissolving into molten Al [90, 91]. Moreover, an increase in Ni content results in a boost in the volume fraction of Al_3Ni fibers [92]. According to Fig.4-13, Ni weight percent for all samples is in the range of 10-20 wt.%, which falls within the range of hypereutectic alloys. As described in Chapter 2, for a hypereutectic alloy, primary Al_3Ni, which forms a coarse structure, is first formed in the molten alloy, and the remaining molten alloy solidifies into a eutectic structure with fine Al_3Ni. Fig.S4 and Fig.4-14 depict the structure prior to leaching of S670-0-350, S670-10-350, S700-0-350, and S700-10-350, which includes both primary and eutectic phases of Al_3Ni. After leaching, fine Al_3Ni whiskers and primary Al_3Ni are shown in Fig.4-15.

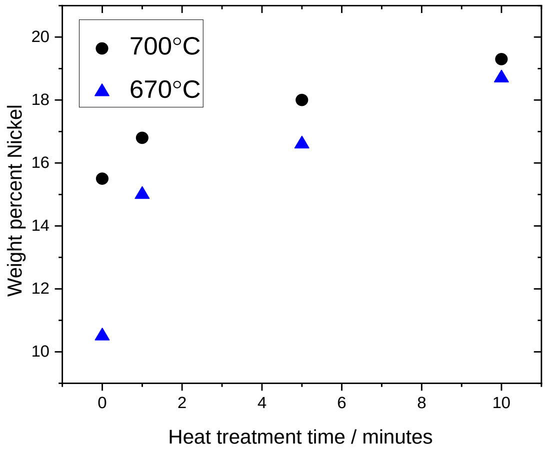

Figure 4-13: Effect of heat treatment time and temperature on Ni content for samples produced using 350 mg Al powder.

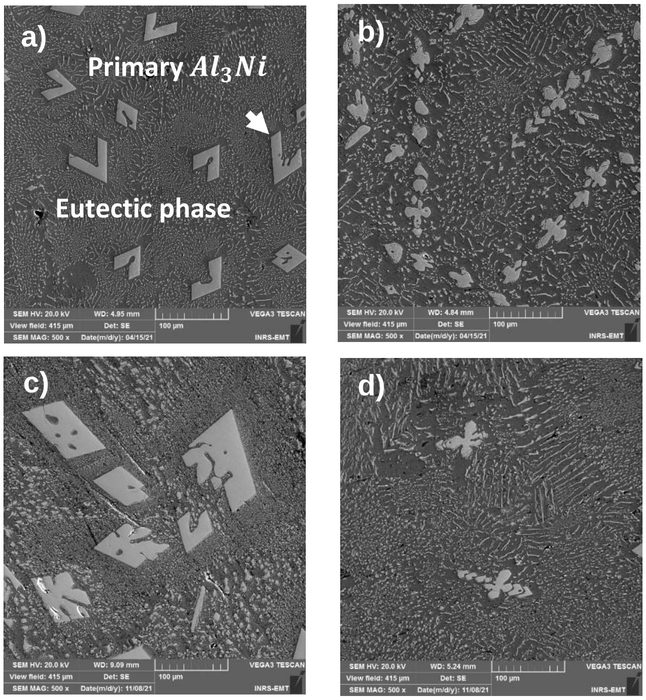

Figure 4-14: SEM images of top view of a) S670-0-350, b) S670-10-350, c) S700-0-350 and d) S700-10-350.

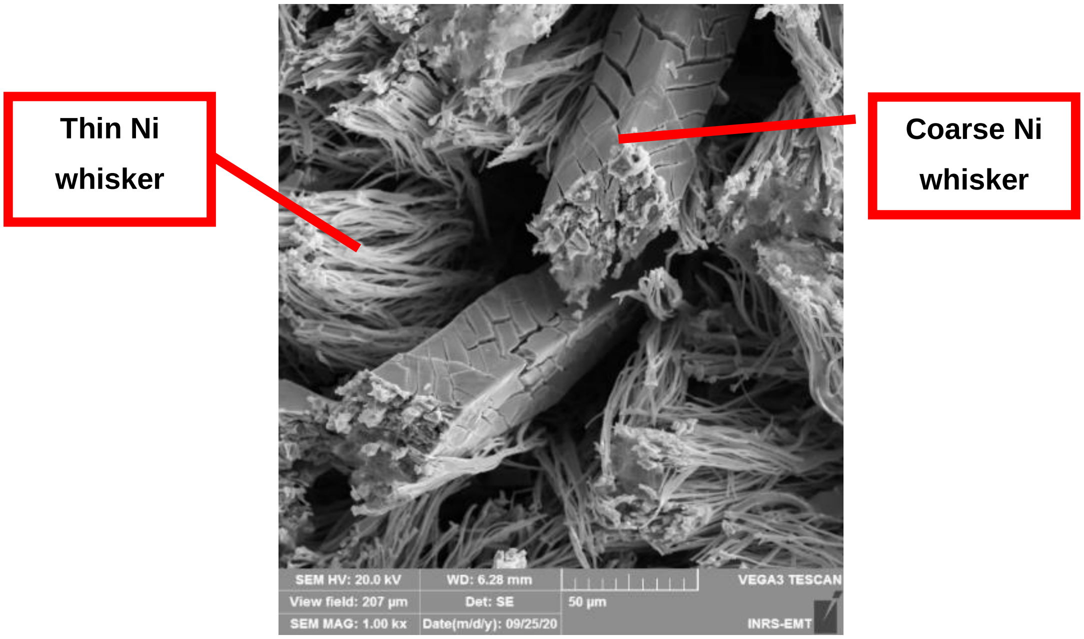

Figure 4-15: SEM top view of S670-1-150 after leaching at magnification 1kx.

The distribution of these fibers is also affected by variations in the heat treatment process [93]. Fig.4-14 demonstrates the impact of heat treatment time on the structure after leaching. It's clear that the structure for S670-10-350 is coarser than S670-0-350. As a result, the coarser structure produces coarser Ni-whiskers after leaching, as shown in Fig.4-16.

The process of forming Al_3Ni fibers in Ni-Al interaction is impeded by increased furnace temperatures [94]. However, it is likely that nucleation of Al_3Ni occurs at a constant temperature, followed by growth and coarsening in the molten alloys [93]. When the Ni-Al diagram phase and Ni content of samples are considered, Al_3Ni fibers may become stable at 670℃. Consequently, a coarser structure is formed.

The results of comparing samples produced at 670°C and 700°C at constant heat treatment time in Fig.4-14 reveal that the structure becomes finer as the temperature increases. The reason for the finer structure can be explained by thermal undercooling and Ni content. Increasing the cooling rate leads to an increase in thermal undercooling, causing the molten alloy to solidify at a temperature far lower than the equilibrium eutectic point. This reduction in temperature reduces the energy barrier of nucleation, leading to an increase in the nucleation rate and the growth of α and β phases. Under these non-equilibrium conditions, the solute content also has an impact on the nucleation rate and growth of phases [195].

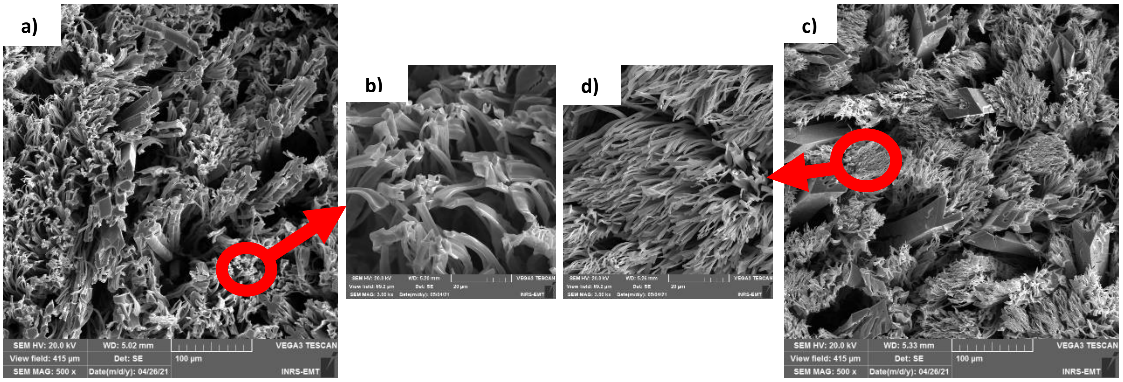

Figure 4-16: Top view S670-10-350 and S670-0-350 after leaching. a) S670-10-350, b) S670-10-350 at higher magnification, c) S670-0-350 and d) S670-0-350 at higher magnification.

The effect of thermal undercooling can be seen in the displacement of the eutectic point. Q.C. Jiang et al investigated the effect of Si content on the displacement of eutectic point for Al-Si Hypereutectic alloy at a non-equilibrium solidification. They reported that at the same cooling rate as molten alloy Si content increases, the eutectic point shifts to higher silicon content. According to the Lever Rule, the shift to higher Si content means less primary Si and more eutectic Si compared to the equilibrium condition [198].

The same interpretation can be given to Ni-Al hypereutectic alloys cooled down relatively rapidly. Ni content in the molten alloy increases with increasing heat treatment temperature. As molten alloy Ni content increases, the eutectic point shifts to higher Ni content (shift to the right). Therefore, the volume fraction of primary phase Al_3Ni (primary phase is coarse) decreases and the volume fraction of eutectic phase Al_3Ni increases (Al_3Ni fibers are fine). Also, a higher Ni content results in a higher Al_3Ni volume fraction. Conclusively, a larger number of finer Al_3Ni fibers are produced resulting in an increased total surface area.

Chapter 2 of the study provides a detailed explanation of how the cooling rate affects the structure. Fig.4-17 depicts SEM top view of S670-1-350, SC40 and SCS samples cooled down using Ar discharge at Ar flow of 10000, 4000 and 18 $mL.min^{-1}$ respectively. A reduction in Ar flow leads to a reduction in cooling rate. As seen in Fig.4-17, reducing the cooling rate coarsens the morphology of Al_3Ni intermetallic. The results are consistent with the findings of other researchers who have stated that increasing the cooling rate will result in a finer Ni-Al structure [203].

The cooling rate affects the growth direction of Al_3Ni fibers as well. Fig.4-18 demonstrates that the tendency of Al_3Ni fibers to grow perpendicular to the nickel surface increases with increasing cooling rate. For SCS, colonies of Al_3Ni fibers are seen that have grown in different directions. But for S670-1-350, Al_3Ni fibers have a much greater tendency to grow perpendicular to the surface.

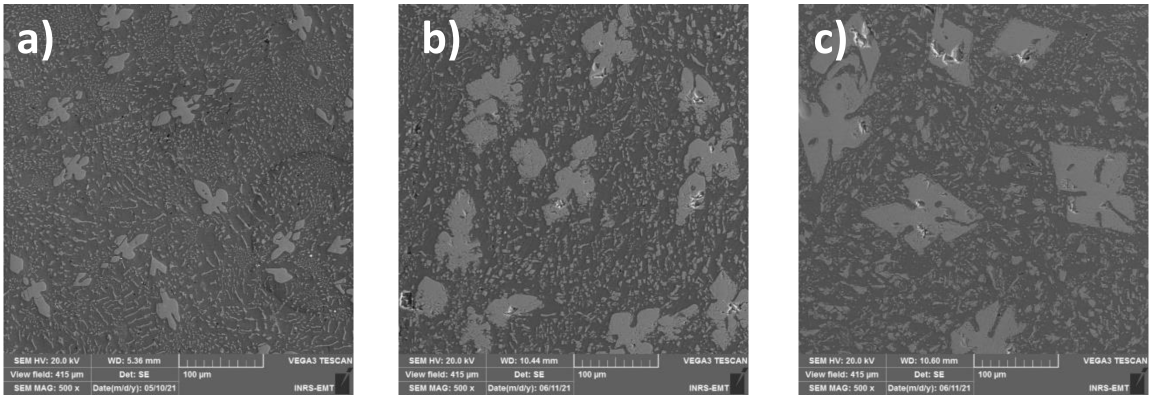

Figure 4-17: SEM top view of a) S670-1-350 b) SC40 c) SCS before leaching.

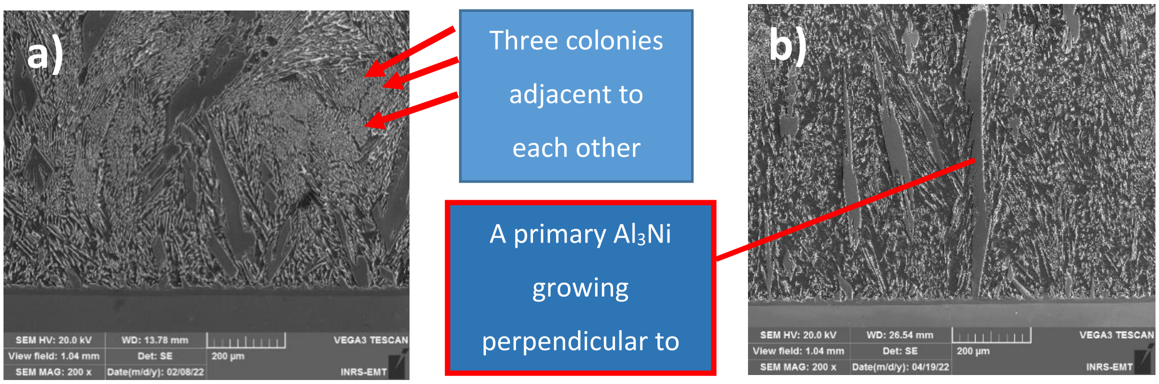

Figure 4-18: SEM cross section of a) SCS and b) S670-1-350 after one minute leaching.

The effect of Al mass on the total surface area of Al_3Ni fibers in α-Al can be studied by comparing S670-1-150, S670-1-250 and S670-1-350 samples. Increasing Al mass results in a thicker or more voluminous solidified layer but does not significantly affect the Ni content. As Ni content and heat treatment process are the same, the density and distribution of Al_3Ni fibers in all samples should also be the same. Fig.4-19 and Fig.4-20 depict a top view of the samples before and after leaching, respectively. A higher magnification SEM image of Ni whiskers can be found in Fig.4-21.

The sole variation between the samples lies in the volume of the solidified structure, implying that the total surface area of Al_3Ni fibers is directly proportional to the thickness of the solidified structure (Fig.S5).

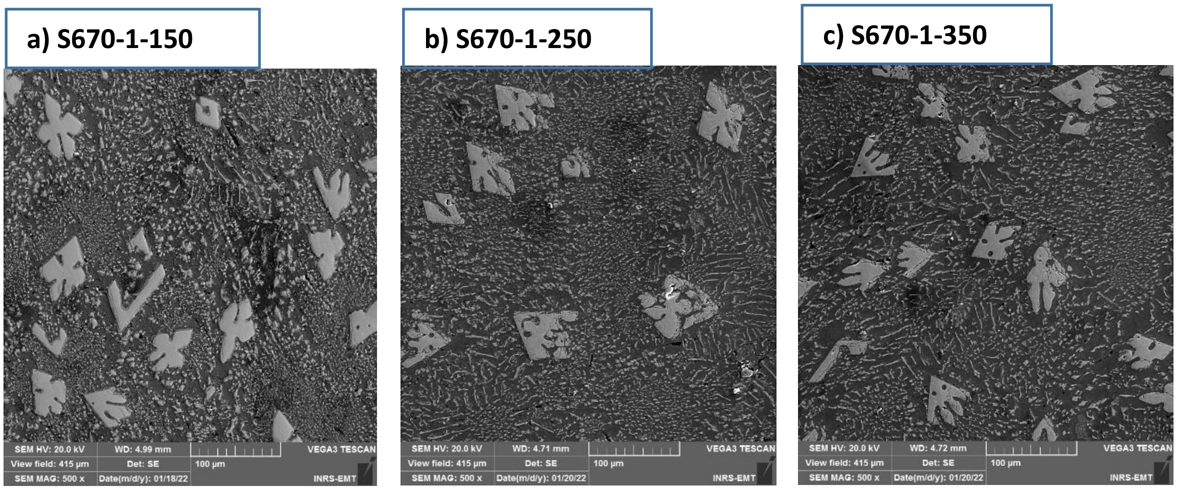

Figure 4-19: SEM top view of S670-1-150, S670-1-250 and S670-1-350 before leaching.

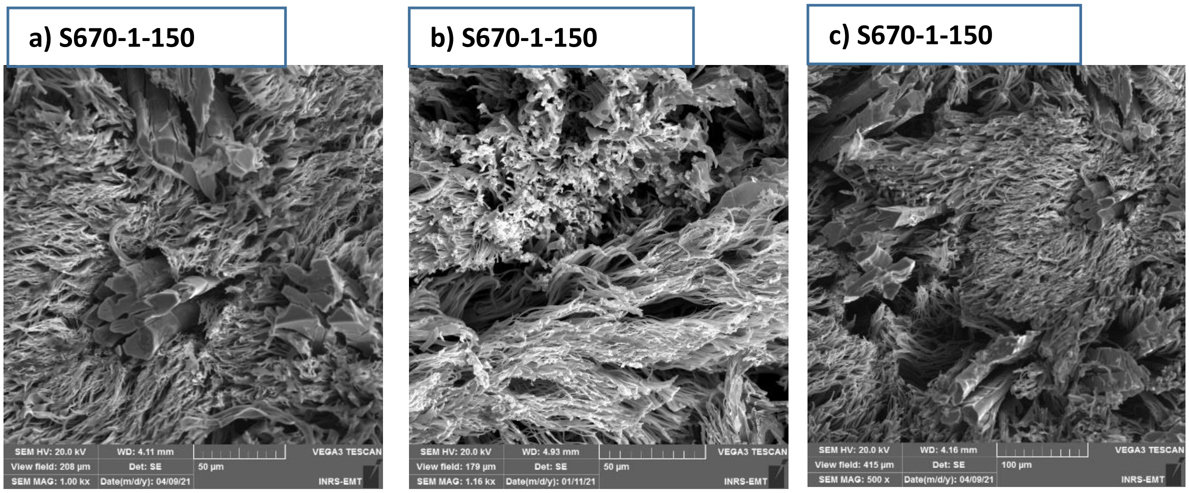

Figure 4-20: SEM top view of S670-1150, S670-1250 and S670-1-350 after leaching.

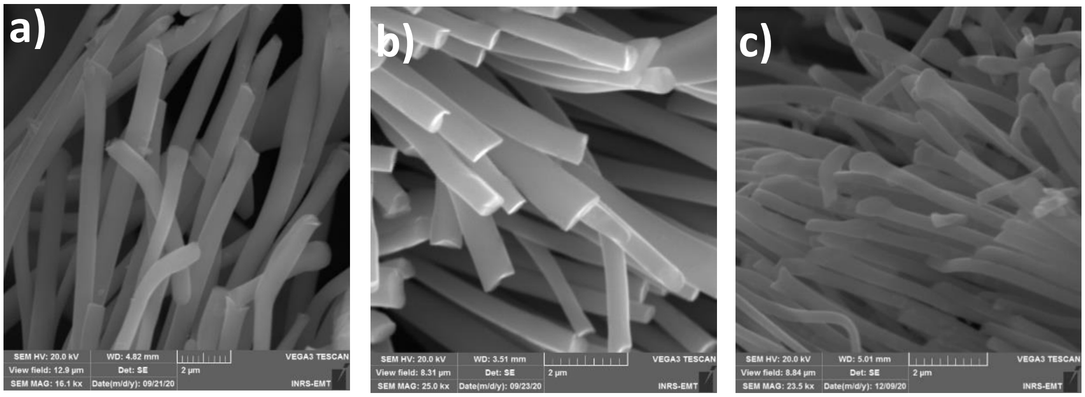

Figure 4-21: Thin Ni whiskers for a) S670-1-150, b) S670-1-250, c) S670-1-350.

4.3.2. Production of self supported Ni-whiskers

The SEM cross-section and variations in atomic percent Al along the cross-section for samples SH0, SH1, SH4, and SH9 are shown in Fig.4-22. It should be noted that the magnification varies depending on the sample. The EDX mapping and analysis in Fig.4-22 and 4-23a show that the Ni:Al composition along D1 layer is consistent for all samples and is about 57 at.% Al. As a result, as previously stated for SH0 in the previous section, D1 layer for all the samples is also a layer of Ni_2AL_3.

Based on the data presented in Fig.4-23, it can be inferred that the thickness of the D1 layer increases with longer heat treatment times at 570℃. In spite of the observed increase in thickness, D1 retains its chemical composition. Thus, it can be concluded that heat treatment at this temperature does not significantly affect the chemical composition of D1.

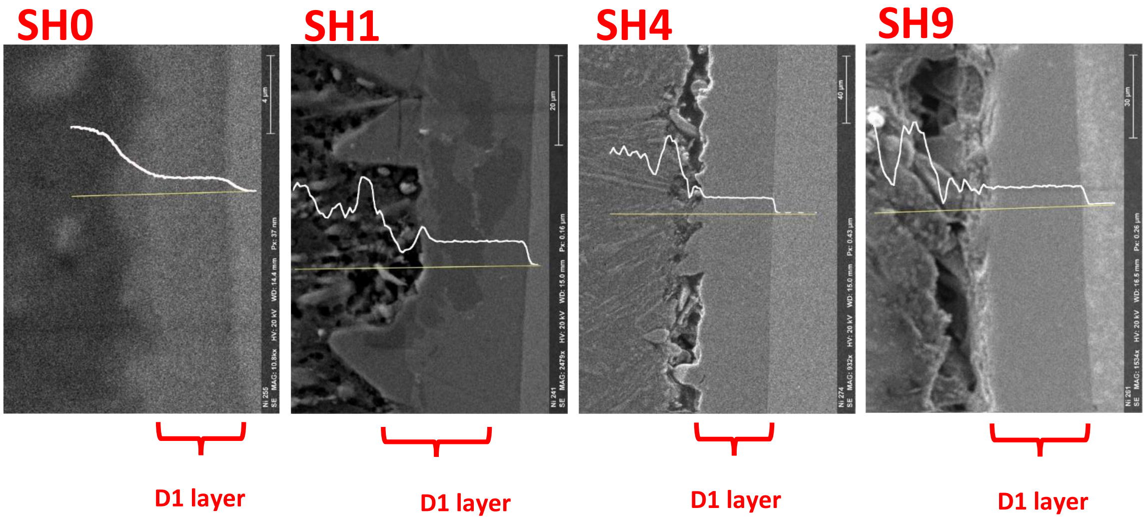

Figure 4-22: The variation of Al concentration in the structure before leaching, along the yellow lines. The magnification for each image is different.

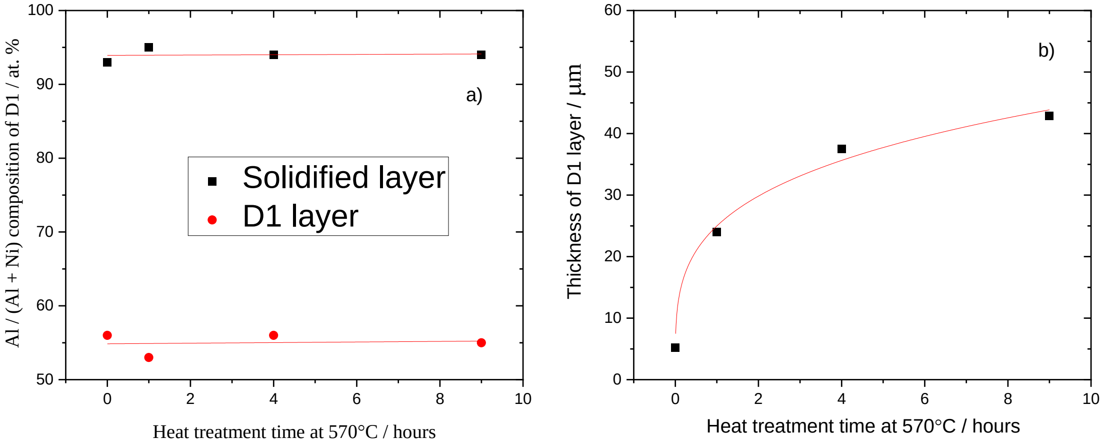

Figure 4-23: The effect of heat treatment at 570℃ on a) atomic percent Al, b) thickness of solidified layer.

As a result of heat treatment at 570°C for one hour, the thickness of layer D1 increased by over five times, indicating that the Ni and Al atoms diffused effectively during the process. The growth of the D1 layer resulted in voids forming at the Ni/solidified layer interface, as shown in Fig.4-22 and Fig.4-24. In Fig.4-24, it is evident that a portion of the D2 layer adjacent to the D1 layer has faded after being exposed to four hours of heat treatment at 570°C (SH4), and between D1 and

D2 layers voids have formed. For the SH9 sample, the D2 layer was almost entirely consumed and a thicker D1 layer was formed.

The changes in D1 and D2 layer thickness and the formation of voids have previously been investigated. The results of S.M Arbo et al. [134] and H Alimadadi [135] indicated that during heat treatment at 550℃ and 610℃, Ni_2Al_3 (D1 layer) grows at the expense of Al_3Ni (D2 layer). Additionally, the Al_3Ni_2 phase emerged as the dominant phase after one hour of heat treatment at 620°C [234].

The voids are formed due to large differences in the diffusion rate of Ni and Al in intermetallics. The diffusion rate of Al in both Ni_2Al_3 and Al_3Ni is much higher than Ni in these intermetallics. As a result, vacancies are accumulated on one side to compensate for the effect of the difference in atomic flux. This phenomenon is known as Kirkendall effect [235, 236].

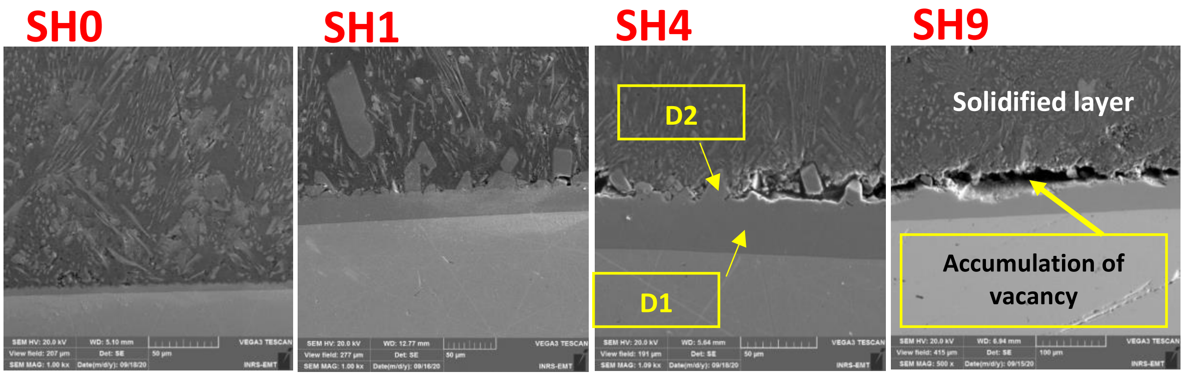

Figure 4-24: Growth of void at the interface between Solidified layer and Ni plate.

Nevertheless, the researchers found that the growth of Al_3Ni fibers in eutectic structures almost stops at temperatures below eutectic temperature due to the coherence interface between $\alpha - Al$ and Al_3Ni fibers [82].

The coherent interface has low mobility and is forced to migrate by ledge mechanisms [237]. The growing ledge can be depicted most simply as seen in Fig.4-25. Ledges (h) are tiny movable stairs whose atomic transfer occurs only across them, resulting in lateral ledge movement with velocity, V, and net growth of the phase boundary, G, in a direction perpendicular to the ledge motion [238]. Therefore, although the growth of D1 layer in Fig.4-23 indicates a high diffusion rate of Al and Ni in the intermetallic at 570℃, the growth of Al_3Ni fibers is limited due to the coherent interface.

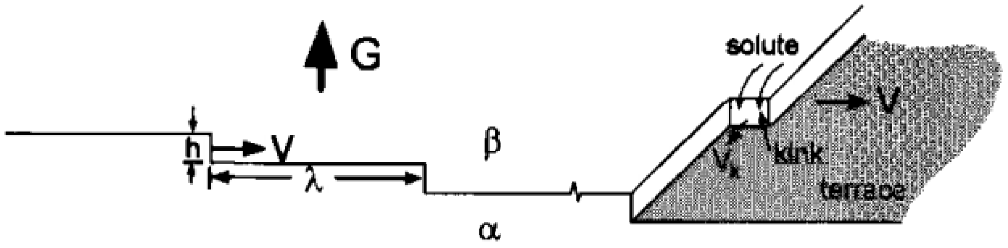

Figure 4-25: A two-dimensional (left-hand side) and perspective sketch of a growing ledge (right-hand side). The perspective sketch depicts the notion of ledge-on-ledge [238].

Ni-whiskers detached from Ni plates after leaching SH0-SH9 samples, without causing any damage. The detachment results from Kirkendall pores forming at the interface between Ni and Ni-Al [239]. During leaching, the violent production of hydrogen generates compressive stress within the pores, which gradually increases. The heightened compressive stress eventually separates Ni-whiskers from the Ni-Al interface.

Fig.4-26 displays SEM images of the detached Ni-whiskers and the surface of the D1 layer after detaching the Ni-whiskers from the SH4 sample. The Ni-whiskers exhibit enough mechanical stability to be transported and analyzed by SEM or BET. Moreover, the detached Ni-whiskers represent a unique 3D structure of Ni that may have various applications.

After leaching, only the Ni-whiskers of the SH1 sample remained attached among all heat-treated samples. SH0 and SH1 cathodic charge values were measured according to Chapter 3, yielding 2963 mC and 3128 mC, respectively. The almost identical cathodic charge values indicate that the Al_3Ni fibers remained unchanged during heat treatment at 570℃.

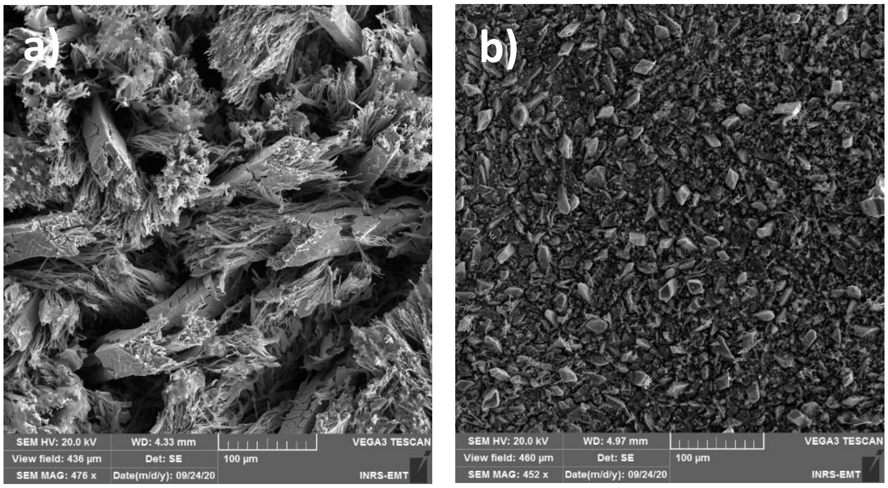

Figure 4-26: SEM image of a) detached Ni-whiskers, b) the surface of Ni plate after detaching Ni-Whiskers (D1 after leaching).

4.3.3. Study of Ni whisker using BET analysis

Fig.S6 displays the detached Ni-whiskers of S670-1-350 at various magnifications, which indicates that they were detached without structural damage.

Fig.4-27a illustrates the relationship between the volume of N_2 gas adsorption and desorption and the relative pressure (P/P0) for sample S670-1-350. Based on Section 3-3-5, the data suggest that the sample follows a Type IV isotherm, which is consistent with previous reports on Raney Ni structures [85, 223]. Adsorbents with mesopore sizes between 2 and 50 nm commonly exhibit type IV isotherms [222, 223].

Using quantachrome nova software, the slope of the isotherm was computed as 24.094 and the intercept was determined to be -5.082. Considering the mass of the detached Ni-whiskers (32 mg), the total surface area was obtained 183 $m^2.g^{-1}$. The computed value is more than the surface area of Raney nickel, which is commercially accessible (100 $m^2.g^{-1}$). Commercial Raney Ni is obtained by leaching Al from Al-Ni 50:50 wt. % alloy including both Ni_2Al_3 and Al_3Ni [85]. While Ni-whiskers is made by leaching Al from Al_3Ni, which results in more active Raney Ni with a larger specific surface area [192].

Fig.4-27b shows pore size distributions of Ni-whiskers. Ni-whiskers are shown as mesoporous structures with a narrow distribution of pore sizes centred around 3 nm. Also, the average pore size is 6 nm which is comparable with other reported Raney Ni [85, 189].

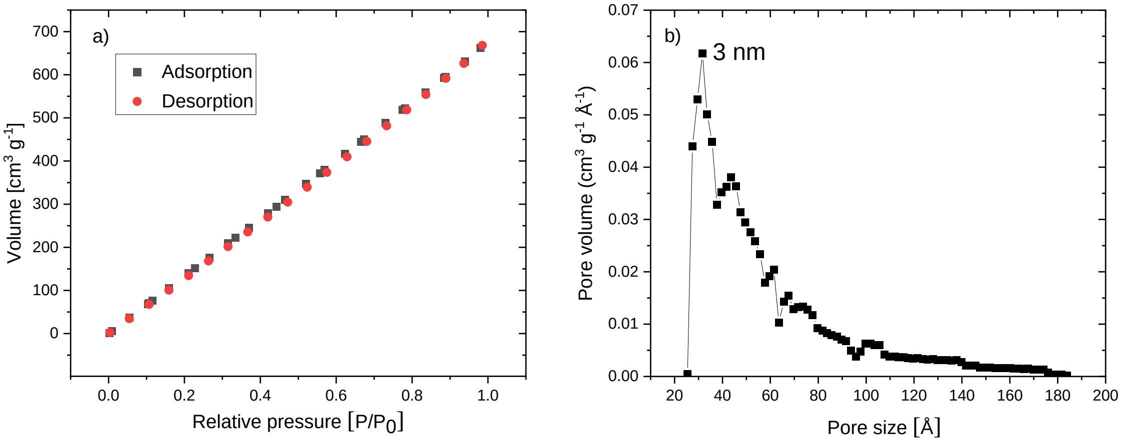

Figure 4-27: BET analysis result for S670-1-350. a) N_2 adsorption–desorption isotherms. b) Pore size distributions of Ni-whiskers.

4.3.4. INVESTIGATION OF DIFFERENT APPROACHED TO SEPARATE FIBERS FOR TEM ANALYSIS

Fig.4-28a and 4-28b show detached fibers of S670-0-350 and S670-1-350 using the sticky tape process on the microscope slide. Both figures show agglomerated fibers that are not separated from each other, indicating that the sticky tape process creates clusters of fibers.

Fibers detached using the scraping process are seen in Fig.4-29. Both agglomerated and separated fibers are seen on the microscope-slide.

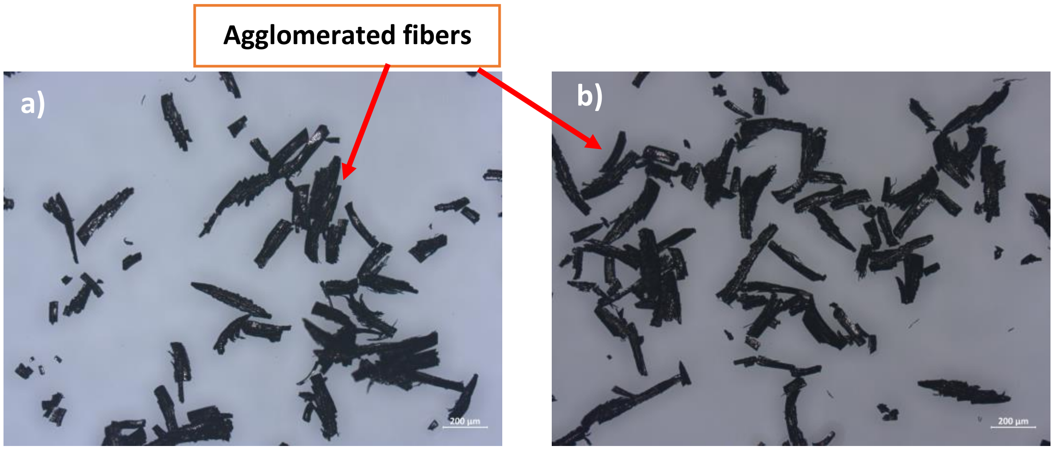

Figure 4-28: Detached fibers on the surface of microscope-slides, at the magnification of 50X. a) S670-0-350 , b) S670-1-350.

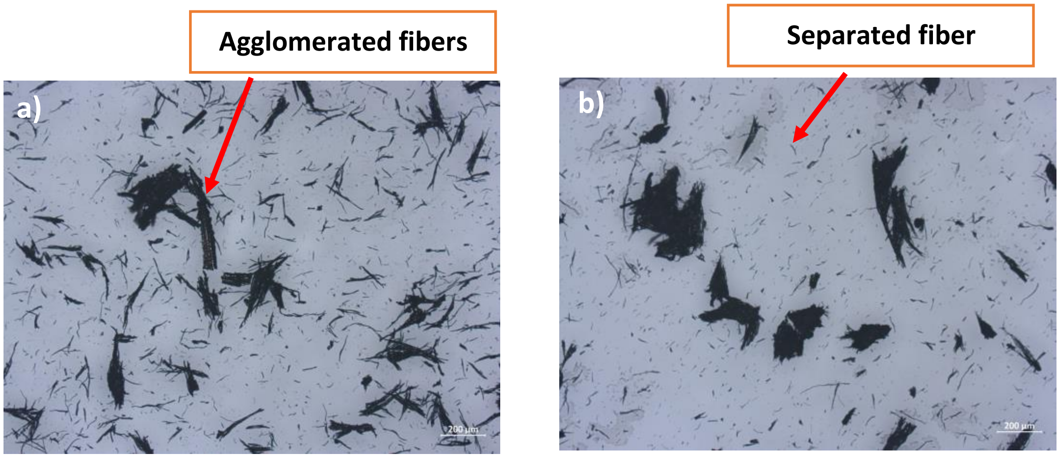

Figure 4-29: Detached fibers on the surface of microscope-slide, at the magnification of 50X. a) S670-0-350, b) S670-1-350.

The detached fibers obtained by the sonication process are displayed in Fig.4-30. It is evident that the sonication process is the best process to produce separated fibers.

As the sonication time increases, the number of fibers obtained also increases. An increased number of fibers is desirable to increase the likelihood of finding fibers during TEM examination. We therefore chose a sonication time of 10 minutes. Furthermore, S670-0-350 was selected for

TEM analysis due to its finer structure. In conclusion, S670-0-350(10 min) was chosen for TEM analysis.

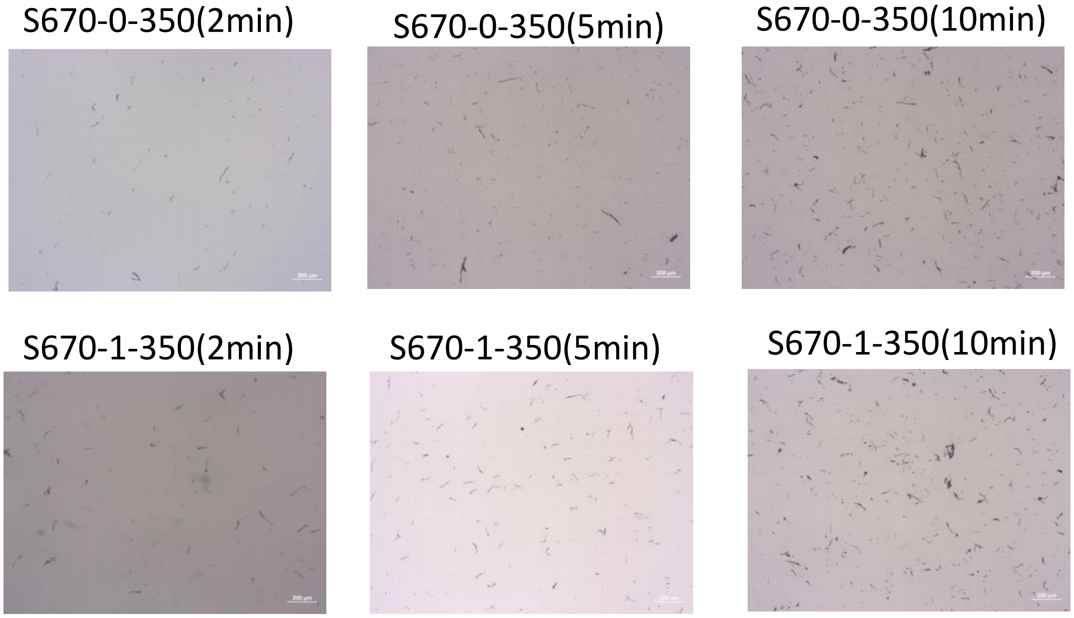

S670-0-350(2min) S670-0-350(5min) S670-0-350(10min)

S670-1-350(2min) S670-1-350(5min) S670-1-350(10min)

Figure 4-30. Detached fibers on the surface of microscope-slide, at the magnification of 50X.

4.3.5. STUDY OF FIBERS USING TEM ANALYSIS.

According to Section 4.3.1, the crystalline structure of Ni whiskers is FCC, which is similar to the morphologies of Raney Ni [240]. Due to the fact that Ni whiskers are produced by leaching Al from Al_3Ni grains, which have a preferred crystal orientation, we investigated whether Ni whiskers have a preferred crystal orientation. This was done by comparing the projection planes (the plane is perpendicular to the beam direction) of different Ni whiskers.

In Fig.4-31, all the morphologies visible on the grids are displayed. The long black strip in Fig.4-31a (Part 1) represents a Ni whisker. In order to obtain an acceptable diffraction pattern, we focused on areas of fibers that were not completely black. These are regions where electron beams can pass through the fiber and reach the camera, giving the camera a brighter image of the fiber. TEM images of such a region are shown in Fig.4-31c, magnified at 38 kx. In contrast, another area, shown in Fig.4-31b (Part 2), close to the Ni fibers, depicts the outcome of chemical reactions between the nickel fibers and elements such as oxygen and hydrogen. The research results were grouped into two categories, namely Part 1, related to Ni fibers, and Part 2, related to Ni compounds.

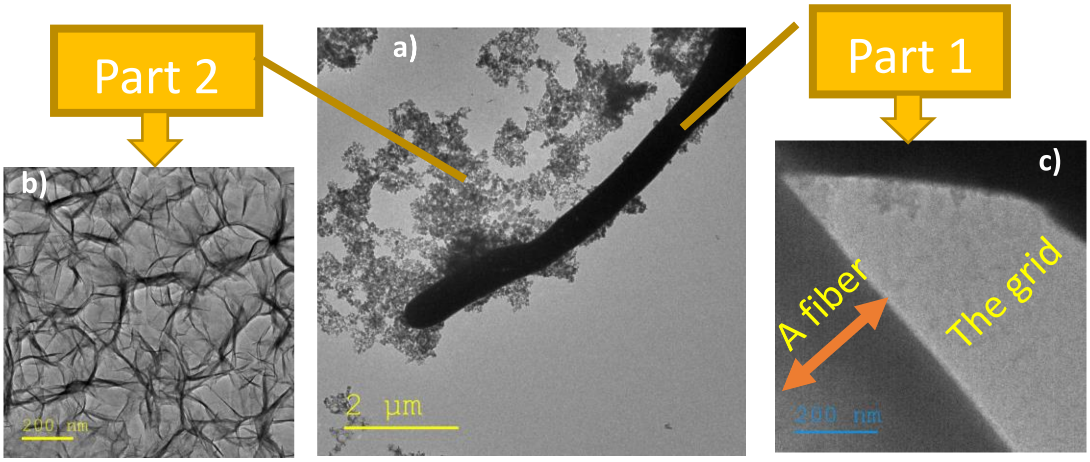

Figure 4-31. Different morphologies that can be seen on the grid.

Many diffraction patterns were taken from fibers (part 1). Most of the diffraction patterns depicted a single diffraction pattern. However, a few polycrystalline diffraction patterns were also taken from fibers.

The first step was to examine several polycrystalline diffraction patterns. Fig.4-32 and Table 4-7 show the diffraction pattern and measured d-spacing of a polycrystalline structure. Using the measured d-spacing of the diffraction and the known d-spacing of Nickel, we concluded that the diffraction corresponds to a nickel polycrystalline structure. However, it is important to note that Ni whiskers are thin, nanoporous fibers, and TEM sample preparation, which involves sonication, could damage or deform the fibers. Therefore, the presence of minority polycrystalline diffraction patterns could be attributed to the damage sustained by the Ni fibers during the sonication process for TEM sample preparation.

The next step was to examine single-diffraction patterns. In Section 4.2.6, we discussed how two planes were first indexed based on their interplanar spacing, and how the cross-product of two vectors was used to determine the projection plane (i.e., the plane perpendicular to the beam direction). The projection planes for all diffraction patterns were calculated, and it was ultimately determined that the diffraction patterns could be categorized into only three groups based on their projections which are {111}, {110}, and {100} planes.

Fig. 4-33, 4-34 and 4-35 illustrate TEM images and TEM diffraction patterns for three categories, where the black stripes represent Ni whiskers, and the yellow arrow signifies their growth direction. The projection planes for F2, F3, and F4 were determined as {111}, {100}, and {110}, respectively. The results are consistent with the projection planes of {111}, {100}, and {110} shown in Fig.S7, S8, and S9, as determined by the ReciprOgraph software.

Therefore, when X-axis diffraction measurements were taken on different fibers, the Z-axis indicated a random orientation because the three different projection planes were observed. However, each of the three fibers displayed a similar orientation of yellow arrows (Y-axis) along the growth axis, suggesting a preferred direction towards <110>. A schematic representation of the crystallographic orientation of the Ni whiskers is shown in Fig.4-36. The result is in agreement with previous findings [233].

Table 4-7: The relationship between the interplanar spacing and the related (hkl) plane for Ni.

(hkl)	d (Å)/ Ni	Measured d (Å) for F1	Measured d (Å) for F2	Measured d (Å) for F3	Measured d (Å) for F4
(111)	2.034	2.03			2.03
(200)	1.762	1.76		1.75	1.75
(220)	1.246	1.24	1.24	1.24	1.23
(311)	1.0624	1.06			
(222)	1.0172				
(400)	0.881				
(331)	0.8084				
(420)	0.788				

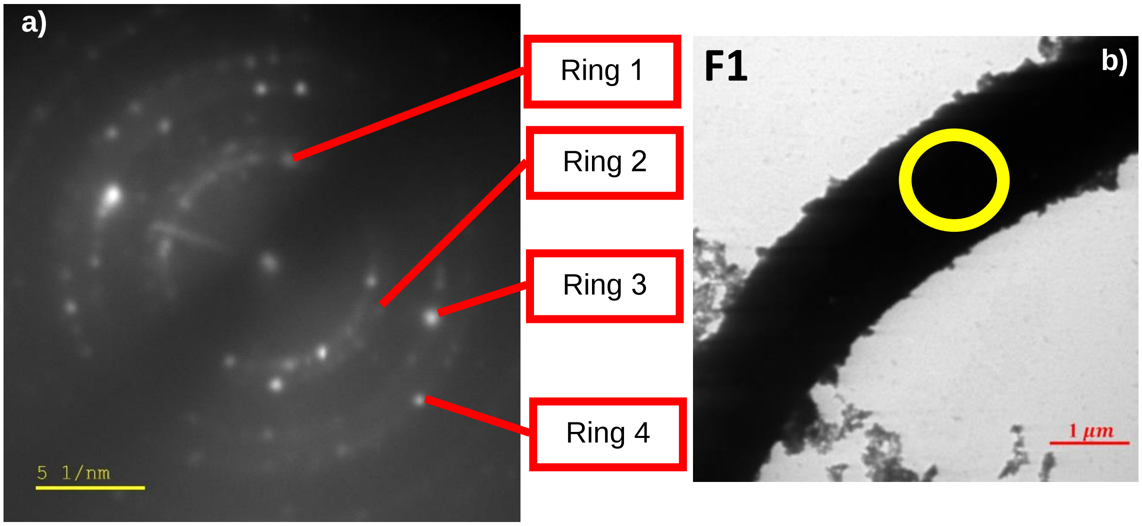

Figure 4-32: a) TEM diffraction pattern of F1, b) TEM image of F1 in the mode of diffraction pattern. The yellow circle determines which area was selected for the diffraction pattern.

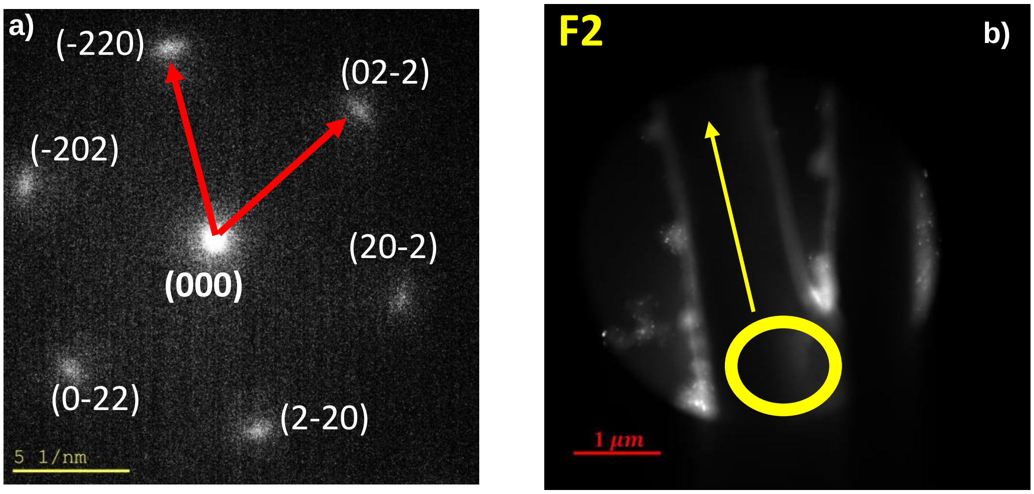

Figure 4-33. TEM diffraction pattern of F2, b) TEM image of F2 in the mode of diffraction pattern. The yellow circle determines which area was selected for the diffraction pattern. The projection plane is {111}.

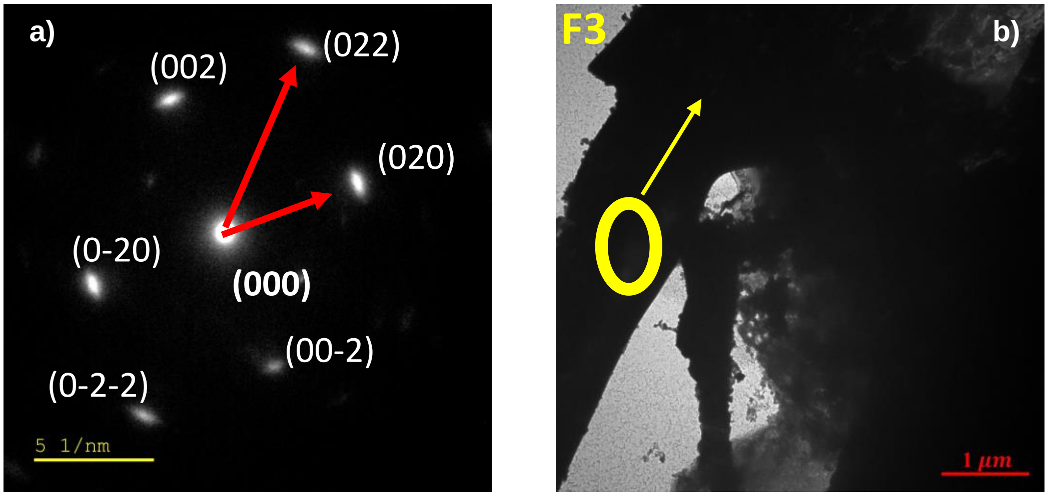

Figure 4-34. TEM diffraction pattern of F3, b) TEM image of F3 in the mode of diffraction pattern. The yellow circle determines which area was selected for the diffraction pattern. The projection plane is {100}.

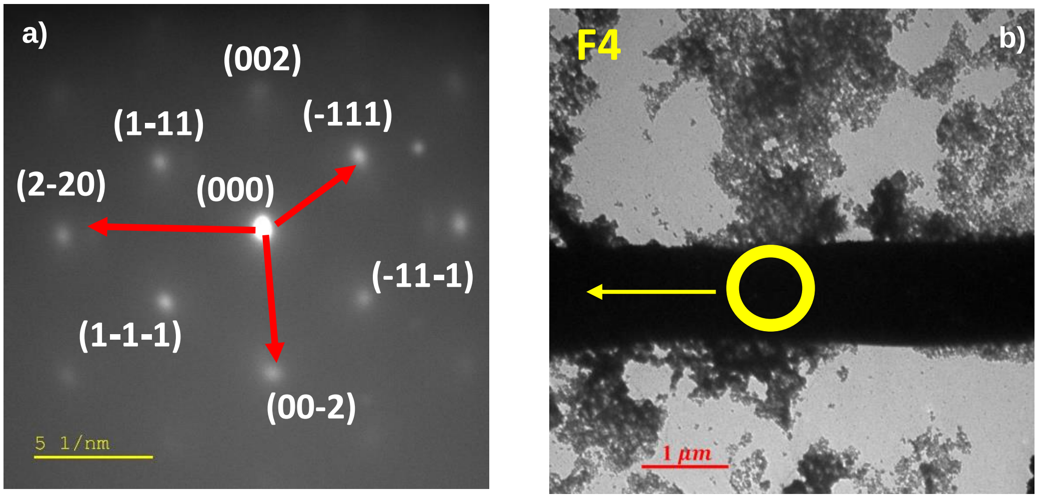

Figure 4-35: TEM diffraction pattern of F4, b) TEM image of F4 in the mode of diffraction pattern. The yellow circle determines which area was selected for the diffraction pattern. The projection plane is {110}.

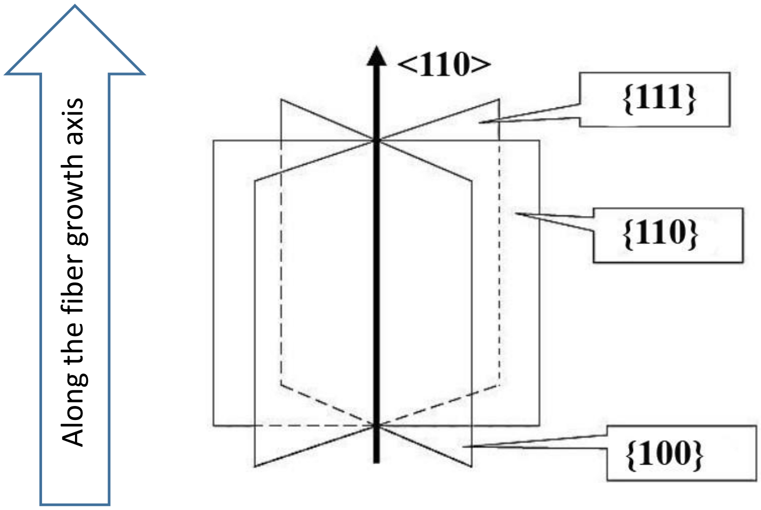

Figure 4-36: Schematic view of the crystallographic orientation of Ni whisker.

The findings of P. Colin et al. have shown that Ni fibers with a <110> crystallographic orientation, similar to our own results, were formed by leaching aluminum from preferentially oriented Al_3Ni, where the (010) planes were aligned in the <001> direction [233]. Despite this similarity, a question arises as to why the (230) plane exhibits the highest intensity in the XRD pattern in Fig.4-8 and 4-9. This can be attributed to the specific angle of 33° between the (230) and (010) crystallographic planes, calculated using the cross-product of their respective vectors. Furthermore, it has been noted that Al_3Ni fibers do not exhibit a perfect perpendicular orientation to the Ni plate. When these whiskers tilt at an angle greater than 15°, there is a higher likelihood of observing the diffraction pattern corresponding to the (230) plane. Consequently, the peaks associated with the (230) plane become more intensified compared to those of the (010) plane.

Fig.S10 and S11 illustrate the unit cell of Al_3Ni and the arrangement of Ni atoms on the (010) plane of Al_3Ni, respectively. In Fig.S11, Al atoms are removed from the structure for clarity. Fig. S12 displays the front and side views of the (230) planes of Al_3Ni after the removal of Al atoms. The close correlation between atomic distances suggests that only the (010) planes of Al_3Ni significantly contribute to the formation of (110) planes in Ni. On the other hand, the (230) planes of Ni lack the organized atomic structure necessary for the formation of (110) planes.

As reported in previous studies [72, 74, 85], Raney Ni has a crystallite size of less than 10 nm. The XRD analysis of the Ni whiskers in Fig.4-8 showed broad peaks similar to those observed in previous studies on Raney Ni structures. On the basis of XRD analysis of Ni whiskers, one could report a crystallite size of 5 nm. However, the TEM study results did not support a crystallite size of 5 nm. For S670-0-350, the average thickness of the Ni whisker was about 100 nm, so if crystallites were 5 nm in size, the diffraction pattern would show several crystallites. Additionally, the diameter of the area analyzed for the TEM diffraction pattern was 600 nm, and the single-crystal patterns showed that crystallite sizes were on the order of at least 600 nm. Similar observations have been made in other studies, which also showed a significant difference between the crystallite size estimated from XRD patterns and TEM analysis for nanopores obtained from dealloying [87, 88].

M. Graf et al. studied nanoporous gold to discover why the coherency of X-ray scattering in nanoporous structures produced by dealloying is broken down. Their findings revealed that in addition to internal stress, stacking defects, and crystallite smallness [87], ligament size also breaks down the coherency of X-rays scattering [88]. They concluded that Bragg reflection should have two distinct components; a narrow central component representing the long-range coherency of the crystal lattice, plus a broad foot created from the partial loss of atomic neighbors due to the nanopores. Their theoretical results showed that despite being quasi-single crystalline, the ligament size of the porous network influences the scattering, and the experimental results also showed that coherent scattering domain size is equal to the ligament size [88].

We were not able to quantify the ligament size using SEM or TEM; however, the literature suggests that Raney Ni ligaments are between 5-10 nm in size [89]. the coherent scattering domain size calculated from the XRD pattern of Ni whiskers is 5 nm. In light of M. Graf et al.'s findings [88], Ni whiskers have an average ligament size of 5 nm, which is within the range reported for Raney Ni [89]. Therefore, the average pores and ligament size of Ni whiskers is around 5 nm.

Two distinct regions were observed in the TEM images of part 2 of the study, namely A1 and A2. Fig.4-37 and 4-38 show TEM images and diffraction patterns of A1 and A2, respectively. The ring-like diffraction patterns suggest that the structures of these regions are polycrystalline in nature. Based on the comparison of the measured ring radii of A1 and A2 in Table 4-9 with those of Ni Oxide and Ni Hydroxide in Table 4-8, it was concluded that A1 corresponds to Ni hydroxide and A2 to Ni oxide.

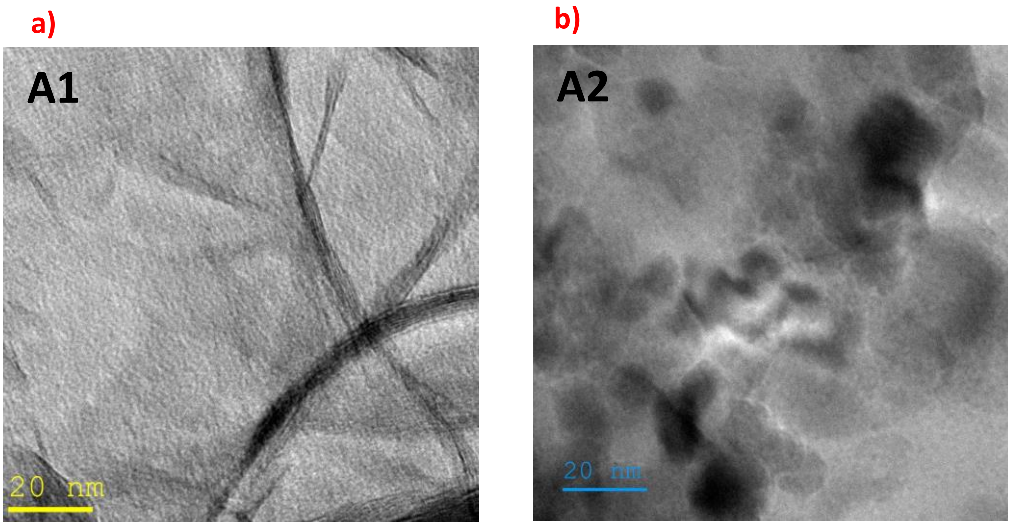

Figure 4-37: TEM images of two different areas in part 2 of Fig.4-31. The areas are named a) A1 and b) A2.

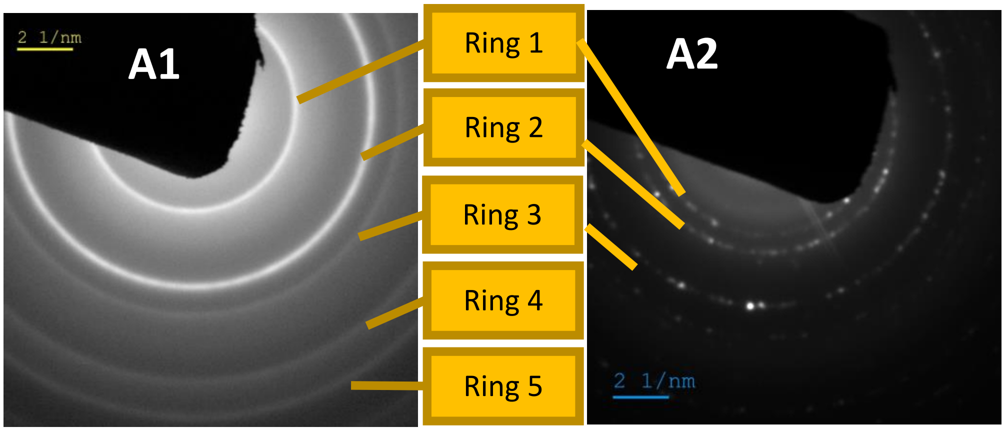

Figure 4-38: TEM diffraction pattern of A1 and A2.

Table 4-8: The relationship between the interplanar spacing and related (hkl) plane for Nickel oxide (NiO) and Nickel hydroxide.

(hkl)	d (Å) / Ni(OH)$_2$		(hkl)	d (Å) / NiO
(100)	2.68		(111)	2.4
(002)	2.33		(200)	2.08
(102)	1.75		(220)	1.47
(003)	1.55		(311)	1.26
(111)	1.48		(222)	1.2
(103)	1.34		(400)	1.04
(112)	1.29		(331)	0.96
(004)	1.16		(420)	0.93

Table 4-9: Comparing A1 and A2 with Nickel hydroxide and Nickel oxide.

Measured d (Å) for A1	(hkl) of Nickel hydroxide		Measured d (Å) for A2	(hkl) of Nickel oxide
2.68	(100)		2.4	(111)
1.55	(003)		2.08	(200)
1.34	(103)		1.47	(220)
1.29	(112)			
1.16	(004)			

4.3.6. Effect of mass of Al on electrochemical characteristics

In Section 4.3.1, it was observed that an increase in Al mass resulted in a corresponding increase in the volume of the solidified layer. However, this increase had no significant effect on the Ni content and microstructure of the solidified layer. Thus, the only variable among the samples is the volume of the solidified layer, indicating that the total surface area of Al_3Ni fibers is directly proportional to the thickness of solidified layer. It should be noted that upon melting Al, Al oxide is formed on the surface of the molten alloy [94], indicating that not all molten Al is converted to the solidified layer.

To evaluate the effect of Al mass, electrodes of samples were prepared using the methods described in Section 3.4.1, and their electrochemical characteristics were assessed by cyclic voltammetry and OER overpotential at varying current densities. In Fig.4-39 you can see the CV (5 $mV.s^{-1}$), while in Fig.4-40 you can see the cathodic charge and double-layer capacitance measurements of S670-1-150, S670-1-250, and S670-1-350. According to the figures, the cathodic charge and double-layer capacitance increase linearly with Al mass, indicating a correlation between Al mass and the total surface area of Ni whiskers. Additionally, Fig.S14 shows a linear relationship between the double-layer capacitance and the cathodic charge for all Ni whiskers evaluated in this thesis. As a result, the total surface area of Ni whiskers can be represented either by a cathodic charge or by a double-layer capacitance.

Due to the high electrochemical active surface area, Ni whiskers require sufficient time to stabilize during galvanostatic oxidation. The S670-1-350 sample, for instance, required a minimum of 10 minutes to achieve stability at a current density of 10 $mA.cm^{-2}$, as seen in Fig.S15a. As a consequence of this, Tafel slopes ranging from 40-80 mV/dec were obtained for different samples at various scan rates. For instance, the S670-1-350 sample yielded Tafel slopes of 53 mV/dec and 62 mV/dec at low scan rates of 1 mV/s and 0.05 mV/s, respectively (Fig.S15b). Since all Ni whiskers are converted to Ni hydroxides, they should have identical Tafel slopes. These differences may be due to the very high current density required to convert Ni hydroxide to oxy Ni hydroxide or other factors that need to be further investigated. Thus, this study compared the OER performance of Ni whiskers exclusively through galvanostatic oxidation at both low and high current density (Fig.S16).

Fig.4-41a illustrates the relationship between OER overpotential and Al mass in 1M KOH. Increasing the mass of Al and consequently, the cathodic charge, a more active surface area is provided, leading to a higher reaction rate at the same overpotential [241]. Therefore, as Al mass increases, the overpotential at the same current density decreases. Among these three samples, S670-1-350 has the lowest overpotential, requiring overpotentials of 240 mV to deliver 10 mA.cm^{-2}. To confirm that the low overpotential is not caused by Fe incorporation into the electrolyte, 10 ppm Fe was added to the electrolyte and the overpotential was again measured. By adding 10 ppm Fe, the overpotential at 10 mA.cm^{-2} decreased to 185 mV (Fig.4-41b). Furthermore, at an overpotential of 240 mV, a current density of 500 mA.cm^{-2} was achieved, which is approximately 50 times greater than that of the electrolyte without Fe.

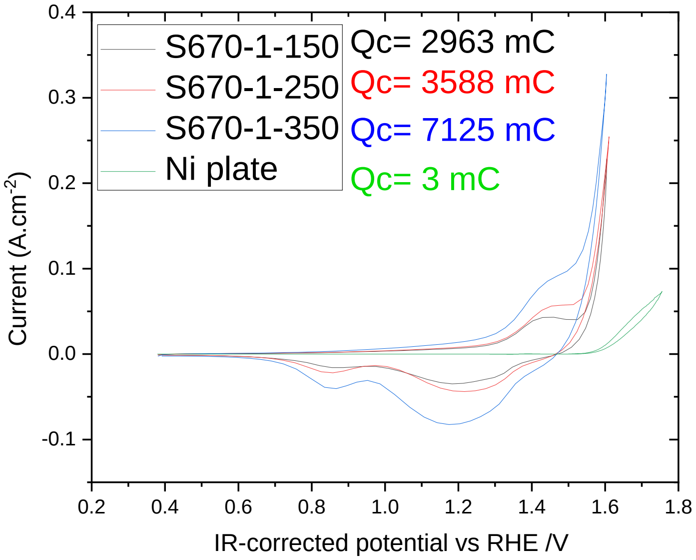

Figure 4-39: Cyclic voltammograms (5 mV/s) for Ni plate, S670-1-150, S670-1-250, and S670-1-350.

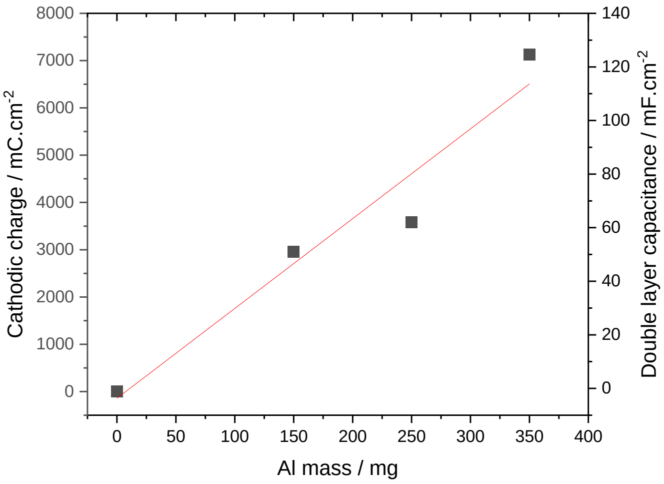

Figure 4-40: Effect of mass of Al on cathodic charges and double layer capacitance for Ni plate, S670-1-150, S670-1-250 and S670-1-350.

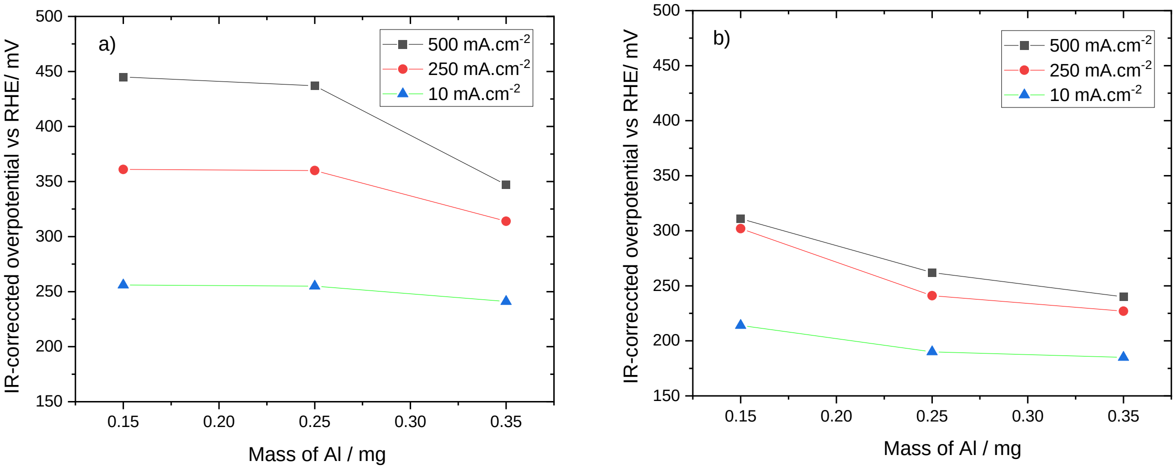

Figure 4-41: The relation between OER overpotential and mass of Al in a) 1M KOH b) 1M KOH spiked with 10 ppm Fe.

4.3.7. Effect of the cooling rate on electrochemical characteristics

According to Section 4.2.1, less Ar flow results in a slower cooling rate, which leads to coarser Al_3Ni fibers. Further, the cooling rate was found to influence the direction of fiber growth. With increasing cooling rates, Al_3Ni fibers tend to grow perpendicularly to nickel surfaces, leading to a closer alignment of eutectic colonies.

Fiber morphology and orientation impact electrochemical characteristics. In Fig.4-42, samples produced at a lower cooling rate exhibit a lower cathodic charge. Low cooling rates result in a coarser structure, which reduces the total surface area of Ni whiskers exposed to the electrolyte, resulting in a decrease in cathodic charge. By reducing the cooling rate (Ar flow), less electrochemical surface area is available for OER, resulting in an increase in OER overpotential, as shown in Fig.4-43.

A comparison of S670-1-350 and SC40 shows that there is no significant difference in cathodic charge, however, S670-1-350 has a significantly lower overpotential at all current densities. The reason for this difference lies in the orientation of Ni whisker fibers in S670-1-350, which tend to grow perpendicular to Ni surfaces. It is believed that this orientation aids in the release of bubbles from the structure, reducing the OER overpotential.

The selection of the highest possible cooling rate (Ar flow 10000 mL.min^{-1}) is based on its favorable impact on the OER overpotential.

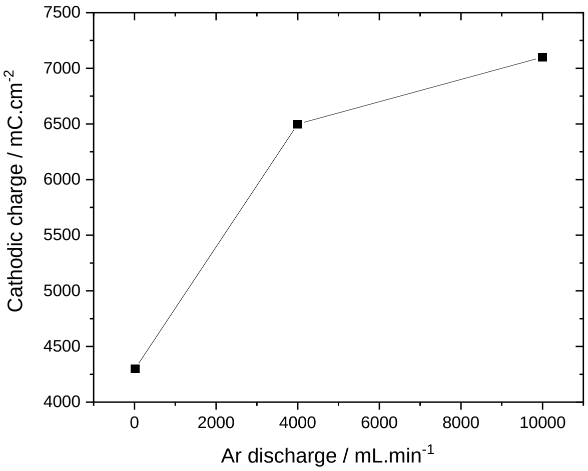

Figure 4-42: Effect of Ar flow on cathodic charge of S670-1-350, SCS40 and SCS samples.

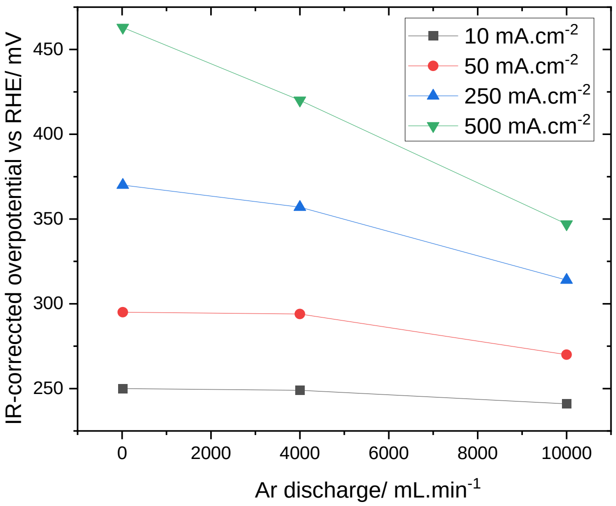

Figure 4-43: The effect of Ar flow on OER overpotential of S670-1-350, SCS40 and SCS samples.

4.3.8. Effect of heat treatment time and temperature on electrochemical characteristics

As stated in section 4.3.1, the total surface area of Al_3Ni fibers in $\alpha -$Al is influenced by two factors: 1) the distribution of Al_3Ni fibers and 2) the Al_3Ni volume fraction. A finer distribution of Al_3Ni fibers or a higher Al_3Ni volume fraction, or both, results in an increase in surface area.

While increasing the elapsed time at maximum heat treatment temperature (heat treatment time) increase Al_3Ni volume fraction, it also leads to coarser Al_3Ni fibers. Based on Fig.4-44, the cathodic charge decreases with increasing heat treatment time, indicating that coarsening of the structure is the dominant factor determining the total surface area of fibers.

On the other hand, an increase in the temperature leads to an increase in the total surface area of fibers due to the increase in Ni content, which subsequently increases the density and the volume fraction of Al_3Ni fibers, as described in Section 4.3.1.

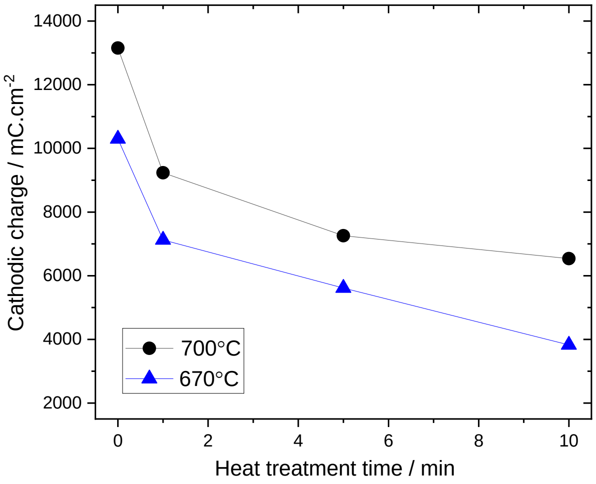

Figure 4-44: Variation of the cathodic charge with respect the time elapsed at the maximum heat treatment temperature. The mass of Al was 350 mg in each case and the maximum heat treatment temperature was either 670 or 700 °C.

When the electrochemical active surface area rises, the current density increases at the same overpotential. Therefore, decreasing the heat treatment time reduces the overpotential at the same current density (Fig.4-45a). Overpotentials for S670-0-350 and S670-1-350 are almost identical at 10 mA.cm^{-2}, indicating that this overpotential represents the minimum achievable for the Raney Ni structure at 10 mA.cm^{-2}. In Chapter 5, this matter will be further discussed.

At high current densities (i.e., a large number of bubbles), the overpotential for S670-0-35 is higher than S670-1-350, which is related to whisker density. When whiskers are very closely packed (resulting in a short distance between them), bubbles get trapped between them, hindering the bubble escape from the structure. By trapping the bubble, the electrolyte is pushed away from the whisker surface. As a result, mass transport is hindered, and reaction rates are decreased (as described in section 2.7.3). In other words, the overpotential is determined by two factors: 1) the electrochemical active surface area and 2) the facilitation of bubble escape.

A similar effect of trapped bubbles inside the structure can also be seen in samples produced at 700°C (see Fig.4-45b). Fiber density is much higher in S700-0-350 and S700-1-350 than in S670-1-350, making bubble escape difficult. They, therefore, exhibit higher OER overpotentials at higher current densities than S670-1-350. In any case, OER overpotentials for S700-10-350 and

S670-1-350 could be considered the same, indicating a cathodic charge of approximately 7000 mC.cm^{-2} would be optimal.

Considering S670-1-350 requires less energy and time to produce, it is considered to be the optimal structure. Based on the comparison of a Ni foam (500 m^{2}.g^{-1}, 1.7mm thickness, 94%) with a thickness approximately twice that of S670-1-350, the normalized electrochemical active surface area (C.m^{-3}) of S670-1-350 is 312 times higher than the Ni foam (as shown in Fig.4-46a). In spite of its large surface area, S670-1-350 also shows superior performance compared to Ni foam, indicating that the structure does not hinder mass transport.

As shown in Fig.4-46b, we evaluated the mechanical stability of the S670-1-35 sample using a stability test that ran for 6 days (144 hours) at 3 different current densities (10, 50, and 500 mA.cm^{-2}). The continuous lines on the galvanostatic plot represent 10 and 50 mA.cm^{-2}, while the dots represent 500 mA.cm^{-2}. A description of the experiment and the reasons for the dot plot are in Fig.S17.

S670-1-35 exhibits high mechanical stability at both low and high current densities, despite having a performance and specific surface area that are much higher than Ni foam. This high mechanical stability is likely due to the 3D structure of the Ni-whiskers, which consists of long and thin fibers of Raney Ni surrounded by electrolyte, with the distance between the fibers in the micrometer range. This structure facilitates the movement of ions and electrolytes between the fibers, as well as bubble escape, reducing the probability of structural damage caused by trapped bubbles [64, 65].

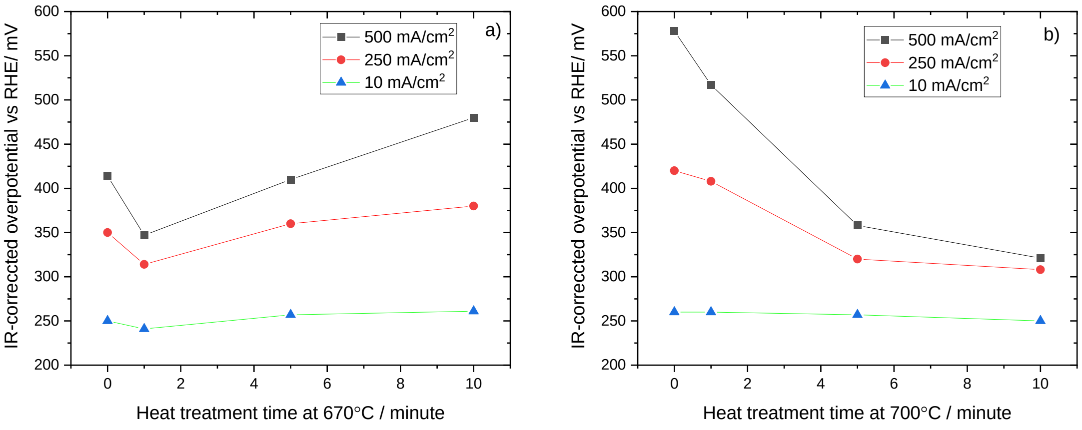

Figure 4-45: Variation of the OER overpotential with respect the time elapsed at the maximum heat treatment temperature. The mass of Al was 350 mg in each case and the maximum heat treatment temperature was either *a)* 670 or *b)* 700 °C.

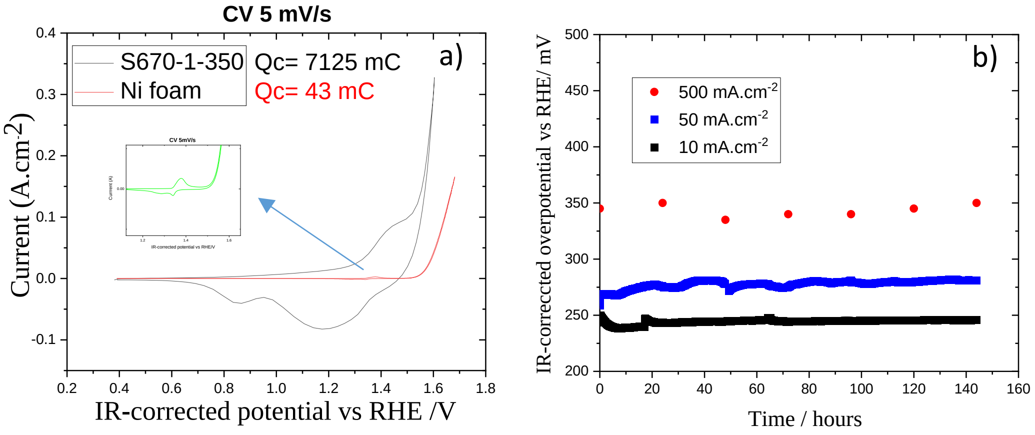

Figure 4-46: a) Cyclic voltammograms (5 mV/s) for S670-1-35 and a Ni foam (500 m^2.g^{-1}, 1.7mm thickness, porosity 94%). b) Recorded galvanostatic at 10, 50 and 500 mA.cm^{-2} for 6 days (144 hours) for S670-1-35 in 1M KOH.

Based on Table 4-10 and 4-11, Ni-whiskers outperform many catalysts in terms of both OER performance and mechanical stability. The information is also particularly helpful when selecting a catalyst to be synthesized on the surface of Ni-whiskers.

Table 4-10: The table compares OER overpotential for various high-performance catalysts in 1M KOH electrolyte at a current density of 10 mA.cm^{-2}.

Material	Overpotential (mV)	References	Material	Overpotential (mV)	References
NiO/NF	310	[242]	Fe-NiO	310	[243]
Fe-NiO/NF	206	[244]	$NiCoO_2$ nanowires	303	[245]
NiFeO	300	[246]	$MnO_2/NiCo_2O_4$	340	[247]
$NiO/NiFe_2O_4$	302	[248]	Ni_3Fe	248	[249]
Boron-doped NiFe	350	[250]	NiFe	257	[251]
Ni-Fe-LDHs	290	[210]	Ni-Fe-LDHs	210	[252]
Ni_2P	290	[211]	Fe-NiP/NF	192	[253]
Co_3O_4 nanostructure	356	[254]	Co_3O_4 nanosheet	330	[255]
$CoWO_4$	389	[256]	CoFeP	267	[257]
Mn_2O_3	427	[258]	$Ni-Mn_3O_4$	283	[259]

Table 4-11: The table compares mechanical stability as well as OER overpotential for several high-performance catalysts in a 1M KOH electrolyte at high current density.

Material	Current density	OER overpotential	Stability (h)	References
WCoFe$_{0.3}$-Carbon nanoflakes	20	270	100	[260]
NiCoP-NiCoSe$_2$	24	330	80	[261]
Gelled FeCoWOOH	30	200	550	[262]
NiCo LDH nanowire on Ni foam	50	300	24	[263]
Ni$_{50}$Fe$_{50}$	100	300	72	[264]
NiFe NTA	100	238	20	[265]
Fe$_2$O$_3$@Cuo on Ni foam	100	398	15	[266]
N-NiVFeP	100	450	100	[267]
N, Fe-NiSe	100	267	100	[268]
(Ni,Fe)OOH on Ni foam	500	260	42	[269]
NiFeOOH on Ni foam	500	280	10	[270]
Fe-CoP on Ni foam	500	295	30	[271]

Co-MoF	500	490	120	[272]
Fe(PO$_3$)$_2$/Ni$_2$P on Ni foam	500	273	20	[273]
NiFeOOH on porous Ni mesh	500	290	32	[274]

4.3.9. The effect of aging process on OER overpotential

In this section, we discuss the oxidation peaks of Ni whiskers and the aging process of the structure. More detailed information can be found in Section 2.11.2. Additionally, the experiments are explained in Section 4.2.8.

The cyclic voltammograms at 5 mV.s^{-1} for S1 is seen in Fig.4-47a. The oxidation peak of Ni(OH)$_2$/NiOOH redox can be seen in the anodic region of the S1 sample at potential 1.4 V. Cathodic region of the S1 shows two peaks, the first at 1.2 V, caused by the reduction of β-NiOOH into β-Ni(OH)$_2$, and the second at 0.9 V caused by reducing the γ- NiOOH into α-Ni(OH)$_2$ [207].

However, α-Ni(OH)$_2$ is not stable in the presence of water, and all the α-Ni(OH)$_2$ chemically transforms to β-Ni(OH)$_2$ through the aging process. Aging can be achieved by keeping α-Ni(OH)$_2$ in the water for enough time or induced by cyclic voltammetry after performing enough cycles. Furthermore, increasing the temperature of the liquid surrounding the electrode accelerates the transformation process [208].

The S1 sample oxidized by CV was immersed at 70℃ in 0.1 KOH solution for 20 minutes to accelerate the aging process (to obtain S1-A). As seen in Fig.4-47a, the reduction peak of γ-NiOOH disappears after aging. This indicates that the transformation has been completed. The cathodic charge for S1 decreases from 7.1 to 6.2 C.cm^{-2} after the transformation is completed. The changes in cathodic charge for other samples can be seen in Fig.4-47b. This decrease is attributed to the lower capacity of β-Ni(OH)$_2$ compared to α-Ni(OH)$_2$ [208].

Previous studies have reported that the OER activity of β-Ni(OH)$_2$ is higher than that of α-Ni(OH)$_2$ [208]. However, the increase in OER activity for Ni-whiskers of S0-S10 is negligible. There is evidence that the increased OER activity observed with aging in KOH is not due to the transition of γ-NiOOH to β-NiOOH, but rather, it is due to Fe impurities present in KOH electrolytes which readily incorporate into NiOOH films [209]. In our experiments, we used a high-purity KOH solution to minimize Fe incorporation into the NiOOH structure, resulting in no changes in OER activity at low and high current densities.

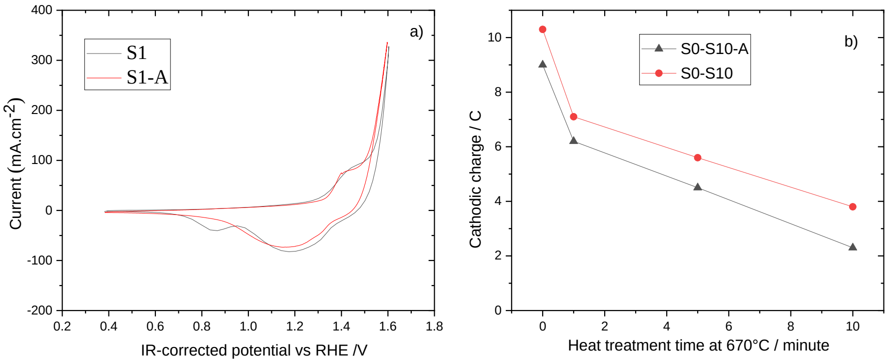

Figure 4-47: Cyclic voltammograms at 5 mV/s between 0.4 and 1.6 V vs. RHE for S1 and S1-A.

4.3.10. Production of Ni whisker on the surface of Ni foam

This section describes the creation of Raney Ni foam by the production of Raney Ni structures on the surface of Ni foam. The Raney Ni foam was then compared to Ni-whiskers. Even though some research has been conducted on Raney Ni foam and Raney Ni mesh [80, 275], it has been focused only on HER, and no information is available on the electrochemical active surface area of Raney Ni foam. To address this gap, the electrochemical active surface area and OER performance of Raney Ni foam were compared to Ni-whiskers.

According to Section 4.3.1, three distinct Raney Ni morphologies were generated, including whiskers, a coarse structure produced by leaching primary Al_3Ni, and D1 or D2 layers. This section of the thesis focuses on the formation of these various Raney Ni morphologies on Ni foam.

Fig.4-48a and 4-48b show SEM images of the Ni Foam utilized in the experiments, which has a thickness of 1.7mm and a surface area of 500 $m^2.g^{-1}$. X-ray diffraction patterns of the Ni foam in Fig.4-48c also show intense peaks, indicating a polycrystalline structure of Ni.

In accordance with our previous findings, N670-1-150 and N670-0-150 samples were initially manufactured at 670°C and then leached in 3M KOH. As a result of the leaching process, both samples disintegrated, indicating that the Ni foam grid was dissolved by the molten Al during heat treatment. Thus, the heat treatment temperature and time were reduced to minimum values (0-

minute heat treatment time and 660 °C, which is the melting point of Al) resulting in samples N660-0-150, N660-0-250, and N660-0-350.

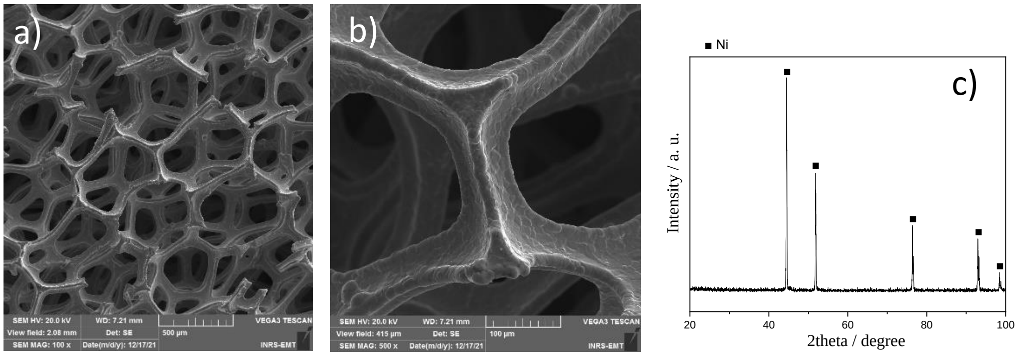

Figure 4-48: a,b) SEM images of Ni foam at two different magnification and c) X-ray diffraction of Ni foam.

The samples were analyzed through SEM after the leaching process. Fig.4-49 shows the surface of the samples and reveals two distinct areas, designated Area 1 and Area 2.

Area 1, which resembles samples produced in Section 4.3.1, exhibits two distinct structures, whiskers and coarse structures. Like the samples in section 4.3.1, this structure is believed to have been formed through leaching a hypereutectic microstructure. The whiskers in this area appear intertwined and have not grown perpendicular to the surface. This area's formation can be attributed to the complete dissolution of Ni foam grids in molten Al during heat treatment, resulting in the formation of a hypereutectic alloy.

Alternatively, Area 2 displays Ni whiskers forming on the surface of the Ni foam grid. Area 2 is further magnified in Fig.4-50, revealing Ni whiskers (Fig.4-50b) and a D2 layer underneath them (Fig.4-50c). Although all grids do not appear to have whiskers, a D2 layer appears to have developed on their surfaces. Area 2 does not exhibit coarse structure, suggesting the heat treatment process formed Eutectic or Hypoeutectic microstructures on the grid surface instead.

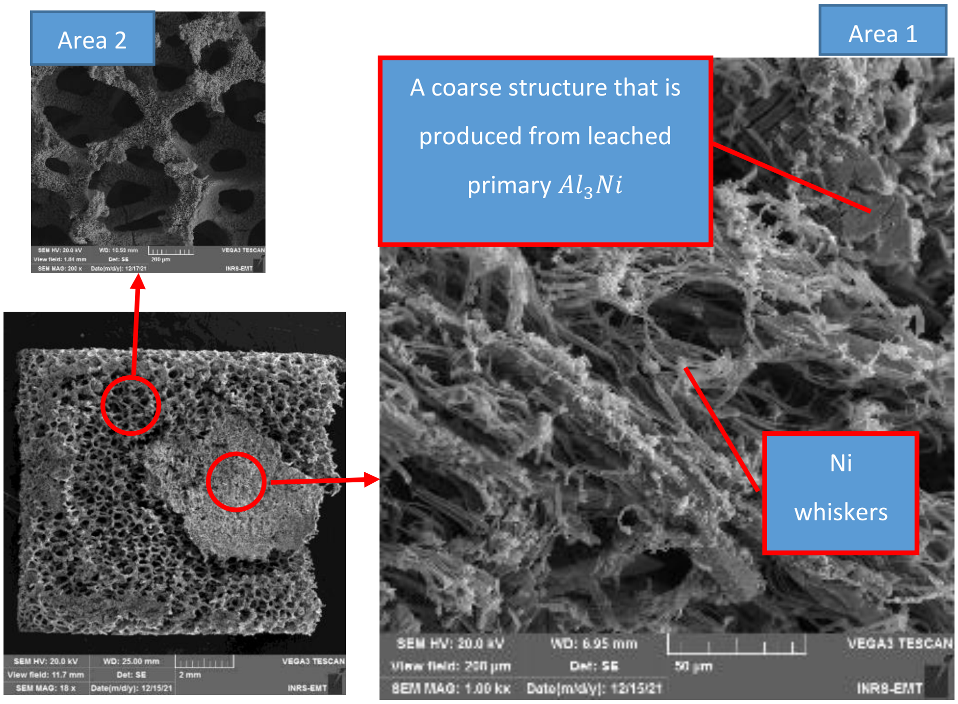

Figure 4-49: SEM images of N660-0-350 after leaching.

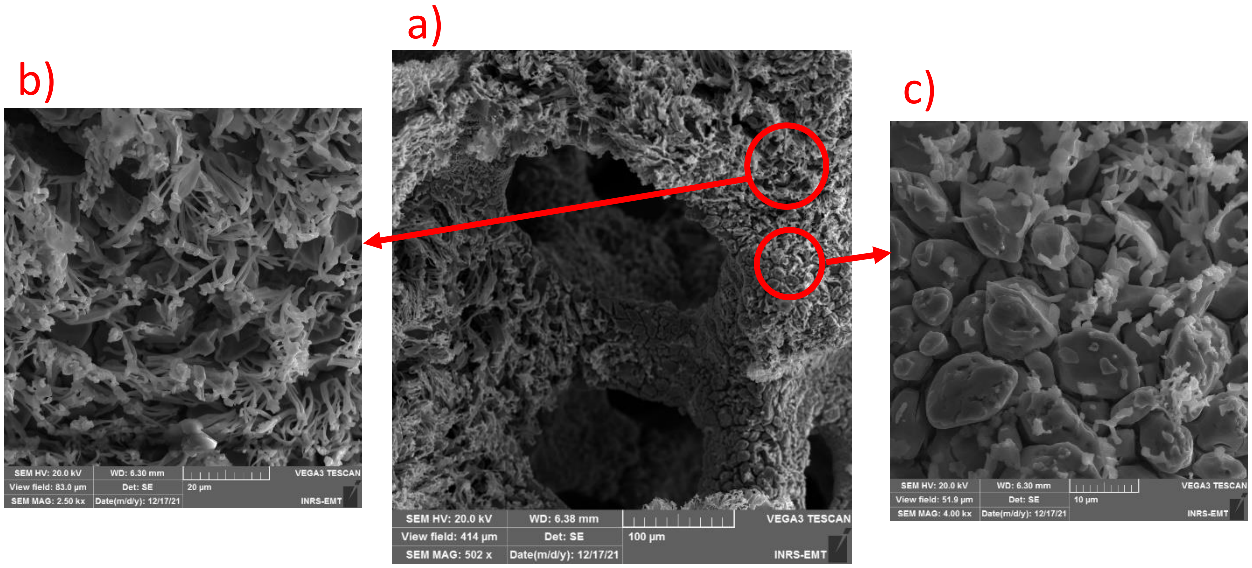

Figure 4-50: SEM images of N660-0-350 for Area 2 at higher magnifications.

Fig.4-51a presents the EDX mapping result, revealing that the chemical composition of the samples is Ni-8 at. % Al. In addition, the XRD pattern of the samples, shown in Fig.4-51b, is similar to that obtained in Section 4.3.1. These results indicate that Raney Ni structures (at least one of their morphologies) have formed on all Ni grids, suggesting the samples are Raney Ni foams.

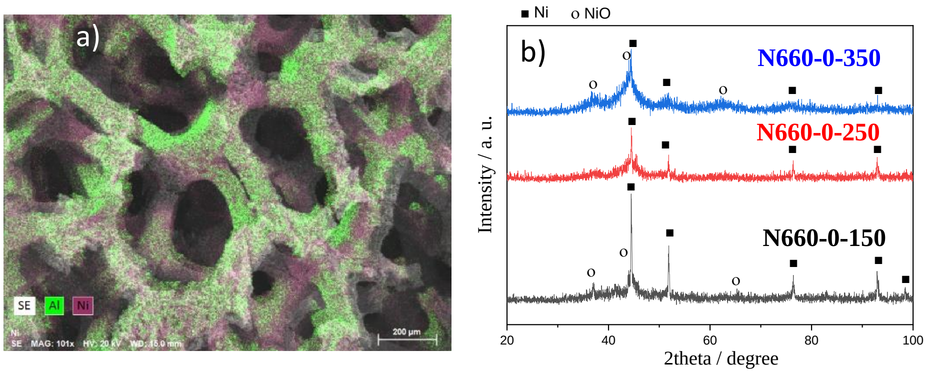

Figure 4-51: EDX mapping of N660-0-350 and, XRD patterns of all samples after leaching.

Al mass has two distinct effects on the structure of samples. The first effect is on the number of Ni whiskers observed in Area 2, and the second is on the surface area of Area 1.

For N660-0-150, N660-0-250, and N660-0-350, 3%, 12%, and 22% of the total surface area are covered by Area 1 respectively, indicating that increasing Al mass results in increased Area 1. Notably, Area 1 decreases the mechanical stability of Ni foam. The N660-0-350 sample disintegrated twice during transportation, while the other samples remained intact. Despite this, N660-0-350 did not disintegrate during the electrochemical test.

Fig.4-52 illustrates the effect of Al mass on Ni whiskers numbers in Area 2. It shows that an increase in Al mass results in the formation of more Ni whiskers on the surface of Ni foam grids.

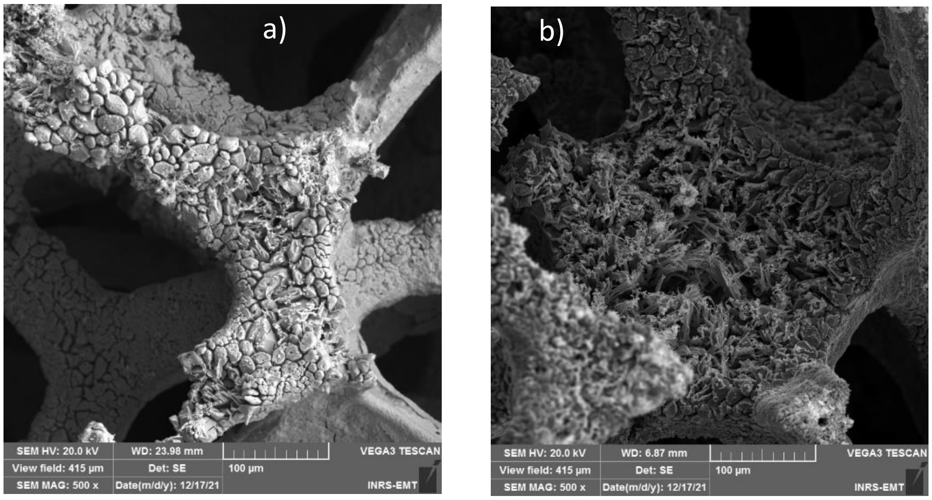

Figure 4-52: SEM images of samples after leaching. a) N660-0-150 and b) N660-0-350.

Electrochemical tests were then conducted on the samples. Fig.4-53 shows the cathodic charge and double layer capacitance for Ni foam and Raney Ni foam, where Ni foam is represented by zero mg Al. In comparison with Ni foam, Raney Ni foam produced by 150-350 mg Al has a significantly higher cathodic charge and double layer capacitance and can significantly decrease OER overpotential. According to galvanostatic oxidation tests, Ni foam needs an overpotential of 300 mV to deliver 10 mA.cm^{-2}, but Raney Ni foam only needs 250 mV.

By increasing Al mass, more Ni whiskers form on the sample, resulting in a higher cathodic charge and double layer capacitance. In turn, this leads to a lower OER overpotential at high current densities. As a result of the higher mass of Al used during the manufacturing of the N660-0-250 sample, it shows better OER performance than the N660-0-150 sample (Fig.4-54).

Despite having a greater number of Ni whiskers on its grids compared to N660-0-250, N660-0-350 had almost identical cathodic charge, capacitance, and overpotential. It may be due to Area 1, which destroys Ni foam grids to produce interwoven fibers. Thus, N660-0-250 was found to be the best sample both in terms of OER and mechanical stability.

Despite exposing a 1cm x 1cm section of Raney Ni foams with a thickness of 1.7 mm to the electrolyte for an electrochemical test, they cannot outperform S670-1-350 with a thickness of 0.9 mm. S670-1-350 exhibits a cathodic charge of 7.2 C, twice that of N660-0-250. Moreover, the

OER overpotential of S670-1-350 is significantly lower than that of N660-0-250 at high current densities.

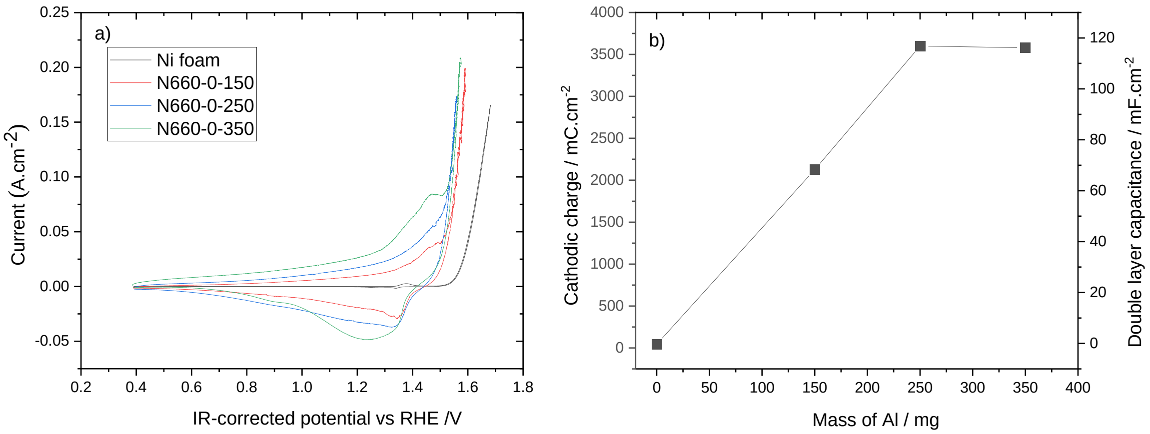

Figure 4-53: Effect of Al mass on electrochemical characteristics of N660-0-150, N660-0-250 and N660-0-350. a) Cyclic voltammograms (5 mV/s) for all samples. b) Cathodic charge and Double layer capacitance for all samples.

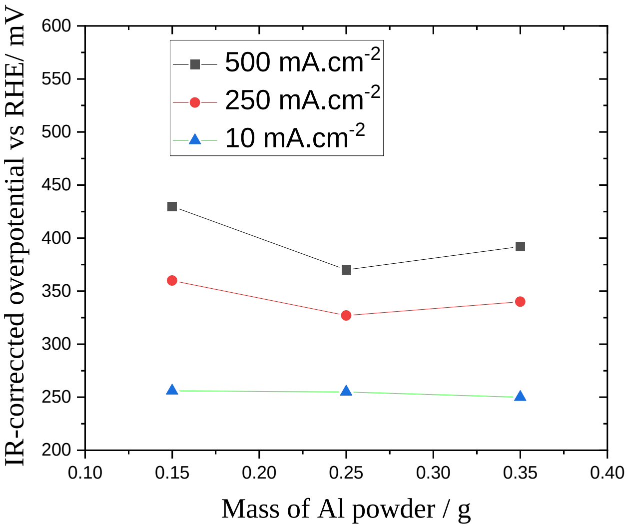

Figure 4-54: The relationship between OER overpotential and mass of Al powder in 1M KOH for N660-0-150, N660-0-250 and N660-0-350 samples. A galvanostatic test for 15 minutes was performed and potential was acquired after 15 minutes.

This chapter introduced and contrasted Ni-whiskers with two other nickel-based structures, specifically Ni foam and Raney Ni foam. Notably, Ni-whiskers exhibit an impressively low OER overpotential of 250 mV to achieve a current density of 10 mA.cm^{-2}. It is crucial to acknowledge that directly comparing the OER activity of Ni-whiskers with other catalysts may be misleading, as the low overpotential of Ni-whiskers is attributed to an exceptionally high electrochemical active surface area (ECSA). Drawing from the information in Chapter 2, the only structures available for comparison with Ni-whiskers are Ni foam and Raney Ni foam. Since there was no existing data on cathodic charge and OER activity to compare Ni-whiskers with Ni foam and Raney Ni foam, both structures were manufactured, and a comprehensive comparison was conducted. Ni-whiskers demonstrated superior performance in terms of effective surface area and OER efficiency.

To produce Ni whiskers with dimensions of 1000mm×1000mm×1mm, a Ni-Al molten eutectic alloy containing 85wt.% Al is required. The composition of the alloy includes 3.1kg of aluminum (priced at US$ 2240 per ton), 0.55kg of nickel (priced at US$ 16630 per ton), and 7kg of sodium hydroxide (priced at US$ 560 per ton). The heat treatment process, which takes only a few minutes, incurs negligible costs compared to the material expenses. Consequently, the primary manufacturing cost is estimated at 19 US dollars. It is noteworthy that Ni foam is available for purchase at varying prices, ranging from US$ 20 per square meter to over US$ 500 per square meter [276, 277, 278].

4.4. Conclusion

Inspired by Ni-Al eutectic alloy and directional solidification, we created an innovative 3D skeleton structure of nickel (Ni whiskers). This structure consists of a vast number of Ni whiskers, which have an exceptionally high electrochemical active surface area. In order to produce these Ni whiskers, we first melted Al onto the surface of Ni in order to create a hypereutectic alloy of Ni-Al. In subsequent steps, this alloy underwent directional solidification and was leached.

SEM, EDX, and XRD analyses confirmed that the Ni whiskers are indeed Raney Ni whiskers.

Brunauer Emmett Teller (BET) analysis revealed that Ni whiskers are nanopores with an average pore size of around 6 nm.

TEM and SEM analyses revealed that Ni whiskers have a thickness of a few hundred nanometers and a distinct crystallographic orientation, distinguishing them from polycrystalline Raney Ni. In addition, the results indicated that the ligament size of the Ni whiskers is approximately 5 nm.

The density (number per cm^{-2}) and distribution of Ni whiskers, which determine the total surface area of Ni-whiskers, are directly proportional to the total surface area of Al_3Ni fibers. Parameters that affect the total surface area of Al_3Ni in α-Al include: (1) volume of solidified structure, (2) Al_3Ni fiber distribution, and (3) Al_3Ni volume fraction. These three variables can be altered by changing Al mass and heat treatment process.

By increasing the mass of Al, double layer capacitance and cathodic charge increase, reducing overpotential at all measured current densities.

As the elapsed time at the maximum temperature (heat treatment time) increases, coarser Ni whiskers are produced. This leads to a decrease in the density of Ni whiskers, an increase in the distance between Ni whiskers, and a reduction in the cathodic charge.

On the other hand, increased maximum temperature increases Ni content in the molten alloy, which results in a greater density of Ni whiskers, which results in a smaller distance between Ni whiskers and an increase in cathodic charge.

Initially, an increase in cathodic charge reduces the overpotential required for oxygen evolution reactions (OERs) at high current densities. However, for Ni whiskers with too much density, this increase in cathodic charge can cause a subsequent increase in the overpotential required for the OER. The reason for this phenomenon is the existence of trapped bubbles within the Ni whiskers structure, which hinder mass transport. Therefore, it is imperative to adjust the distance between Ni whiskers to facilitate effective mass transport and avoid hindering OERs.

The optimal sample was produced at 670°C and a heat treatment time of 1 minute, requiring overpotentials of 245 mV and 345 mV to deliver 10 $mA.cm^{-2}$ and 50 $mA.cm^{-2}$, respectively. The low overpotential is believed to be caused by the very high electrochemical surface area, not by the incorporation of Fe, since adding 10 ppm $FeCl_2$ to the electrolyte led to significant reductions in overpotential.

These whiskers are also highly mechanically stable, as shown by galvanostatic experiments conducted over six days at a current density of 500 $mA.cm^{-2}$.

5 SYNTHESIZE OF CATALYST ON NI WHISKERS

5.1. Introduction

In the previous chapter, pore sizes were optimized for the lowest OER overpotentials so that the best sample (S670-1-350) needed an overpotential of 250 and 350 mV to deliver a current density of 10 and 500 mA.cm^{-2}, respectively.

In this chapter, the focus is on further reducing OER overpotentials for Ni-whiskers by synthesizing Ir oxide and Ni-Fe LDH, two highly active catalysts, onto Ni-whiskers.

The initial catalyst chosen is Iridium oxide, recognized as one of the most active OER catalysts in alkaline media [27]. Despite its high OER activity, its application is constrained in alkaline media due to two key factors: the substantial cost and rarity of iridium, and the exploration of alternative cost-effective catalysts for alkaline media. However, researchers frequently benchmark their catalysts against Iridium oxide, especially commercial IrO_2 electrodes [279, 280, 281]. The reported OER overpotential of commercial Ir oxide at 10 mA.cm^{-2} is 350 mV [279]. This value is notably higher than the OER overpotential of Ni-whiskers at 10 mA·cm^{-2}, which is 250 mV. This discrepancy is attributed to the low electrochemical active surface area (ECSA) of commercial Ir catalysts compared to Ni-whiskers, limiting the rate of reaction. When the ECSA of Ir oxide is sufficiently high, the OER overpotential at 10 mA.cm^{-2} decreases to 197 mV [98]. Therefore, in this case, instead of utilizing a commercial Ir electrode, Ir oxide is synthesized on the surface of Ni-whiskers to offer a significantly higher ECSA for comparison with Ni-whiskers or other catalysts synthesized on Ni-whiskers.

The second is Ni-Fe hydroxide, also widely recognized as a highly active and cost-effective catalyst. Some researchers claim that NiFe-based layered hydroxides are the most active OER catalysts in alkaline media. This is probably the reason NiFe-based layered hydroxides are the catalysts of choice for industrial water electrolysis [106, 107]. Given that Ni-whiskers provide a higher effective surface area than Ni foam, Ni-Fe is synthesized on Ni-whiskers to explore the possibility of reducing OER overpotential at high current densities compared to other references.

Besides considering the activation OER overpotential of each catalyst, it is also essential to consider how to synthesize the catalyst on Ni-whiskers in order to facilitate the mass transport.

Various methods, such as the cation exchange process [96], electrochemical deposition [282], Adams fusion method [283], Colloidal protocol [284], Sulfite complex route [285], Vapor deposition processes [286, 287], and Thermal decomposition [288] are available to prepare Ir oxide for oxygen evolution. Among the processes, the cation exchange process and electrochemical deposition have been studied to deposit Ir on the surface of the 3D structures of Ni [96, 289]. Nonetheless, it has been reported that porous Ir with high OER activity can be easily formed on the surface of Ni structures by the cation exchange process [96].

In the cation exchange process, Ni^{+2} on the surface of Ni is substituted with Ir^{2+}, which is one of the most cathodic metals (a noble metal). As a result, iridium is deposited onto nickel spontaneously [96]. Therefore, the process is a simple and low-cost method to deposit Ir on the surface of Ni.

There are numerous studies on Ni-Fe hydroxide for oxygen evolution in alkaline media, and many different structures and morphologies of Ni-Fe hydroxides have been developed as OER catalysts [101, 108]. In general, Ni-Fe hydroxide can be synthesized using three methods: 1- Fe doping by immersion of Ni electrodes in acid solution + Fe salt (such as $HCl+FeCl_3$) [102, 103, 105], 2- Fe doping by cyclic voltammetry after enough cycling of Ni electrodes in alkaline solution + Fe salt (such as $KOH+FeCl_2$) [104, 216], and 3- Co-electrodeposition of Ni and Fe [106, 214, 215].

However, several studies have reported that Fe-doped Ni hydroxide generated by immersing Ni electrodes in the acidic solution or cycling Ni electrodes in the alkaline solution has a higher OER activity [101, 102, 109]. Q. Zhou and his co-workers reported that Fe-doped $Ni(OH)_2$ nanosheets have higher activity than Ni-Fe LDH produced by coelectrodeposition [102]. The results of M.B. Stevens also revealed the same results. They reported that for Fe doped-Ni hydroxide, Fe is adsorbed on the defects and edges; therefore, a higher OER active area is formed in comparison with Ni-Fe LDH produced by co-electrodeposition [101]. Doping Fe into $Ni(OH)_2$ is a well-known process to create highly active sites. Ni-Fe hydroxide is formed by first adsorbing Fe ions onto Ni hydroxide and then incorporating them into the lattice to produce Ni-Fe hydroxide [101, 102, 109].

Another factor affecting the Ni-Fe catalyst OER activity is the Fe content. C. Wang et al. claimed that the OER activity increases by increasing the Fe content in $Ni_xFe_{(1-x)}(OH)_2$. However, excessive Fe content results in a significant amount of FeOOH, which is nearly electrochemically inert for the OER and causes the overpotential to rise again [103]. Zhou, Q et al. [102] reported that $Ni_{0.83}Fe_{0.17}(OH)_2$ and C. Wang et al. [103] reported that $Ni_{0.75}Fe_{0.25}$ has the highest OER activity among $Ni_xFe_{(1-x)}(OH)_2$ catalysts. In this study, we demonstrate that sufficient Fe to achieve high OER activity can be doped only by immersing the Ni-whiskers in KOH + $FeCl_2$.

Here, Ni-whiskers are studied for activation and mass transport overpotentials at low and high current densities before and after the Ni-Fe LDH and Ir oxides synthesis. The activation overpotential should be measured at low current densities, whereas the impact of mass transport can be observed at high current densities. The researchers measure the onset of OER for catalysts with small active surface areas to study the activation overpotential. Under high current density (200-500 mA.cm^{-2}), the mass transport becomes a bottleneck of electrochemical reaction kinetics [23, 26]. We evaluate the OER activity at 50 mA.cm^{-2}, particularly at 10 mA. cm^{-2} for the activation overpotential, and at 250 and 500 mA.cm^{-2} for the mass transport overpotential. It should be noted that since IR-corrected overpotentials are calculated, the effect of ohmic overpotential can be ignored.

5.2. Experimental

In accordance with Section 4.2.1, we generated S670-1-350 samples. However, to simplify the nomenclature of the samples, we renamed it S1, as shown in Table 5-1.

The samples were immersed in 0.001M K_2IrCl_6 + 0.01M HCl precursor solution for the duration specified in Table 5-2 to deposit iridium on the surface of Ni fibers. The samples are named based on the used sample's name in Table 5-1 and the immersion time.

Table 5-1: Parameters of heat-treatment protocol

Sample Name	Maximum Heat-Treatment Temperature (℃)	Time at Maximum Heat-Treatment Temperature (min)	Mass of Aluminum Deposited on Substrate Surface (mg)
S1	670	1	350

Table 5-2: Name and used parameters for Ir-deposited samples.

Sample Name	Immersion Time / Minute
S1-2Ir	2
S1-5Ir	5
S1-12Ir	12
S1-20Ir	20
Ni foam-12Ir	12

To investigate the synthesis of Ni-Fe hydroxide whiskers, we followed a two-step process involving cyclic voltammograms (CVs) and immersion. The cyclic voltammograms (CVs) in 1M KOH, between 0.4 and 1.8 V vs. RHE at 50 mV s^{-1} and 5 mV s^{-1} were performed three times to convert the Ni whiskers of S1 samples into $Ni(OH)_2$. The samples were next immersed in 80 mL of 0.1 M KOH or 0.1 M KOH+10 ppm $FeCl_2.4H_2O$ for 20 minutes while the solution was stirred at 70℃. Then, the samples were washed and kept in 100 mL of distilled water for one hour to remove any contamination from the depth of the 3D structure. The samples were renamed after the treatment as seen in Table 5-3.

Table 5-3: Name and used parameters for Fe doing.

Solution Type	Sample Name
0.1M KOH	S1-A
0.1M KOH+10 ppm $FeCl_2.4H_2O$	S1-Fe

Electrochemical experiments were carried out in the same manner as in Section 4.2.7. The sample surface morphology was characterized by scanning electron microscopy (JEOL, JSM-6300F), and the chemical composition was assessed by energy-dispersive X-ray spectroscopy (EDX) (VEGA3 TESCAN).

5.3. Result

We here aim to evaluate the optimization of the activation overpotential and mass transport overpotential of Ni-whiskers.

The scatter plot in Fig.5-1 illustrates how the OER overpotential of Ni-whiskers at 10 mA.cm^{-2} changes with increasing the electrochemical active surface area (cathodic charge). The overpotential decreases with the increase in the cathodic charge and reaches 250 mV. Further increases in the cathodic charge do not decrease the overpotential at 10 mA.cm^{-2}. Researchers claim the onset of OER for Ni(OH)$_2$ is 250 mV [216], equal to the OER overpotential of Ni-whiskers at 10 mA.cm^{-2}. Since the Ni-whiskers have a very high electrochemical active surface area, the onset of OER is the same as the OER at 10 mA.cm^{-2}. Fig.5-1 indicates that the only factor preventing the OER overpotentials from falling below 250 mV is the activation overpotential of the Ni-whiskers.

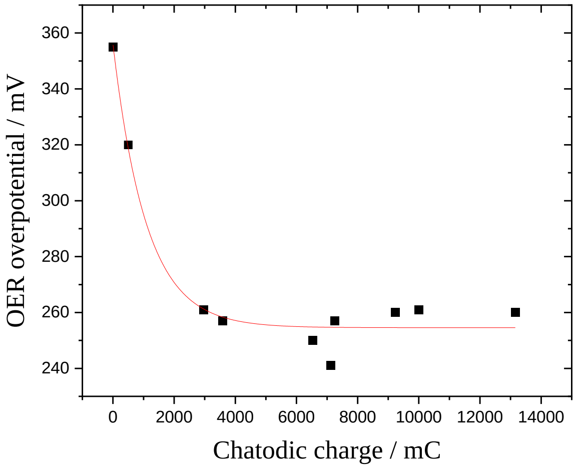

Figure 5-1: OER overpotentials in 1M KOH for a) Ni whiskers at 10 mA.cm-2 with different cathodic charge.

Next, two highly active catalysts (Ir oxide and NiFe) are synthesized on a 3D structure, and their effect on activation and mass transport is evaluated.

5.3.1. Effect of Ir Oxide Synthesis

The samples were analyzed after immersion in the solution using SEM and EDX analyses. SEM images for S1 and S1-20Ir in Fig.5-2 demonstrate that the majority of Ir prefers to precipitate in clusters on top of fibers and forms a non-continuous Ir coating on the surface. The Ni whiskers in Fig.5-2a are visible on top of the structure. However, as seen in Fig.5-2b, Ir is deposited over Ni whiskers after immersion, particularly at the top of the structure, preventing the Ni whiskers from being visible in the SEM images.

The mechanism of Ir formation consists of the dissolution of Ni in acidic media and the deposition of Ir according to the following equation [96, 97]:

$$[IrCl_6]^{2-} + 2Ni \rightleftarrows Ir + 2Ni^{2+} + 6Cl^{-} \qquad (47)$$

Ni is dissolved in the solution as Ni^{2+} and, Ir^{2+} are reduced on the surface of fibers [97]. As Fig.5-3 shows, the atomic percent of Ir deposited is 3.5 at. % after 2 hours of immersion. The atomic percent of Ir rises to more than 10 at. % after 20 hours of immersion.

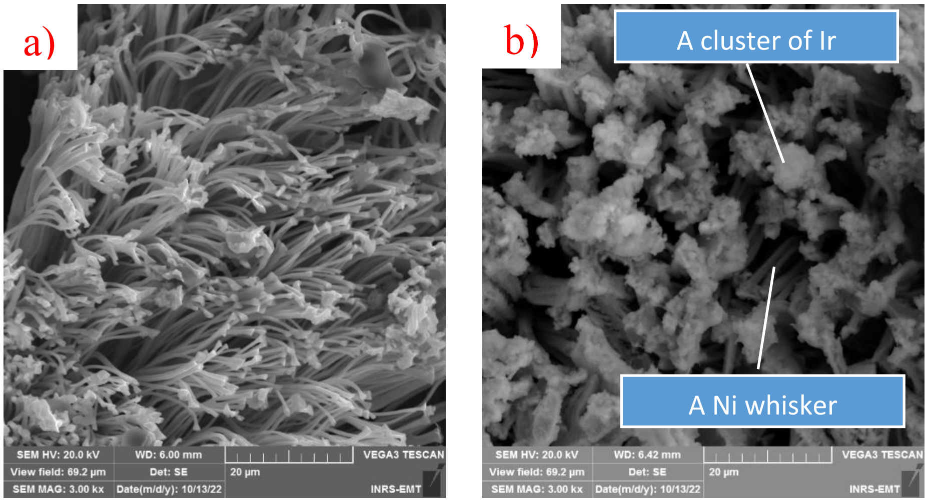

Figure 5-2: Top view SEM image of a) S1, b) S1-20Ir.

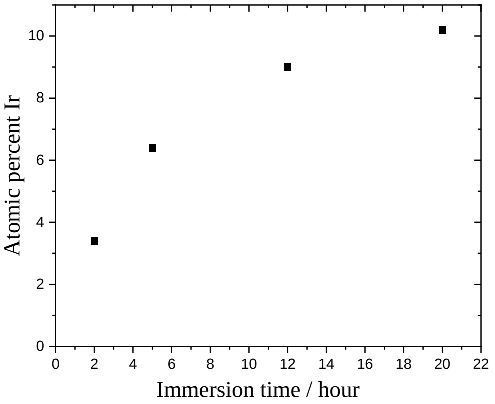

Figure 5-3: EDX analysis of S1-2Ir, S1-5Ir, S1-12Ir, and S1-20Ir. The figure depicts the effect of immersion time on atomic percent Ir.

The Ni whiskers of samples shown in Fig.5-3 were physically processed by scraping, crushing, and mixing with a scalpel. Then, the resulting mixture was subjected to EDX analysis. Based on the EDX results, S1-20Ir contains only about 1 at. % or 3.3 wt.% iridium. Other samples with lower immersion times have lower atomic percentages of Ir. Considering the mass of nickel whiskers in S1, which is about 0.45 mg, the deposited iridium mass of S1-20Ir is about 0.015 mg. Hence, the Ir loading is determined to be 0.015 mg.cm^{-2}, a value significantly lower than the typical Ir loading in the industry [290]. However, EDX analysis from the top of the structure reveals a value higher than several percent, up to 10 atomic percent, indicating the presence of a very thin layer of Ir on the surface of Ni whiskers. This indicates that most of the iridium is deposited on the top of the structure. While nickel may dissolve uniformly in the acid during the cation exchange process, most of the iridium precipitates in the upper region because $[IrCl_6]^{2-}$ ions are more likely to be present there.

As stated, a CV at a rate of 50 mV.s^{-1} was performed three times. During the CV acquisition process, some fibers detached from the Ni-Whiskers and settled at the bottom of the container. The number of fibers was negligible for S1-2Ir and S1-5Ir but significant for S1-20Ir. As shown in Fig.S18 (Appendix), more than half of the S1-20Ir fibers detach after performing CV at 50 mV.s^{-1}. The dissolution of Ni in the acidic media causes fibers detachment.

After performing CV at 50 mV.s^{-1}, the experiments were conducted in a fresh solution of 1M KOH. Fig.5-4 illustrates the cyclic voltammograms at 5 mV.s^{-1} for S1-A and S1-5Ir. Both samples exhibit a reduction and oxidation peak at the same potential, which belongs to the β-Ni(OH)$_2$/ β-NiOOH redox.

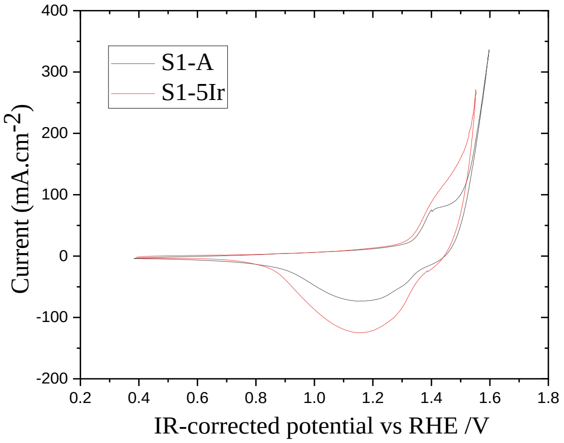

Figure 5-4: Cyclic voltammograms at 5 mV/s between 0.4 and 1.6 V vs. RHE for S1-A and S1-5Ir samples.

Based on the comparison of S1-A with S1-5Ir in Fig.5-4, we can conclude that Ir deposition significantly increases the cathodic charge and OER activity. The OER overpotential of S1-5Ir is around 200 mV at 10 mA.cm^{-2}, which is 50 mV lower than that of S1-A. The researchers reported that the onset of OER (at 1μA.cm^{-2}) for the Ir deposited on Ni foil using the cation exchange process is 200 mV [96], which is the same as the overpotential for Ir deposited on Ni whiskers at 10 mA.cm^{-2}. As stated before, this is due to the high effective surface area provided by the Ni whiskers. M. Hao has also reported an overpotential of around 200 mV for the Ir deposited on a Ni-DHBT structure [98].

The effect of different immersion times on the cathodic charge for S1-A sample is seen in Fig.5-5. The cathodic charge increases as the immersion time increases. However, some fibers are detached (while performing CV at 50 mV.s^{-1}) due to significant Ni dissolution after 12 hours and cause a decrease in the cathodic charge. The cathodic charge increases by two mechanisms depending on the atomic percentage of Ir: 1) Incorporating Ir into the Ni oxyhydroxide film alters the redox behavior of the Ni(OH)$_2$/NiOOH redox couple and 2) Surface roughening caused by Ni dissolution [96].

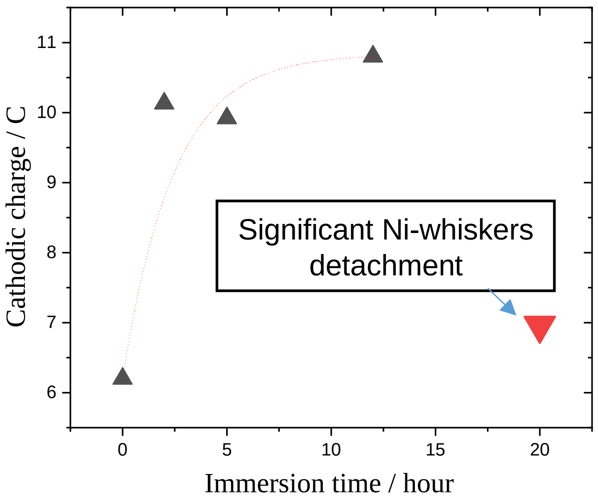

Figure 5-5: Effect of immersion time in 0.001M K_2IrCl_6 + 0.01M HCl precursor solution on cathodic charge for S1 sample.

In addition to the increase in the OER activity and cathodic charge of $Ni(OH)_2$/NiOOH redox, the researchers also used a cyclic voltammogram at a switching potential of 0-1 V to determine the presence of Ir. The reversible Ir (III)/Ir(IV) redox transitions occur at 0.4-0.8 V vs. RHE in an alkaline solution. Within this range, there are two broad redox peaks observed at 0.64 and 0.53 V, which correspond to the oxidation and reduction of Ir (III)/Ir(IV) redox transitions, respectively [96, 98, 291]. In addition, Ir deposition was reported to significantly increase the background currents of Ir (III)/Ir(IV) redox transition [96, 98]. CVs at a rate of 1 and 5 mv.s^{-1} at a switching potential of 0-1 V were recorded for samples with and without Ir deposition (Fig.5-6) to study the redox peaks. Fig.5-6 demonstrates that no oxidation and reduction peaks of Ir (III)/Ir(IV) redox are seen in the potential range of 0.4 to 0.8V. There is also no increase in the background current density of S1-12Ir at 0-1 V compared to S1-A. Redox peaks and increases in the background current density were not observed on other Ir-deposited samples.

There remains a question as to why EDX analysis and OER activity confirm the presence of Iridium but Ir (III)/Ir(IV) redox transitions cannot be observed. The reason is probably due to the atomic percentage of Ir, which is less than 1 at. %, as well as the supercapacitor properties of Ni-whiskers. As seen in Fig.3-9, S1 acts like a supercapacitor with a capacity of 124 μF.cm^{-2}. Thus, CV at 0-1 V is controlled by Ni-whiskers, preventing Ir from manifesting its Ir(III)/Ir(IV) redox peaks.

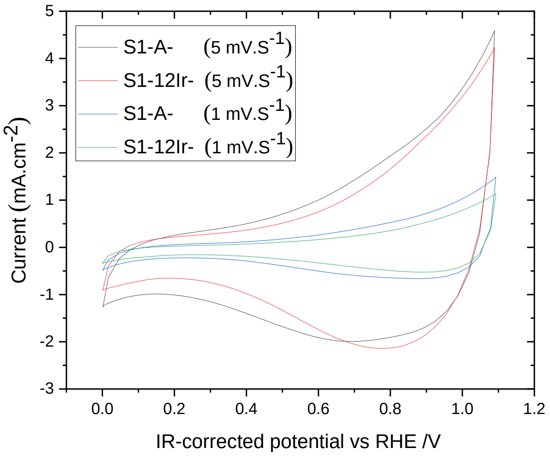

Figure 5-6: Cyclic voltammograms at 1 and 5 mV/s between 0 and 1 V vs. RHE for S1-A and S1-12Ir samples.

Fig.5-7 shows the effect of Ir deposition and Ni fiber detachment on the OER overpotential at 10, 50, 250, and 500 mA.cm^{-2} for S1-A sample at different immersion times. It should be mentioned that the zero-immersion time in the figure is the OER overpotential for S1-A. The results demonstrate that an increase in the immersion time reduces the overpotential at 10 mA.cm^{-2}. The OER overpotential for S1-12Ir significantly reduces, reaching 197 mV, which is comparable with the results of M. Hao et al. [98].

Ir deposition also positively impacts the OER overpotential at 50 mA.cm^{-2}. The overpotential at 50 mA.cm^{-2} for S1-5Ir and S1-12Ir is 255 mV, which is 15 mV less than S1-A. However, although Ir deposition has a positive effect on OER overpotential at low current density, the recorded overpotential at high current density (250 and 500 mA.cm^{-2}) is greater than S1-A. The rise in overpotential is attributed to two factors: the detachment of fibers and the formation of clusters of iridium that block the structure. These issues further limit mass transport at high current densities, causing the overpotential to increase at those levels [33, 99, 100].

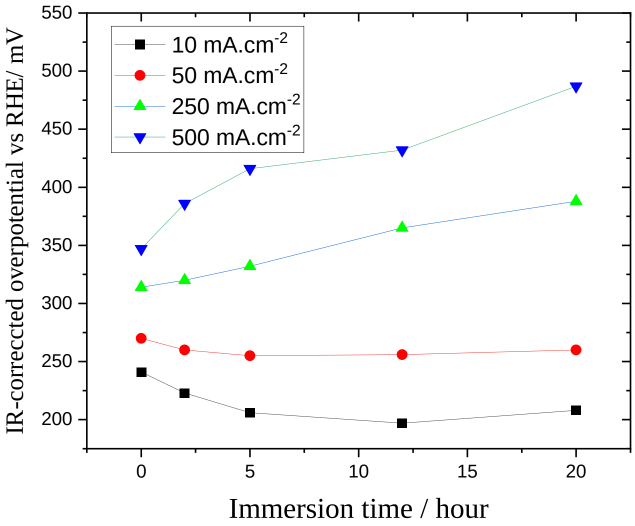

Figure 5-7: OER overpotential at 10, 50, 250, and 500 mA. cm^{-2} for the S1 sample at different immersion times in 0.001M K_2IrCl_6 + 0.01M HCl precursor solution.

To avoid fiber detachments, in the next step, catalyst synthesis on Ni-whiskers was performed in a basic media.

5.3.2. Ni-Fe Hydroxide Synthesis

The samples after Fe doping were analyzed using SEM and EDX analyses. Fig.5-8 shows that 3 at.% Fe is doped uniformly into Ni fibers without blocking the structure. Like the previous section, Ni-Fe whiskers were crushed, mixed and analyzed once more by the EDX analysis. It was found that the atomic percent Fe in the whole structure is 3 at.%, which means Fe is distributed equally throughout the structure in the upper and lower parts.

The incorporation of Fe into Ni hydroxide is a well-known phenomenon that produces the most active catalyst for OER in a basic solution. During the immersion of $Ni(OH)_2$, Fe^{+2} is first adsorbed on the surface of Ni whiskers and then incorporated with Ni hydroxide to form Ni-Fe hydroxide [101, 102, 103, 104, 105].

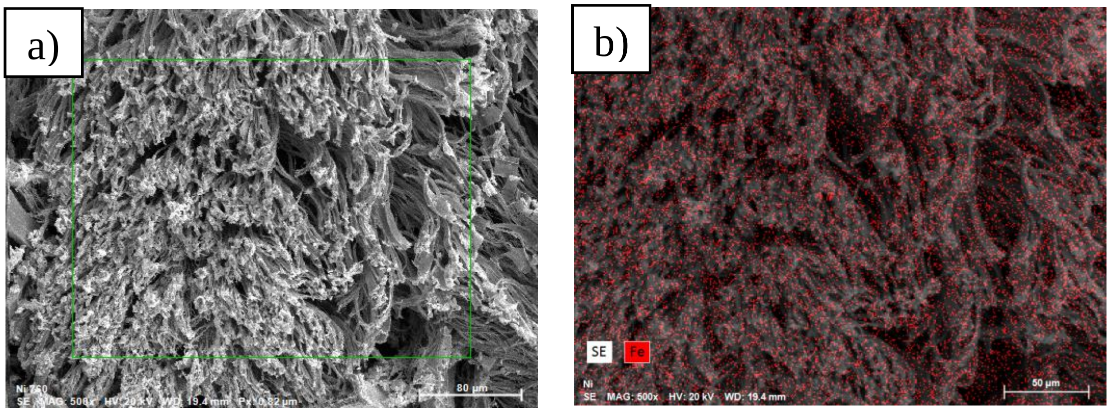

Figure 5-8: a) SEM analyses and b) EDX mapping of S1-Fe sample.

A comparison between S1-A and S1-Fe samples can be found in Fig.5-9. At potentials 1.4 V and 1.2 V, respectively, S1-A samples exhibit oxidation and reduction peaks due to the redox transition of β-Ni(OH)$_2$/ β-NiOOH. When Fe is added to the S1-A sample, the onset of the oxidation shifts to higher potentials. The cathodic region of S1-Fe shows two peaks. One peak is observed at 1.4 V, which belongs to β-Ni(OH)$_2$/ β-NiOOH redox transition, and another at 1.3 V, which is related to Ni-Fe hydroxide active sites. Similar observations have also been reported by other researchers [101, 103, 104, 216]. An increase in the reduction potential is associated with a change in the electronic structure, which can be used as a criterion to determine whether Fe has been incorporated [101].

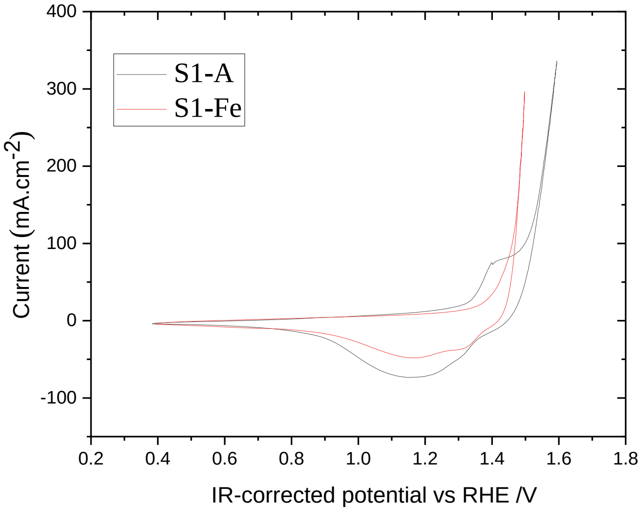

Figure 5-9: Cyclic voltammograms (5 mV.s^{-1}) for a) S10-A and S10-Fe, b) S5-A and S5-Fe, c) S1-A and S1-Fe and d) S0-A and S0-Fe.

Based on the oxidation and reduction curves for S1-A and S1-Fe samples, it is evident that the current density of oxidation or reduction redox decreases when Fe is incorporated. This can be observed in Fig.5-9, where the oxidation peak becomes significantly broader and more difficult to identify after Fe incorporation. Additionally, the current density for reduction (cathode charge) is reduced by 30% after Fe incorporation. M.B. Stevens et al. [101] explored the impact of Fe content on cathodic charge in Fe doped-$Ni(OH)_2$. The study's findings demonstrated that by increasing Fe content in the structure, the cathodic charge falls while OER activity improves and that the cathodic charge drops by 30% for samples with 25 at. % Fe doped [103]. It should be noted that the changes in the electronic structure of the co-electrodeposition of Ni-Fe hydroxide are different from Fe doped-$Ni(OH)_2$. Fe is homogeneously dispersed in the co-electrodeposition of the Ni-Fe hydroxide structure, which leads to changes in the electronic structure so that the cathodic charge for this structure rises as Fe is added [101].

The EDX mapping demonstrated that only 3 at. % Fe is doped into the structure. However, for the S1-Fe sample, the drop in the cathodic charge is 30%, indicating that the Fe/Ni ratio on the surface is greater than 3 at. % Fe. Most Fe is deposited on the surface of fibers, resulting in a high Fe content surface (possibly 25% Fe) [101]. Conclusively, the significant increase in OER activity and decrease in cathodic charge shows that a Ni hydroxide with high Fe content is formed on the surface of Ni fibers.

The addition of Fe to Ni hydroxide always enhances the OER activity, and there is no correlation between the cathodic charge and OER activity. The distinction is in the quantity of OER activities of different structures of NiFe hydroxide. Fe is adsorbed on the defects and edges of the Fe-doped structure; therefore, a higher OER active area is formed compared to Ni-Fe LDH produced by the co-electrodeposition [101]. In addition, Fe-doped Ni hydroxide has the advantage of a reduced cathodic charge since less energy is wasted during the electrochemical oxidation, which probably affects the efficiency when intermittent renewable energy is used to power the water electrolysis.

Fig.5-10 shows the OER overpotential at four current densities for S1-A and S1-Fe doped. Fe doping in S1 sample decreases OER overpotential at 10 $mA.cm^{-2}$ to 208 mV, which is comparable to Ir deposition samples. X.Li et al. claimed that the OER activity of NiFe is even higher than the benchmark Ir catalysts in the alkaline media [106]. Also, the Ni-Fe catalyst formation does not block or damage the structure of S1-Fe and causes S1-Fe to need significantly less OER overpotential at high current densities than the S1-Ir deposited.

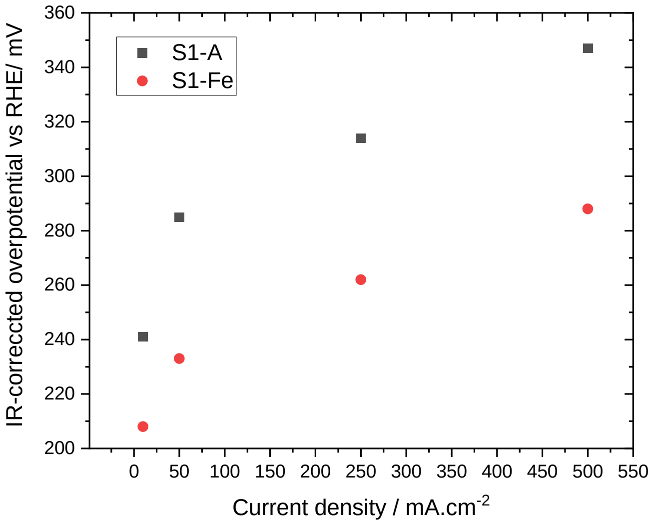

Figure 5-10: OER overpotential at 10, 50, 250, and 500 mA.cm-2 for S1-A and S1-Fe samples.

Ni-Fe LDH fibers in this study perform better than the other reported Ni-Fe LDH catalysts or 3D structures of Ni-Fe LDH at both low and high current density in 1 M KOH [101, 102, 103, 106, 107, 108, 109]. It is noteworthy that Ni whiskers contain 7 at.% Al. It has been suggested that aluminum has an additive effect on the OER activity of Ni-Fe LDH [109, 292].

When comparing the results with the literature, it is noteworthy that all the overpotentials in this study were recorded by galvanostatic polarization, after 30 minutes of polarization. Galvanostatic polarization is a more reliable analysis to record the overpotential for a 3D structure with a huge electrochemical active surface area.

5.4. Conclusion

A non-continuous coating of iridium is formed on the surface of Ni whiskers using the cation exchange process. The deposited Ir decreases the OER overpotential at low current densities but increases it at high current densities. The increased current density is due to the blockage structures caused by deposited Ir and the fiber detachment caused by Ni dissolution in acidic environments.

While the EDX, SEM analysis, and the increase in OER activity indicate that Ir is deposited and plays a role in oxygen evolution, no oxidation or reduction peak of Ir (III)/Ir(IV) redox was observed. This is due to the non-homogeneous distribution of Ir on the surface, as well as the very low mass of Ir. In other words, Ir is not formed on the surface of the whole fibers.

A simple immersion process is used to dope Fe into Ni whiskers. EDX and SEM analyses demonstrate that Fe is distributed evenly throughout the structure without blocking and detaching the fibers. Doping Fe shifts the oxidation and reduction peaks of the $Ni(OH)_2$/NiOOH redox anodically and reduces the background density. Additionally, adding Fe increases the OER activity significantly. Fe-doped Ni hydroxide performs almost equal to the Ir deposited samples at low current density while maintaining a high OER performance at high current density.

The new 3D skeleton of the Ni-Fe catalyst can be simply manufactured at a low cost on a large scale, giving it a high potential for industrial application.

6 PRODUCTION OF 3D SKELETHON ELECTRODE OF TITANIUM FOR PEM WATER ELECTROLYSIS

6.1. Introduction

Proton exchange membrane water electrolyzer (PEMWE) represents a promising technology for storing renewable energy through water electrolysis. Due to an acidic environment in PEMWE, currently, noble catalysts and corrosion-resistant materials are used as anodic-part components. Although using these materials increases the capital cost, the PEMWE has several advantages over other water electrolysis methods. The process has higher efficiency and lower hydrogen crossover rates than other processes. Also, the process has a fast dynamic response with high efficiency to intermittent renewable energies in partial load or overload mode [6, 9, 10, 11].

Despite the advantages of the process, the capital cost of PEMWE should be reduced and the efficiency of the PEMWE should be increased to make it economically viable for use on an industrial scale [13]. The energy inefficiency of PEMWEs is reflected in the presence of overpotential, which comes from three components: activation overpotential that overcomes the activation energy of the electrochemical reactions; the ohmic overpotential related to all the resistance in the system; and the mass transport overpotential related to the transport of reactants (water) and reaction products (hydrogen and oxygen) [293]. Studies are underway to develop catalysts [5, 294, 295] and optimize the compression of electrolyzer components [296] to reduce the activation and ohmic overpotential. Here, we focus on the mass transport overpotential by porous transport layer (PTL), which accounts for about 25% of the PEMWE overpotential. The PTL is an essential component sandwiched between the catalyst-coated membrane and the flow channel. They are responsible for transporting water and reaction products to and from the catalyst surface, as well as transferring electrons to the catalyst surface.

As the current density increases, oxygen bubbles accumulate in the pores and prevent water from reaching the active sites of the catalyst leading to increased mass transport overpotential. Therefore, it is very important to facilitate bubble removal and water delivery from and to the catalyst surface [10]. Additionally, PTLs should have a high electrical and thermal conductivity to reduce ohmic resistance and prevent membrane thermal damage.

The manufacturing parameters for PTL include material type, pore size, and porosity [34, 35, 36, 37, 38, 39]. While carbon materials can be used for the cathode part of PEMWE, state-of-the-art materials for the anode part are titanium due to its high anodic potential. Titanium has very high corrosion resistance in the anodic part of PEMWE, acceptable electrical and thermal conductivity, and high specific strength [40, 41, 42].

Increasing porosity by increasing the permeability of two phases (water and oxygen) increases the efficiency of PEMWE [10]. However, an increase in porosity increases oxygen gas saturation leading to a decrease in PEMWE efficiency [46, 185]. The findings indicate that the optimal range of porosity for the PTL is 50% to 75% [36, 43].

When the pore size increases, the distance between the two connections on the catalyst increases, leading to a decrease in efficiency due to the increase in ohmic resistance [35]. Over-reduction of pore size also reduces efficiency again by hindering the gas escape. For PTL produced by the powder metallurgy process, as the particle size decreases, the pore size decreases. In this technique, an optimal pore size of 10 microns has been reported, which is produced by particle sizes of 50-75 μm [16].

The PTLs are fabricated with different methods, including furnace-sintered metal powders, lithography, tape casting, and vacuum plasma spray [44, 45, 46]. Although lithography allows the creation of desired 3D structures, the process is significantly time-consuming and labor-intensive. Also, despite the benefits of furnace-sintered metal powders and tape-casting technologies, the sintering process in these approaches increases manufacturing time and costs [47]. Vacuum plasma spray (VPS) has been studied to remove the heat treatment step. In this process, the powders are melted and accelerated by a plasma jet and impact the substrate surface, producing a porous structure with metallurgical bonding. The protective environment of VPS minimizes the oxidation of melted powders [48]. However, due to the melting of the powders, the porosity value is limited to less than 30% [49].

To benefit from the advantages of VPS without powder melting, we investigate the production of PTL by Cold Gas Dynamic Spray (CGDS) [51] and Shock-Wave Induced Spraying (SWIS) processes [49]. In CGDS, the particles are accelerated in a supersonic gas to achieve high velocity before impacting the surface. One advantage of the process is that the particle temperature remains below the melting point, lowering the risk of powder microstructure change, or oxidation [51, 52, 53]. Since the particle temperature in this technique decreases significantly in the nozzle of CGDS, the particle velocity should be high enough to provide an adequately strong bond between particles. The particles are considerably deformed due to the high velocity, resulting in a reduction in porosity, which is why the porosity for CGDS coating is limited to 30% [51, 52, 53].

Shock-Wave Induced Spraying (SWIS) process is another method for producing porous coatings. This process displays advantages similar to both VPS and CGDS. The rapid opening and closing of a valve in this process generates a series of shock waves. The created shock waves travel through the spraying gun, accelerating and heating the powder already in the gun. The particles then impact the substrate like CGDS but at a higher particle impact temperature than the CGDS [50]. Consequently, adequate bond strength can be achieved at lower powder speeds than CGDS. As such, higher porosity for the SWIS process could be obtained in comparison to CGDS while keeping the advantages of CGDS [49].

Using a porogen and then removing it can increase the porosity of the coating in all the mentioned processes. The heat treatment or leaching processes are approaches that have been used to remove the porogen. J.Sun et al. created a porous cold spray coating with 49 % porosity by cold spraying a Ti+Mg mixture and then sintering it in a vacuum chamber at 1250°C to evaporate the Mg [54]. D. Qiu et al. also produced a porous cold spray coating with 48% porosity by cold spraying a mixture of Ti+Al and then removing the Al in a NaOH solution [55]. An advantage of the leaching process over the sintering is that it can be performed at room temperature, lowering the risk of oxidation and microstructure changes.

Here, we compare CGDS and SWIS processes to produce a porous coating. Also, aluminum and copper particles are used as porogen, which is ultimately removed using the leaching process.

6.2. Experiment

The experiment is described in six sections.

6.2.1. Material

Three different Ti powders with different particle sizes and two types of porogen, namely Cu and Al powders, were used throughout the present study. Ti powder particles had D50 values of 30 μm (AP&C, spherical, purity> 99.5%), 73 μm (Wah Chang, irregular), and 90 μm (Goodfellow, irregular, purity> 99.5%), while Al and Cu powders had D50 values of 83 μm (Metco 55, spherical, purity> 91%, 7 wt.% Si) and 70 μm (A357, spherical, purity> 99.3%). In the following, they will be referred to using their D50 values.

The deposition process was carried out on mild steel substrates (76.2 mm x 76.2 mm x 6.5 mm). Prior to deposition, the substrates underwent cleaning with ethanol and grit blasting with alumina.

6.2.2. Deposition techniques

Two deposition techniques were utilized to deposit powders onto the substrates. The Shock-Wave Induced Spray (SWIS) deposition system was supplied by Centerline Ltd. It utilized a stainless-steel tube nozzle (650 mm long with 5 mm internal diameter) connected to a divergent stainless steel tube coated with Inconel (5 mm inlet diameter, 6 mm outlet diameter, and 120 mm long). The second deposition technique was Cold Spray process (CGDS) (Kinetiks 4000 from CGT-GmbH, currently part of Impact-Innovations, Germany) with a SiC nozzle. Nitrogen gas was used as the carrier gas in both of these processes.

6.2.3. Deposition of Ti powder using SWIS technique

In the first set of experiments, three Ti powders of different sizes were deposited on the surface of mild steel substrates using the SWIS process to find the optimal size to maximize the porosity of the resulting coating. Table 6-1 shows the names of samples, whereas Table 6-2 provides the deposition parameters used for this first set of experiments.

6.2.4. Deposition of Ti+Cu mixture powder and leaching process

In a second series of experiments, Ti powder with D50 = 73 μm was blended with different weight percents of Cu powder (Table 6-1). Subsequently, this powder mixture was deposited on the surface of mild steel substrates, once using the SWIS process and a second time using the CGDS process. The deposition parameters of both processes are given in Table 6-2. In some cases, these samples were leached in 5M HNO_3 for one hour under stirring conditions to separate the coating from its substrate. The self-standing coating was then washed in boiling de-ionized water for one hour under stirring conditions.

Table 6-1: Powders used for the deposition.

Sample Name	Process Type	Ti particle, Particle Size D50 / µm	Porogen particle, Particle Size D50 / µm	Porogen content (wt.%)
Ti-30	SWIS	Ti, 30	---	---
Ti-73	SWIS	Ti, 73	---	---
Ti-90	SWIS	Ti, 90	---	---
Ti5Cu	SWIS	Ti, 73	Cu, 70	5
Ti30Cu	SWIS	Ti, 73	Cu, 70	30
Ti60Cu	SWIS	Ti, 73	Cu, 70	60
CTi5Cu	CGDS	Ti, 73	Cu, 70	5
CTi30Cu	CGDS	Ti, 73	Cu, 70	30
CTi60Cu	CGDS	Ti, 73	Cu, 70	60
Ti20Al	SWIS	Ti, 73	Al, 83	20
Ti30Al	SWIS	Ti, 73	Al, 83	30
Ti40Al	SWIS	Ti, 73	Al, 83	40

Table 6-2: Deposition parameters of SWIS and CGDS processes.

Powder	Ti	Ti+Cu		Ti+Al
Spray System	SWIS	SWIS	CGDS	SWIS
Gas Nature	N_2	N_2	N_2	N_2
Gas Temperature (°C)	600	600	650	550-600
Gas Pressure (psi)	600	600	580	550-600
Valve Frequency (Hz)	25-30	30	---	30
Stand-Off Distance (mm)	25	25	25	25
Powder Pre-Heating (°C)	600	600	None	None
Powder Feeder Wheel Speed (rpm)	0.25-1	1	1	0.5-3
Traverse Speed (mm/s)	10-100	100	300	10-100
Step Size (mm)	1	1	1	1

6.2.5. Deposition of Ti+Al mixture powder and leaching process

In a third series of experiments, the Ti powder with D50 = 73 μm was blended with different weight percent of Al powder (Table 6-1) and sprayed on the surface of mild steel substrates using the SWIS process with the parameters given in Table 6-2. For the Al porogen, a different leaching treatment was used. In the first step, the samples were immersed in a freshly prepared 6M NaOH solution held at 70-90℃ for 1 hour. Following that, the samples were rinsed for 1 h in boiling de-ionized water. This step was repeated three times. Then, the samples were immersed for 1 hour in 0.5 M H_2SO_4 under stirring to detach the substrate from the coating and rinsed for 1 h in boiling de-ionized water. This procedure was repeated until the coating was detached from the substrate. Finally, step one was repeated two times to make sure Al was completely dissolved.

6.2.6. Physical characterization

The coatings were mounted in resin, then cross-sectioned and polished. Then, macroscopy images were captured using an Olympus microscope equipped with automated stitched image capture software (Olympus stream motion 2.3.2, build 17014) at a magnification of 100X. The porosity was subsequently measured using the same software. Scanning Electron Microscopy (JEOL, JSM-6300F) and Energy Dispersive X-Ray (EDX, VEGA3 TESCAN) measurements were carried out on all samples before and after leaching. All SEM images were taken in SE (secondary electron) mode. EDX analysis was conducted on the coatings at a magnification of 55X and at three distinct spots on each sample. The resulting data were then used to calculate the average content of Al or Cu in the coatings.

6.3. Results

The results are described in five sections.

6.3.1. Particle size and morphology

Fig.6-1 shows the particle size distribution and D50 values of Ti powder and porogen. Ti-73 μm and Ti-90 μm have a larger particle size distribution when compared to Ti-30 μm and porogen. The D90 values for Ti particles are 38 μm, 100 μm, and 130 μm, respectively. Furthermore, for Cu and Al particles, D90 is 80 and 86 μm, respectively.

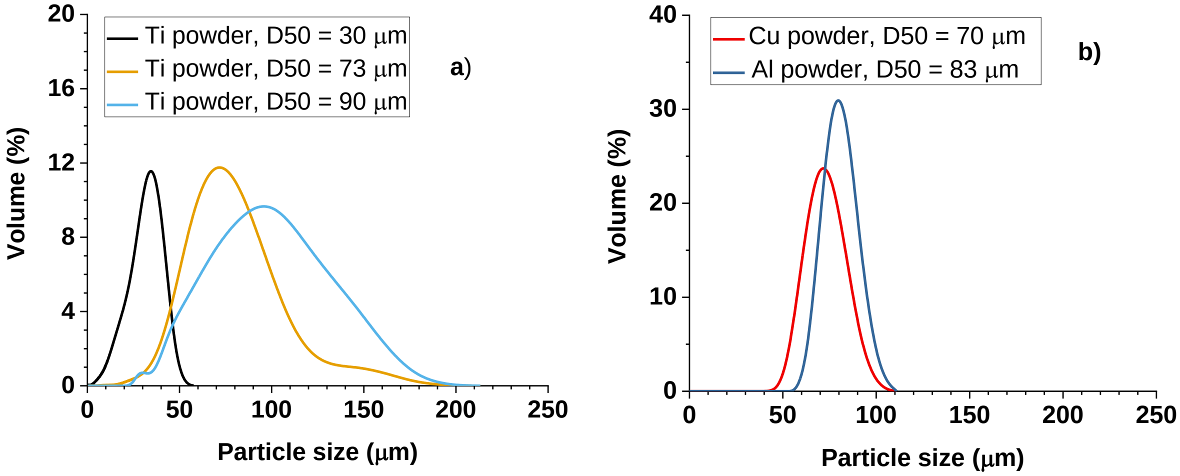

Figure 6-1: Particle Size Distribution of the powders used in the present study. In a), Ti powders, and in b) Al and Cu powders.

Fig.6-2 depicts the SEM micrographs of the different powders used in the present study. The aluminum and copper powders are made of particles with spherical shape. This is also the case for the Ti powder with D50 = 30 μm. In contrast, the Ti powder with D50 = 73 µm (Ti-73 µm) and D50 = 90 µm (Ti-90 μm) have irregular shapes.

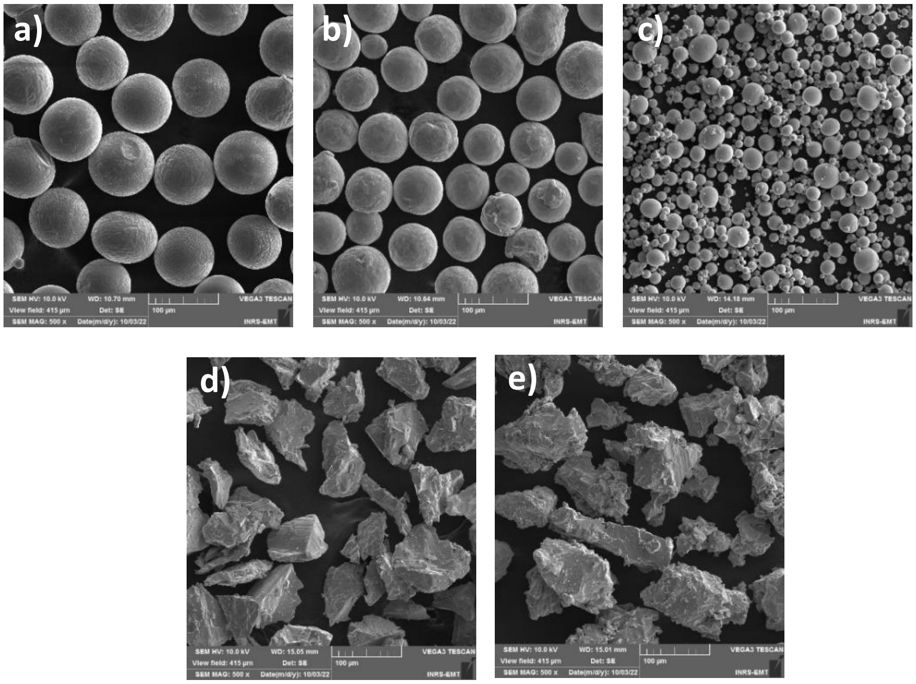

Figure 6-2: SEM micrographs of three different Ti powders and two different porogens used for the preparation of the CGDS and SWIS coatings. a) Al powder, b) Cu powder, c) Ti-30 μm powder, d) Ti-73 μm powder, e) Ti-90 μm powder.

6.3.2. Optimization of the coating porosity

In the first series of experiments, three different types of Ti powder were sprayed onto mild steel substrates to determine the effect of particle size on the porosity of the resulting coating. Fig.6-3 shows cross-section SEM images of Ti-30, Ti-73, and Ti-90 samples produced by the SWIS process. The white areas are Ti, and the black areas are the pores filled by epoxy. In order to determine the porosity, an optical microscope image of the entire coating was acquired (Fig.S19). Then, using the Olympus software, the ratio of (pore surface area) / (pore surface area + Ti surface area) was calculated. The porosity of the different coatings is shown in Table 6-3.

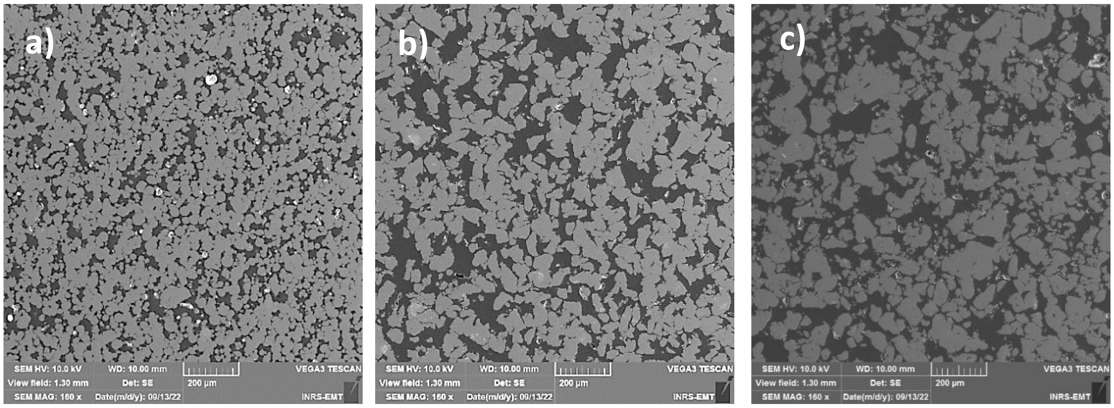

Figure 6-3: SEM cross-section of a) Ti-30, b) Ti-73, and c) Ti-90 samples.

Table 6-3: Porosity of the SWIS coatings prepared using three different Ti particle sizes.

Sample	Porosity (%)
Ti-30	25 ± 3
Ti-73	38 ± 4
Ti-90	40± 4

The porosity of the coatings increases as the Ti particle size is increased from 30 to 73 μm. However, this effect levels off as the Ti particle size is further increased. In the SWIS process, the impact velocity of the particles decreases with increasing particle size, which leads to a reduction of the particle deformation at the point of impact and causes an increase in the coating porosity [111, 112]. However, in our experimental conditions, this effect levels for the larger Ti particles. Under our operating conditions, the maximum coating porosity that can be achieved by changing the Ti particle size is 40%.

In an effort to further increase the porosity of Ti-based PTL, a porogen was used. In a first attempt, different weight percentages of Cu-70 μm powder were blended with the Ti-73 μm powder, and the mixture was deposited on mild steel substrates, first using the SWIS process, and then the CGDS process.

6.3.3. Effect of Cu porogen on the porosity of Ti coatings prepared by the SWIS technique

Fig.6-4 depicts the cross-section SEM micrographs of the Ti+Cu coatings produced by the SWIS technique. The gray particles are Ti and the white particles are Cu. The Cu particles are dispersed homogeneously in the coating. After leaching in HNO_3, most of the initially present Cu particles were dissolved and are not observed anymore in the SEM micrographs of Fig.6-4.

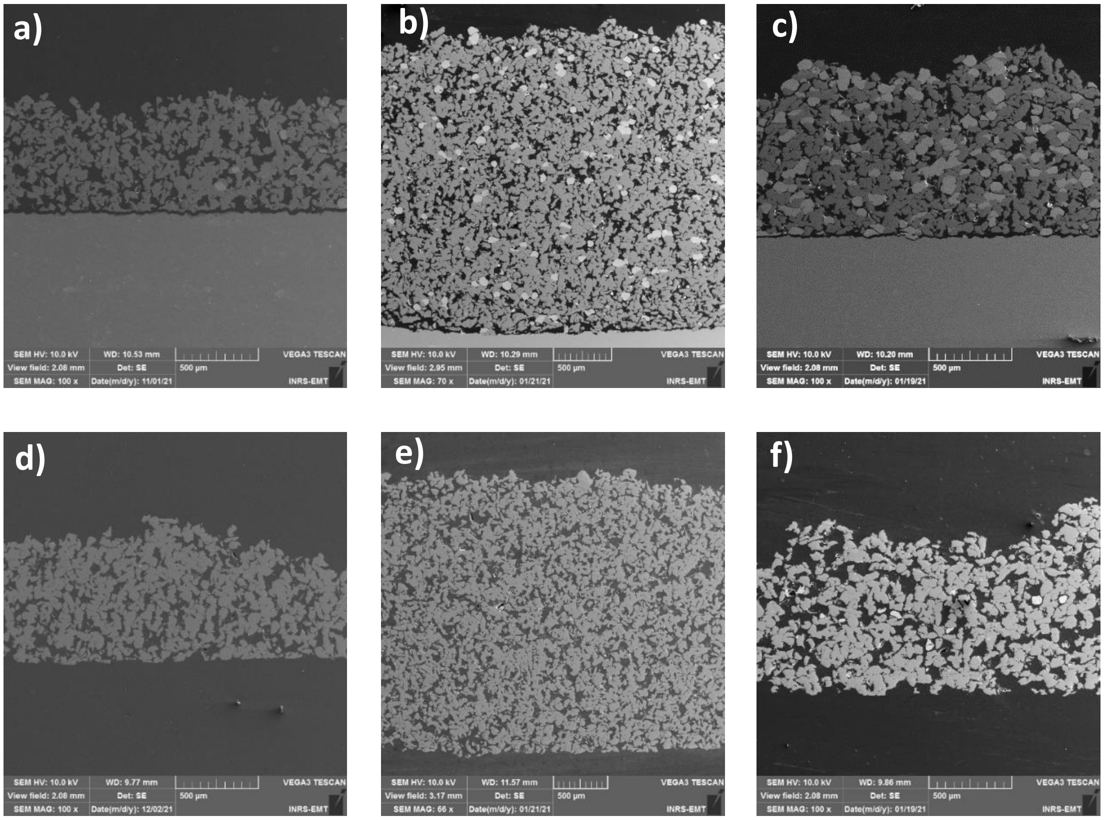

Figure 6-4: SEM cross-section of a) and d) Ti5Cu sample; b) and e) Ti30Cu sample and c) and f) Ti60Cu sample. In a), b) and c, as-deposited samples. In d), e) and f), after leaching. All samples were deposited by the SWIS process on mild steel substrates.

The effect of the Cu content in the powder feeder on the Cu content of the as-deposited coatings was assessed. As seen in Fig.6-5a, an increase in the Cu content in the powder feeder causes an increase in the Cu content of the coating. However, there is a significant difference between the Cu content in the feeder and the coating.

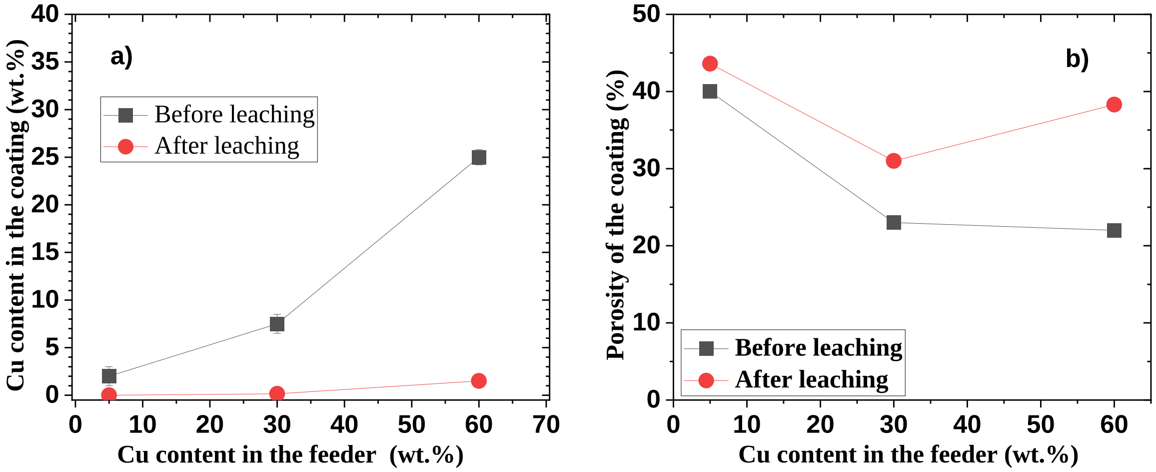

Figure 6-5: Variation of a) the Cu content and b) porosity in the coating prepared by the SWIS technique with respect to the Cu content in the deposited powder.

Previous reports have shown that the composition of a coating made of two different materials A and B depends on the A and B content in the powder feeder and the ratio of the Deposition Efficiency (*DE*) of A and B, $\frac{DE_A}{DE_B}$. The deposition efficiency of a material depends on the spray parameters, particle size, and the type of material. Furthermore, when the mechanical and physical properties of two powders are significantly different, powder interaction can affect the chemical composition of the coating [113].

To determine the DE of Cu particles, Cu-70 μm powder was deposited on mild steel utilizing the same SWIS parameters as detailed in Table 6-2. The findings revealed that no Cu-70 μm particles were deposited, even with an increase in gas temperature to 800 ℃ or a decrease to 350℃. However, we were able to successfully deposit a copper layer by using a smaller particle size of copper (with a D50 value of 50 μm). A comparison of the results indicates that Cu-70 μm did not achieve a high enough particle velocity using the deposition parameters due to the density of Cu particles being twice that of Ti. Nevertheless, owing to powder interaction or entrapped Cu particles in the Ti powder matrix, some Cu particles were incorporated into the coating.

As shown in Fig.6-5b an increase in the Cu content in the feeder decreases the porosity of the resulting coating, although this effect levels off for the highest the Cu content. This is most probably related to the higher deformation of Cu particles upon impacting the substrate compared to the Ti particles [51, 53]. After leaching, all coatings separate from the substrate because the corrosion rate of mild steel in HNO_3 is large [114]. As noted above, there is almost no Cu particles left in the coating after leaching, indicating that the acidic solution must have ready access to both the surface and the bulk of the coating. This is so even for the thickest coating. Diffusion of the acidic solution to the bulk of the coating must be favored by the initial porosity of the coating, which results from the use of Ti particles with a D50 value of 73 μm. Even the thickest coating investigated in the present study is not damaged or cracked as a result of the leaching process (Fig.S20). As expected, the leaching of Cu particles from a coating increases its porosity (Fig.6-5b). This increase is such that the porosity of the film after leaching does not exceed *ca.* 45%, which is the porosity of films prepared using only Ti particles of the same size. This observation reinforces the fact that Cu particles are more deformable than Ti particles and block the pores that the assembly of Ti particles creates. Thus, with the objective of maximizing the porosity of Ti coating, we switched from the SWIS to the CGDS process, using always Cu as a porogen.

6.3.4. Effect of Cu porogen on the porosity of Ti coatings prepared by the CGDS technique

Fig.6-6a shows a typical SEM cross-section micrograph of an as-deposited Ti+Cu coating prepared by the cold spray technique. The dark gray particles are Ti, and the light gray particles are Cu. The SEM micrograph of the as-deposited Ti + Cu CGDS coating shows it is dense with almost no porosity. CGDS coatings prepared using different Ti + Cu feeder mixtures exhibited the same morphology, with almost no pores, and as shown in Fig.6-6d, the porosity of all CGDS coatings is below 8%. There is a sizeable reduction of the CGDS coating porosity compared to coatings prepared by the SWIS technique. This is thought to occur as a result of the higher velocity of the particles in the CGDS process that deforms them considerably when impacting the substrate, thereby leading to denser deposits [51, 52, 53].

There are more Cu particles in the CGDS coatings than in the corresponding SWIS coatings obtained using the same feeder mixture. This is confirmed by the data in Fig.6-6c, which shows the variation in the Cu content in the CGDS coating with respect to the Cu content in the feeder mixture. For the highest Cu content in the feeder mixture (60 wt.%), the Cu content in the CGDS deposited coating is 35 wt.% compared to 25 wt.% for the SWIS technique. As previously described for SWIS coatings, the low weight percentage of Cu observed in the Ti-Cu coating can be attributed to the lower particle velocity. However, in contrast to the SWIS technique, the high deformation of Ti particles produced a dense coating in CGDS, indicating a higher particle velocity in CGDS. Consequently, this resulted in an increase in both the velocity of Cu particles and the deposition efficiency of Cu particles.

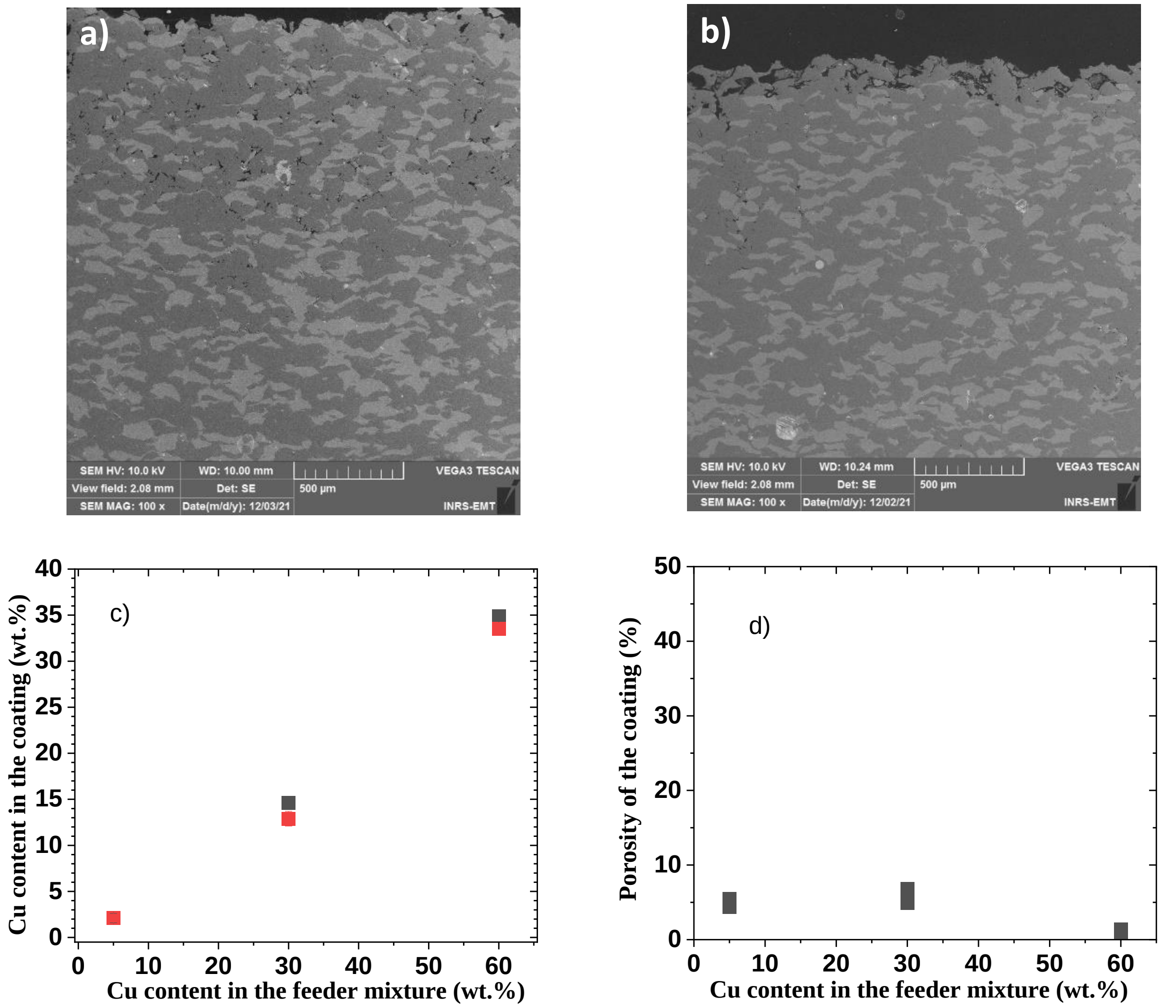

Figure 6-6: Cross-section SEM micrographs of Ti60Cu coating prepared by the CGDS technique. In a), as-deposited, and in b) after leaching. In c), variation of the Cu content in the coating with respect to the Cu content in the feeder mixture. In d), variation of the porosity of the coating with respect to the Cu content in the powder mixture.

The samples were leached in an acidic medium to dissolve Cu and increase the porosity. As shown in Fig.6-6b, the SEM image of the leached coating indicates that Cu particles have been dissolved from the surface of the coating. However, they are still present in the core of the coating. Consequently, a rough surface with high porosity has formed on the coating surface, but the porosity of the bulk of the coating has not increased. Obviously, the acidic solution does not reach the Cu particles embedded in the core of the coating because the as-deposited coating has very low porosity, and the Cu particles are not connected together.

Although the films prepared by the CGDS technique contain more Cu than the corresponding films prepared by SWIS, the lack of porosity and wt.% Cu in the as-deposited CGDS films means that the acid solution has limited access to the Cu particles. Indeed, the acid solution only has access to the particles that are close to the surface, and thus cannot dissolve the Cu particles that are in the core of the coating. Obviously, the choice of a porogen in the CGDS deposition technique must take into account the particularities of this deposition technique. Because of the particle velocities involved in the CGDS or SWIS process, it is essential to decrease the density of the porogen particles in order to increase the particle velocity and DE of the porogen. Accordingly, Al particles were chosen as a porogen.

6.3.5. Effect of Al porogen on the porosity of Ti coatings prepared by the SWIS technique

Fig.6-7 shows the cross-section optical microscopy images of as-deposited Ti20Al, Ti30Al, and Ti40Al samples before leaching. The gray areas are Al, and the white areas are Ti particles. As seen, Al particles are distributed homogeneously throughout the coatings. According to the EDX analysis, an increase in the Al content of the feeder mixture led to an increase in the Al content in the coating (Fig.6-8a). The Al content in the SWIS coating is larger than the Al content in the feeder, which contrasts with the results of Ti+Ni deposited by Nikbakht et al. [115] and our own results for Ti+Cu deposited by the CGDS or SWIS technique. As stated before, this is due to the lower density of Al compared to Ni and Cu, which results in higher particle velocity and higher deposition efficiency of the Al particles [111, 115].

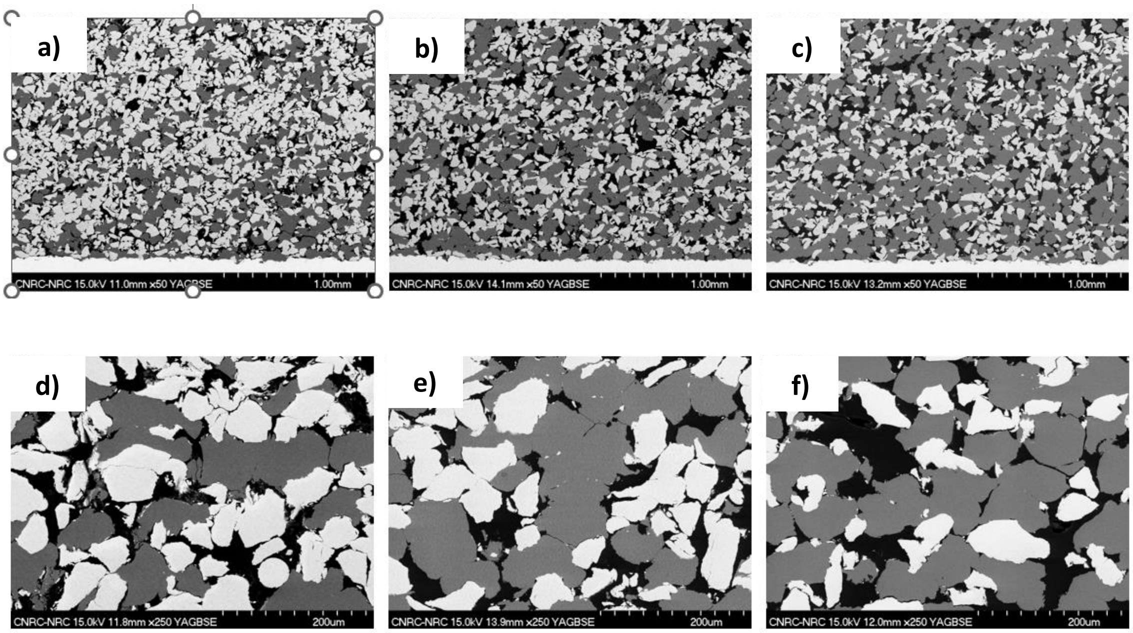

Figure 6-7: Cross-Section Optical Microscopy of a) and d)Ti20Al, b) and e) Ti30Al, and c) and f) Ti40Al. Two magnifications are displayed.

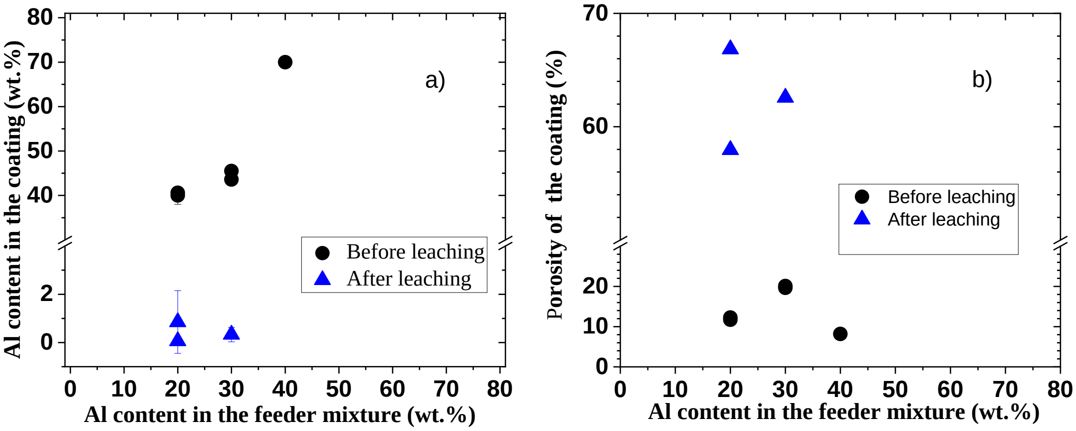

Figure 6-8: In a), variation of Al content of the coating with respect to the Al content of the feeder mixture. In b) variation of the porosity of the coating with respect to the Al content of the feeder mixture.

The porosity of the as-deposited Ti + Al coatings were ca. 15%, which is smaller than the porosity of SWIS coatings prepared using only the Ti-73 powder (Table 6-3) and smaller than the porosity of SWIS coatings prepared using a mixture of Ti and Cu powders (Fig.6-5b). Again, this must be related to the ability of Al particles to deform upon impacting the substrate and filling in the porosity that would otherwise be formed if only the Ti-73 powder would have been used.

Leaching of the Ti + Al SWIS coatings was performed following the procedure described in the experimental section, and cross-section optical microscopy analysis was performed following each step. The first step of the leaching process, which consists in successively immersing the Ti20Al SWIS coating in an alkaline solution before immersing it in deionized water, is able to dissolve most of the Al particles from the top and the sides of the coating (Fig.6-9b). However, several Al particles were still present in the coating near the interface between the substrate and the coating. To create a self-supported 3D Ti skeleton and remove what is left of Al particles in the coating, the sample was immersed in 0.5 M H_2SO_4 to detach the coating from the substrate (see the experimental section for details). Once detached from the substrate, the self-supported coating was leached three times in NaOH to dissolve the remaining Al particles. At the end of the process, all Al particles were dissolved without causing any damage to the self-supported coating that kept its mechanical integrity (Fig.6-9c). After leaching, the Al content in the self-supported coating was close to zero (Fig.6-8a) and the porosity was increased to value larger than 60%, as can be appreciated in Fig.6-8b. Two replicates were performed, leading to similar results (Fig.6-8a and 6-8b).

Al leaching from SWIS Ti40Al coatings led to the complete disintegration of these samples. The aluminum content of these samples is so high that the number of contacts between the Ti particles is not high enough to ensure the mechanical integrity of the electrode once the aluminum particles are dissolved. Some parts of the leached Ti30Al SWIS coatings were mechanically stable, although full electrodes the size of those seen in Fig.6-9 could not be obtained.

Self-supported porous Ti electrodes with thickness exceeding 2 mm and geometrical area exceeding 1 cm^2 could be prepared with porosity exceeding 60%. This porosity is larger than that obtained from Ti-based PTL prepared by the powder sintering process [116], cold spray [54, 55], and vacuum plasma spray process [117]. Using these preparation techniques, the porosity is lower than 50% [49], which is below the optimal porosity for PTLs, which should be within the 50-75% range [43].

In this study, our focus was on exploring the feasibility of fabricating a titanium porous coating with a porosity surpassing 60% using shock wave-induced spraying. Our investigation also delved into the influence of various porogens, aiming to identify crucial parameters for porogen selection. Nevertheless, to finalize the project, several tasks remain. Firstly, it is essential to produce a high-porosity coating with smaller particle sizes and conduct electrochemical and corrosion tests.

Secondly, there is a need to calculate the deposition efficiency of the powder (namely, the mass of material effectively deposited in contrast to the mass of material applied to the surface) and optimize this process to minimize manufacturing costs.

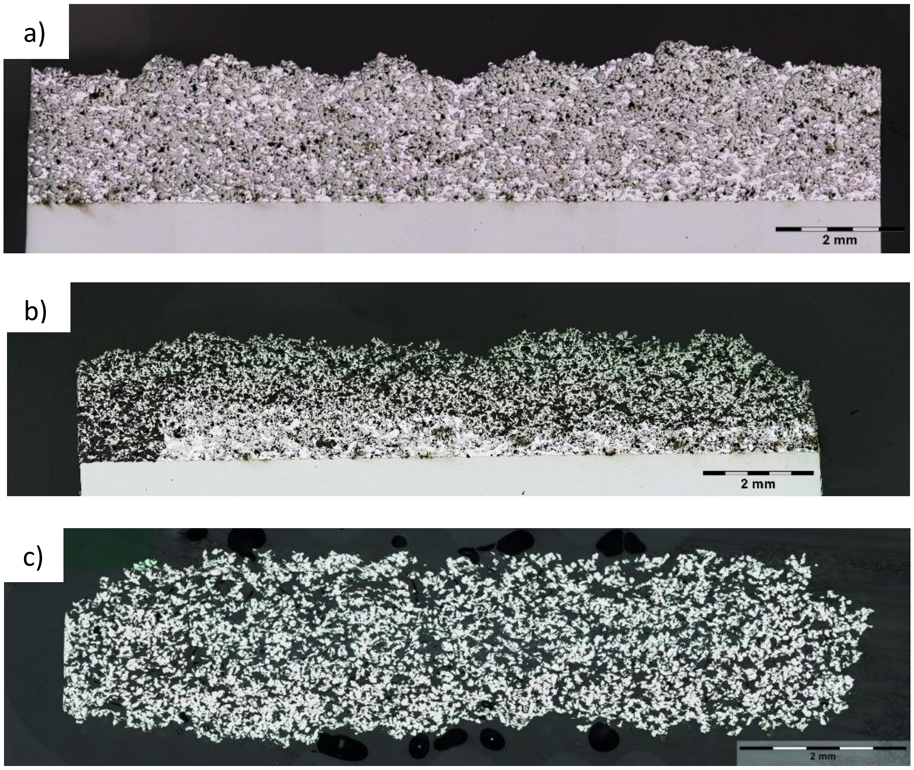

Figure 6-9: Cross-section optical microscopy of Ti20Al sample: a) as-deposited, b) after three leaching in alkaline solution, and c) after a subsequent leaching in alkaline solution once the coating was detached from the substrate. The details of the leaching procedure are given in the experimental section.

6.4. Conclusion

Porous Ti coatings with a maximum porosity of 40±5% have been successfully prepared using the SWIS deposition technique. Increasing the size of the particles from 30 μm up to 73 μm increases the porosity of the coating from 25% up to 40%. No more gain in porosity has been measured for powders with particle sizes larger than 73 μm.

In the subsequent phase, Cu was employed as a porogen, blended with Ti powder, and deposited on mild steel using SWIS process. Despite incorporating copper to enhance porosity, the resultant leached coating showed no porosity increase beyond 40%. This limitation was attributed to the low Cu content caused by insufficient Cu particle velocity.

To address this issue and boost the velocity of copper particles, a transition was made to CGDS method. However, in this approach, copper particles did not leach from the core of the CS coating due to its dense structure.

Ultimately, we reverted to SWIS process, using Al particles as the porogen. Given that aluminum has a density 40% lower than that of titanium, we successfully generated a composite coating with a high aluminum content. A porosity exceeding ca 60% has been obtained after leaching Al from the Ti20Al coating.

7 CONCLUSION AND FUTURE PERSPECTIVES

Innovative methods have been used to produce two different 3D skeleton electrodes for Alkaline Water Electrolysis (AWE) and Proton Exchange Membrane Water Electrolysis (PEMWE).

For AWE, a novel 3D skeleton structure of nickel (Ni whiskers) has been developed, which consists of a large number of Ni whiskers with an exceptionally high electrochemical surface area. In order to produce Ni whiskers, Al was melted onto the surface of Ni to create a hypereutectic alloy of Ni-Al, which was then directionally solidified followed by leaching. Ni whiskers are nanopores with a thickness of a few hundred nanometers. Their preferred crystallographic orientation makes them distinct from polycrystalline structures. These whiskers are also highly mechanically stable, as shown by galvanostatic experiments conducted over six days at a current density of 500 mA.cm^{-2}.

The mass of Al and the heat treatment process control the volume, size, and distribution of Ni whiskers.

By increasing the mass of Al, double layer capacitance and cathodic charge increase, reducing overpotential at all measured current densities.

As the time elapsed at a maximum temperature (heat treatment time) increases, coarser Ni whiskers form. This results in a reduction in Ni whisker density, an increase in Ni whisker spacing, and a decrease in cathodic charge.

On the other hand, increased maximum temperature increases Ni content in the molten alloy, which results in a greater density of Ni whiskers, which results in a smaller distance between Ni whiskers and an increase in cathodic charge.

Initially, an increase in cathodic charge reduces the overpotential required for oxygen evolution reactions (OERs) at high current densities. However, for Ni whiskers with too much density, this increase in cathodic charge can cause a subsequent increase in the overpotential required for the OER. The reason for this phenomenon is the existence of trapped bubbles within the Ni whiskers structure, which hinder mass transport. Therefore, it is imperative to adjust the distance between Ni whiskers to facilitate effective mass transport and avoid hindering OERs.

The optimal sample was produced at 670°C and a heat treatment time of 1 minute, requiring overpotentials of 245 mV and 345 mV to deliver 10 mA.cm^{-2} and 500 mA.cm^{-2}, respectively. The low overpotential is believed to be caused by the very high electrochemical active surface area, not by the incorporation of Fe, since adding 10 ppm $FeCl_2$ to the electrolyte led to significant reductions in overpotential.

To reduce the activation overpotential, two different catalysts were synthesized on Ni whiskers.

The first catalyst was Ir, which is well known for its high activity in OER. A cation exchange process was used to deposit Ir on Ni whiskers. An Ir non-continuous coating was observed on Ni whiskers using SEM and EDX analysis. As a result of the deposited Ir, the OER overpotential was significantly reduced at low current densities. Even though SEM, EDX, and a significant decrease in OER overpotential confirmed the presence of Ir on the surface of Ni whiskers, no oxidation or reduction peak of Ir (III)/Ir(IV) redox was observed. The reason is that Ir was not uniformly distributed on the surface, and its mass was very low.

While deposited Ir reduces OER overpotentials at low current densities of Ni whiskers, it increases them at high current densities. Increases in mass transport are attributed to blockage structures caused by uneven Ir distribution and fiber detachment due to Ni dissolution in acidic environments.

Doping Fe in Ni-whiskers as another catalyst was achieved through the use of a simple immersion process. EDX and SEM analyses confirmed that Fe was evenly distributed throughout the structure without blocking or detaching fibers. As a result of Fe doping, the $Ni(OH)_2$/NiOOH redox peaks were shifted anodically and the background density of oxidation and reduction redox was reduced. In addition, Fe significantly increased the activity of the OER. The Fe-doped Ni hydroxide performed almost as well as the Ir-deposited samples at low current densities while maintaining high OER performance at high current densities.

According to the study, the SWIS deposition technique is capable of creating porous Ti coatings with a porosity of up to 40%. As the particle size increased from 30 μm to 73 μm, the porosity of the coating increased from 25% to 40%. There was no further increase in porosity for particle sizes larger than 73 mm, however.

To enhance the porosity of the SWIS Ti coating, Cu particles were utilized as the porogen. SWIS techniques were successfully applied to deposition Ti+Cu coatings, incorporating feeder mixtures containing a maximum of 60% Cu. However, despite the incorporation of Cu particles, the leached coating demonstrated no increase in porosity beyond 40%. This limitation was linked to insufficient Cu particle velocity, resulting in a lower Cu content within the coating.

By using CGDS, higher particle velocity was achieved, leading to a higher Cu wt.% in CGDS coatings compared to SWIS coatings. However, CGDS coatings lacked interconnectivity, which meant Cu could not be leached from their core.

Ultimately, we reverted to SWIS process, using Al particles as the porogen. SWIS was able to produce Ti+Al coatings with a high Al content from feeder mixtures containing up to 40% Al. The coating in this case contained a much higher content of Al than the feeder mixture. The higher deposition efficiency of Al particles can be attributed to their higher velocity due to the lower density compared to Ti. Upon leaching the Al from the Ti20Al coating, a porosity exceeding 60% was achieved.

7.1. Future perspectives

The upcoming report provides future perspectives and recommendations for future research, in light of the numerous potential applications of the innovative 3D structures of Ni and Ti.

Reference sources indicate that Raney Ni catalysts can be enhanced by adding a third metal, such as zinc or chromium, to the molten alloy [297]. In order to examine this effect, additional elements can be added to Al powder and heat treatment can be used to form triple alloys. The addition of elements can be assessed by examining the resulting microstructure and OER activity.

Using a novel technique, we have separated Ni whiskers from Ni plates. Detached nickel whiskers can be utilized as a porous transport layer in Alkaline membrane water electrolyzers (AEMWE), and their performance can subsequently be evaluated. As an alternative method for producing a porous transport layer for AEMWE, Ni whiskers can also be grown on Ni mesh.

In the literature, applying a magnetic field can improve the alignment of Al_3Ni fibers in the direction of the magnetic field [298]. Ni whiskers could benefit from this approach as it could improve mass transport and performance, especially at high current densities.

It is also possible to explore Ni whiskers as a possible supercapacitor. As a result of our research, we found that increasing the maximum temperature, the time elapsed at the maximum temperature, or the cooling rate significantly increased fiber density. Using a metallic boat instead of a ceramic boat or increasing Ar discharge can increase the cooling rate. The findings suggest that optimizing the manufacturing process for Ni whiskers may enhance their suitability for supercapacitors.

It may be beneficial to examine the structures prior to leaching using TEM analysis, particularly since the XRD pattern of the samples differs from that reported by other researchers. Additionally, investigating the mechanism of Ni whisker growth during leaching could provide valuable insight into the material's behaviour.

Research into Ni-Fe catalysts formed on Ni whiskers may also be worthwhile. Doping Fe into Ni whiskers can be achieved through cyclic voltammograms with varying Fe content in the electrolyte and for varying time periods. Changes in parameters affect Fe content in Ni whiskers, which affects OER activity. Since the optimal Fe content in Ni is still unclear, experimental measurement is necessary. Some studies found $Ni_{0.83}Fe_{0.17}(OH)_2$ [102] to have the highest OER activity, whereas others suggested $Ni_{0.75}Fe_{0.25}(OH)_2$ [103]. It appears that Ni-Fe hydroxides might further increase OER activity in 1M KOH since an overpotential of 185 mV was observed in 1M KOH electrolyte spiked with 10 ppm Fe.

Further research could focus on synthesizing catalysts with different structures on Ni whiskers. OER and bubble escape performance can be evaluated by synthesizing 3D nanostructures, nanoporous or nanoparticles of high-performance catalysts on Ni whiskers. It is possible to adjust the spacing between Ni whiskers for each catalyst to optimize its performance. The nanostructure can also enhance double-layer capacitance, making them potentially useful for supercapacitors as well. This area may yield important insights and potential applications if further research is conducted.

Many things need to be done for the Ti porous transport layer. SWIS process is introduced for the first time to use for PTL production. Using Cu and Al, we increased porosity and achieved a porosity of over 60%. This thesis did not have time to examine the electrochemical characteristics, which can be done in the future.

For our study, we only examined three different particle sizes of Ti (30, 73, and 90 μm) to produce the porous transport layer. However, it would be worthwhile to investigate other particle sizes as well, as decreasing particle size can lead to an increase in PEMWE efficiency due to smaller pore sizes. Further, Al particles of different sizes could be used to create PTL with optimal porosity and pore size.

The next step could be to coat the PTL with a highly active catalyst. It is critical to ensure that the catalyst deposit does not impede mass transport. In other words, the PTL should have a specific porosity and pore size to fit the catalysts, so that the pore size and porosity can be optimized after catalyst synthesis. As previously mentioned, optimal pore size depends on surface properties. 3D nanostructures with low bubble adhesion can decrease optimal pore size, leading to improved specific surface area and overall efficiency. Also, it is recommended to use nanoporous or nanoparticle catalysts among 3D nanostructures due to their mechanical stability.

8 BIBLOGRAPHY

[1] F. Song, L. Bai, A. Moysiadou, S. Lee, C. Hu, L. Liardet and X. Hu, "Transition Metal Oxides as Electrocatalysts for the Oxygen Evolution Reaction in Alkaline Solutions: An Application-Inspired Renaissance," *Journal of the American Chemical Society,* vol. 140, no. 25, pp. 7748-7759, 2018.

[2] L. Han, S. Dong and E. Wang, "Transition-Metal (Co, Ni, and Fe)-Based Electrocatalysts for the Water Oxidation Reaction," *Advanced Materials,* vol. 28, no. 42, pp. 9266-9291, 2016.

[3] H. Dau, C. Limberg, T. Reier, M. Risch, S. Roggan and P. Strasser, "The Mechanism of Water Oxidation: From Electrolysis via Homogeneous to Biological Catalysis," *ChemCatChem,* vol. 2, no. 7, pp. 724-761, 2010.

[4] N. S. Lewis and D. G. Nocera, "Powering the planet: Chemical challenges in solar energy utilization," *Proceedings of the National Academy of Sciences of the United States of America,* vol. 103, no. 43, pp. 15729-15735, 2006.

[5] M. A. Khan, H. Zhao, W. Zou, Z. Chen, W. Cao, J. Fang, J. Xu, L. Zhang and J. Zhang, "Recent Progresses in Electrocatalysts for Water Electrolysis," *Electrochemical Energy Reviews,* vol. 1, no. 4, pp. 483-530, 2018.

[6] C. Santoro, A. Lavacchi, P. Mustarelli, V. Di Noto, L. Elbaz, D. R. Dekel and F. Jaouen, "What is Next in Anion-Exchange Membrane Water Electrolyzers? Bottlenecks, Benefits, and Future," *ChemSusChem,* vol. 15, no. 8, 2022.

[7] S. M. Steen, J. Mo, Z. Kang, G. Yang and F. Y. Zhang, "Investigation of titanium liquid/gas diffusion layers in proton exchange membrane electrolyzer cells," *International Journal of Green Energy,* vol. 14, no. 2, pp. 162-170, 2017.

[8] S. Shiva Kumar and V. Himabindu, "Hydrogen production by PEM water electrolysis – A review," *Materials Science for Energy Technologies,* vol. 2, no. 3, pp. 442-454, 2019.

[9] R. Maric and H. Yu, "Proton Exchange Membrane Water Electrolysis as a Promising Technology for Hydrogen Production and Energy Storage," *Intech,* 2018.

[10] X. Z. Yuan, N. Shaigan, C. Song, M. Aujla, V. Neburchilov, J. T. H. Kwan, D. P. Wilkinson, A. Bazylak and K. Fatih, "The porous transport layer in proton exchange membrane water electrolysis: perspectives on a complex component," *Sustainable Energy and Fuels,* vol. 6, no. 8, pp. 1824-1853, 2022.

[11] A. Pozio, F. Bozza, G. Nigliaccio, M. Platter and G. Monteleone, "Development perspectives on low-temperature electrolysis," *Energia, ambiente e innovazione,* pp. 66-71, 2021.

[12] O. Schmidt, A. Gambhir, I. Staffell, A. Hawkes, J. Nelson and S. Few, "Future cost and performance of water electrolysis: An expert elicitation study," *International Journal of Hydrogen Energy,* vol. 42, no. 52, pp. 30470-30492, 2017.

[13] S. Shiva Kumar and V. Himabindu, "Hydrogen production by PEM water electrolysis – A review," *Materials Science for Energy Technologies,* vol. 2, no. 3, pp. 442-454, 2019.

[14] M. G. Walter, E. L. Warren, J. R. McKone, S. W. Boettcher, Q. Mi, E. A. Santori and N. S. Lewis, "Solar water splitting cells," *Chemical Reviews,* vol. 110, no. 11, pp. 6446-6473, 2010.

[15] J. Jin, K. Walczak, M. R. Singh, C. Karp, N. S. Lewis and C. Xiang, "An experimental and modeling/simulation-based evaluation of the efficiency and operational performance characteristics of an integrated, membrane-free, neutral pH solar-driven water-splitting system," *Energy and Environmental Science,* vol. 7, no. 10, pp. 3371-3380, 2014.

[16] D. K. Bediako, B. Lassalle-Kaiser, Y. Surendranath, J. Yano, V. K. Yachandra and D. G. Nocera, "Structure-activity correlations in a nickel-borate oxygen evolution catalyst," *Journal of the American Chemical Society,* vol. 134, no. 15, pp. 6801-6809, 2012.

[17] C. C. McCrory, S. Jung, J. C. Peters and T. F. Jaramillo, "Benchmarking heterogeneous electrocatalysts for the oxygen evolution reaction," *Journal of the American Chemical Society,* vol. 135, no. 45, pp. 16977-16987, 2013.

[18] R. Subbaraman, D. Tripkovic, K. C. Chang, D. Strmcnik, A. P. Paulikas, P. Hirunsit, M. Chan, J. Greeley, V. Stamenkovic and N. M. Markovic, "Trends in activity for the water electrolyser reactions on 3d M(Ni,Co,Fe,Mn) hydr(oxy)oxide catalysts," *Nature Materials,* vol. 11, no. 6, pp. 550-557, 2012.

[19] M. Risch, A. Grimaud, K. J. May, K. A. Stoerzinger, T. J. Chen, A. N. Mansour and Y. Shao-Horn, "Structural changes of cobalt-based perovskites upon water oxidation investigated by EXAFS," *Journal of Physical Chemistry C,* vol. 117, no. 17, pp. 8628-8635, 2013.

[20] S. W. Lee, C. Carlton, M. Risch, Y. Surendranath, S. Chen, S. Furutsuki, A. Yamada, D. G. Nocera and Y. Shao-Horn, "The nature of lithium battery materials under oxygen evolution reaction conditions," *Journal of the American Chemical Society,* vol. 134, no. 41, pp. 16959-16962, 2012.

[21] S. Wang, A. Lu and C. J. Zhong, "Hydrogen production from water electrolysis: role of catalysts," *Nano Convergence,* vol. 8, no. 1, 2021.

[22] M. A. Khan, H. Zhao, W. Zou, Z. Chen, W. Cao, J. Fang, J. Xu, L. Zhang and J. Zhang, "Recent Progresses in Electrocatalysts for Water Electrolysis," *Electrochemical Energy Reviews,* vol. 1, no. 4, pp. 483-530, 2018.

[23] P. Liu, B. Chen, C. Liang, W. Yao, Y. Cui, S. Hu, P. Zou, H. Zhang, H. J. Fan and C. Yang, "Tip-Enhanced Electric Field: A New Mechanism Promoting Mass Transfer in Oxygen Evolution Reactions," *Advanced Materials,* vol. 33, no. 9, pp. 1-9, 2021.

[24] M. Carmo and D. Stolten, "Energy storage using hydrogen produced from excess renewable electricity: Power to hydrogen," in *Science and Engineering of Hydrogen-Based Energy Technologies: Hydrogen Production and Practical Applications in Energy Generation*, 2018, pp. 165-199.

[25] G. Inzelt, "Kinetics of electrochemical reactions," in *Electroanalytical Methods: Guide to Experiments and Applications*, Berlin, Springer, 2010, pp. 33-53.

[26] B. Bernard, S. Huaneng, P. Sivakumar and L. Vladimir, "Overview of Membrane Electrode Assembly Preparation Methods for Solid Polymer Electrolyte Electrolyzer Chapter," in *Electrolysis*, Intech, 2012, pp. 45-60.

[27] T. Naito, T. Shinagawa, T. Nishimoto and K. Takanabe, "Recent advances in understanding oxygen evolution reaction mechanisms over iridium oxide," *Inorganic Chemistry Frontiers,* vol. 8, no. 11, pp. 2900-2917, 2021.

[28] J. Yin, J. Luo, B. Wanjala, B. Fang, R. Loukrakpam and C. J. Zhong, "Nanoalloy Catalysts in Electrochemical Energy Conversion and Storage," in *New and Future Developments in Catalysis: Batteries, Hydrogen Storage and Fuel Cells*.

[29] S. J. Weusten, L. C. Murrer, M. T. de Groot and J. van der Schaaf, "Mass transfer in 3D-printed electrolyzers: The importance of inlet effects," *AIChE Journal,* vol. 67, no. 6, pp. 1-12, 2021.

[30] R. Andaveh, G. B. Darband, M. Maleki and S. Rouhaghdama, "Superaerophobic/superhydrophilic surfaces as advanced electrocatalysts for the hydrogen evolution reaction: a comprehensive review," *Journal of Materials Chemistry A,* no. 10, pp. 5147-5173, 2022.

[31] N. K. Chaudhari, H. Jin, B. Kim and K. Lee, "Nanostructured materials on 3D nickel foam as electrocatalysts for water splitting," *Nanoscale,* vol. 9, no. 34, pp. 12231-12247, 2017.

[32] J. Lai, A. Nsabimana, R. Luque and G. Xu, "3D porous carbonaceous electrodes for electrocatalytic applications," *Joule,* vol. 2, no. 1, pp. 76-93, 2018.

[33] Z. Liu, X. Yuan, S. Zhang, J. Wang, Q. Huang, N. Yu, Y. Zhu and L. Fu, "Three-dimensional ordered porous electrode materials for electrochemical energy storage," *NPG Asia Materials,* vol. 11, no. 1, 2019.

[34] H. Becker, L. Castanheira and G. Hinds, "Local measurement of current collector potential in a polymer electrolyte membrane water electrolyser," *Journal of Power Sources,* vol. 448, 2020.

[35] S. A. Grigoriev, P. Millet, S. A. Volobuev and V. N. Fateev, "Optimization of porous current collectors for PEM water electrolysers," *International Journal of Hydrogen Energy,* vol. 34, no. 11, pp. 4968-4973, 2009.

[36] H. Ito, T. Maeda, A. Nakano, C. M. Hwang, M. Ishida, A. Kato and T. Yoshida, "Experimental study on porous current collectors of PEM electrolyzers," *International Journal of Hydrogen Energy,* vol. 37, no. 9, pp. 7418-7428, 2012.

[37] W. Ji, S. Wang, Y. Sun, H. Lv, X. Shen and C. Zhang, "Research on the influence of collector microstructure on the performance of pem electrolyzer," *World Electric Vehicle Journal,* vol. 12, no. 4, 2021.

[38] L. Zielke, A. Fallisch, N. Paust, R. Zengerle and S. Thiele, "Tomography based screening of flow field / current collector combinations for PEM water electrolysis," *RSC Advances,* vol. 4, no. 102, pp. 58888-58894, 2014.

[39] H. Ito, "Current Collectors (GDLs) and Materials," in *PEM Electrolysis for Hydrogen Production*, CRC Press, 2015.

[40] J. O. Majasan, F. Iacoviello, P. R. Shearing and D. J. Brett, "Effect of microstructure of porous transport layer on performance in polymer electrolyte membrane water electrolyser," *Energy Procedia,* vol. 151, pp. 111-119, 2018.

[41] A. S. Pushkarev, I. V. Pushkareva, M. A. Solovyev, M. Prokop, T. Bystron, S. K. Rajagopalan, K. Bouzek and S. A. Grigoriev, "On the influence of porous transport layers parameters on the performances of polymer electrolyte membrane water electrolysis cells," *Electrochimica Acta,* vol. 399, 2021.

[42] K. Zhenye, J. M.Alia, L.Young and B. Guido, "Effects of various parameters of different porous transport layers in proton exchange membrane water electrolysis," *Electrochimica Acta,* vol. 354, 2020.

[43] H. Ito, T. Maeda, A. Nakano, A. Kato and T. Yoshida, "Influence of pore structural properties of current collectors on the performance of proton exchange membrane electrolyzer," *Electrochimica Acta,* vol. 100, pp. 242-248, 2013.

[44] H. Ito, T. Maeda, A. Nakano, C. M. Hwang, M. Ishida, A. Kato and T. Yoshida, "Experimental study on porous current collectors of PEM electrolyzers," *International Journal of Hydrogen Energy,* vol. 37, no. 9, pp. 7418-7428, 2012.

[45] F. J. Hackemüller, E. Borgardt, O. Panchenko, M. Müller and M. Bram, "Manufacturing of Large-Scale Titanium-Based Porous Transport Layers for Polymer Electrolyte Membrane Electrolysis by Tape Casting," *Advanced Engineering Materials,* vol. 21, no. 6, pp. 1-10, 2019.

[46] J. K. Lee, C. H. Lee and A. Bazylak, "Pore network modelling to enhance liquid water transport through porous transport layers for polymer electrolyte membrane electrolyzers," *Journal of Power Sources,* vol. 437, 2019.

[47] G. Ryan, A. Pandit and D. P. Apatsidis, "Fabrication methods of porous metals for use in orthopaedic applications," *Biomaterials,* vol. 27, no. 13, pp. 2651-2670, 2006.

[48] M.J.Lance, J.A.Haynes and B.A.Pint, "Performance of vacuum plasma spray and HVOF bond coatings at 900° and 1100 °C," *Surface and Coatings Technology,* vol. 337, pp. 136-140, 2018.

[49] E. IRISSOU and L.-P. LEFEBVRE, "Porous metal coatings using shockwave induced spraying". Canada Patent WO/2017/191611, 05 05 2017.

[50] M. Karimi, G. W. Rankin and B. Jodoin, "Shock-wave induced spraying: Gas and particle flow and coating analysis," *Surface and Coatings Technology,* vol. 207, pp. 435-442, 2012.

[51] C. Cao, W. Li, Z. Zhang, X. Yang and Y. Xu, "Cold Spray Additive Manufacturing of Ti6Al4V: Special Nozzle Design Using Numerical Simulation and Experimental Validation," *Coatings,* vol. 12, no. 2, p. 210, 2022.

[52] H. Assadi, F. Gärtner, T. Stoltenhoff and H. Kreye, "Bonding mechanism in cold gas spraying," *Acta Materialia,* vol. 51, no. 15, pp. 4379-4394, 2003.

[53] A. Moridi, E. J. Stewart, A. Wakai, H. Assadi, F. Gartner, M. Guagliano, T. Klassen and M. Dao, "Solid-state additive manufacturing of porous Ti-6Al-4V by supersonic impact," *Applied Materials Today,* vol. 21, 2020.

[54] J. Sun, Y. Han and K. Cui, "Innovative fabrication of porous titanium coating on titanium by cold spraying and vacuum sintering," *Materials Letters,* vol. 62, no. 21-22, pp. 3623-3625, 2008.

[55] D. Qiu, M. Zhang and L. Grøndahl, "A novel composite porous coating approach for bioactive titanium-based orthopedic implants," *Journal of Biomedical Materials Research - Part A,* vol. 101 A, no. 3, pp. 862-872, 2013.

[56] M. Hao, V. Charbonneau, N. N. Fomena, J. Gaudet, D. R. Bruce, S. Garbarino, D. A. Harrington and D. Guay, "Hydrogen bubble templating of fractal Ni catalysts for water oxidation in alkaline media," *ACS Applied Energy Materials,* vol. 2, no. 8, pp. 5734-5743, 2019.

[57] M. Hao, S. Garbarino, S. Prabhudev, T. Borsboom-Hanson, G. A. Botton, D. A. Harrington and D. Guay, "Vertically aligned Ni nanowires as a platform for kinetically limited water-splitting electrocatalysis," *Journal of Physical Chemistry C,* vol. 123, no. 2, pp. 1082-1093, 2019.

[58] X. Hu, X. Tian, Y. W. Lin and Z. Wang, "Nickel foam and stainless steel mesh as electrocatalysts for hydrogen evolution reaction, oxygen evolution reaction and overall water splitting in alkaline media," *RSC Advances,* vol. 9, no. 54, pp. 31563-31571, 2019.

[59] W. Fang, D. Liu, Q. Lu, X. Sun and A. M. Asiri, "Nickel promoted cobalt disulfide nanowire array supported on carbon cloth: An efficient and stable bifunctional electrocatalyst for full water splitting," *Electrochemistry Communications,* vol. 63, pp. 60-64, 2016.

[60] M. Ishizaki, H. Fujii, K. Toshima, H. Tanno, H. Sutoh and M. Kurihara, "Preparation of Co-Fe oxides immobilized on carbon paper using water-dispersible Prussian-blue analog nanoparticles and

their oxygen evolution reaction (OER) catalytic activities," *Inorganica Chimica Acta,* vol. 502, no. 119345, 2020.

[61] A. Korjenic and K. S. Raja, "Electrochemical Stability of Fluorine Doped Tin Oxide (FTO) Coating at Different pH Conditions," *Journal of The Electrochemical Society,* vol. 166, no. 6, pp. C169-C184, 2019.

[62] N. K. Chaudhari, H. Jin, B. Kim and K. Lee, "Nanostructured materials on 3D nickel foam as electrocatalysts for water splitting," vol. 9, no. 34, pp. 12231-12247, 2017.

[63] X. Huang, X. Chen, A. Li, D. Atinafu, H. Gao, W. Dong and G. Wang, "Shape-stabilized phase change materials based on porous supports for thermal energy storage applications," *Chemical Engineering Journal,* vol. 356, pp. 641-661, 2019.

[64] Z. Liu, X. Yuan, S. Zhang, J. Wang, Q. Huang, N. Yu, Y. Zhu, L. Fu, F. Wang, Y. Chen and Y. Wu, "Three-dimensional ordered porous electrode materials for electrochemical energy storage," *NPG Asia Materials,* vol. 11, no. 1, 2019.

[65] T. Kadyk, D. Bruce and M. Eikerling, "How to Enhance Gas Removal from Porous Electrodes?," *Scientific Reports,* vol. 6, pp. 1-14, 2016.

[66] M. Zafari, M. Panjepour, M. D. Emami and M. Meratian, "3D numerical investigation of fluid flow through open-cell metal foam using micro-tomography images," *Journal of Porous Media,* pp. 1934-0508, 2014.

[67] F. J. Keil and C. Rieckmann, "Optimization of three-dimensional catalyst pore structures," *Chemical Engineering Science,* vol. 49, pp. 4811-4822, 1994.

[68] Q. Xu, J. Zhang and C. Yang, "Nickel foam electrode with low catalyst loading and high performance for alkaline direct alcohol fuel cells," *IntechOpen,* pp. 1-19, 2021.

[69] Z. Sun, Z.-H. Zhang, T.-Q. Yuan, X. Ren and Z. Rong, "Raney Ni as a versatile catalyst for biomass conversion," *ACS Catal,* vol. 11, no. 16, p. 10508–10536, 2021.

[70] D. Delgado, F. Bizzotto, A. Zana and M. Arenz, "Accelerated Durability Test for High-Surface-Area Oxyhydroxide Nickel Supported on Raney Nickel as Catalyst for the Alkaline Oxygen Evolution Reaction," *ChemPhysChem,* vol. 20, no. 22, pp. 3147-3153, 2019.

[71] W. J. Gannon and C. W. Dunnill, "Raney Nickel 2.0: Development of a high-performance bifunctional electrocatalyst," *Electrochimica Acta,* vol. 322, p. 134687, 2019.

[72] S. D. Robertson and R. B. Anderson, "The structure of Raney nickel. IV. X-ray diffraction studies," *Journal of Catalysis,* vol. 23, no. 2, pp. 286-294, 1971.

[73] R. Wang, Z. Lu and T. Ko, "The structural transitions during leaching of Ni2Al3 phase in a Raney Ni-Al alloy," *Journal of Materials Science,* vol. 36, no. 23, pp. 5649-5657, 2001.

[74] J. E. Kim, K. K. Bae, C. S. Park, S. U. Jeong, K. H. Baik, J. W. Kim, K. S. Kang, K. B. Lee and Y. H. Kim, "Electrochemical characterization of Raney nickel electrodes prepared by atmospheric plasma spraying for alkaline water electrolysis," *Journal of Industrial and Engineering Chemistry,* vol. 70, pp. 160-168, 2019.

[75] M. Cooper and G. G. Botte, "Optimization of the electrodeposition of Raney nickel on titanium substrate," *Journal of Materials Science,* vol. 41, no. 17, pp. 5608-5612, 2006.

[76] D. Chade, L. Berlouis, D. Infield, P. T. Nielsen and T. Mathiesen, "Deactivation mechanisms of atmospheric plasma spraying Raney Nickel electrodes," *Journal of The Electrochemical Society,* vol. 163, no. 3, pp. F308-F317, 2016.

[77] A. Soutelo-Maria, J. L. Dubois, J. L. Couturier, M. Brebion and G. Cravotto, "Regeneration of raney®-nickel catalyst for the synthesis of high-value amino-ester renewable monomers," *Catalysts,* vol. 10, no. 2, pp. 1-13, 2020.

[78] F. Razmjooei, T. Liu, D. A. Azevedo, E. Hadjixenophontos, R. Reissner, G. Schiller, S. A. Ansar and K. A. Friedrich, "Improving plasma sprayed Raney-type nickel–molybdenum electrodes towards high-performance hydrogen evolution in alkaline medium," *Scientific Reports,* vol. 10, no. 1, pp. 1-13, 2020.

[79] L. F. Arenas, C. Ponce de León and F. C. Walsh, "Three-dimensional porous metal electrodes: Fabrication, characterisation and use," *Current Opinion in Electrochemistry,* vol. 16, pp. 1-9, 2019.

[80] C. I. Bernäcker, T. Rauscher, T. Büttner, B. Kieback and L. Röntzsch, "A powder metallurgy route to produce raney-nickel electrodes for alkaline water electrolysis," *Journal of The Electrochemical Society,* vol. 166, no. 6, pp. F357-F363, 2019.

[81] C. Dörfelt, R. Kolvenbach, A. S. Wirth, M. Albert and K. Köhler, "Catalytic properties of a novel Raney-Nickel foam in the hydrogenation of Benzene," *Catalysis Letters,* vol. 146, no. 12, pp. 2425-2429, 2016.

[82] Y. Fan and M. M. Makhlouf, "The Al-Al3Ni Eutectic Reaction: Crystallography and Mechanism of Formation," *Metallurgical and Materials Transactions A: Physical Metallurgy and Materials Science,* vol. 46, no. 9, pp. 3808-3812, 2015.

[83] G.-R. Stacy and B. Thomas, "The Powder Diffraction File: a quality materials characterization database," *Powder Diffr,* vol. 34, no. 4, 2019.

[84] S.-i. Tanaka, N. Hirose, T. Tanaki and Y. H. Ogata, "Effect of Ni-Al precursor alloy on the catalytic activity for a Raney-Ni cathode," *Journal of The Electrochemical Society,* vol. 147, no. 6, pp. 2242-2245, 2000.

[85] J. Zhang, "Preparation and catalytic performance of an efficient Raney nickel catalyst for syngas methanation," *Journal of Materials Science,* vol. 54, no. 22, pp. 14197-14208, 2019.

[86] J. Freel, W. J. Pieters and R. B. Anderson, "The structure of Raney nickel: I. Pore structure," *Journal of Catalysis,* vol. 14, no. 3, pp. 247-256, 1969.

[87] T. Ungár, G. Tichy, J. Gubicza and R. J. Hellmig, "Correlation between subgrains and coherently scattering domains," *Powder Diffraction,* vol. 20, no. 4, pp. 366-375, 2005.

[88] M. Graf, B. N. D. Ngô, J. Weissmüller and J. Markmann, "X-ray studies of nanoporous gold: Powder diffraction by large crystals with small holes," *Physical Review Materials,* vol. 1, no. 7, pp. 1-13, 2017.

[89] L. Wang and T. J. Balk, "Synthesis of nanoporous nickel thin films from various precursors," *Philosophical Magazine Letters,* vol. 94, no. 9, pp. 573-581, 2014.

[90] J. Zhao, C. Unuvar, U. Anselmi-Tamburini and Z. A. Munir, "Microstructural evolution during the dissolution of nickel in liquid aluminum under the influence of an electric field," *Acta Materialia,* vol. 56, no. 8, pp. 1840-1848, 2008.

[91] J. F. Zhao, C. Unuvar, U. Anselmi-Tamburini and Z. A. Munir, "Kinetics of current-enhanced dissolution of nickel in liquid aluminum," *Acta Materialia,* vol. 55, no. 16, pp. 5592-5600, 2007.

[92] T. Massalski and H. Okamoto, Binary alloy phase diagrams, Ohio: ASM International, 1990.

[93] T. Gladman, Grain Size Control, CRC Press, 2020.

[94] Z. Ding, Q. Hu, F. Yang, W. Lu, T. Yang, T. Yang, S. Cao and J. Li, "A New Sight of the Growth Characteristics of Solidified Al3Ni at the Liquid–Solid Interface by Synchrotron Radiography and 3D Tomography," *Metallurgical and Materials Transactions A: Physical Metallurgy and Materials Science,* vol. 51, no. 6, pp. 2689-2696, 2020.

[95] F. Yang, M. J. Kim, M. Brown and B. J. Wiley, "Alkaline Water Electrolysis at 25 A cm−2 with a Microfibrous Flow-through Electrode," *Advanced Energy Materials,* vol. 10, no. 25, pp. 1-10, 2020.

[96] S. R. Mellsop, A. Gardiner and A. T. Marshall, "Spontaneous Deposition of Iridium onto Nickel Substrates for the Oxygen Evolution Reaction," *Electrocatalysis,* vol. 7, no. 3, pp. 226-234, 2016.

[97] M. Duca, E. Guerrini, A. Colombo and S. Trasatti, "Activation of Nickel for Hydrogen Evolution by Spontaneous Deposition of Iridium," *Electrocatalysis,* vol. 4, no. 4, pp. 338-345, 2013.

[98] M. Hao, J. Gaudet and D. Guay, "Ir Decorated Fractal Ni Catalysts for the Oxygen Evolution Reaction," in *The Electrochemical Society*, 2020.

[99] Q. Liang, G. Brocks and A. Bieberle-Hütter, "Oxygen evolution reaction (OER) mechanism under alkaline and acidic conditions," *JPhys Energy,* vol. 3, no. 2, 2021.

[100] M. Ni, M. K. Leung and D. Y. Leung, "An electrochemical model of a solid oxide steam electrolyzer for hydrogen production," *Chemical Engineering and Technology,* vol. 29, no. 5, pp. 636-642, 2006.

[101] M. B. Stevens, C. D. Trang, L. J. Enman, J. Deng and S. W. Boettcher, "Reactive Fe-Sites in Ni/Fe (Oxy)hydroxide Are Responsible for Exceptional Oxygen Electrocatalysis Activity," *Journal of the American Chemical Society,* vol. 139, no. 33, pp. 11361-11364, 2017.

[102] Q. Zhou, Y. Chen, G. Zhao, Y. Lin, Z. Yu, X. Xu, X. Wang, H. K. Liu, W. Sun and S. X. Dou, "Active-Site-Enriched Iron-Doped Nickel/Cobalt Hydroxide Nanosheets for Enhanced Oxygen Evolution Reaction," *ACS Catalysis,* vol. 8, no. 6, pp. 5382-5390, 2018.

[103] C. Wang, R. B. Moghaddam, M. J. Brett and S. H. Bergens, "Simple Aqueous Preparation of High Activity and Stability NiFe Hydrous Oxide Catalysts for Water Oxidation," *ACS Sustainable Chemistry and Engineering,* vol. 5, no. 1, pp. 1106-1112, 2017.

[104] L. Trotochaud, S. L. Young, J. K. Ranney and S. W. Boettcher, "Nickel-Iron oxyhydroxide oxygen-evolution electrocatalysts: The role of intentional and incidental iron incorporation," *Journal of the American Chemical Society,* vol. 136, no. 18, pp. 6744-6753, 2014.

[105] D. Sengupta, S. M. Privitera, R. G. Milazzo, C. Bongiorno, S. Scalese and S. Lombardo, "Ni foam electrode solution impregnated with Ni-Fe: X(OH)ycatalysts for efficient oxygen evolution reaction in alkaline electrolyzers," *RSC Advances,* vol. 10, no. 43, pp. 25426-25434, 2020.

[106] X. Lu and C. Zhao, "Electrodeposition of hierarchically structured three-dimensional nickel-iron electrodes for efficient oxygen evolution at high current densities," *Nature Communications,* vol. 6, 2015.

[107] F. Dionigi, Z. Zeng, I. Sinev, T. Merzdorf, S. Deshpande, M. B. Lopez, S. Kunze, I. Zegkinoglou, H. Sarodnik, D. Fan, A. Bergmann, J. Drnec, J. F. d. Araujo, M. Gliech, D. Teschner and Zh, "In-situ structure and catalytic mechanism of NiFe and CoFe layered double hydroxides during oxygen evolution," *Nature Communications,* vol. 11, no. 1, pp. 1-10, 2020.

[108] B. W. Xue, C. H. Zhang, Y. Z. Wang, W. W. Xie, N. W. Li and L. Yu, "Recent progress of Ni-Fe layered double hydroxide and beyond towards electrochemical water splitting," *Nanoscale Advances,* vol. 2, no. 12, pp. 5555-5566, 2020.

[109] Q. Zhou, G. Huang and C. Feng, "Iron-Doped Ni−Al Layered Double Hydroxide as an Efficient Oxygen Evolution Reaction Electrocatalyst," *ChemNanoMat,* vol. 8, no. 4, 2022.

[110] "An innovative approach to prepare porous Ni whisker for the oxygen evolution reaction".

[111] H. Assadi, T. Schmidt, H. Richter, J. O. Kliemann, K. Binder, F. Gärtner, T. Klassen and H. Kreye, "On parameter selection in cold spraying," *Journal of Thermal Spray Technology,* vol. 20, no. 6, pp. 1161-1176, 2011.

[112] D. Goldbaum, R. R. Chromik, S. Yue, E. Irissou and J. G. Legoux, "Mechanical property mapping of cold sprayed Ti splats and coatings," *Journal of Thermal Spray Technology,* vol. 20, no. 3, pp. 486-496, 2011.

[113] T. Schmidt, H. Assadi, F. Gärtner, H. Richter, T. Stoltenhoff, H. Kreye and T. Klassen, "From particle acceleration to impact and bonding in cold spraying," *Journal of Thermal Spray Technology,* vol. 18, no. 5-6, pp. 794-808, 2009.

[114] E. Osarolube, I. O. Owate and N. C. Oforka, "Corrosion behaviour of mild and high carbon steels in various acidic media," *Scientific Research and Essays,* vol. 3, no. 6, pp. 224-228, 2008.

[115] R. Nikbakht, H. Assadi, K. Jahani, M. Saadati and B. Jodoin, "Cold spray deformation and deposition of blended feedstock powders not necessarily obey the rule of mixture," *Surface and Coatings Technology,* vol. 424, pp. 1-15, 2021.

[116] E. Borgardt, O. Panchenko, F. J. Hackemüller, J. Giffin, M. Bram, M. Müller, W. Lehnert and D. Stolten, "Mechanical characterization and durability of sintered porous transport layers for polymer electrolyte membrane electrolysis," *Journal of Power Sources,* vol. 374, pp. 84-91, 2018.

[117] C. Jaeggi, R. Mooser, V. Frauchiger and P. Wyss, "3D characterization of open porous vacuum plasma sprayed titanium coatings by means of high resolution micro computer tomography," *Materials Letters,* vol. 63, no. 30, pp. 2643-2645, 2009.

[118] A. K. Tiwari, "On the dynamics of energy consumption and employment in public and private sector," *Journal of Applied Sciences Research,* vol. 6, no. 12, pp. 6525-6533, 2010.

[119] T. Kober, H. W. Schiffer, M. Densing and E. Panos, "Global energy perspectives to 2060 – WEC's World Energy Scenarios 2019," *Energy Strategy Reviews,* vol. 31, 2020.

[120] "World Oil Reserves," 01 01 2023. [Online]. Available: https://www.worldometers.info/oil/.

[121] S. C. Bhattacharyya, "The Economics of Renewable Energy Supply," *Energy Economics,* pp. 217-248, 2019.

[122] T. S. Adebayo, "Renewable Energy Consumption and Environmental Sustainability in Canada: Does Political Stability Make a Difference?," *Environmental Science and Pollution Research,* vol. 29, no. 40, pp. 61307-61322, 2022.

[123] J. Abbess, An Introduction to Renewable Gas, CRC press, 2015.

[124] L. Yao, B. Yang, H. Cui, J. Zhuang, J. Ye and J. Xue, "Challenges and progresses of energy storage technology and its application in power systems," *Journal of Modern Power Systems and Clean Energy,* vol. 4, no. 4, pp. 519-528, 2016.

[125] M. Y. Worku, "Recent Advances in Energy Storage Systems for Renewable Source Grid Integration: A Comprehensive Review," *Sustainability,* vol. 14, no. 10, 2022.

[126] S. Freund, M. Abarr, J. D.McTigue, K. L.Frick, A. Mathur, D. Reindl, A. V. Asselt and G. Casubolo, "Chapter 3. Sensible Thermal Energy Storage Materials," in *Thermal, Mechanical, and Hybrid Chemical Energy Storage Systems*, Elsevier Inc., 2021, pp. 42-54.

[127] S. Chavan, R. Rudrapati and S. Manickam, "A comprehensive review on current advances of thermal energy storage and its applications," *Alexandria Engineering Journal,* vol. 61, no. 7, pp. 5455-5463, 2022.

[128] Y. Miao, P. Hynan, A. Von Jouanne and A. Yokochi, "Current li-ion battery technologies in electric vehicles and opportunities for advancements," *Energies,* vol. 12, no. 6, pp. 1-20, 2019.

[129] "Lithium-ion batteries need to be greener and more ethical," *Nature,* vol. 595, p. 7, 2021.

[130] J. Sadhukhan and M. Christensen, "An in-depth life cycle assessment (Lca) of lithium-ion battery for climate impact mitigation strategies," *Energies,* vol. 14, no. 17, 2021.

[131] A. Züttel, "Hydrogen storage methods," *Naturwissenschaften,* vol. 91, no. 4, pp. 157-172, 2004.

[132] D. J. Jovan and G. Dolanc, "Can Green Hydrogen Production Be Economically Viable under Current Market Conditions," *Energy,* vol. 13, no. 6599, 2020.

[133] G. Chisholm, T. Zhao and L. Cronin, "Hydrogen from water electrolysis," in *Storing Energy: with Special Reference to Renewable Energy Sources*, Elsevier Inc., 2022, pp. 559-591.

[134] V. Grimnes and R. GMartinsen, "Electrodes," in *Electroencephalography and clinical neurophysiology. Supplement*, Elsevier Ltd., 2015, pp. 179-254.

[135] B. Sundén, "Electrochemistry and thermodynamics," in *Hydrogen, Batteries and Fuel Cells*, Elsevier, 2019, pp. 15-36.

[136] F. Torabi and P. Ahmadi, "Fundamentals of batteries," in *Simulation of Battery Systems*, Elsevier Inc, 2020, pp. 55-81.

[137] Y. Li, P. C. Tu, L. Zhou, A. M. Kirillov, R. Fang and L. Yang, "How Does the Catalyst Affect the Reaction Pathway? DFT Analysis of the Mechanism and Selectivity in the 1,6-Diyne Ester Cycloisomerization," *Organometallics,* vol. 37, no. 2, pp. 261-270, 2018.

[138] L. Du, L. Xing, G. Zhang, X. Liu, D. Rawach and S. Sun, "Engineering of electrocatalyst/electrolyte interface for ambient ammonia synthesis," *SusMat,* vol. 1, no. 2, pp. 150-173, 2021.

[139] P. K. Sahoo, S. R. Bisoi, Y. J. Huang, D. S. Tsai and C. P. Lee, "2d-layered non-precious electrocatalysts for hydrogen evolution reaction: Fundamentals to applications," *Catalysts,* vol. 11, no. 6, pp. 1-24, 2021.

[140] S. Wang, A. Lu and C. J. Zhong, "Hydrogen production from water electrolysis: role of catalysts," *Nano Convergence,* vol. 8, no. 1, 2021.

[141] C. Walter, P. W. Menezes and M. Driess, "Perspective on intermetallics towards efficient electrocatalytic water-splitting," *Chemical Science,* vol. 12, no. 25, pp. 8603-8631, 2021.

[142] S. Divanis, T. Kutlusoy, I. M. Ingmer Boye, I. C. Man and J. Rossmeisl, "Oxygen evolution reaction: A perspective on a decade of atomic scale simulations," *Chemical Science,* vol. 11, no. 11, pp. 2943-2950, 2020.

[143] I. Dincer and A. A. AlZahrani, "Electrolyzers," in *Comprehensive Energy Systems*, Elsevier, 2018.

[144] S. A. Grigoriev, V. N. Fateev, D. G. Bessarabov and P. Millet, "Current status, research trends, and challenges in water electrolysis science and technology," *International Journal of Hydrogen Energy,* vol. 45, no. 49, pp. 26036-26058, 2020.

[145] M. T. de Groot and A. W. Vreman, "Ohmic resistance in zero gap alkaline electrolysis with a Zirfon diaphragm," *Electrochimica Acta,* vol. 369, 2021.

[146] I. Vincent and E. C. H. M. Lee, "Comprehensive impedance investigation of low-cost anion exchange membrane electrolysis for large-scale hydrogen production," *Scientific Reports,* vol. 11, no. 1, pp. 1-12, 2021.

[147] H. MICHISHITA, H. MATSUMOTO and T. ISHIHARA, "Effects of Pressure on the Performance of Water Electrolysis of the Cell Using Nafion Membrane Electrode," *Electrochemistry,* vol. 76, no. 4, pp. 288-292, 2008.

[148] Q. Xu, L. Zhang, J. Zhang, J. Wang, Y. Hu, H. Jiang and C. Li, "Anion Exchange Membrane Water Electrolyzer: Electrode Design, Lab-Scaled Testing System and Performance Evaluation," *EnergyChem,* vol. 4, no. 5, 2022.

[149] A. Nechache and S. Hody, "Alternative and innovative solid oxide electrolysis cell materials: A short review," *Renewable and Sustainable Energy Reviews,* vol. 149, 2021.

[150] M. Çelikbilek, A. E. Ersundu and S. Aydın, "Advances in Crystallization Processes," in *Crystallization Kinetics of Amorphous Materials*, INTECH Open Access Publisher, 2011.

[151] A. J. Bard and L. R. Faulkner, Fundamentals and Applications Plasmonics : Fundamentals and Applications, Wiley, 2004.

[152] R. Anghilante and J. Lefebvre, "Coupling of a 3 Phase Methanation Reactor and a High Temperature Electrolyser using Matlab Simulink," in *11th European SOFC and SOE Forum 2014*, Luzern, 2014.

[153] W. Li, H. Tian, L. Ma, Y. Wang, X. Liu and X. Gao, "Low-temperature water electrolysis: fundamentals, progress, and new strategies," *Materials Advances,* vol. 3, no. 14, pp. 5598-5644, 2022.

[154] M. Mori, T. Mržljak, B. Drobnič and M. Sekavčnik, "Integral characteristics of hydrogen production in alkaline electrolysers," *Strojniski Vestnik/Journal of Mechanical Engineering,* vol. 59, no. 10, pp. 585-594, 2013.

[155] K. Bohinc, V. Kralj-Iglič and A. Iglič, "Thickness of electrical double layer. Effect of ion size," *Electrochimica Acta,* vol. 46, no. 19, pp. 3033-3040, 2001.

[156] E. Partheniades, "Forces between Clay Particles and the Process of Flocculation," in *Cohesive Sediments in Open Channels*, Elsevier, 2009, pp. 47-88.

[157] M. M. Waegele, C. M. Gunathunge, J. Li and X. Li, "How cations affect the electric double layer and the rates and selectivity of electrocatalytic processes," *Journal of Chemical Physics,* vol. 151, no. 16, 2019.

[158] E. J. F. Dickinson and G. Hinds, "The Butler-Volmer Equation for Polymer Electrolyte Membrane Fuel Cell (PEMFC) Electrode Kinetics: A Critical Discussion," *Journal of The Electrochemical Society,* vol. 166, no. 4, pp. F221-F231, 2019.

[159] T. Shinagawa, A. T. Garcia-Esparza and K. Takanabe, "Insight on Tafel slopes from a microkinetic analysis of aqueous electrocatalysis for energy conversion," *Scientific Reports,* vol. 5, no. 1, 2015.

[160] K. Scott, "Electrochemical Principles and Characterization of Bioelectrochemical Systems," in *Microbial Electrochemical and Fuel Cells: Fundamentals and Applications*, Elsevier, 2016.

[161] A. Vazhayil, L. Vazhayal, J. Thomas, S. Ashok C and N. Thomas, "A comprehensive review on the recent developments in transition metal-based electrocatalysts for oxygen evolution reaction," *Applied Surface Science Advances,* vol. 6, 2021.

[162] H. Ooka, A. Yamaguchi, T. Takashima, K. Hashimoto and R. Nakamura, "Efficiency of Oxygen Evolution on Iridium Oxide Determined from the pH Dependence of Charge Accumulation," *Journal of Physical Chemistry C,* vol. 121, no. 33, pp. 17873-17881, 2017.

[163] W. Wang, X. Wei, D. Choi, X. Lu, G. Yang and C. Sun, "Electrochemical cells for medium-and large-scale energy storage: Fundamentals," in *Advances in Batteries for Medium and Large-Scale Energy Storage: Types and Applications*, Elsevier, 2015.

[164] S. Trasatti, "Electrokinetics," *Encyclopedia of Electrochemical Power Sources,* pp. 23-31, 2009.

[165] A. Angulo, P. van der Linde, H. Gardeniers, M. Modestino and D. Fernández Rivas, "Influence of Bubbles on the Energy Conversion Efficiency of Electrochemical Reactors," *Joule,* vol. 4, no. 3, pp. 555-579, 2020.

[166] C. Lamy and P. Millet, "A critical review on the definitions used to calculate the energy efficiency coefficients of water electrolysis cells working under near ambient temperature conditions," *Journal of Power Sources,* vol. 447, 2020.

[167] K. Harrison, R. Remick and G. Martin, "Hydrogen Production: Fundamentals and Case Study Summaries; Preprint," in *18th World Hydrogen Energy Conference*, Essen, 2010.

[168] K. Zeng and D. Zhang, "Recent progress in alkaline water electrolysis for hydrogen production and applications," *Progress in Energy and Combustion Science,* vol. 36, no. 3, pp. 307-326, 2010.

[169] S. Saini, J. Halldin Stenlid and F. Abild-Pedersen, "Electronic structure factors and the importance of adsorbate effects in chemisorption on surface alloys," *npj Computational Materials,* vol. 8, no. 1, pp. 1-12, 2022.

[170] E. Fabbri, A. K. Habereder, R. Kötz and T. J. Schmidt, "Developments and perspectives of oxide-based catalysts for the oxygen evolution reaction," *Catalysis Science and Technology,* vol. 4, no. 11, pp. 3800-3821, 2014.

[171] Y. Wang, C. Xie, Z. Zhang, D. Liu, R. Chen and S. Wang, "In Situ Exfoliated, N-Doped, and Edge-Rich Ultrathin Layered Double Hydroxides Nanosheets for Oxygen Evolution Reaction," *Advanced Functional Materials,* vol. 28, no. 4, pp. 1-6, 2018.

[172] T. Tang, Z. Wang and J. Guan, "A review of defect engineering in two-dimensional materials for electrocatalytic hydrogen evolution reaction," *Chinese Journal of Catalysis,* vol. 43, no. 3, pp. 636-678, 2022.

[173] J. Zhang and S. Eslava, "Understanding charge transfer, defects and surface states at hematite photoanodes," *Sustainable Energy and Fuels,* vol. 3, no. 6, pp. 1351-1364, 2019.

[174] R. Zhang, Y. C. Zhang, L. Pan, G. Q. Shen, N. Mahmood, Y. H. Ma, Y. Shi, W. Jia, L. Wang, X. Zhang, W. Xu and J. J. Zou, "Engineering Cobalt Defects in Cobalt Oxide for Highly Efficient Electrocatalytic Oxygen Evolution," *ACS Catalysis,* vol. 8, no. 5, pp. 3803-3811, 2018.

[175] J. Li, Oxygen Evolution Reaction in Energy Conversion and Storage: Design Strategies Under and Beyond the Energy Scaling Relationship, Singapore: Springer Nature , 2022.

[176] Y. Zhao, X. Jia, G. Chen, L. Shang, G. I. Waterhouse, L. Z. Wu, C. H. Tung, D. Ohare and T. Zhang, "Ultrafine NiO Nanosheets Stabilized by TiO2 from Monolayer NiTi-LDH Precursors: An Active Water Oxidation Electrocatalyst," *Journal of the American Chemical Society,* vol. 138, no. 20, pp. 6517-6524, 2016.

[177] Z. Quan, Y. Wang and J. Fang, "High-index faceted noble metal nanocrystals," *Accounts of Chemical Research,* vol. 46, no. 2, pp. 191-202, 2013.

[178] H. Zhuang, A. J. Tkalych and E. A. Carter, "Surface Energy as a Descriptor of Catalytic Activity," *Journal of Physical Chemistry C,* vol. 120, no. 41, pp. 23698-23706, 2016.

[179] K. M. Cho, P. R. Deshmukh and W. G. Shin, "Hydrodynamic behavior of bubbles at gas-evolving electrode in ultrasonic field during water electrolysis," *Ultrasonics Sonochemistry,* vol. 80, 2021.

[180] H. Matsushima, T. Iida and Y. Fukunaka, "Gas bubble evolution on transparent electrode during water electrolysis in a magnetic field," *Electrochimica Acta,* vol. 100, pp. 261-264, 2013.

[181] M. Wang, Z. Wang and Z. Guo, "Understanding of the intensified effect of super gravity on hydrogen evolution reaction," *International Journal of Hydrogen Energy,* vol. 34, no. 13, pp. 5311-5317, 2009.

[182] R. Kaniowski, R. Pastuszko, J. Kowalczyk and Ł. Nowakowski, "Bubble departure diameter determination for pool boiling on surface with microchannels," in *E3S Web of Conferences*, 2018.

[183] I. Pranoto, U. F. Ramadhan, M. Habtry and L. Kai, "Characteristics of boiling bubble departure diameter and frequency from porous foam structures," *Integrated Lab Journal,* vol. 6, no. 2, pp. 75-84, 2018.

[184] J. Mo, Z. Kang, S. T. Retterer, D. A. Cullen, T. J. Toops, J. B. Green, M. M. Mench and F. Y. Zhang, "Discovery of true electrochemical reactions for ultrahigh catalyst mass activity in water splitting," *Science Advances,* vol. 2, no. 11, 2016.

[185] J. K. Lee, C. H. Lee, K. F. Fahy, P. J. Kim, J. M. LaManna, E. Baltic, D. L. Jacobson, D. S. Hussey, S. Stiber, A. S. Gago and K. A. A. Friedrich, "Spatially graded porous transport layers for gas evolving electrochemical energy conversion: High performance polymer electrolyte membrane electrolyzers," *Energy Conversion and Management,* vol. 226, 2020.

[186] T. S. Tshephe, S. O. Akinwamide, E. Olevsky and P. A. Olubambi, "Additive manufacturing of titanium-based alloys- A review of methods, properties, challenges, and prospects," *Heliyon,* vol. 8, no. 3, 2022.

[187] S. Kumar, R. Kumar and H. S. Sidhu, "The Role of Thermal Spray Coating to Combat Hot corrosion of Boiler Tubes: A Study," *Journal of Xidian University,* vol. 14, no. 5, 2020.

[188] R. Lupoi and W. O'Neill, "Powder stream characteristics in cold spray nozzles," *Surface and Coatings Technology,* vol. 206, no. 6, pp. 1069-1076, 2011.

[189] J. Freel, W. J. Pieters and R. B. Anderson, "The structure of Raney nickel. I. Pore structure," *Journal of Catalysis,* vol. 14, no. 3, pp. 247-256, 1969.

[190] G. D. Lee, M. J. Moon, J. H. Park, S. S. Park and S. S. Hong, "Raney ni catalysts derived from different alloy precursors part II. CO and CO2 methanation activity," *Korean Journal of Chemical Engineering,* vol. 22, no. 4, pp. 541-546, 2005.

[191] H. Lei, Z. Song, D. Tan, X. Bao, X. Mu, B. Zong and E. Min, "Preparation of novel Raney-Ni catalysts and characterization by XRD, SEM and XPS," *Applied Catalysis A: General,* vol. 214, no. 1, pp. 69-76, 2001.

[192] S. i. Tanaka, N. Hirose, T. Tanaki and Y. H. Ogata, "Effect of Ni-Al precursor alloy on the catalytic activity for a Raney-Ni cathode," *Journal of The Electrochemical Society,* vol. 147, no. 6, pp. 2242-2245, 2000.

[193] H. Fredriksson and U. Ãkerlind, Solidification and Crystallization Processing in Metals and Alloys, Wiley, 2012.

[194] R. Elliott, Eutectic Solidification Processing: Crystalline and Glassy Alloys, Elsevier Science, 2013.

[195] D. Stefanescu, "Eutectic Solidification," in *Science and Engineering of Casting Solidification*, Boston, Springer, 2002.

[196] R. Kakitani, R. V. Reyes, A. Garcia, J. E. Spinelli and N. Cheung, "Relationship between spacing of eutectic colonies and tensile properties of transient directionally solidified Al-Ni eutectic alloy," *Journal of Alloys and Compounds,* vol. 733, pp. 59-68, 2018.

[197] B. Lu, Y. Li, H. Wang, Y. Wang, W. Yu, Z. Wang and G. Xu, "Effects of cooling rates on the solidification behavior , microstructural evolution and mechanical properties of Al e Zn e Mg e Cu alloys," *Journal of Materials Research and Technology,* vol. 22, 2022.

[198] Q. C. Jiang, C. L. Xu, H. Y. Wang, J. G. Wang and Y. F. Yang, "Estimation of the shifting distance of the eutectic point in hypereutectic Al-Si alloys by the lever rule," *Scripta Materialia,* vol. 56, no. 5, pp. 329-332, 2007.

[199] M. A. Martínez-Villalobos, I. A. Figueroa, M. A. Suarez, G. Á. L. Rodríguez, O. N. Peralta, G. G. Reyes and I. A. López, "Microstructural evolution of rapid solidified Al-Ni alloys," *Journal of the Mexican Chemical Society,* vol. 60, no. 2, pp. 67-72, 2016.

[200] X. Li, J. Wang, L. Hou, A. Gagnoud and Y. Fautrelle, "Studying on the morphology of primary phase by 3D-CT technology and controlling eutectic growth by tailoring the primary phase," *Journal of Alloys and Compounds,* vol. 821, 2020.

[201] F. Hasse and Å. Ulla, "Faceted and Dendritic Solidification Structures," in *Solidification and Crystallization Processing in Metals and Alloys*, Sweden, Wiley, 2012.

[202] Y. X. Zhuang, X. M. Zhang, L. H. Zhu and Z. Q. Hu, "Eutectic spacing and faults of directionally solidified Al-Al3Ni eutectic," *Science and Technology of Advanced Materials,* vol. 2, no. 1, pp. 37-39, 2001.

[203] A. P. Carrara, R. Kakitani, A. Garcia and N. Cheung, "Effect of cooling rate on microstructure and microhardness of hypereutectic Al–Ni alloy," *Archives of Civil and Mechanical Engineering,* vol. 21, no. 1, pp. 1-9, 2021.

[204] G. Li, S. Li, J. Ge, C. Liu and W. Xing, "Discontinuously covered IrO2-RuO2@Ru electrocatalysts for the oxygen evolution reaction: How high activity and long-term durability can be simultaneously

realized in the synergistic and hybrid nano-structure," *Journal of Materials Chemistry A,* vol. 5, no. 33, pp. 17221-17229, 2017.

[205] D. Ruchira Liyanage, D. Li, Q. B. Cheek, H. Baydoun and S. L. Brock, "Synthesis and oxygen evolution reaction (OER) catalytic performance of Ni2-:XRuxP nanocrystals: Enhancing activity by dilution of the noble metal," *Journal of Materials Chemistry A,* vol. 5, no. 33, pp. 17609-17618, 2017.

[206] "Ir Decorated Fractal Ni Catalysts for the Oxygen Evolution Reaction".

[207] D. E. Pissinis, L. E. Sereno and J. M. Marioli, "Utilization of Special Potential Scan Programs for Cyclic Voltammetric Development of Different Nickel Oxide-Hydroxide Species on Ni Based Electrodes," *Open Journal of Physical Chemistry,* vol. 02, no. 01, pp. 23-33, 2012.

[208] D. Delgado, F. Bizzotto, A. Zana and M. Arenz, "Accelerated Durability Test for High-Surface-Area Oxyhydroxide Nickel Supported on Raney Nickel as Catalyst for the Alkaline Oxygen Evolution Reaction," *ChemPhysChem,* vol. 20, no. 22, pp. 3147-3153, 2019.

[209] S. Klaus, Y. Cai, M. W. Louie, L. Trotochaud and A. T. Bell, "Effects of Fe electrolyte impurities on Ni(OH)2/NiOOH structure and oxygen evolution activity," *Journal of Physical Chemistry C,* vol. 119, no. 13, pp. 7243-7254, 2015.

[210] M. Wilhelm, A. Bastos, C. Neves, R. Martins and J. Tedim, "Ni-Fe layered double hydroxides for oxygen evolution Reaction: Impact of Ni/Fe ratio and crystallinity," *Materials and Design,* vol. 212, 2021.

[211] M. Serhan, M. Sprowls, D. Jackemeyer, M. Long, I. D. Perez, W. Maret, N. Tao and E. Forzani, "Ni2P as a Janus catalyst for water splitting: the oxygen evolution activity of Ni2P nanoparticles," *Energy Environ. Sci,* vol. 8, p. 2347–2351, 2015.

[212] S. Shetty, M. Mohamed Jaffer Sadiq, D. K. Bhat and A. C. Hegde, "Electrodeposition and characterization of Ni-Mo alloy as an electrocatalyst for alkaline water electrolysis," *Journal of Electroanalytical Chemistry,* vol. 796, pp. 57-65, 2017.

[213] M. Praveen Kumar, M. Sasikumar, A. Arulraj, V. Rajasudha, G. Murugadoss, M. R. Kumar, S. Gouse Peera, R. Mangalaraja and Viswanathan, "NiFe Layered Double Hydroxide Electrocatalyst Prepared via an Electrochemical Deposition Method for the Oxygen," *Catalysts,* vol. 12, no. 11, 2022.

[214] T. T. Hoang and A. A. Gewirth, "High Activity Oxygen Evolution Reaction Catalysts from Additive-Controlled Electrodeposited Ni and NiFe Films," *ACS Catalysis,* vol. 6, no. 2, pp. 1159-1164, 2016.

[215] V. Torabinejad, M. Aliofkhazraei, S. Assareh, M. H. Allahyarzadeh and A. S. Rouhaghdam, "Electrodeposition of Ni-Fe alloys, composites, and nano coatings–A review," *Journal of Alloys and Compounds,* vol. 691, pp. 841-859, 2017.

[216] M. S. Ali Akbari, R. Bagheri, Z. Song and M. M. Najafpour, "Oxygen-evolution reaction by nickel/nickel oxide interface in the presence of ferrate(VI)," *Scientific Reports,* vol. 10, no. 1, pp. 1-11, 2020.

[217] J. I. Goldstein, D. E. Newbury, J. R. Michael, N. W. Ritchie, J. H. J. Scott and D. C. Joy, Scanning Electron Microscopy and X-Ray Microanalysis, Springer, 2017.

[218] M. Lee, X-Ray Diffraction for Materials Research: From Fundamentals to Applications, Apple Academic Press, 2017.

[219] G.-C. Wang and T.-M. Lu, "RHEED Transmission Mode and Pole Figures," in *RHEED Transmission Mode and Pole Figures: Thin Film and Nanostructure Texture Analysis*, New York, NY, Springer New York, 2014.

[220] D. B. Williams and C. B. Carter, Transmission Electron Microscopy: A Textbook for Materials Science, Springer, 2009.

[221] M. Naderi, "Surface Area: Brunauer-Emmett-Teller (BET)," Elsevier, 2015, pp. 585-608.

[222] M. D. Donohue and G. L. Aranovich, "A new classification of isotherms for Gibbs adsorption of gases on solids," *Fluid Phase Equilibria,* Vols. 158-160, pp. 557-563, 1999.

[223] Z. A. Alothman, "A review: Fundamental aspects of silicate mesoporous materials," *Materials,* vol. 5, no. 12, pp. 2874-2902, 2012.

[224] N. Elgrishi, K. J. Rountree, B. D. McCarthy, E. S. Rountree, T. T. Eisenhart and J. L. Dempsey, "A Practical Beginner's Guide to Cyclic Voltammetry," *Journal of Chemical Education,* vol. 95, no. 2, pp. 197-206, 2018.

[225] C. M. A. Brett and A. M. O. Brett, Electrochemistry: Principles, Methods, and Applications, Oxford University Press, 1993.

[226] D. M. Morales and M. Risch, "Seven steps to reliable cyclic voltammetry measurements for the determination of double layer capacitance," *JPhys Energy,* vol. 3, no. 3, 2021.

[227] F. Yu, H. Zhou, Y. Huang, J. Sun, F. Qin, J. Bao, W. A. Goddard, S. Chen and Z. Ren, "High-performance bifunctional porous non-noble metal phosphide catalyst for overall water splitting," *Nature Communications,* vol. 9, no. 1, pp. 1-9, 2018.

[228] A. U. Birnin-Yauri and M. Aliyu, "Synthesis and Analysis of Potassium Aluminium Sulphate (Alum) from Waste Aluminium Can," *International Journal of Advanced Research in Chemical Science (IJARCS),* vol. 1, no. 8, pp. 1-6, 2014.

[229] S. Sadamatsu, M. Tanaka, K. Higashida and S. Matsumura, "Transmission electron microscopy of bulk specimens over 10μm in thickness," *Ultramicroscopy,* vol. 162, pp. 10-16, 2016.

[230] E. Mignaioli, G. Capitani, F. Nieto and M. Mellini, "Accurate and precise lattice parameters by selected-area electron diffraction in the transmission electron microscope," *American Mineralogist,* vol. 94, pp. 793-800, 2009.

[231] Z. Ding, Q. Hu, W. Lu, S. Sun, M. Xia and J. Li, "In situ observation on the formation of intermetallics compounds at the interface of liquid Al/solid Ni," *Scripta Materialia,* vol. 130, pp. 214-218, 2017.

[232] Y. Sun, E. Yousefi, A. Kunwar, N. M. Seveno and M. Guo, "Study of the interfacial reactions controlling the spreading of Al on Ni," *Applied Surface Science,* vol. 571, no. 1, 2021.

[233] P. Colin, S. Hamar-Thibault and J. C. Joud, "Metallurgical structure and alkali leaching of the Al/Al3Ni eutectic," *Journal of Materials Science,* vol. 27, no. 9, pp. 2326-2334, 1992.

[234] M. Konieczny, R. Mola, P. Thomas and M. Kopcial, "Processing, microstructure and properties of laminated Ni-intermetallic composites synthesised using Ni sheets and Al foils," *Archives of Metallurgy and Materials,* vol. 56, no. 3, pp. 693-702, 2011.

[235] S. M. Arbo, T. Bergh, B. Holmedal, P. E. Vullum and I. Westermann, "Relationship between al-ni intermetallic phases and bond strength in roll bonded steel-aluminum composites with nickel interlayers," *Metals,* vol. 9, no. 8, 2019.

[236] H. Alimadadi, C. Kjartansdóttir, A. Burrows, T. Kasama and P. Møller, "Nickel-aluminum diffusion: A study of evolution of microstructure and phase," *Materials Characterization,* vol. 130, pp. 105-112, 2017.

[237] D. A. Porter, K. E. Easterling and M. Y. Sherif, "Crystal Interfaces and Microstructure," in *Phase Transformations in Metals and Alloys*, London, CRC Press, 2014.

[238] G. J. Shiflet, M. A. Mangan and W. G. Meng, "Growth by Ledges," *Interface Science,* vol. 6, no. 1-2, pp. 133-154, 1998.

[239] A. E. Paz y Puente and D. C. Dunand, "Effect of Cr content on interdiffusion and Kirkendall pore formation during homogenization of pack-aluminized Ni and Ni–Cr wires," *Intermetallics,* vol. 117, 2020.

[240] E. M. Hofer and H. E. Hintermann, "Correlation between the catalytic activity of Raney nickel and its structure," *Transactions of the Faraday Society,* vol. 60, pp. 1457-1465, 1964.

[241] S. Sun, H. Li and Z. J. Xu, "Impact of Surface Area in Evaluation of Catalyst Activity," *Joule,* vol. 2, no. 6, pp. 1024-1027, 2018.

[242] P. T. Babar, H. Zhao, W. Zou, Z. Chen, W. Cao, J. Fang, J. Xu, L. Zhang and J. Zhang, "Thermally oxidized porous NiO as an efficient oxygen evolution reaction (OER) electrocatalyst for electrochemical water splitting application," *Electrochemical Energy Reviews,* vol. 1, no. 4, pp. 483-530, 2018.

[243] T. Zhang, M. Y. Wu, D. Y. Yan, J. Mao, H. Liu, W. B. Hu, X. W. Du, T. Ling and S. Z. Qiao, "Engineering oxygen vacancy on NiO nanorod arrays for alkaline hydrogen evolution," *Nano Energy,* vol. 43, pp. 103-109, 2018.

[244] S. Fierro, T. Nagel, H. Baltruschat and C. Comninellis, "Investigation of the oxygen evolution reaction on Ti/IrO2 electrodes using isotope labelling and on-line mass spectrometry," *Electrochemistry Communications,* vol. 9, no. 8, pp. 1969-1974, 2007.

[245] Y. Yang, M. Zhou, W. Guo, X. Cui, Y. Li, F. Liu, P. Xiao and Y. Zhang, "NiCoO2 nanowires grown on carbon fiber paper for highly efficient water oxidation," *Electrochimica Acta,* vol. 174, pp. 246-253, 2015.

[246] J. Jiang, C. Zhang and L. Ai, "Hierarchical iron nickel oxide architectures derived from metal-organic frameworks as efficient electrocatalysts for oxygen evolution reaction," *Electrochimica Acta,* vol. 208, pp. 17-24, 2016.

[247] K. L. Yan, X. Shang, W. K. Gao, B. Dong, X. Li, J. Q. Chi, Y. R. Liu, Y. M. Chai and C. G. Liu, "Ternary MnO2/NiCo2O4/NF with hierarchical structure and synergistic interaction as efficient electrocatalysts for oxygen evolution reaction," *Journal of Alloys and Compounds,* vol. 719, pp. 314-321, 2017.

[248] G. Liu, X. Gao, X. Gao, D. He and J. Li, "Uniformly mesoporous NiO/NiFe2O4 biphasic nanorods as efficient oxygen evolving catalyst for water splitting," *International Journal of Hydrogen Energy,* vol. 41, no. 40, pp. 17976-17986, 2016.

[249] H. A. Bandal, A. R. Jadhav and H. Kim, "Facile synthesis of bicontinuous Ni3Fe alloy for efficient electrocatalytic oxygen evolution reaction," *Journal of Alloys and Compounds,* vol. 726, pp. 875-884, 2017.

[250] Y. Yang, L. Zhuang, R. Lin, M. Li, X. Xu, T. E. Rufford and Z. Zhu, "A facile method to synthesize boron-doped Ni/Fe alloy nano-chains as electrocatalyst for water oxidation," *Journal of Power Sources,* vol. 349, pp. 68-74, 2017.

[251] Y. Zhu, Y. Wang, S. Liu, R. Guo and Z. Li, "Facile and controllable synthesis at an ionic layer level of high-performance NiFe-based nanofilm electrocatalysts for the oxygen evolution reaction in alkaline electrolyte," *Electrochemistry Communications,* vol. 86, pp. 38-42, 2018.

[252] D. H. Youn, Y. B. Park, J. Y. Kim, G. Magesh, Y. J. Jang and J. S. Lee, "One-pot synthesis of NiFe layered double hydroxide/reduced graphene oxide composite as an efficient electrocatalyst for electrochemical and photoelectrochemical water oxidation," *Journal of Power Sources,* vol. 294, pp. 437-443, 2015.

[253] C. Xiao, B. Zhang and D. Li, "Partial-sacrificial-template Synthesis of Fe/Ni Phosphides on Ni Foam: A Strongly Stabilized and Efficient Catalyst for Electrochemical Water Splitting," *Electrochimica Acta,* vol. 242, pp. 260-267, 2017.

[254] C. K. Ranaweera, C. Zhang, S. Bhoyate, P. K. Kahol, M. Ghimire, S. R. Mishra, F. Perez, B. K. Gupta and R. K. Gupta, "Flower-shaped cobalt oxide nano-structures as an efficient, flexible and stable electrocatalyst for the oxygen evolution reaction," *Materials Chemistry Frontiers,* vol. 1, no. 8, pp. 1580-1584, 2017.

[255] X. Wang, T. T. Li and Y. Q. Zheng, "Co3O4 nanosheet arrays treated by defect engineering for enhanced electrocatalytic water oxidation," *International Journal of Hydrogen Energy,* pp. 2009-2017, 2018.

[256] S. M. Alshehri, J. Ahmed, T. Ahamad, P. Arunachalam, T. Ahmad and A. Khan, "Bifunctional electro-catalytic performances of CoWO4 nanocubes for water redox reactions (OER/ORR)," *RSC Advances,* vol. 7, no. 72, pp. 45615-45623, 2017.

[257] R. Souleymen, Z. Wang, W. K. Gao, B. Dong, X. Li and J. Q. Chi, "Microwave-assisted synthesis of graphene-like cobalt sulfide freestanding sheets as an efficient bifunctional electrocatalyst for overall water splitting," *Journal of Alloys and Compounds,* vol. 719, pp. 314-321, 2017.

[258] S. Lian, M. P. Browne, C. Domínguez, S. N. Stamatin, H. Nolan, G. S. Duesberg, M. E. Lyons, E. Fonda and P. E. Colavita, "Template-free synthesis of mesoporous manganese oxides with catalytic activity in the oxygen evolution reaction," *Sustainable Energy and Fuels,* vol. 1, no. 4, pp. 780-788, 2017.

[259] V. Maruthapandian, T. Pandiarajan, V. Saraswathy and S. Muralidharan, "Oxygen evolution catalytic behaviour of Ni doped Mn3O4 in alkaline medium," *RSC Advances,* vol. 6, no. 54, pp. 48995-49002, 2016.

[260] Y. Li, T. Zhao, M. Lu, Y. Wu, Y. Xie, H. Xu, J. Gao, J. Yao, G. Qian and Q. Zhang, "Enhancing Oxygen Evolution Reaction through Modulating Electronic Structure of Trimetallic Electrocatalysts Derived from Metal–Organic Frameworks," *Small,* vol. 15, no. 43, pp. 1-6, 2019.

[261] T. Wang, X. Liu, Z. Yan, Y. Teng, R. Li, J. Zhang and T. Peng, "Facile Preparation Process of NiCoP-NiCoSe2 Nano-Bilayer Films for Oxygen Evolution Reaction with High Efficiency and Long Duration," *ACS Sustainable Chemistry and Engineering,* vol. 8, no. 2, pp. 1240-1251, 2020.

[262] B. Zhang, X. Zheng, O. Voznyy, R. Comin, M. Bajdich, M. García-Melchor, M. García-Melchor, L. Han, J. Xu, M. Liu, L. Zheng, F. P. G. De Arquer, C. T. Dinh, F. Fan, M. Yuan, E. Yassitepe and N. Chen, "Homogeneously dispersed multimetal oxygen-evolving catalysts," *Science,* vol. 352, no. 6283, pp. 333-337, 2016.

[263] W. Chen, Y. Zhang, G. Chen, Y. Zhou, X. Xiang and K. K. Ostrikov, "Interface Coupling of Ni-Co Layered Double Hydroxide Nanowires and Cobalt-Based Zeolite Organic Frameworks for Efficient Overall Water Splitting," *ACS Sustainable Chemistry and Engineering,* vol. 7, no. 9, pp. 8255-8264, 2019.

[264] T. T. Hoang and A. A. Gewirth, "High Activity Oxygen Evolution Reaction Catalysts from Additive-Controlled Electrodeposited Ni and NiFe Films," *ACS Catalysis,* vol. 6, no. 2, pp. 1159-1164, 2016.

[265] L. Xu, F. T. Zhang, J. H. Chen, X. Z. Fu, R. Sun and C. P. Wong, "Amorphous NiFe Nanotube Arrays Bifunctional Electrocatalysts for Efficient Electrochemical Overall Water Splitting," *ACS Applied Energy Materials,* vol. 1, no. 3, pp. 1210-1217, 2018.

[266] Y. Gao, N. Zhang, C. Wang, F. Zhao and Y. Yu, "Construction of Fe2O3@CuO Heterojunction Nanotubes for Enhanced Oxygen Evolution Reaction," *ACS Applied Energy Materials,* vol. 3, no. 1, pp. 666-674, 2020.

[267] H. Fan, W. Chen, G. Chen, J. Huang, C. Song, Y. Du, C. Li and K. (. Ostrikov, "Plasma-heteroatom-doped Ni-V-Fe trimetallic phospho-nitride as high-performance bifunctional electrocatalyst," *Applied Catalysis B: Environmental,* vol. 268, 2020.

[268] J. Chen, J. Chen, H. Cui and C. Wang, "Electronic Structure and Crystalline Phase Dual Modulation via Anion-Cation Co-doping for Boosting Oxygen Evolution with Long-Term Stability under Large Current Density," *ACS Applied Materials and Interfaces,* vol. 11, no. 38, pp. 34819-34826, 2019.

[269] H. Zhou, F. Yu, Q. Zhu, J. Sun, F. Qin, L. Yu, J. Bao, Y. Yu, S. Chen and Z. Ren, "Water splitting by electrolysis at high current densities under 1.6 volts," *Energy and Environmental Science,* vol. 11, no. 10, pp. 2858-2864, 2018.

[270] J. Yuan, X. Cheng, C. Lei, B. Yang, Z. Li, K. Luo, K. H. Koko Lam, L. Lei, Y. Hou and K. K. Ostrikov, "Bimetallic Oxyhydroxide as a High-Performance Water Oxidation Electrocatalyst under Industry-Relevant Conditions," *Engineering,* vol. 7, no. 9, pp. 1306-1312, 2021.

[271] L. M. L. M. Cao, Y. W. Hu, S. F. Tang, A. J. W. Iljin, Z. M. Zhang and T. B. Lu, "Fe-CoP Electrocatalyst Derived from a Bimetallic Prussian Blue Analogue for Large-Current-Density Oxygen Evolution and Overall Water Splitting," *Advanced Science,* vol. 5, no. 10, pp. 1-9, 2018.

[272] A. Bucci, S. S. Mondal, V. Martin-Diaconescu, A. Shafir and J. Lloret-Fillol, "Cobalt Amide Imidate Imidazolate Frameworks as Highly Active Oxygen Evolution Model Materials," *ACS Applied Energy Materials,* vol. 2, no. 12, pp. 8930-8938, 2019.

[273] H. Zhou, F. Yu, J. Sun, R. He, S. Chen, C. W. Chu and Z. Ren, "Highly active catalyst derived from a 3D foam of Fe(PO3)2/Ni2P for extremely efficient water oxidation," *Proceedings of the National Academy of Sciences of the United States of America,* vol. 114, no. 22, pp. 5607-5611, 2017.

[274] Y. Wu, H. Wang, S. Ji, X. Tian, G. Li, X. Wang and R. Wang, "Ultrastable NiFeOOH/NiFe/Ni electrocatalysts prepared by in-situ electro-oxidation for oxygen evolution reaction at large current density," *Applied Surface Science,* vol. 564, pp. 1-8, 2021.

[275] C. I. Müller, "RANEY-NI ELECTRODES FOR THE ALKALINE ELECTROLYSIS OF WATER," in *International conference on electrolysis*, 2017.

[276] "Alibaba Group Official Website," 21 11 2023. [Online]. Available: https://www.alibaba.com/.

[277] "Amazon," 21 11 2023. [Online]. Available: https://www.amazon.com/.

[278] "Fisher Scientific," 21 11 2023. [Online]. Available: https://www.fishersci.com/.

[279] K. Jiang, M. Luo, M. Peng, Y. Yu, Y.-R. Lu, T.-S. Chan, P. Liu, F. M. F. de Groot and Y. Tan, "Dynamic active-site generation of atomic iridium stabilized on nanoporous metal phosphides for water oxidation," *Nature Communications,* vol. 11, no. 1, 2020.

[280] A. Raveendran, M. Chandran and R. Dhanusuraman, "A comprehensive review on the electrochemical parameters and recent material development of electrochemical water splitting electrocatalysts," *RSC Advances,* vol. 13, no. 6, 2023.

[281] A. Wang, W. Wang, J. Xu, C. Zhao, M. Yu, L. Wang, H. Zhang, X. Zhou, X. Bao and W. Wang, "Recent advances in the rational design of alkaline OER catalysts: from electronic structures to industrial applications," *Materials Chemistry Frontiers,* vol. 7, no. 21, 2023.

[282] B. S. Lee, S. H. Ahn, H. Y. Park, I. Choi, S. J. Yoo, H. J. Kim, D. Henkensmeier, J. Y. Kim, S. Park, S. W. Nam, K. Y. Lee and J. H. Jang, "Development of electrodeposited IrO2 electrodes as anodes in polymer electrolyte membrane water electrolysis," *Applied Catalysis B: Environmental,* vol. 179, pp. 285-291, 2015.

[283] D. F. Abbott, D. Lebedev, K. Waltar, M. Povia, M. Nachtegaal, E. Fabbri, C. Copéret and T. J. Schmidt, "Iridium oxide for the oxygen evolution reaction: Correlation between particle size, morphology, and the surface hydroxo layer from operando XAS," *Chemistry of Materials,* vol. 28, no. 18, pp. 6591-6604, 2016.

[284] S. Song, H. Zhang, X. Ma, Z. Shao, R. T. Baker and B. Yi, "Electrochemical investigation of electrocatalysts for the oxygen evolution reaction in PEM water electrolyzers," *International Journal of Hydrogen Energy,* vol. 33, no. 19, pp. 4955-4961, 2008.

[285] S. Siracusano, V. Baglio, A. Stassi, R. Ornelas, V. Antonucci and A. S. Aric, "Investigation of IrO2 electrocatalysts prepared by a sulfite-couplex route for the O2 evolution reaction in solid polymer electrolyte water electrolyzers," *International Journal of Hydrogen Energy,* vol. 36, no. 13, pp. 7822-7831, 2011.

[286] E. Slavcheva, I. Radev, S. Bliznakov, G. Topalov, P. Andreev and E. Budevski, "Sputtered iridium oxide films as electrocatalysts for water splitting via PEM electrolysis," *Electrochimica Acta,* vol. 52, no. 12, pp. 3889-3894, 2007.

[287] W. Yang, L. Zhang, Y. Hua and L. Cheng, "Thermal stability of iridium coating prepared by MOCVD," *International Journal of Refractory Metals and Hard Materials,* vol. 27, no. 1, pp. 33-36, 2009.

[288] D. Chandra, D. Takama, T. Masaki, T. Sato, N. Abe, T. Togashi, M. Kurihara, K. Saito, T. Yui and M. Yagi, "Highly Efficient Electrocatalysis and Mechanistic Investigation of Intermediate IrOx(OH)y Nanoparticle Films for Water Oxidation," *ACS Catalysis,* vol. 6, no. 6, pp. 3946-3954, 2016.

[289] M. Luba, T. Mikolajczyk and B. Pierozynski, "Hydrogen Evolution Reaction on Iridium-Modified Nickel Foam Surfaces," *Electrocatalysis,* vol. 11, no. 3, pp. 347-353, 2020.

[290] G. R. Lee, J. Kim, D. Hong, Y. J. Kim, H. Jang, H. J. Han, C.-K. wang, D. Kim, J. Y. Kim and Y. S. Jung, "Efficient and sustainable water electrolysis achieved by excess electron reservoir enabling charge replenishment to catalysts," *Nature Communications,* vol. 14, no. 1, 2023.

[291] J. Juodkazyte, B. Šebeka, G. Stalnionis and K. Juodkazis, "EQCM study of iridium anodic oxidation in H2SO4 and KOH solutions," *Electroanalysis,* vol. 17, no. 19, pp. 1734-1739, 2005.

[292] J. G. Baker, J. R. Schneider, J. A. Garrido Torres, J. A. Singh, A. J. MacKus, M. Bajdich and S. F. Bent, "The Role of Aluminum in Promoting Ni-Fe-OOH Electrocatalysts for the Oxygen Evolution Reaction," *ACS Applied Energy Materials,* vol. 2, no. 5, pp. 3488-3499, 2019.

[293] P. Ayivor, J. Torres, J. Torres, R. Van Der Pluijm and B. Stouwie, "Modelling of Large Size Electrolyzer for Electrical Grid Stability Studies in Real Time Digital Simulation," *3rd International Hybrid Power Systems Workshop,* 2018.

[294] C. V. Pham, D. K. Escalera-López, S. Cherevko and S. Thiele, "Essentials of High Performance Water Electrolyzers – From Catalyst Layer Materials to Electrode Engineering," *Advanced Energy Materials,* vol. 11, no. 44, 2021.

[295] M. Bernt, A. Hartig-Weiß, M. F. Tovini, H. A. El-Sayed, C. Schramm, J. Schröter, C. Gebauer and H. A. Gasteiger, "Current Challenges in Catalyst Development for PEM Water Electrolyzers," *Chemie-Ingenieur-Technik,* vol. 92, no. 1-2, pp. 31-39, 2020.

[296] O. F. Selamet and M. S. Ergoktas, "Effects of bolt torque and contact resistance on the performance of the polymer electrolyte membrane electrolyzers," *Journal of Power Sources,* vol. 281, pp. 103-113, 2015.

[297] W. J. Gannon and C. W. Dunnill, "Raney Nickel 2.0: Development of a high-performance bifunctional electrocatalyst," *Electrochimica Acta,* vol. 322, 2019.

[298] X. Li, J. Wang, L. Hou, A. Gagnoud and Y. Fautrelle, "Studying on the morphology of primary phase by 3D-CT technology and controlling eutectic growth by tailoring the primary phase," *Journal of Alloys and Compounds,* vol. 821, 2020.

9 APPENDIX

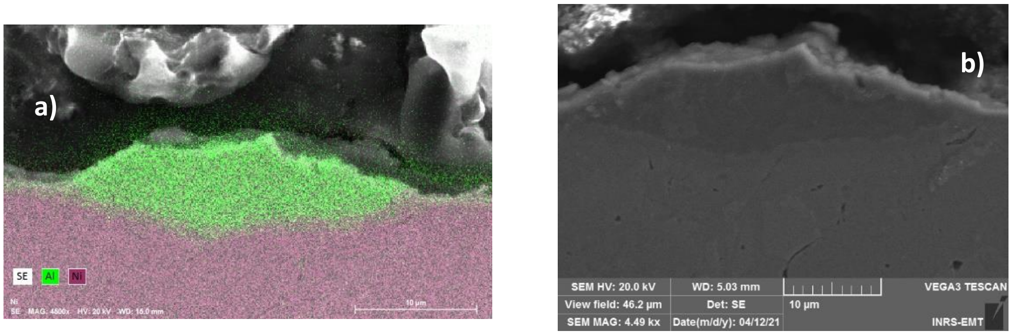

Figure S1: Cross section of S670-1-0.3 a) before leaching and b) after 24 hours of leaching. The image shows an Al particle that has melted onto a Ni surface to form Ni_2Al_3.

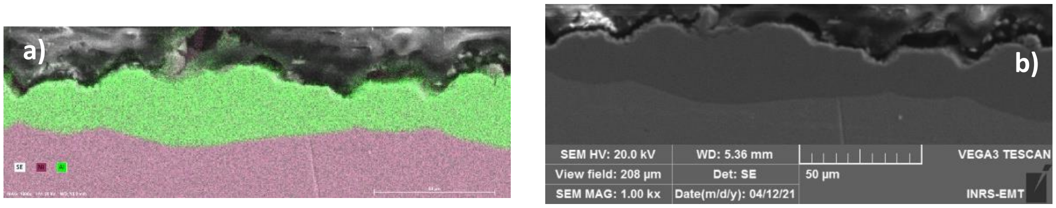

Figure S2: Cross section of S670-1-1.5 a) before leaching and b) after 24 hours of leaching. No Ni whiskers is seen after leaching.

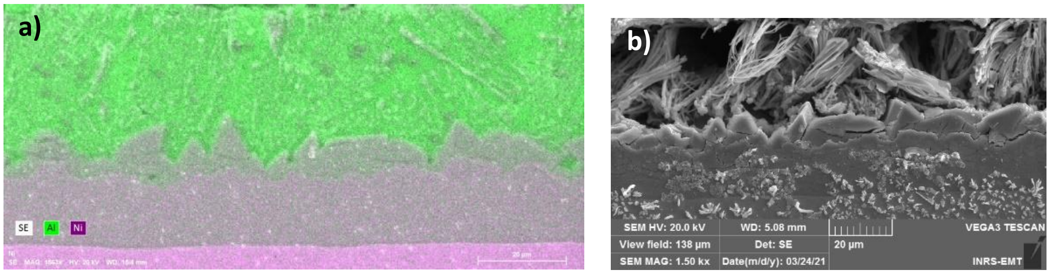

Figure S3: Cross section of S670-1-15 a) before leaching and b) after 24 hours of leaching.

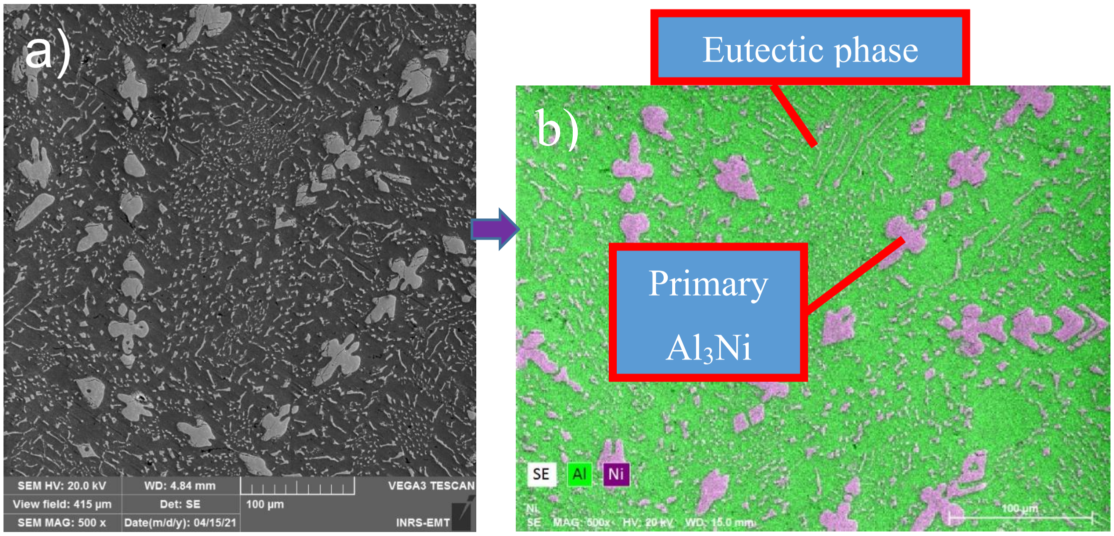

Figure S4: Top view of S670-10-350. a) SEM image, b) EDX mapping.

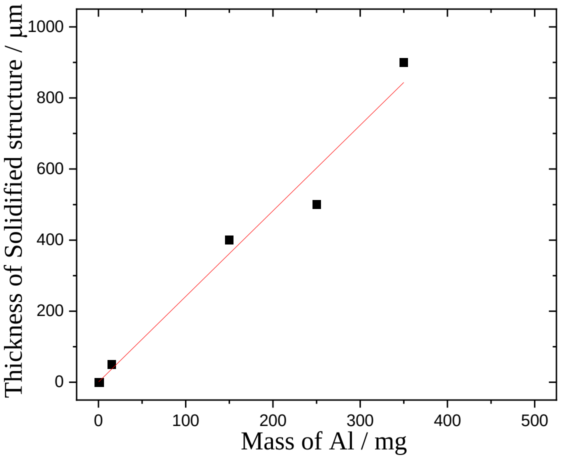

Figure S5: The effect of Al mass on the thickness of solidified layer for samples produced by 0.3-350 mg Al. The maximum operating temperature was 670 °C and the elapsed time at the maximum operating temperature was 1 minute.

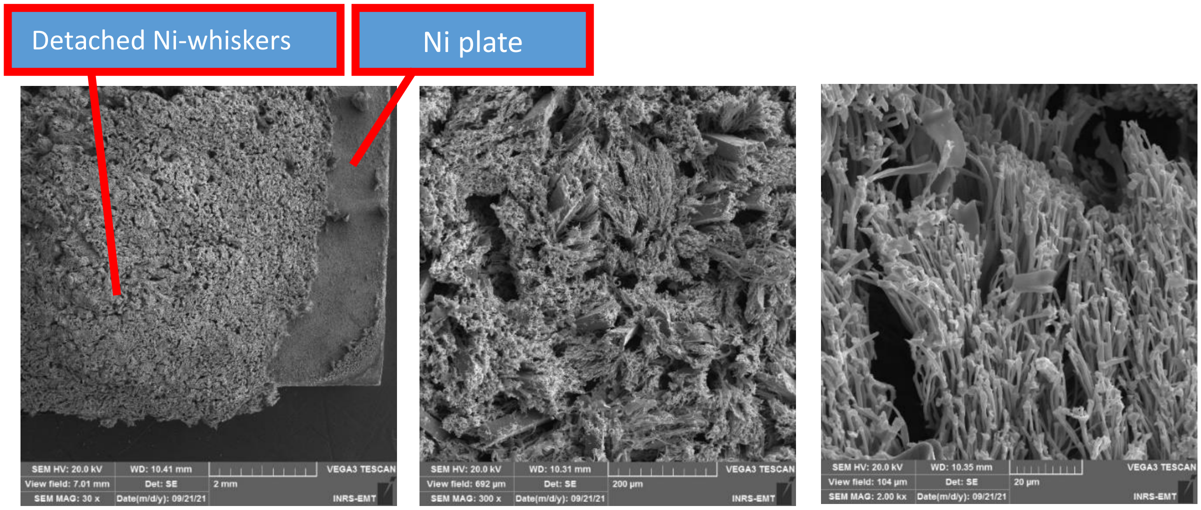

Figure S6: The top surface of detached Ni-whiskers of S670-1-350 at different magnification

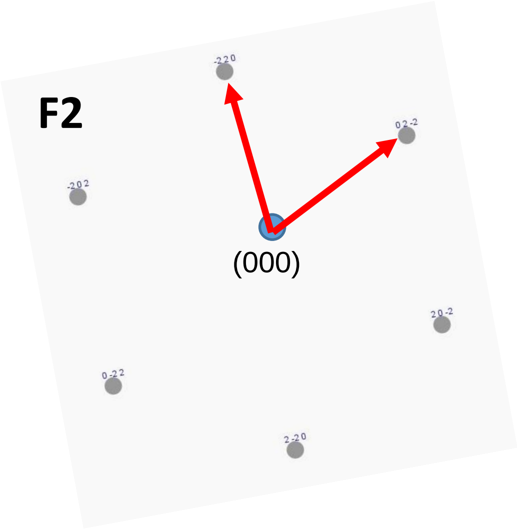

Figure S7: The schematic illustration displays the diffraction pattern of a single crystal of Ni, where the projection plane is {111} plane.

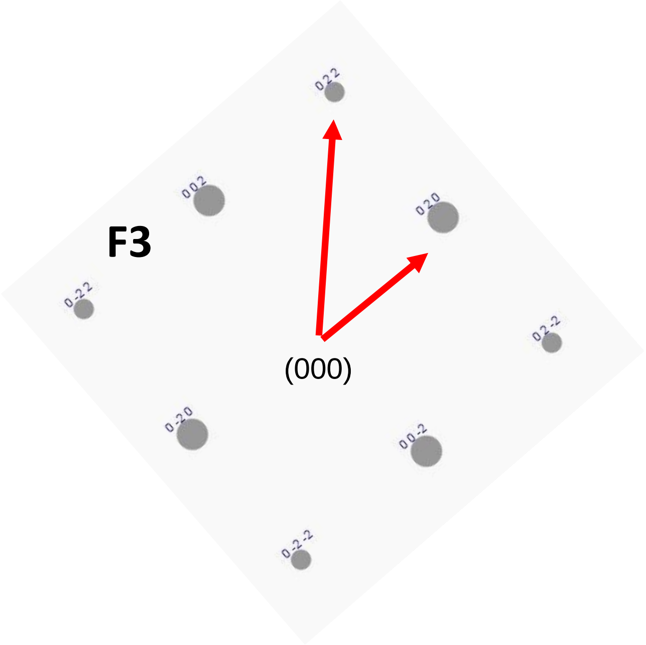

Figure S8: The schematic illustration displays the diffraction pattern of a single crystal of Ni, where the projection plane is {100} plane.

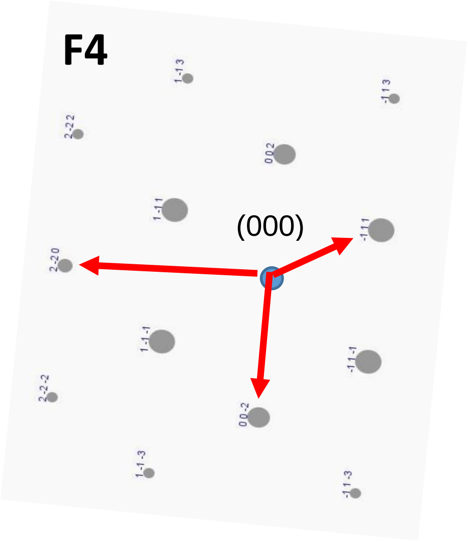

Figure S9: The schematic illustration displays the diffraction pattern of a single crystal of Ni, where the projection plane is {110} plane.

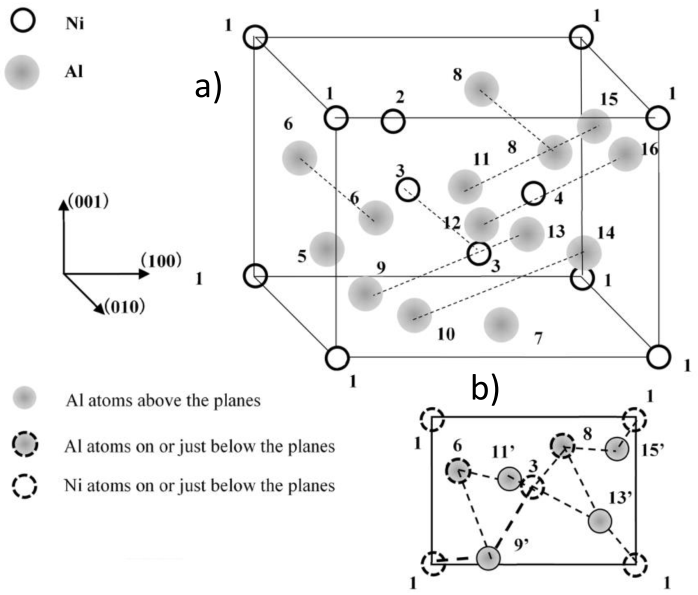

Figure S10: A visual depiction of the crystal lattice of Al3Ni is presented, illustrating the arrangement of Al and Ni atoms within a) a unit cell and b) along the (010) plane [82].

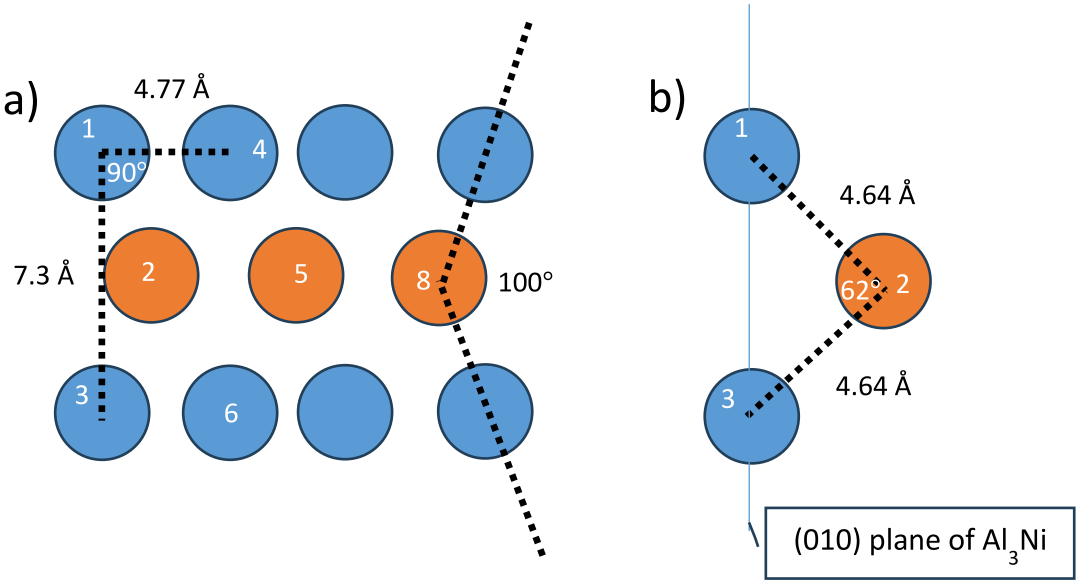

Figure S11: Ni atoms orientation on (010) planes of Al3Ni. Blue atoms are located in the (010) plane, while orange atoms are positioned just above the (010) plane. a) Front view, b) Side view.

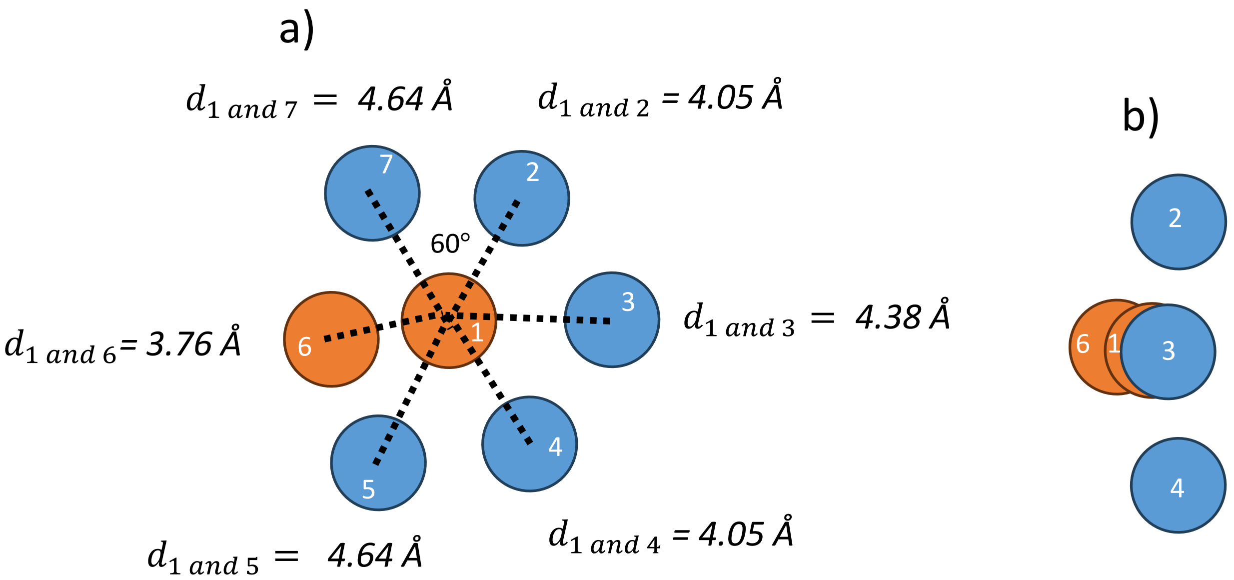

Figure S12: Ni atoms orientation on (230) planes of Al3Ni. Blue atoms are located in (230) plane, while orange atoms are positioned just above the (230) plane. a) Front view, b) Side view.

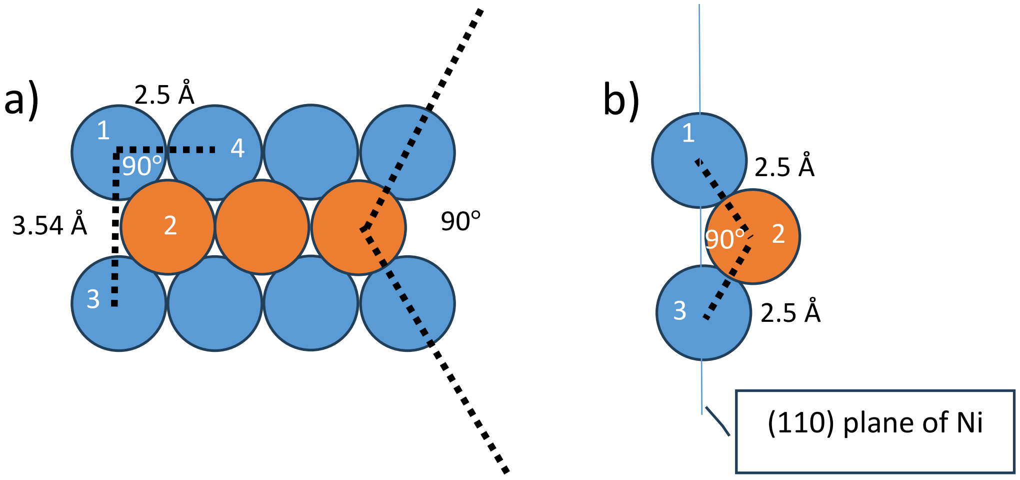

Figure S13: (110) planes of Ni. Blue atoms are located in the (110) plane, while orange atoms are positioned just above the (110) plane. a) Front view, b) Side view.

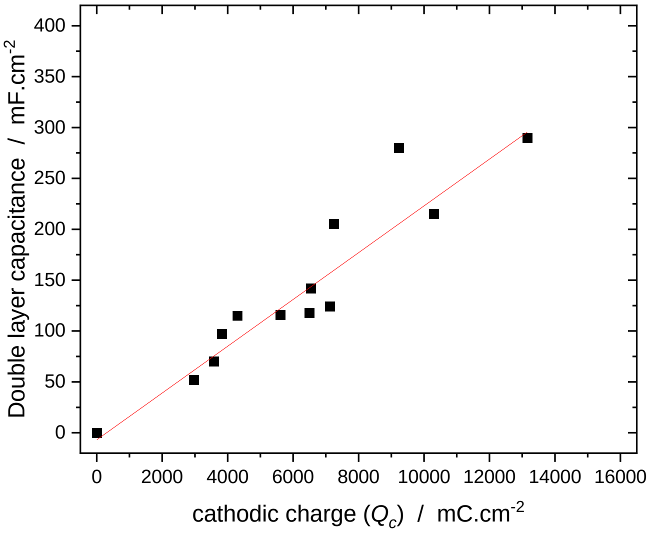

Figure S14: The linear relationship between the double-layer capacitance and the cathodic charge is established among all the Ni whiskers examined in this study.

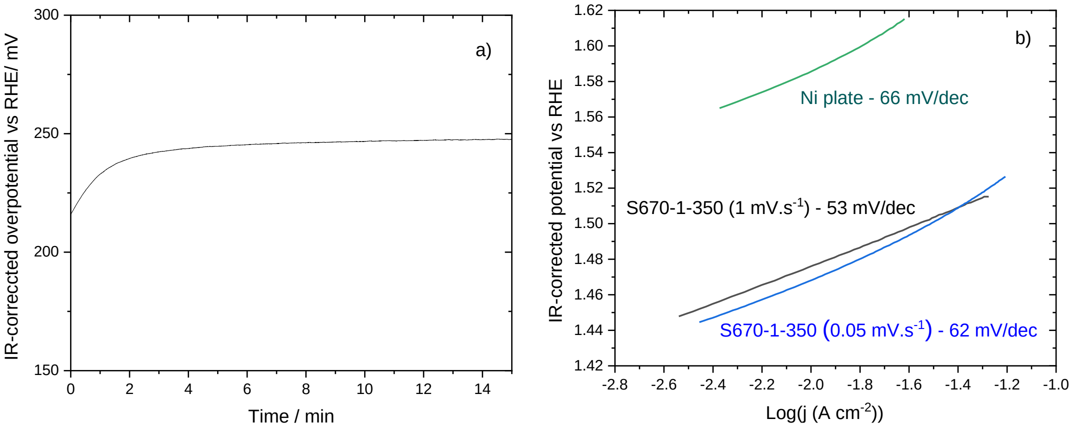

Figure S15: a) Recorded galvanostatic at 10 mA.cm^{-2} for S60-1-350. b) Recorded Tafel plot for S670-1-350 at scan rates of 1 mV.s^{-1} and 0.05 mV.s^{-1}.

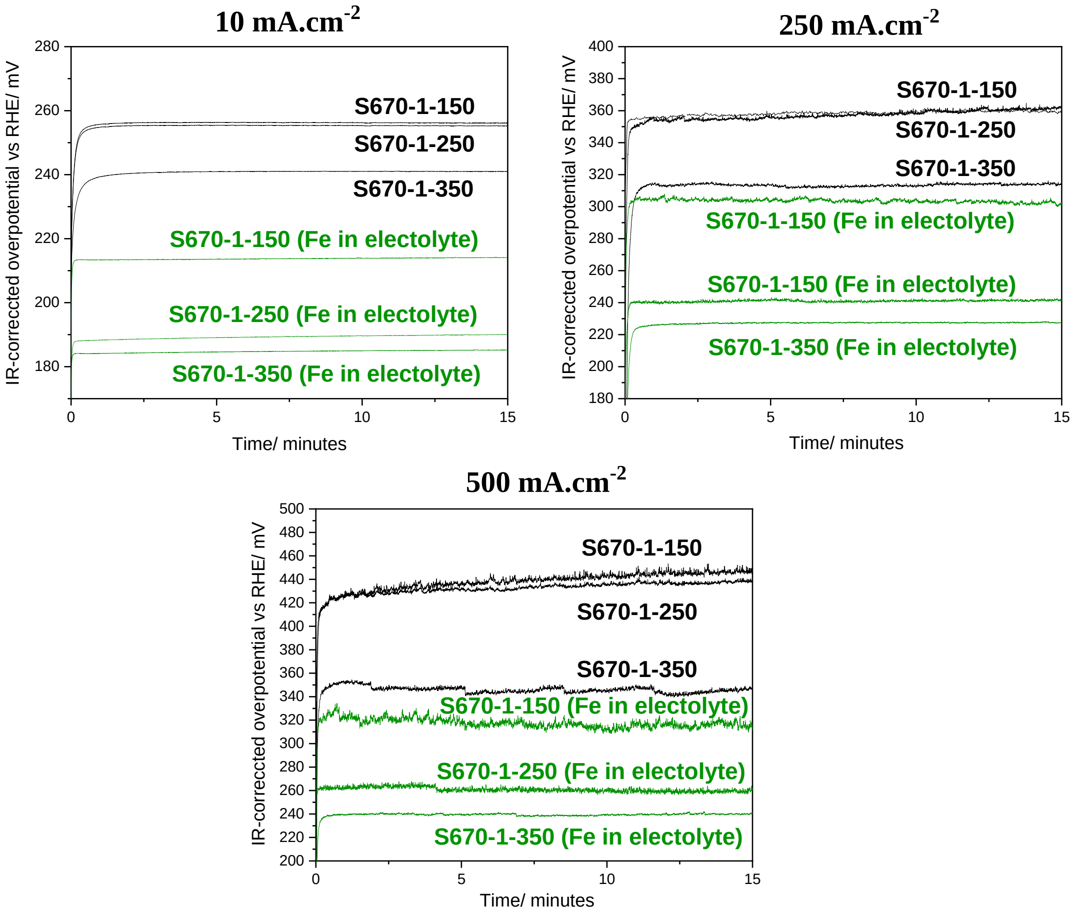

Figure S16: Recorded galvanostatic at 10, 250 and 500 mA.cm^{-2}.

Stability test

The galvanostatic oxidation process consisted of three stages, each lasting for 48 hours. Fresh electrolyte was used for each stage, and potential was measured after 30 minutes of polarization, indicated by green stars. Additionally, after 24 hours into each stage, distilled water was added to the electrolyte, and potential was measured again after 30 minutes of polarization, indicated by orange stars. After the completion of the three stages (totaling 144 hours), the potential was measured in fresh electrolyte after 30 minutes of polarization, indicated by the last green star. The experiment utilized only one sample, which operated for the entire 144 hours.

For current densities of 10 and 50 mA.cm^{-2}, the electrolyte was not replaced, and only distilled water was added to it.

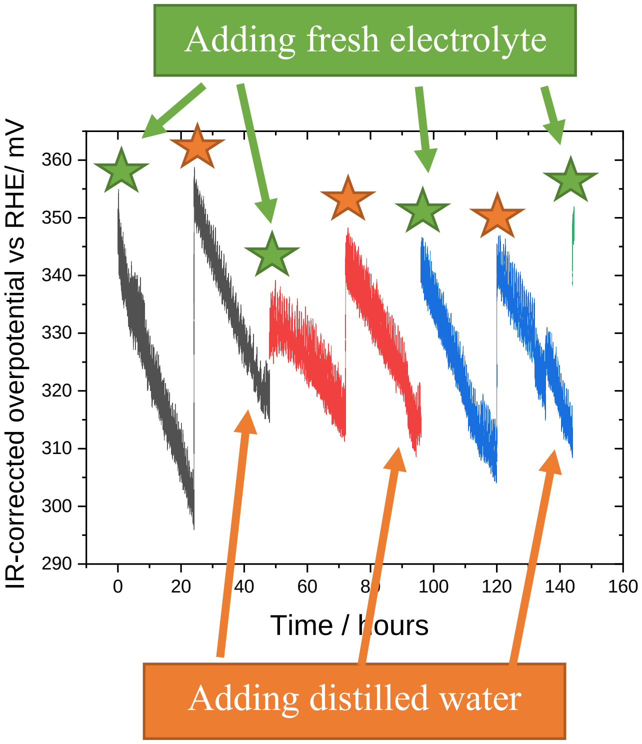

Figure S17: Recorded galvanostatic for S670-1-350 sample at 500 mA.cm^{-2} for 144 hours.

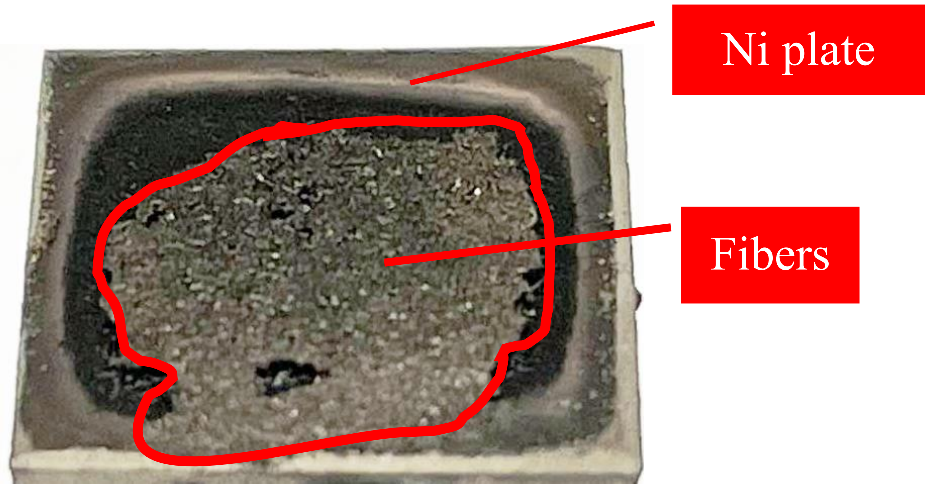

Figure S18: Image of S1-20Ir after performing cyclic voltammograms at 50 mV.s^{-1}.

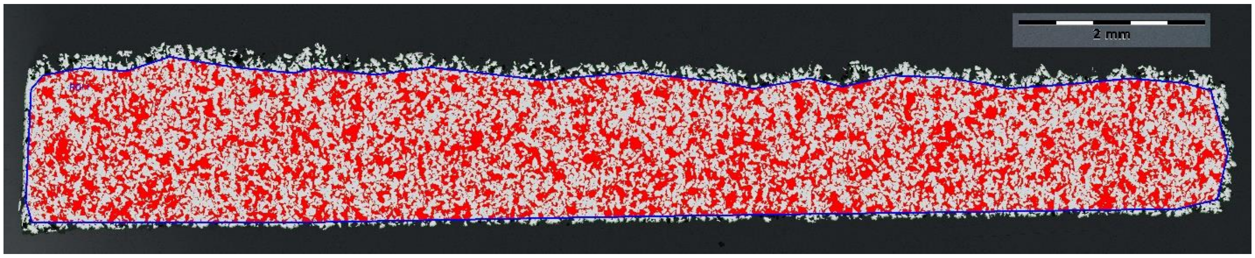

Figure S19: Typical example of a cross-section optical microscopy image used to estimate the porosity of coatings. In this figure, the optical microcopy image of the as-deposited Ti-73 sample deposited by the SWIS technique is shown. The white areas are the Ti particles, while the red area are the pores.

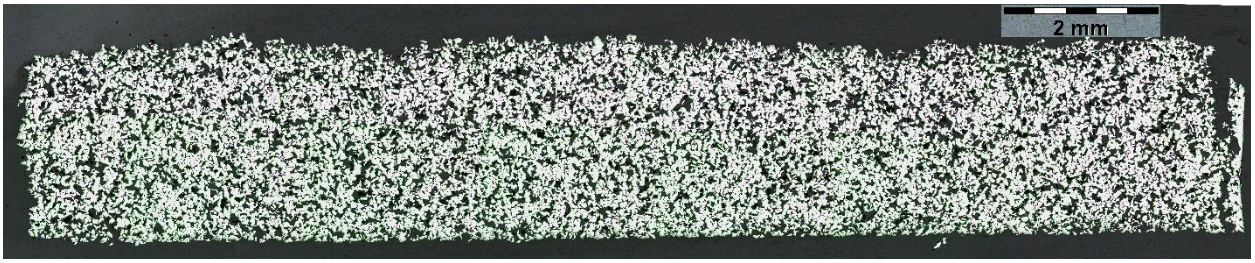

Figure S20: Ti30Cu Sample after leaching in HNO_3. All Cu particles are dissolved from the coating. Also, the coating is detached from the substrate.